Imperial College London
National Heart & Lung Institute

Development of whole-heart myocardial perfusion magnetic resonance imaging

Merlin John Casper Fair

2017

Supervised by Dr Peter Gatehouse and Prof David Firmin

Submitted in part fulfilment of the requirements for the degree of Doctor of Philosophy from the National Heart & Lung Institute of Imperial College London and the Diploma of Imperial College London

I hereby certify that the following thesis is entirely my own work, and that any ideas or quotations from other work contained within are appropriately referenced.

Signed:

Merlin Fair

Copyright

Abstract

Myocardial perfusion imaging is of huge importance for the detection of coronary artery disease (CAD), one of the leading causes of morbidity and mortality worldwide, as it can provide non-invasive detection at the early stages of the disease. Magnetic resonance imaging (MRI) can assess myocardial perfusion by capturing the first-pass perfusion (FPP) of a gadolinium-based contrast agent (GBCA), which is now a well-established technique and compares well with other modalities. However, current MRI methods are restricted by their limited coverage of the left ventricle. Interest has therefore grown in 3D volumetric "whole-heart" FPP by MRI, although many challenges currently limit this. For this thesis, myocardial perfusion assessment in general, and 3D whole-heart FPP in particular, were reviewed in depth, alongside MRI techniques important for achieving 3D FPP. From this, a 3D 'stack-of-stars' (SOS) FPP sequence was developed with the aim of addressing some current limitations. These included the breath-hold requirement during GBCA first-pass, long 3D shot durations corrupted by cardiac motion, and a propensity for artefacts in FPP. Parallel imaging and compressed sensing were investigated for accelerating whole-heart FPP, with modifications presented to potentially improve robustness to free-breathing. Novel sequences were developed that were capable of individually improving some current sequence limits, including spatial resolution and signal-to-noise ratio, although with some sacrifices. A final 3D SOS FPP technique was developed and tested at stress during free-breathing examinations of CAD patients and healthy volunteers. This enabled the first known detection of an inducible perfusion defect with a free-breathing, compressed sensing, 3D FPP sequence; however, further investigation into the diagnostic performance is required. Simulations were performed to analyse potential artefacts in 3D FPP, as well as to examine ways towards further optimisation of 3D SOS FPP. The final chapter discusses some limitations of the work and proposes opportunities for further investigation.

In loving memory of Vivien Mary Fair

Acknowledgements

I owe a great deal to many people throughout the duration of my PhD, who have made its completion not only possible but enjoyable.
I would first like to thank my supervisors, who have been a constant source of support. Both Peter and David have always been available for advice and have, I hope, enabled me to reach my full potential. I could not have asked for better supervision.
I would like to thank all my colleagues at the Royal Brompton Hospital for creating such an enjoyable working environment, in particular the rest of the Physics group, all of whom I will greatly miss.
I would also like to extend my thanks to Prof DiBella and his group at the University of Utah, not only for their invaluable assistance in the project, but also for being so warm and welcoming during my visits.
I am extremely grateful to my examiners for their time spent in assessing this thesis, as well as for their advice and guidance provided during the examination that I hope to take forward into my future work.
I am also very fortunate to have had a great group of friends supporting me throughout the PhD in many different ways. Last but certainly not least, many thanks to my family, whose belief and support has, as ever, been unwavering.
Finally, I would like to thank the British Heart Foundation (BHF), whose funding of the project (FS/13/21/30143) made all of this possible.

Contents

List of Tables

List of Figures

List of Acronyms

AA	average all
ASL	arterial spin labelling
$BOLD$	blood-oxygen-level dependent
$bSSFP$	balanced steady-state free precession
$BWTP$	bandwidth-time product
CS	compressed sensing
CAD	coronary artery disease
CT	computed tomography
CTA	computed tomography angiography
CNR	contrast-to-noise ratio
CRM	constraint reordering method
CXA	coronary x-ray angiography
DRA	dark-rim artefact
ECG	electrocardiogram
EPI	echo-planar imaging
ETL	echo-train length
FFR	fractional flow reserve
FFT	fast Fourier transform
$FLASH$	fast low angle shot
FOV	field-of-view
FPP	first-pass perfusion
$FWHM$	full-width at half-maximum
$GBCA$	gadolinium based contrast agent
$h-EPI$	hybrid echo-planar imaging
HLA	horizontal long axis
KL	Karhunen-Loève
LAD	left anterior descending (coronary artery)
LAX	long-axis
LCx	left circumflex (coronary artery)
LDL	low density lipoprotein

LGE	late gadolinium enhancement
LV	left ventricle
MA	moving average
MFP	multiple free-breathing prescans
MI	myocardial infarction
MPS	myocardial perfusion scintigraphy
MRI	magnetic resonance imaging
$NICE$	National Institute for Health and Care Excellence
$NUFFT$	non-uniform fast Fourier transform
PCA	principal component analysis
$PDRA$	partition dark-rim artefact
PET	positron emission tomography
PI	parallel imaging
$POCS$	projections onto convex sets
PSF	point spread function
QCA	quantitative coronary angiography
RF	radiofrequency
rPF	read partial Fourier
RCA	right coronary artery
$RRMSE$	relative root-mean-square error
SAR	specific absorption rate
SAX	short-axis
$SGRE$	spoiled gradient-echo
SNR	signal-to-noise ratio
SOS	stack-of-stars
$SPECT$	single-photon emission computed tomography
sPF	slice partial Fourier
SRT	saturation recovery time
$STCR$	spatio-temporally constrained reconstruction
TCR	temporally constrained reconstruction
TV	total variation
US	ultrasound
VLA	vertical long axis
VU	variable undersampling

1. Myocardial Perfusion

1.1. Introduction

To understand the desire for whole-heart myocardial perfusion imaging using MRI and its potential role within the clinical setting, an introduction to myocardial perfusion is required. This includes its physiological basis, diagnostic relevance, different methods for assessment and how these compare to current MRI techniques.

Much of the information stated within this chapter is considered "textbook" knowledge and can be found in books such as [Fuster et al., 2011], [Betts et al., 2016] and [Haacke et al., 1999], along with the further reading provided.

1.2. Cardiovascular Physiology

1.2.1. Basic Cardiac Anatomy

The heart is a muscular organ, located in the middle mediastinum and typically offset to the left of the chest, approximately 12x8x6cm in size [Betts et al., 2016]. The heart acts as the pump of the circulatory system, to provide oxygen and nutrients to the body and aid in metabolic waste removal.

The normal human heart is divided into 4 chambers (Figure 1.1): the right atrium and right ventricle (the right heart), and the left atrium and the left ventricle (the left heart). The ventricles are separated by the interventricular septum, and four valves exist, occurring at each connection between the atria and ventricles as well as at the exit of each ventricle.

The heart wall is made up of three layers enclosed by a pericardial "sac" (Figure 1.2). The endocardial layer is the innermost of the three, lining the chamber cavities. It is a thin layer made up of connective tissue and cells that act in the same way as the endothelial cells which form the lining of blood vessels. The outer layer, the epicardium, is a serous membrane attached to the myocardium that forms the inner wall of the pericardial sac,

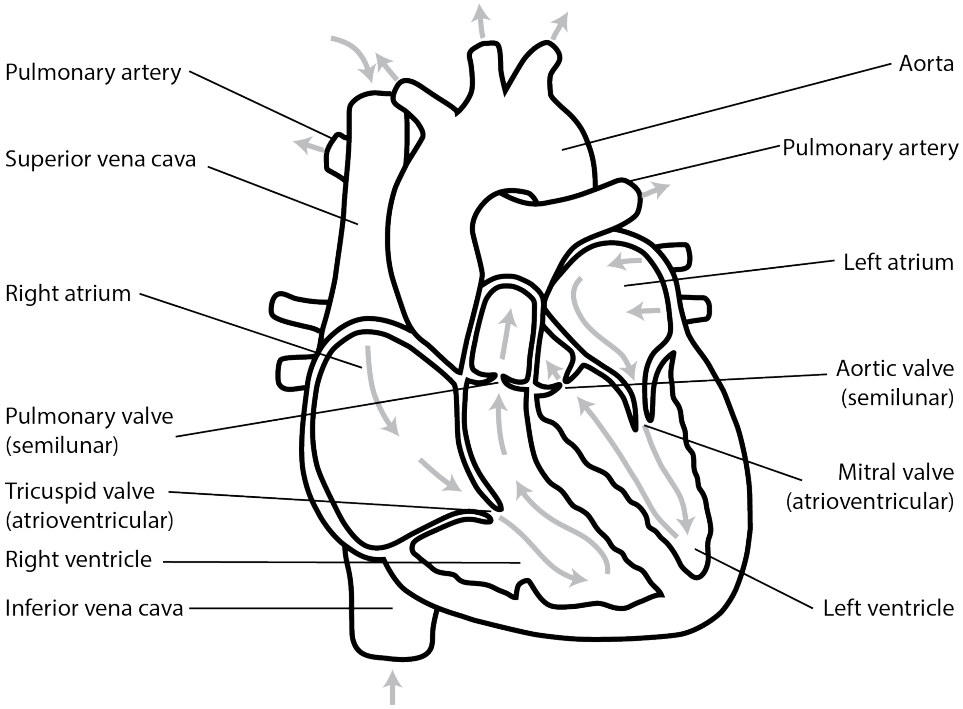

Figure 1.1.: Cardiac structure. Overview of the four chambers of the heart and the great vessels.

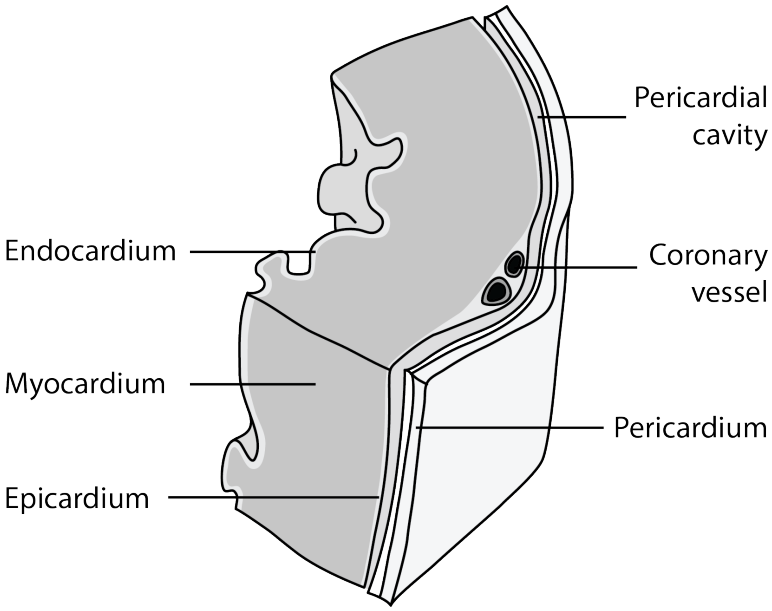

Figure 1.2.: Layers of the heart wall.

discussed later.

The myocardium is the middle layer of the heart muscle. It is by far the thickest layer, measuring about 6mm in healthy male adults during cardiac relaxation (but varying depending on age, sex, and many other factors). The majority (70-85%) of the myocardium is made up of cardiomyocytes, differing from myocytes found in skeletal-muscle to be specially adapted to aid the performance and coordination of the heartbeat. These are connected together in complex structures, such as by so-called intercalated discs, again aiding in both electrical and mechanical transmission. Other cell types within the myocardium, at a much smaller volume percentage, include fibroblasts, endothelial cells and perivascular cells [Zhou and Pu, 2016].

The pericardium is a tough, fluid-filled, sac enveloping the heart. The pericardium itself is made up of two layers - a serous inner layer that surrounds the pericardial cavity and a fibrous outer layer. The pericardial cavity is filled with pericardial fluid, which helps allow movement of the heart within the chest by acting as a lubricant.

Different types of fat deposits are also often found in this region. Epicardial fat is adipose tissue located between the pericardium and the myocardium. Fat also occurs on the fibrous outer layer of the pericardium and is referred to by multiple names (e.g. pericardial fat). These two types of fat, whilst distinctly separate, are sometimes referred to together. Fat deposits are naturally found in these regions in small quantities, helping in many cardiac mechanisms, but can increase in quantity potentially leading to increases in risk factors [Bertaso et al., 2013].

1.2.2. Tomographic Representation & Nomenclature

For general body imaging, there are three orthogonal "anatomical planes" - transverse, coronal and sagittal. The orientation of the heart is subject specific and does not typically align with these anatomical planes. Instead the following cardiac planes are often used in reference to cardiac anatomy and imaging.

The cardiac planes are typically referred to as short axis (SAX), vertical long axis (VLA) and horizontal long axis (HLA) views (Figure 1.3). The long axis orientations should have one in-plane dimension aligned along the major ("long") axis of the LV ellipsoid, to transect the apex and the plane of the mitral valve. The other in-plane dimension of this view should cross the LV through its centre and either cross the RV centre (for HLA) or be

perpendicular to this (for VLA). These views are sometimes also referred to as 4-chamber and 2-chamber views respectively. SAX views are orthogonal to both these planes and can cut across at any level between the base and apex of the LV, typically with a "stack" of SAX slices for complete left ventricular coverage.

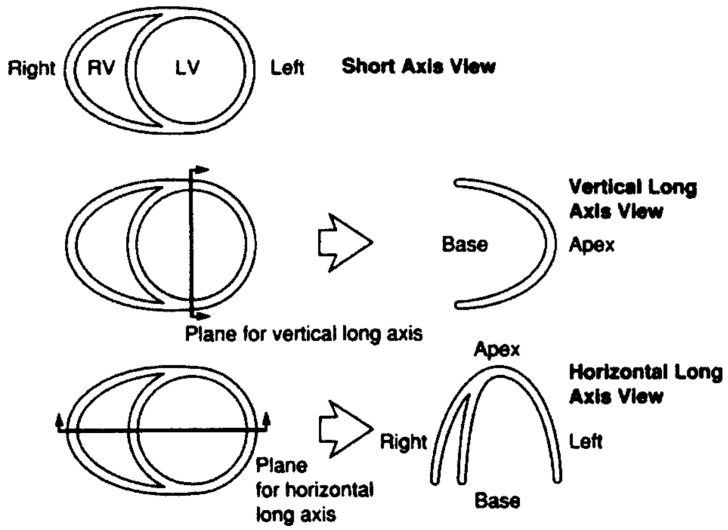

Figure 1.3.: Cardiac planes. Three common views of the heart, as used in cardiac imaging. Reproduced from [Cerqueira et al., 2002].

The LV myocardium can be segmented for definition of specific regions, using these cardiac planes. Segments are defined from their position along the long axis (basal, mid-cavity, apical) as well as their circumferential location around the SAX (anterior/inferior, septal/lateral). The precise number of segments used is variable and depends on the desired application - an example of a typical 17 segment model (American Heart Association, AHA[Cerqueira et al., 2002]), as used in applications such as coronary artery disease, is shown in Figure 1.4.

1.2.3. The Cardiac Cycle

The collection of repetitive electrical and mechanical processes of the heart occurring each heartbeat forms the *cardiac cycle*, which describes the pressure, volume and flow inside the heart as a function of time.

The cardiac cycle, displayed in Figure 1.5 in the form known as a Wiggers Diagram [Mitchell and Wang, 2014], can be split into four major stages: isovolumetric contraction, outflow ("ejection"), isovolumetric relaxation, and

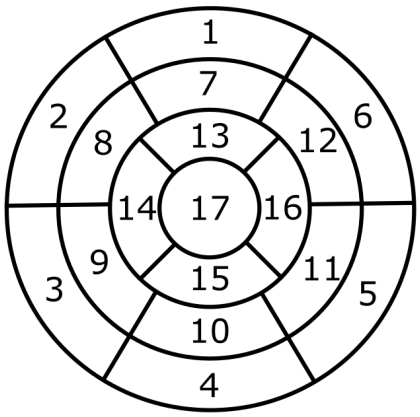

1. basal anterior
2. basal anteroseptal
3. basal inferoseptal
4. basal inferior
5. basal inferolateral
6. basal anterolaterol
7. mid anterior
8. mid anteroseptal
9. mid inferoseptal
10. mid inferior
11. mid inferolateral
12. mid anterolateral
13. apical anterior
14. apical septal
15. apical inferior
16. apical lateral
17. apex

Figure 1.4.: Left ventricular segmentation. The commonly used American Heart Association 17 segment model of the left ventricle. Based on [Cerqueira et al., 2002].

inflow ("filling"). These can be grouped into phases relating to contraction, known as systole, and those relating to relaxation, known as diastole. The stages are broadly similar for both the left and right heart, but as perfusion of the left ventricle is the main focus of this thesis, only the left-heart cardiac cycle will be discussed here.

The QRS complex corresponds to ventricular depolarisation, which starts the process of contraction (systole) after approximately 50ms [Fuster et al., 2011]. During this initial muscle activation, the atrioventricular (mitral) inlet valve closes, making the left ventricle a closed system of constant volume but increasing pressure, termed isovolumetric contraction. When the increasing ventricular pressure exceeds the systemic pressure (i.e. of that in the aorta), the aortic valve opens leading to ventricular ejection. After a period of rapid ejection, the contraction slows and the ventricular pressure reduces. This is the period of minimal cardiac motion within systole. When the ventricular pressure falls below the aortic pressure, the aortic valve closes and ventricular diastole begins. With the closure of this valve, the ventricle is once again a closed system, this time going through isovolumetric relaxation causing a rapid reduction in ventricular pressure. After a short period the ventricular pressure falls below the left atrial pressure, which causes the

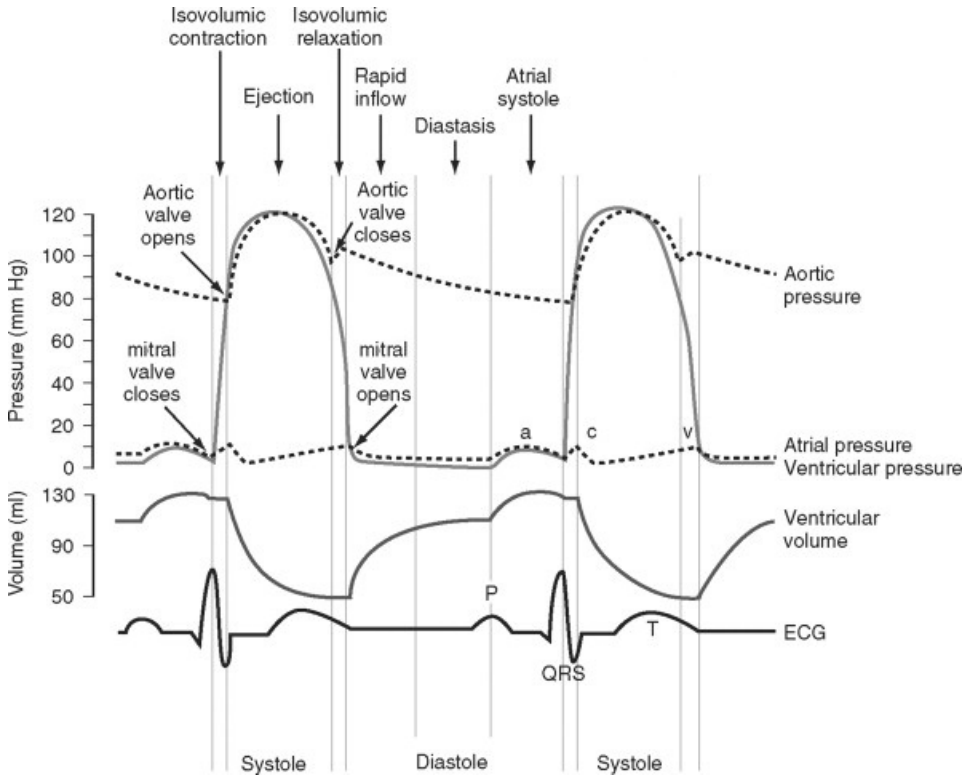

Figure 1.5.: The cardiac cycle. A typical 'Wiggers Diagram' of Pressure + Volume + ECG for the left ventricular cardiac cycle. Modified from [Sidebotham, 2007].

mitral valve to reopen and allows ventricular filling to begin. The initial diastolic filling phase (inflow through the mitral valve) by left ventricular myocardial relaxation is normally very rapid, driven by the elastic recoil of a complex network of fibres within the myocardium that are extended during systole [Robinson et al., 1986]. Later in ventricular diastole a phase of gentler filling occurs which corresponds to minimal cardiac motion, often referred to as diastasis. Atrial depolarisation (P-wave) drives atrial contraction to deliver a final late-diastolic "top-up" of blood into the left ventricle before ventricular depolarisation occurs again to start the next cycle.

1.2.4. Coronary Circulation

Blood is supplied to the myocardium itself through the coronary arteries in the process known as coronary circulation. Most coronary flow occurs during ventricular diastole, when blood flows from the aorta through the aortic sinuses. This begins the process of myocardial perfusion through the coronary circulation.

Typically, two coronary arteries, the left and right coronary arteries, stem from the root of the aorta. These arteries branch many times to supply different areas, going from larger epicardial arteries to smaller arteries and eventually capillaries that perfuse transmurally through to the endocardium (Figure 1.6). The left main coronary artery is usually primarily responsible for providing blood to the left heart, branching early into the left circumflex (LCx) and the larger left anterior descending (LAD) arteries, as well as their many branches. The right coronary artery (RCA) usually primarily supplies the right heart, including the right atrium, some of the right ventricle and, superficially, the left ventricle. Venous blood from the myocardium is collected by coronary veins into the coronary sinus, where it enters back into the right atrium.

Coronary artery branching and distribution follow similar overall patterns in the majority of people, however, the precise location of the arteries on the heart will always have subject specific variation. Population based models have been developed to give an approximate guide to the territories that are most likely supplied by each of the major coronary arteries [Cerqueira et al., 2002]. An example of these territories, overlaid on the AHA 17-segment model discussed earlier (Section 1.2.2), is shown in Figure 1.7. Such models allow estimation of myocardial regions affected by different coronary arteries in the absence of specific information regarding the arteries of the patient in

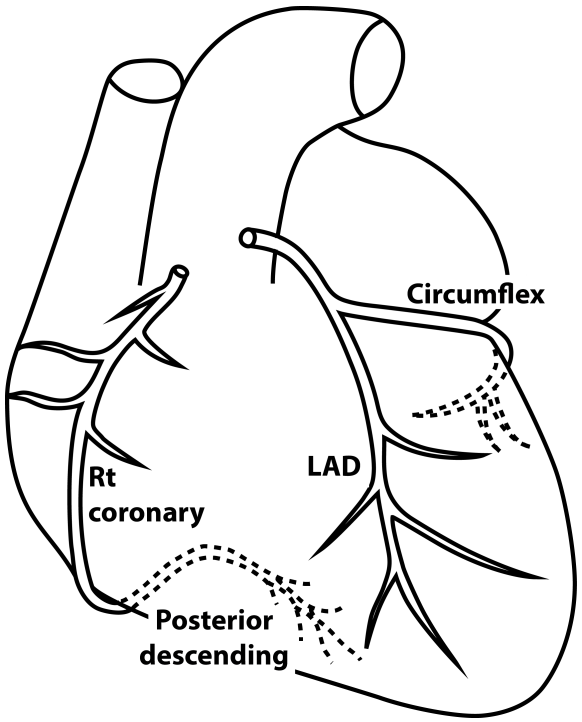

Figure 1.6.: Coronary artery distribution. Diagram of the heart showing approximate typical locations of the coronary arteries. LAD - Left Anterior Descending. Based on [Opie, 2004].

question. Much discussion still continues in the medical community over the alignment and accuracy of the territories.

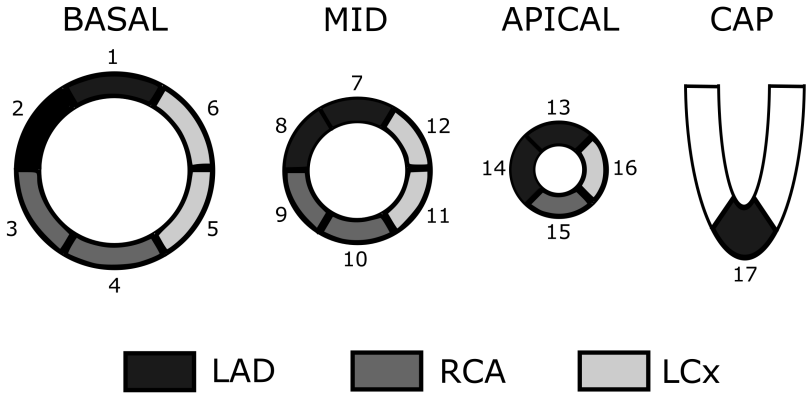

Figure 1.7.: Coronary artery territories. Typical left ventricular territories for the three main coronary arteries, based on the AHA 17 segment model. N.b. the long-axis view only displays the apical segment (17). Information from [Cerqueira et al., 2002].

Healthy coronary flow, at rest, is around 90-120(mL/min/100g of myocardium) but can rapidly increase by a factor of 4-5 under conditions requiring extra flow, such as exercise [Fuster et al., 2011]. The exact feedback mechanisms matching coronary blood flow to myocardial oxygen consumption are still not fully understood [Tune et al., 2004].

1.3. Coronary Artery Disease

1.3.1. Pathophysiology

Coronary artery disease (CAD) is the restriction of blood supply through the coronary arteries, which typically develops through the process of atherosclerosis. With atherosclerosis the coronary artery lining becomes hard and stiff, forming deposits that develop to become plaque. The exact process behind atherosclerosis is complex and includes areas that are less well understood, but can in basic terms be described by infiltration and accrual of macrophages (white blood cells). The process is activated by the inflammatory response within the wall of the coronary arteries in response to low density lipoprotein (LDL) particles. LDL undergoes increased oxidation by free radicals whilst in the vessel wall. This process causes white-blood cells to be attracted and enter the wall, converting into macrophages. While macrophages are able to

absorb the oxidised LDL, turning into what are known as foam cells, if they are not able to complete the process of removing the fats quickly enough they will grow and rupture. Rupturing releases the LDL and causes the process to repeat and escalate. This is the process of developing atherosclerotic plaque (atheroma), which undergoes many stages (Figure 1.8).

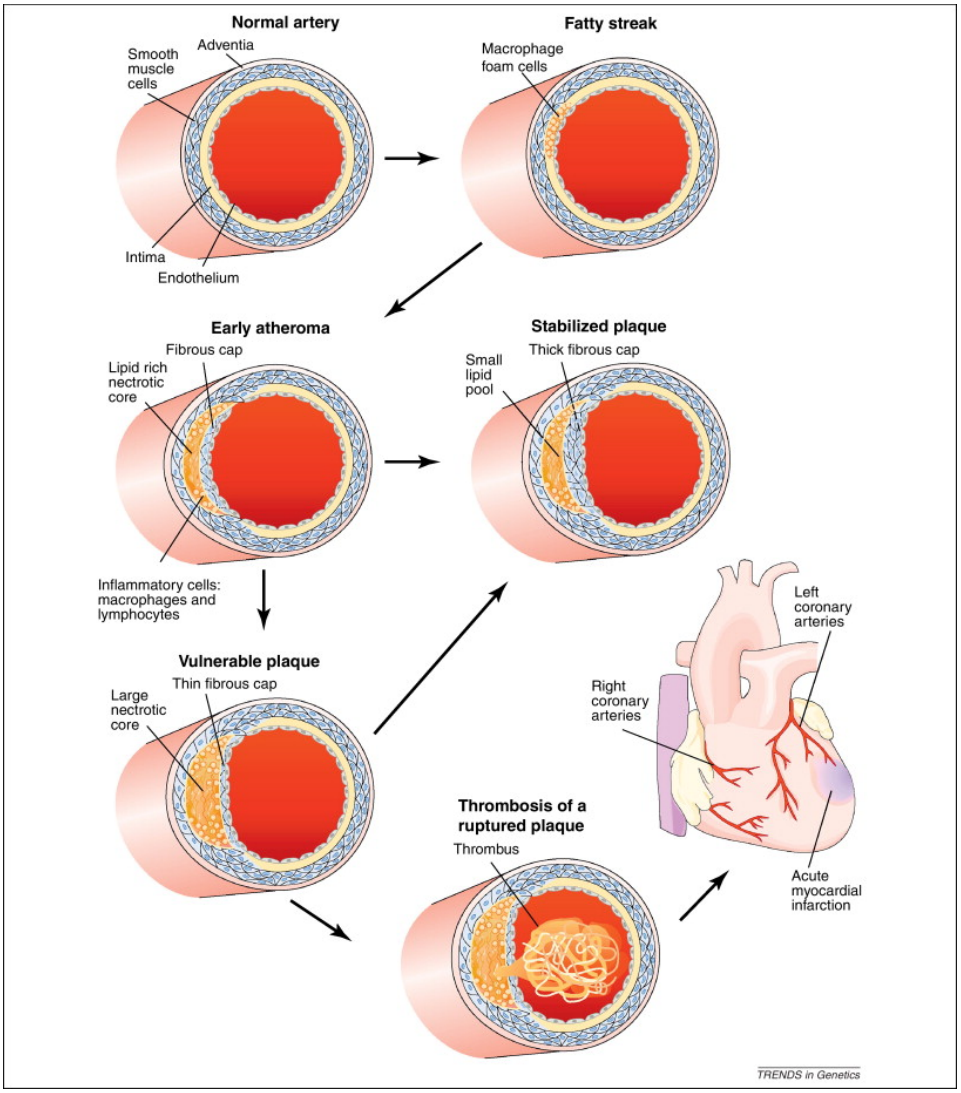

Figure 1.8.: Process of atherosclerosis. The stages of atherosclerosis are shown, from the early development of macrophages in the wall, through to the development of atheroma into either stable or unstable plaque. The final potential stage is plaque rupture, which can lead to the formation of a thrombus. Reproduced from [Lusis, 2012].

A build-up of atherosclerotic plaque eventually leads to a narrowing

(stenosis) of the lumen of the coronary arteries. Stenoses restrict the ability of the heart to receive, through myocardial perfusion, the required levels of oxygenation and other nutrients. This state of insufficient nutrition for proper cellular metabolism is known as myocardial ischaemia, whereby the heart muscle is no longer able to fully function. Prolonged and severe ischaemia will lead to irreversible muscle death, known as a myocardial infarction (MI) [Opie, 2004].

Coronary circulation is "end circulation" in that it is the only supply to the heart. This makes any restriction in the coronary circulation particularly dangerous. There is also a lack of many anastomoses (cross-connections) in coronary arteries, increasing the risk of infarction in cases of flow obstruction. The LAD coronary artery is the most commonly occluded. As the LAD provides blood to multiple regions of the myocardium, including much of the LV, any stenosis of this artery is of particularly high risk [Scott, 1986]. Stenosis of any coronary artery may occur, each with myocardial territories of risk associated with them (see Section 1.2.4).

During atherosclerosis the vessel wall stretches and the lining becomes thicker. The lumen diameter may be preserved to some extent while disease builds up in the wall (known in cardiology as "outward remodelling" or the "Glagov effect") [Glagov et al., 1987]. The associated stiffening of the wall becomes an issue in situations, such as exercise, when the coronary blood flow would otherwise typically increase, because the artery is not able to adapt to enable this. Therefore, the effects and symptoms of CAD are initially or only observed under stress conditions, i.e. where vasodilation of the coronary arteries would be expected or required.

1.3.2. Clinical Significance

CAD is a major cause of morbidity and mortality in the UK. Cardiovascular diseases are responsible for a similar number of deaths per annum as cancer and coronary artery disease is responsible for the vast majority of cardiovascular disease related deaths according to latest available statistics [Townsend et al., 2015]. CAD alone was the recorded cause for over 69,000 deaths in this country in 2015 [Townsend et al., 2015]. Techniques that could help to diagnose CAD at its earliest, reversible, stages are clearly therefore of great importance.

Chest pain is a very common patient complaint, with previous statistics suggesting it accounts for 1% of GP visits and 25% of emergency hospital

admissions [Skinner et al., 2010]. Angina pectoris is chest pain caused by CAD and can be a serious warning sign of future cardiac events. Angina can be defined as either stable or unstable. Stable angina is predictable in terms of its frequency/severity and is often triggered during physical exercise. Unstable angina is angina occurring without a pattern, including without the presence of exercise, and is deemed particularly serious. Both types are a symptom of coronary artery disease and therefore a potential warning of future myocardial infarction. However, other causes of chest pain can be very mild conditions, including gastro-oesophageal conditions (acid reflux), strained muscles in the chest wall, and many more of varying severity.

The ability to accurately diagnose those presenting with chest pain in a quick and non-invasive manner is therefore of great importance.

1.3.3. Diagnosis of CAD

The sequence of events associated with ischaemia is known as the ischaemic cascade [Nesto and Kowalchuk, 1987], as seen in Figure 1.9. As the majority of ischaemic events occur without warning symptoms [Schang and Pepine, 1977], it would be preferred to diagnose CAD as early along the ischaemic cascade as possible. In routine clinical care, electrocardiogram (ECG) changes are the main diagnostic criteria to diagnose severe myocardial damage caused by CAD [NICE, 2010]. However, these ECG changes only occur after both diastolic and systolic dysfunction. Many imaging techniques therefore aim to investigate events that occur earlier in the cascade.

Coronary x-ray angiography (CXA) is regarded as the gold standard in detecting CAD [Storm and Slump, 2010]. Through x-ray fluoroscopy of a catheterised injection of contrast agent, CXA provides very high resolution ($\approx$0.1mm) cine ($\approx$30 frames/second) projection views of vessel lumina. It is therefore excellent for determining stenoses in the coronary arteries [Timmis et al., 1997]. It is commonly used as the standard of reference in studies comparing assessment of CAD through different modalities [Giang et al., 2004][Schwitter et al., 2012]. As well as providing high imaging quality, the catheterisation process and sterile environment in which it is performed means that clinicians are well placed to immediately act on any clearly identified stenoses. This intervention can be, for example, through installation of supporting stents in the coronary arteries to open stenoses or by using expanding balloon angioplasty [Timmis et al., 1997]. This ability to combine diagnosis and immediate treatment makes CXA a powerful and popular

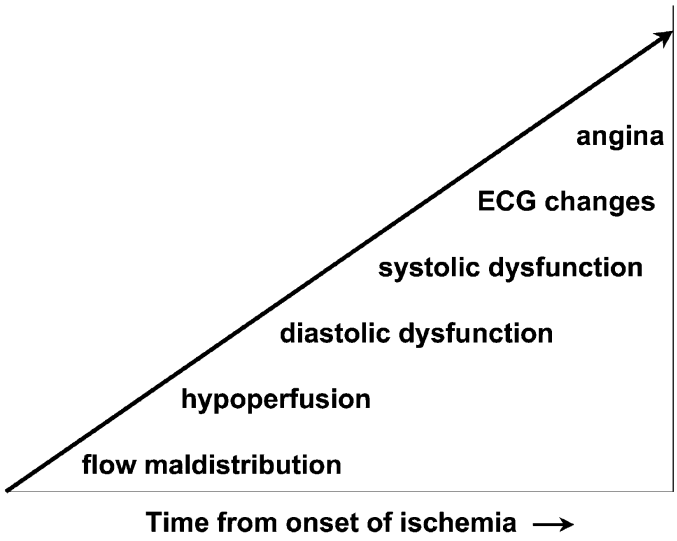

Figure 1.9.: Ischaemic cascade. The ordered sequence of events associated with ischaemia. Modified from [Schinkel et al., 2003].

technique clinically.

Whilst there are many advantages to CXA, there are also drawbacks that would make some reductions in its use preferable. The catheterisation process means that the procedure is invasive and carries a small risk of serious complications. CXA also has the negative feature of using ionising radiation. This is a problem shared with many imaging modalities, but as the radiation dose varies with operator experience, along with the potential for dangerous skin doses, extra consideration is required for this technique [Einstein et al., 2007]. Lastly, but significantly, there is a financial benefit in limiting the use of CXA by conducting initial testing with other less expensive methods [Shaw et al., 1999]. For patients with obvious symptoms, CXA will likely be required for treatment regardless of diagnosis method. For patients with greater uncertainty in their diagnosis and therefore uncertain imminent requirement for treatment, a "gatekeeper" test to allow CXA to be applied more selectively would be beneficial. Myocardial perfusion assessment attempts to fill this role.

1.4. Myocardial Perfusion Assessment

1.4.1. Principles of Perfusion Imaging

Ischaemia is directly caused by failures in myocardial perfusion. This has led to the development of imaging techniques that measure myocardial perfusion directly. Myocardial perfusion methods study the passage of blood through the coronary arteries and the capillaries of the myocardium rather than examining the narrowing of coronary arteries. As well as avoiding the requirement for catheterisation ("non-invasive"; requiring only peripheral venous access), measuring perfusion directly can potentially also have an advantage in detecting true flow limitations [Gerber et al., 2008]. Perfusion defects under stress conditions occur very early in the ischaemic cascade, so perfusion measurements are more sensitive in detecting restrictive stenoses than diagnostic techniques that identify events later in the cascade [Leong-Poi et al., 2002]. Perfusion imaging aims to provide accurate, early assessment of CAD, without the less desirable features of CXA. The importance of performing perfusion imaging of the heart in response to angina pectoris and other warning signs has recently been recognised in revisions to National Institute for Clinical Excellence guidelines [NICE, 2010] among others.

The majority of perfusion techniques use a signal enhancing agent capable of entering the microvasculature, to examine the blood arriving into the myocardium, typically under "stress" conditions that would cause increased blood flow in a healthy response. This process enables examination of any regions of the myocardium where arrival is reduced compared with regions of "remote" myocardium (assumed to be normal) [Gerber et al., 2008]. It has been shown that the degree of a stress-induced perfusion defect is a strong indicator for long-term mortality of patients with CAD [Schwitter, 2006].

Some of the more general features required from a modality attempting to image myocardial perfusion are shown in Table 1.1. High resolution and sensitivity are commonly some of the most important imaging goals, although they are often not possible to achieve simultaneously without limiting the acquisition in other ways [Salerno and Beller, 2009].

Various methods of performing myocardial perfusion exist, based on the different imaging modalities in common clinical practice, each of which are capable of achieving at least some of these idealised parameters. These are reviewed next.

Table 1.1.: Idealised perfusion imaging attributes

Attribute
High sensitivity
High spatial / temporal resolution
Adequate spatial coverage of the left ventricle
Quantifiable relationship between signal intensity and concentration of agent
Reproducible - no operator dependence
High diagnostic utility
Easy to use
Widely available
Low cost

Modified from [Salerno and Beller, 2009]

1.4.2. SPECT

Single-photon emission computed tomography (SPECT) is the most common clinical modality for non-invasive assessment of myocardial perfusion [Nagel et al., 2003]. Use of SPECT for examination of myocardial perfusion is typically referred to as myocardial perfusion scintigraphy (MPS) and encompasses a range of different protocols.

SPECT uses a gamma camera detector (either a scintillation based Anger camera, or more recently semiconductor based systems [Peterson and Furenlid, 2011]) to detect radiation from a gamma-emitting radioisotope that has been injected into the subject. SPECT is an extension to original planar gamma camera techniques, acquiring projections at multiple angles around the subject to enable reconstruction of the 3D distribution of the isotope. After collimation of the acquired gamma rays and various correction factors, resolutions of 1-2cm are typically achieved.

Various nuclear isotopes are available, most common for MPS being thallium (Tl-201) and various technetium (Tc-99m) labelled isotopes (e.g. Sestamibi, Tetrofosmin). Tl-201 and Tc-99m radioligands vary in their half life (Tl-201: 73 hours, Tc-99m: 6 hours), myocardial extraction, counting statistics and radiation dosimetry (which vary based on the precise ligand) [Fathala, 2011]. ECG-gated Tc-99m methods also exist [Taillefer et al., 1997], which are popular as they also allow measurement of myocardial function combined with the MPS acquisition.

Exact protocols depend on the isotope used and the centre but typically

consist of stress imaging (∼15 minutes), a pause (either several hours or next day imaging), and then a rest scan. This order can sometimes be reversed. Inducement of stress in MPS can be performed with exercise prior to the scan using a graded treadmill protocol, sometimes preferred due to generation of additional diagnostic information. Pharmacological stress (see Section 1.5.3 for further details) can instead be used for simplification of the protocol or if required due to the patient's impaired ability to exercise.

1.4.3. PET

Whilst less common clinically, there are a number of other modalities that allow imaging of perfusion within the heart. Positron emission tomography (PET) uses positron emitting isotopes as positrons travel just a short distance (up to a few millimetres) inside the body before annihilating with electrons to produce a gamma ray pair emitted in opposite directions. These gamma rays are detected by a ring detector, either used as part of a tomographic reconstruction or, more recently, using the relative timings of the detection for calculation of a more accurate location ("time-of-flight" PET).

PET is often compared with SPECT due to similarities in their use of radioisotopes to provide excellent examination of physiological processes (metabolism, blood flow, etc) and therefore both have high potential for perfusion imaging [Go et al., 1990][Chen et al., 1997][Di Carli and Hachamovitch, 2006]. It has been predicted that PET may overtake SPECT in its diagnostic performance for myocardial perfusion [Bateman et al., 2006], with PET additionally offering quantification of perfusion. The most up-to-date comparison study in patients with known or suspected CAD has shown that PET gives greater interpretive confidence [Flotats et al., 2012]. Despite a higher inherent resolution [Gould et al., 1986], PET still suffers from many of the shortfalls that SPECT does, including ionising radiation and poor structural imaging. PET also has the significant additional problem of lower clinical availability [Barkhausen et al., 2004] linked mainly to expense and radioisotope generation.

1.4.4. Ultrasound

The low cost and portability of ultrasound (US) as a modality are clear benefits [Picano et al., 1991] as is the absence of ionising radiation. Echocardiography (ECHO), the use of US in imaging the heart, is able to detect perfusion defects through the use of microbubbles as contrast agents during

vasodilation [Armstrong et al., 1982]. The clinical utility is currently still being determined, with limitations including attenuation, non-linear signal issues and incomplete microbubble destruction [Porter and Xie, 2010].

Ultrasound is currently more commonly used for detection of wall motion abnormalities [Armstrong, 1991], known as "stress ECHO", but this diagnoses abnormalities later in the ischaemic cascade [Schinkel et al., 2003]. A review of trials comparing wall-motion stress ECHO with MPS showed that whilst wall-motion stress ECHO produced fewer false positive diagnoses, it was poorer at identifying ischaemia [Schinkel et al., 2003].

1.4.5. Computed Tomography

Computed tomography (CT) can be used for computed tomographic angiography (CTA), a non-catheter based extension of CXA projection imaging to a tomographic acquisition method. While CTA, as with CXA, can provide excellent information regarding anatomy and narrowing of the coronary arteries, it is still limited in its ability to determine the haemodynamic significance of any detected stenoses [De Cecco et al., 2015][Varga-Szemes et al., 2015]. Dynamic CT methods have therefore been developed to provide information regarding myocardial perfusion during the first-pass of a contrast agent.

A relatively new technique, CT myocardial perfusion is now beginning to go through different trials [Caruso et al., 2016]. Further work and consensus regarding protocol optimisation along with further clinical validation are still required [Yang and Kim, 2017]. CT myocardial perfusion requires relatively high radiation doses and therefore still requires a reasonably clear call for its application, while it lacks the advantage in CXA of being able to deliver immediate treatment.

1.5. Myocardial Perfusion with MRI

1.5.1. MRI Assumed Knowledge & Definitions

The reader is assumed to understand conventional MRI based on the spin-warp or phase-encoded concepts, and be familiar with the k-space representation of the acquired raw data. Familiarity is also assumed for the extension of this concept to 3D by repetition of another iterative loop of phase slopes through a thick slab. Suggested texts include [Haacke et al., 1999] and [Bernstein et al., 2004].

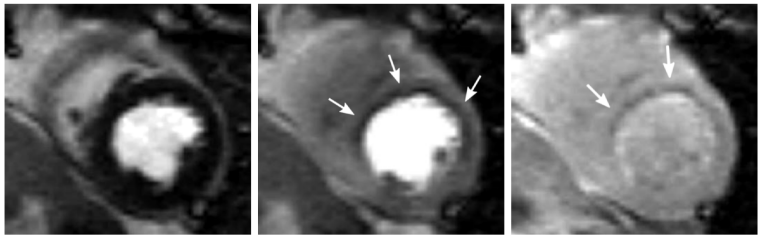

Figure 1.10.: MRI first-pass stress perfusion example. A single image slice is shown at three separate time points during arrival of a GBCA. The time frames are chosen to represent the contrast arrival in the left ventricle, myocardium and recirculation respectively. A hypointense region representing a stress induced perfusion defect is highlighted by the arrows. Reproduced from [Gerber et al., 2008].

Further topics of particular relevance to this thesis are as follows.

- Slice-selective radiofrequency (RF) excitation pulse designs and their relationship to the excited slice profile.
- The longitudinal magnetisation and its recovery back to equilibrium following saturation by a 90-degree pulse, characterised by the spin-lattice relaxation time T_1.
- How this equilibrium level may be a dynamic equilibrium between the recovery and the continuous application of a series of low flip-angle RF excitations for imaging.
- To a lesser extent, the spin-spin relaxation time T_2 is relevant to some of the perfusion review sections.

1.5.2. Basic Principles of First-Pass Perfusion (FPP)

Introduction

MRI can assess myocardial perfusion by several methods, most commonly by use of first-pass contrast-enhanced techniques. By repeating myocardial images rapidly, every cardiac cycle, the dynamics of the "first-pass" arrival of a signal-enhancing contrast agent into the myocardium can be captured. Performed during stress, segments that do not undergo signal enhancement or that have a delayed/reduced enhancement could therefore be affected by a restriction in the supply of blood flow to that region (Figure 1.10).

Such techniques were first established in the early 1990s [Atkinson et al., 1990] [Manning et al., 1991] and are hereafter referred to as myocardial first-pass perfusion (FPP). FPP has since become well established clinically, including recent inclusion in revisions to the National Institute for Health and Care Excellence (NICE) guidelines [Skinner et al., 2010].

T_1-weighting

FPP makes use of a T_1-weighted imaging approach; longitudinal magnetisation is nulled before each image, and allowed to partially undergo T_1 recovery. After a suitably chosen "saturation recovery" delay, the image is acquired, thus making the received signal strength sensitive to the T_1 values of the tissues (among other factors). Early examples achieved this sensitivity to T_1 through use of an inversion pulse but reliability of this was complicated by heart rate variability. Instead, saturation recovery pulses are now almost universally used to "reset" the longitudinal magnetisation at the start of each cycle. Other options for magnetisation preparation include arrhythmia-insensitive modification of the inversion pulse [Tsekos et al., 1995] and for multi-slice imaging the "notched" saturation method [Slavin et al., 2001] but are outside the aims of this thesis. Saturation RF pulses have been optimised so that they null M_z over the range of B_0 (frequency) and RF non-uniformity found in human heart imaging [Kim et al., 2005][Kim et al., 2008]. While of importance clinically and in other work such as quantification, this topic is again outside the thesis aim.

By capturing T_1-weighted images of the myocardium every cardiac cycle during the injection of a T_1-reducing contrast agent, the contrast-enhanced blood can be tracked during its first-passage through the cardiovascular system.

Contrast Agents

Gadolinium enhances the signal for T_1-weighted images by shortening the spin-lattice (T_1) relaxation time. The gadolinium(III) ion has a particularly large effect because of its seven unpaired electrons [Pople et al., 1959], which gives this ion a large paramagnetic dipole moment. This shortens the T_1 relaxation times of hydrogen atoms that interact with the gadolinium ion.

Gadolinium(III) free ions are toxic to all mammalian life. Gadolinium(III) possesses a similar ionic radius to calcium(II), while also having higher charge density, and therefore out-competes it. Gadolinium(III) is deemed toxic to

any organism where calcium(II) is required for proper function [Sherry et al., 2009], so gadolinium based contrast agents (GBCA) used in MRI contain chelated gadolinium(III) ions. The aim of the chelation is to enable the GBCAs to pass through the body and be excreted via the kidneys before they dissociate into a harmful state. The strength of the gadolinium-ligand binding is related to the number of bound sites on the Gadolinium ion. More binding therefore provides greater safety but is balanced with a reduction in the size of the achieved relaxation effect.

Gadolinium(III) chelated with diethylene triamine pentaacetic acid (DTPA) was one of the first *in vivo* GBCAs [Weinmann et al., 1984], used in the earliest first-pass perfusion experiments and is still frequently used today [Gerber et al., 2008]. Many different gadolinium chelates are now clinically approved and in use [Sieber et al., 2008]. These gadolinium complexes are small enough to cross vessel walls but not cell walls (i.e. "extravascular and extracellular") and whilst research into using both larger intravascular and other extravascular agents has been ongoing for a while [Jerosch-Herold et al., 1999][Vallée et al., 1999], the extravascular gadolinium chelates are still very much the standard.

The ability of a GBCA to shorten T_1 is characterised by its relaxivity r_1 , defined by

$$r_1 = \frac{1}{\Delta T_1 \times [Gd]}$$

where [Gd] is the gadolinium concentration. r_1 values are typically stated in $\mathrm{s}^{-1}\mathrm{mM}^{-1}$ and are in the region of 3 to $5\mathrm{s}^{-1}\mathrm{mM}^{-1}$ at standard clinical field strengths [Laurent et al., 2006]. While a related relaxivity applies to T_2, this is less relevant to first-pass perfusion with short echo time spoiled gradient-echo sequences.

GBCA is paramagnetic and at high peak concentrations it is known to cause distortion of B_0 [Ferreira et al., 2008] which could be highly relevant depending on the type of pulse sequence employed for perfusion. As discussed in Section 5.3, this was one factor in the choice of spoiled-gradient-echo imaging with short sampling duration after each short RF excitation pulse.

First-Pass Perfusion Sequences

There are three main sequence types commonly used clinically for FPP [Lyne et al., 2007]: FLASH based sequences that employ a single spoiled gradient-

echo readout after each RF pulse, balanced steady-state free precession (bSSFP) readouts which establish a steady-state of the precessing magnetisation, and hybrid echo-planar (h-EPI) methods which employ spoiled gradient-echo readouts but collect multiple k-space lines per RF excitation. These three types are described next in greater detail, applied in a "single-shot" manner for FPP, capturing a complete acquisition of the required k-space per cardiac cycle.

Spoiled gradient-echo (SGRE) sequences at low flip-angles are widely used in FPP to produce a steady-state of longitudinal magnetisation, where "spoiling" dephases transverse magnetisation to become effectively zero within each voxel, before each RF pulse. Also known as Fast Low Angle Shot (FLASH), these sequences typically further increase the spoiling effectiveness through RF spoiling methods (further detailed information on this topic is in Section 3.4). For SGRE, the choice of flip-angle and the linked impact of B_1-inhomogeneity are important in optimising scarce SNR, as reviewed later (Section 3.2.5).

The transverse magnetisation can effectively be recycled instead of discarded, in the sequence known generically as balanced steady-state free precession (bSSFP) which delivers higher SNR than SGRE, further increased by the higher flip-angles typically used. bSSFP has attributes suitable for FPP but there is also potential for increased unreliability, with errors in the rephasing of the transverse magnetisation causing cancellation artefacts ("black band" artefacts). Furthermore, for single-shot bSSFP as required in FPP, the stabilisation of the precessing magnetisation before acquisition begins may inevitably be incomplete, leading to artefacts in the phase-encoding direction, and the stabilisation itself is perturbed by off-resonance errors. Increased blood-myocardium contrast in bSSFP imaging also causes greater artefacts from ringing [Kellman and Arai, 2007]. The increased flip-angle of bSSFP runs into specific absorption rate (SAR) limits, particularly at 3T, sometimes enforcing a slowdown of the sequence. At 3T there is also increased unreliability of bSSFP due to off-resonance effects, whereas SGRE is more robust in regards to both SAR and off-resonance.

Echo-planar Imaging (EPI) is closer to an SGRE type sequence in its design, but improves efficiency in data collection [Mansfield, 1977]. The premise is to collect multiple lines of k-space by a series of gradient echoes after each RF pulse, allowing acceleration by omitting RF excitations. Due mainly to the limited echo-train length (ETL) achievable as a consequence of

cardiac motion and main-field inhomogeneities around the heart, a "hybrid" form of EPI (h-EPI) uses a series of low-flip angle excitations as in SGRE, but each one collects typically 4 to 8 EPI echoes. This has been proposed in FPP [Ding et al., 1998] because of the limited applicability of true singleshot EPI [Edelman and Li, 1994][Panting et al., 2001] in routine clinical cardiac MRI. The compromise for h-EPI is made between increasing the ETL - which reduces total image time - and the corresponding increased unreliability [Ding et al., 1998] [Ferreira et al., 2012] which also increases with the increased phase-errors associated with higher main field strength.

Comparing the three main approaches (Figure 1.11), FLASH sequences are the most robust, but are intrinsically slow and have low SNR. bSSFP sequences are also relatively slow, but produce greater SNR in equivalent sequence shot duration. h-EPI sequences have reduced SNR (due to wider required readout bandwidths to enable rapid enough sampling to avoid off-resonance and motion phase errors) but are about 2x faster for a typical FPP echo-train length of 4. The benefits of the bSSFP and h-EPI sequences compared to FLASH need to be weighed against the potential for increased artefacts, and the experience of operators can be a factor in sequence selection at a centre. A clinical comparison of the sequences for FPP at 1.5T found that bSSFP had the highest CNR, and h-EPI the lowest [Lyne et al., 2007]. h-EPI was shown to have the lowest rate of false-positive "dark-rim" artefacts and highest diagnostic confidence in this study, but assumptions were made on how the increased acceleration of the sequence could be best utilised. At 3T the difficulties involving off-resonance effects for bSSFP and h-EPI become more pronounced, and for this reason FLASH is the most common sequence type for FPP at 3T.

Within these sequences, there are many variable parameters controlling a trade-off between shot duration, image resolution, CNR between myocardium and defect, and reliability against artefacts such as off-resonance and rapid blood-flow effects.

1.5.3. Clinical Protocols

FPP protocols vary by centre, but generally include the following components:

- Scout images. Fast, low-resolution images are acquired, typically covering the transverse, coronal and sagittal planes around the isocentre, from which future images can be planned.

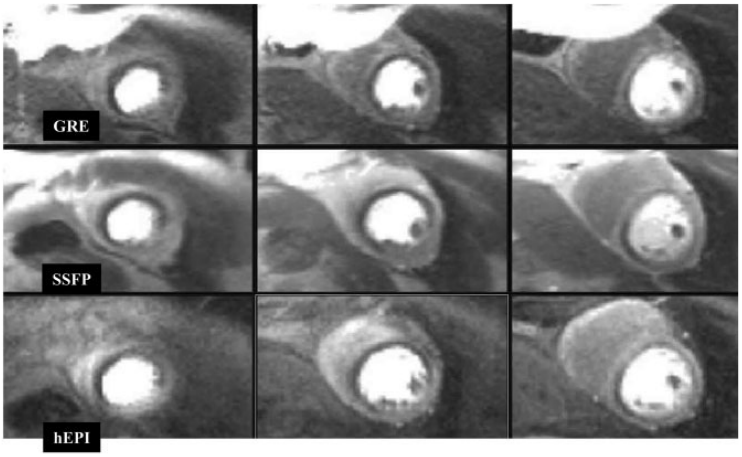

Figure 1.11.: Comparison of FPP sequence types. An example of the three common sequence types, as described above, applied in a patient with significant two-vessel disease (three slices displayed horizontally). Reproduced from [Lyne et al., 2007].

- Cine acquisitions. These are typically acquired in their own right to provide cardiac functional information, but are also used in perfusion protocols for the positioning of the FPP slices. There is also potential to use these for cardiac timings in setting trigger delays, although this is usually skipped due to limited time within the cardiac cycle during stress.

- Stress perfusion. After pharmacologically induced stress (see below), imaging is performed during the power injected first-pass perfusion of contrast agent and saline flush.

- Late enhancement. Late gadolinium enhancement (LGE) images are usually acquired for detection of myocardial scar to provide information on viability and prognosis, as well as for other non-ischaemic clinical diagnoses.

- (Optional) rest perfusion. A second perfusion test can be run after wash-out of the original injection, this time performed without the inducement of stress. For quantification this serves as the baseline for myocardial perfusion reserve = MBF stress/MBF rest. In clinical routine "eyeballing" of perfusion, the rest scan can potentially aid in differentiating inducible ischaemia from various causes of "fixed" defects, as well as nominally aiding in artefact identification. However,

the changes in the image contrast and the cardiac motion between stress and rest limit the usefulness of the rest perfusion and many centres omit it for clinical work.

A typical first-pass myocardial perfusion protocol collects 3 to 4 equi-spaced SAX slices along the LV. In-plane resolutions vary from around 2-3mm, and slice thickness from 8-10mm in standard acquisitions. Slice coverage is typically completed within a single cardiac cycle but alternate-cycle approaches that interleave more slices also exist (reviewed further in Section 1.5.6).

A single saturation pulse can be applied before collection of multiple slices, but saturation is more commonly repeated before each slice acquisition. The single-saturation per cycle technique minimises the period of the cardiac cycle used up by inactive saturation recovery delays, so that a greater number of slices can be achieved per cycle. Application of a separate saturation pulse prior to each slice instead avoids different saturation recovery times for each slice, which would lead to varying image contrast [Biglands et al., 2012].

Higher GBCA concentrations are preferred when possible due to the higher image SNR they provide for the same saturation recovery delay. The concentrations of GBCA in the heart during the first-pass are highly variable depending on, for example, cardiac function but also affected by the dose, its injection rate and the amount of saline fluid injected after the GBCA to "push" it through the venous circulation to the right atrium [Elkington et al., 2005]. For a "single dose" (0.1mmol/kg) with fast injection, the peak concentration reaches in the region of 5-10mM in the left ventricular blood-pool and around 1-3mM in normal resting myocardium. This again emphasises the variability between subjects, even when all controlling parameters are held constant.

The reconstructed signal intensity is non-linear with GBCA concentration, particularly at higher concentrations because of the exponential T_1 recovery. This non-linearity also depends on the GBCA relaxivity, itself dependent on field strength. To avoid excessive non-linearity in the response to GBCA, lower GBCA concentrations may be used for some quantitative perfusion techniques to allow accurate estimations of blood-pool and myocardial concentrations extracted from the image. Alternatively, dual-bolus and dual-sequence approaches for collecting the blood information from separate acquisitions have been devised to avoid this issue [Christian et al., 2004][Gatehouse et al., 2004]. Acquisitions that will only be

used for qualitative interpretation ("eye-balling") analysis have less concern about myocardial signal non-linearity versus concentration and no reason to consider the blood signal.

Myocardial hyperaemia, the increase in blood flow to the myocardium, is induced in the subject during "stress" imaging to examine flow limitations (as discussed in Section 1.3). There are different methods of achieving this response, including physical exercise with several limitations, or far more commonly by pharmacological stress. Various agents are available for inducing hyperaemia, with vasodilators such as adenosine (and more recently regadenoson [Buhr et al., 2008]), being the most popular. Primary in the choice of agent is patient safety and both adenosine and regadenoson perform well in this regard; Adenosine has a short acting half-life once infusion has been stopped and regadenoson can have its effects quickly reversed.

Prior to the scan, a patient ECG is typically performed and patient history is taken to check for asthma or other potential causes of reaction to adenosine. Use of adenosine in large SPECT registries [Cerqueira et al., 1994] as well as multi-centre MRI studies [Giang et al., 2004] [Wolff et al., 2004] has demonstrated the safety of adenosine use for inducing hyperaemia. Subjects are requested to avoid caffeine for 24 hours prior to the scan and this is usually confirmed at this point. Caffeine attenuates the adenosine induced hyperaemia effect, although it is suggested this can be overcome by higher adenosine dose if caffeine consumption is identified [Reyes et al., 2008]. Subjects are monitored for changes in blood-pressure, cardiac rhythm and appearance of other symptoms during hyperaemia. Blood is typically tested for creatinine prior to GBCA injection to enable calculation of estimated Glomerular Filtration Rate (eGFR), which is an estimate for kidney function. This enables a decision to be made on GBCA administration in the presence of any kidney disease based on the type of GBCA used, the clinical requirement of the administration, and other factors.

The inducement of stress is likely to cause discomfort in patients and trigger the angina for which they are usually being investigated. For this reason, some ideal requirements for the imaging protocol may be difficult to achieve, such as breath-hold during the first-pass. Some centres request breath-holding timed to stabilise the key frames of contrast agent arrival into the myocardium. If performed successfully, timed breath-holds enable certain acceleration methods and could improve clinical 2D FPP imaging. With the increased potential for unreliability (see Section 2.4.2) and the potential

discomfort in even short duration breath-holds under pharmacological stress, free-breathing protocols would be preferred if feasible.

1.5.4. Comparison with Other Modalities

Various factors need to be taken into account when comparing different modalities, including cost, accessibility and patient safety. Of central importance though, is the diagnostic capability of the method. Sensitivity and specificity are definitions used to quantify the diagnostic accuracy of a technique. Sensitivity is defined as the percentage of cases in which the pathological condition present is correctly identified, whereas specificity is the percentage of cases in which no pathological condition is present and this absence is correctly identified [Thygesen et al., 2007].

FPP is most often compared against MPS, often using CXA as the gold standard for assessing absolute as well as relative performance of the modalities. From a meta-study analysis the sensitivity and specificity of SPECT MPS are stated as averaging 87% and 75% respectively [Klocke et al., 2003], regarded as respectable values. Multicentre, multivendor studies have now been performed to directly compare the diagnostic performance of these two modalities. The original study found the performance of MRI perfusion to match or exceed that of SPECT, depending on the population sample [Schwitter et al., 2008]. A follow-up study by the same author [Schwitter et al., 2012] reinforces this diagnostic superiority and other studies, including the large CE-MARC trial [Greenwood et al., 2012], show support towards this. The prevalence of SPECT scanners already in clinics and the ability for it to perform whole coverage examination of myocardial perfusion in the heart unlike most current MR variants, goes some way to explaining its current popularity [Ishida et al., 2003]. The use of ionising radiation, poorer spatial resolution and potentially lower diagnostic ability of SPECT compared to FPP suggests the potential for MRI as a replacement.

Direct comparison of other modalities with FPP are less common. PET is increasingly being used to validate quantitative FPP methods [Fritz-Hansen et al., 2008], but non-quantitative comparisons are less common. CT and US methods are relatively new and so cross-modality testing using these techniques has so far been restricted to comparison with the clinically established methods.

An overview table of the different modalities capable of performing myocardial perfusion assessment, modified from [Yang and Kim, 2017] to include

information from [Porter and Xie, 2010], is shown in Table 1.2. The table is provided for approximate comparison only. With values and information taken from multiple sources that use different methods, care should be taken with any inferences drawn from the data.

1.5.5. Alternative MRI Perfusion Methods

First-pass perfusion methods that track the arrival of an exogenous contrast agent are the currently accepted clinical approach for ischaemia detection using MRI. MRI acquisition is extremely flexible and does allow other alternative methods for ischaemia detection, with two main approaches having been proposed that utilise endogenous contrast to avoid the requirement of an external agent.

Arterial spin labelling (ASL) is a technique that "tags" blood upstream of the area of interest, making the blood itself an endogenous contrast agent that can be tracked [Williams et al., 1992] [Detre et al., 1994]. This blood tagging is performed either by saturation or, more commonly for ASL, by inversion. An imaging readout is applied in the region of interest, after a delay that is timed to allow for the arrival of the blood possessing modified magnetisation characteristics and for it to exchange with the water in the tissue. An acquisition is also made downstream of the tagging which is used as a baseline and subtracted from the tagged image. The perfusion in the acquired slice can then be modelled by various processes, depending on the precise acquisition method [Bernstein et al., 2004].

Myocardial ASL has now been investigated by a number of groups [Kober et al., 2016], including a single validation study of detecting myocardial ischaemia [Zun et al., 2011]. Nevertheless, ASL has many difficulties in its application to the heart [Epstein and Meyer, 2011]. Central to this is low signal levels achieved with ASL because myocardial blood flow is relatively low in the time between tagging and acquisition, especially at rest. On top of this, physiological motion strongly affects the subtraction of the tagged images from the baseline which adds high levels of noise comparative to the signal. Breathing motion is particularly intolerable for this reason and requires either shortened acquisition duration for breath-hold, or navigator acquisitions which are sometimes unreliable. Increased myocardial coverage by ASL is also complicated, with 3D ASL very rare due to timing constraints and 2D ASL sometimes restricted to a single slice due to complications in

Table 1.2.: Comparison of non-invasive perfusion modalities

Modality	Common Perfusion Agent	First-Pass Perfusion	Radiation Dose	Quantitative Perfusion Analysis	Wall Motion Analysis	Coronary Stenosis Evaluation	Advantages	Limitations	Sensitivity / Specificity
SPECT	Thallium-201 Tc-99m sestamibi Tc-99m tetrofosmin	Not feasible	8-25 mSv	Not feasible	Not feasible	Not feasible	-Widely available -Extensively validated	-Low spatial resolution -Limited sensitivity for mild to moderate stenoses	0.61/0.84
PET	N-13 ammonia Rubidium-82 O-15	Feasible	2-13 mSv	Feasible	Not feasible	Not feasible	-Spatial res >SPECT -Absolute quantification -Radiation dose <SPECT	-High cost -"Registration artefact"	0.83/0.89
US	Microbubbles	Feasible	Free	Feasible	Feasible	Not Feasible	-No radiation dose -Availability of US	-Low spatial resolution -Limited accuracy -Quantification Issues	0.76/0.78
CT	Iodinated contrast agent	Feasible (dynamic scan)	5-18 mSv	Feasible (dynamic scan)	Feasible (static scan)	Feasible	-High spatial resolution -Rapid acquisition -Additional information (e.g. coronary anatomy)	-High radiation dose -Imaging artefact due to motion -"Beamhardening" effect -Poor contrast agent tolerance -Limited quantification	0.78/0.86
MRI	Gadolinium based contrast agents	Feasible	Free	Feasible	Feasible	Feasible (but limited reliability)	-High spatial resolution -Additional information (e.g. myocardial viability) -No radiation dose	-"Dark-rim" artefact -Incomplete LV coverage -Signal non-linearity (quantification)	0.87/0.91

Modified from [Yang and Kim, 2017], including information from [Porter and Xie, 2010]

both aquisition and modelling with multi-slice methods [Bernstein et al., 2004].

Another technique, blood-oxygen-level dependent (BOLD) imaging, aims to measure the level of oxygenation, and therefore any ischaemic regions, directly. Oxygenated and de-oxygenated haemoglobin have slightly different magnetic properties, with deoxyhaemoglobin being very slighty paramagnetic compared to most other tissues and therefore creating weak local field inhomogeneities. This led to the first demonstrations of deoxyhaemoglobin affecting blood T_2 relaxation [Thulborn et al., 1982] and MR techniques were soon developed to investigate oxygenation in a region of interest using this principle [Ogawa et al., 1990] [Belliveau et al., 1991].

Early myocardial applications of the BOLD response focussed on T_2* prepared sequences. T_2* methods are however prone to susceptibility and field inhomogeneity artefacts and both intra- and inter- subject repeatability were relatively poor. For this reason T_2 contrast methods have become more popular due to greater robustness, despite lower sensitivity to oxygenation [Zheng, 2013]. Myocardial BOLD has been demonstrated in multiple patient studies [Friedrich and Karamitsos, 2013], some showing levels of accuracy close to MPS in patients with severe stenoses [Friedrich et al., 2003].

Both ASL and BOLD techniques are popular in neuro-MRI as they can be more easily applied in a static region. Along with some issues in reliability, achieving a high level of defect contrast-to-noise ratio cannot realistically currently be achieved for cardiac applications, particularly compared with methods using exogenous contrast agents. This remains a major drawback of these alternative methods, that therefore often require more averaging and uncomfortably longer scan time at stress.

1.5.6. Ideal FPP Parameters & Current Limitations

As with most medical imaging, the ideal parameters for FPP are many, interdependent and often contradictory, requiring a trade-off in any realistic setting. An ideal sequence would include: high spatial and temporal resolution, high signal-to-noise ratio (SNR), coverage of the LV that supports the clinical purpose effectively and reliability with a simple acquisition protocol for routine use.

Fine spatial resolution is required in-plane in order to adequately resolve the transmurality and extent of perfusion defects. This also reduces the impact of the problematic dark-rim artefact (DRA) [Di Bella et al., 2005],

which frequently confounds imaging of perfusion defects. The DRA is partly caused by a Gibbs truncation effect at the sharp signal changes between the subendocardial myocardium and brighter contrast-enhanced blood-pool. The DRA width, and thereby its impact, has previously been shown to be reduced by increased spatial resolutions [Plein et al., 2007]. For visual analysis of most defects, isotropic in-plane resolution of <3mm is generally deemed sufficient [Kramer et al., 2013][Hendel et al., 2016], with a trade-off between image acquisition duration and other parameters. Through-plane resolution is usually less important for clinical evaluation because the slice direction is typically along the long-axis of the heart, but more apical slices usually suffer more partial volume artefact.

The temporal resolution of FPP imaging, i.e. imaging each slice every single cardiac cycle ("single-RR") or alternate cycles ("alternate-RR"), is another important consideration without a clear consensus [Gerber et al., 2008]. Acquiring single-RR multi-slice FPP arguably might increase diagnostic confidence, such as in situations involving a rapidly filling defect. On the other hand, alternate-RR can deliver greater myocardial coverage and with careful setup has potential to avoid imaging during phases of rapid cardiac motion [Schwitter, 2006][Schwitter et al., 2001].

SNR and the related contrast-to-noise ratio (CNR) are required to be high in FPP to allow perfusion defects to be distinguished from the normally perfused myocardium, especially as a defect may be only a mild limitation of blood supply, causing only a small difference in myocardial signal. However CNR depends on many other factors such as contrast agent dose/delivery, T_1 sensitivity and sequence type, as described [Gerber et al., 2008].

Reliability of the protocol is also key, as the imaging is performed during the first-pass of a GBCA. Practically, a requirement for breath-hold (in support of certain acceleration methods discussed in the next chapter) introduces unreliability over whether the breath-hold is maintained during the key frames of contrast arrival, although the importance of this is debated. A requirement of breath-hold or gentle breathing is made more difficult by the potential impact of adenosine or other stress agent on respiratory motion. The effect of ECG misgating is another concern for reliability, particularly with the relatively high prevalence of cardiac arrhythmias. In general the potential for image artefacts in FPP, particularly the previously described dark-rim artefact, is a major source of concern for the diagnostic performance.

Coverage of the LV is the final consideration discussed here. With other perfusion modalities offering full coverage of the LV, the conventional 3 or 4 nominally equi-distant SAX slices along the LV for FPP is a potential limitation. There is considerable debate over the clinical utility of coverage of the whole LV [Schwitter, 2006][Biglands, 2012], hereafter referred to as "whole-heart" coverage, particularly when at the expense of other factors such as spatial resolution [Motwani et al., 2013]. Traditional multi-slice FPP has been shown a reliable method of investigating CAD, showing high accuracy suitable for clinical need [Schwitter, 2006]. However, there are some key proposed potential advantages to full coverage FPP (discussed Section 2.1.1), potentially improving clinical confidence if these could be achieved without significant compromise to other imaging parameters. These potential advantages, the techniques required for achieving them and example literature are reviewed next.

2. Extending Myocardial First-Pass Perfusion to 3D

2.1. Introduction

Extension of FPP protocols from 2D non-contiguous coverage of the left ventricle (LV) to 3D whole-heart imaging has been hypothesised as a way of increasing the competitiveness of MRI for myocardial perfusion imaging [Vogel-Claussen, 2012]. Whilst there is debate over the clinical utility of 3D FPP when coverage is at the expense of other imaging parameters (discussed further in Section 2.1.1), there is much interest in its potential advantages; for example, possible increased confidence by obtaining more slices over the same cardiac regions and the slices being all at the same cardiac phase (which was particularly noted as useful by clinicians during the early work of this thesis). There has therefore been a recent increase in publications on 3D FPP (see Table 2.1), and with it increasing application of novel high-acceleration methods.

The purpose of this chapter is exploration of this wide range of current and potential techniques for achieving 3D FPP, in particular the acceleration of data acquisition. The potential benefits of 3D FPP are reviewed first, followed by a justification for the approximate acceleration required to achieve this translation to 3D. A review and explanation of two main categories of acceleration methods is then presented. These are referred to as pulse sequence modification and sub-Nyquist reconstruction techniques, and include non-Cartesian k-space trajectories, k-space efficiencies (defined later), and multiple varieties of parallel imaging and compressed sensing. Having presented these methods concurrent with examples in 3D FPP literature, the smaller amount of clinical research is summarised. The issues arising with applying such acceleration techniques to FPP are then examined before finally discussing future considerations and requirements.

Table 2.1.: Overview of technical developments in 3D whole-heart first-pass perfusion literature

Lead Author	Year	Reconstruction Method	Trajectory	Other Stated Efficiencies	US Factor (Nom.)	US Factor (True)	Reconstructed Resolution /mm	Acquisition Window/ms	Stress Agent	Free Breathing†	Field Strength/T
Shin	2008	TSENSE	Cartesian	-	6	6	$3.0 \times 4.5 \times 10.0$	304	No	No	3
Shin	2010	TSENSE	Cartesian	-	6	6	$4.5 \times 6.7 \times 10.0^{a}$/$2.8 \times 4.2 \times 10.0^{b}$	116-145[a]/254-305[b]	No	No	3
Manka§	2011	k-t SENSE	Cartesian	Partial Fourier	NS	6.3	$2.3 \times 2.3 \times 10.0$	200	Yes	No	3
Vitanis	2011	k-t PCA (compartment based)	Cartesian	Elliptical Shutter (75 %); Partial Fourier (75 %)	10	5.6-7.5	$2.3 \times 2.3 \times 10.0$	225	Yes	No	3
DiBella	2012	CS (temporal)	Radial	-	∼14	∼14	$2.2 \times 2.2 \times 8.0$	310	No	No	3
Manka§	2012	k-t PCA	Cartesian	Partial Fourier	10	7	$2.3 \times 2.3 \times 10.0$	NS	Yes	No	1.5
Jogiya§	2012	k-t PCA	Cartesian	Partial Fourier	10	7	$2.3 \times 2.3 \times 5.0$	NS	Yes	No	3
Chen	2012	CS (spatio-temporal)	Radial	Partial Fourier (75 %)	∼9-11	∼9-11	(1.8-2.8) × (1.8-2.8) × (6.0-10.0)	300	No	No	3
Shin	2013	k-t SENSE	Spiral	-	5	5	$2.4 \times 2.4 \times 9.0$	230	No	No	1.5
Giri	2014	TWIST (GRAPPA)	Cartesian	2D Partial Fourier (87.5 % / 87.5 %)	3	3	$2.2 \times 2.8 \times 8.0$	300-380	No	No	1.5
Motwani	2014	k-t PCA	Cartesian	2D Partial Fourier (70 %/70 %)	10	7	$2.3 \times 2.3 \times 5.0$	192	Yes	No	3
Schmidt	2014	k-t PCA (motion-corrected)	Cartesian	Elliptical Shutter; 3D Partial Fourier (62.5 % / 75 % / 75 %)	10	NS	$2.3 \times 2.3 \times 10.0$	205-225	No	Yes	3
Akçakaya	2014	CS (localised constraints)	Cartesian	Elliptical Shutter (75 %)	10	10	$2.3 \times 2.3 \times 10.0$	250	No	Both	1.5
Jogiya§	2014	k-t PCA	Cartesian	Elliptical Shutter; 2D Partial Fourier (75 % / 75 %)	10	7	$2.3 \times 2.3 \times 5.0$	191	Yes	No	3
Jogiya	2014	k-t PCA	Cartesian	Elliptical Shutter; 3D Partial Fourier (NS/75 %/75 %)	10	7	$2.3 \times 2.3 \times 5.0$	191	Yes	No	3
Manka§	2015	k-t PCA	Cartesian	Elliptical Shutter; 2D Partial Fourier (75 % / 75 %)	10	7	$2.3 \times 2.3 \times 5.0$	200	Yes	No	3
Wang	2017	CS (spatio-temporal)	Cartesian	Partial Fourier (83 %)	11	11	(2.0-2.4) × (2.0-2.4) × (4.0-6.0)	255	No	No	3

§Clinically relevant/tested techniques see Table 2.2 for details
†Imaging during breath-hold assumed in cases where literature did not state
‡US factor estimated from number of radial projections and number of readouts: $N_{Nyquist} = (\pi/2) \times N_{readouts}$
[a]Systolic acquisition values, [b]Diastolic acquisition values
∼Nominal spatial resolution can be affected by off-resonance errors in long spiral readouts
Abbreviations: US undersampling; NS not stated; others as defined in text

2.1.1. Hypothesised advantages of 3D FPP

There are a number of potential advantages to extending FPP to complete coverage of the LV through 3D imaging. The most commonly discussed and possibly the most important of these is in enabling the assessment of the "ischaemic burden", i.e. the proportion of the LV myocardium that is ischaemic. Ischaemic burden has been linked to survival prognosis [Shaw et al., 2008] and would allow FPP to match MPS in delivering this diagnostic feature.

Secondly, complete coverage could improve confidence that no defects have been missed. The coverage achieved by traditional 2D multi-slice has been shown to have sufficient diagnostic ability, as previously discussed, showing high accuracy in comparison to other imaging techniques. Whilst coverage with 3 or 4 short-axis slices may be sufficient for clinical accuracy [Schwitter, 2006] some work has suggested this accuracy may be improved by complete coverage (Section 2.5). Due to cardiac motion between the slices, exact myocardial coverage can be complicated for multi-slice. For example, if acquired in base-mid-apical order during the cycle, the basal motion of contraction towards the apex and its recoil can confound coverage, possibly missing some mid-ventricular muscle. 3D acquisitions give greater assurance of contiguous, non-overlapping, coverage.

Continuous coverage (even if not whole-heart) with 3D imaging also brings a potentially strong benefit in that all the images in each cycle are at the same cardiac phase and respiratory phase, even if both are liable to intra-shot motion artefacts. This avoids the "missing coverage" effect described above but also keeps certain motion artefacts consistent across all slices. This may improve on a major clinical difficulty in reporting, i.e. with cardiac motion artefacts that differ strongly between the 2D FPP slices.

It may also assist in distinguishing between DRAs and true perfusion defects, as complete-coverage may enable improved tracking of the hypointense region through-plane for discriminating between the two, in some situations employing knowledge of typical coronary territories as already used where appropriate in 2D FPP clinical work [Cerqueira et al., 2002].

3D imaging acquires the raw data (k-space) with additional repeated acquisitions of phase-encoding ($N_{partitions}$) used to collect the third dimension (called slice, partition or secondary phase encoding). Along with providing contiguous coverage, this also delivers a fundamental increase in SNR. From Edelstein *et al.* [Edelstein et al., 1986], keeping all other factors the same, it

can be derived that the SNR in 3D compared to its 2D equivalent is

$$SNR_{3D} = SNR_{2D} \times \sqrt{N_{partitions}} \tag{2.1}$$

A limitation to this equation is that it does not account for greater saturation caused by the slab RF excitation pulses compared to multi-slice. No direct measurement of this predicted SNR gain in 3D FPP has been performed to date, largely due to the modification of SNR by the acceleration methods required to achieve 3D.

Extended coverage of the LV can also be obtained by acquisition of a greater number of slices per cardiac cycle with multi-slice methods [Köstler et al., 2003] [Kellman et al., 2004a] [Stäb et al., 2014]. Such multi-slice acquisitions have shorter individual shot-times comparative to 3D, greatly improving robustness to cardiac motion while offering some of the same advantages from the increased coverage. Extended 2D coverage offers some potential to aid in artefact identification as well as reducing the unacquired area for small defects to be missed. However, the variation in cardiac phase during acquisition increases the difficulty in making comparisons across the slices and artefact characteristics will be altered. Inter-slice motion as discussed above creates uncertainty in exact myocardial coverage and this in turn could also lead to inaccuracies in attempted ischaemic burden calculations. As previously mentioned (Section 1.5.2), multi-slice acquisitions will additionally either require different saturation recovery times (and therefore image contrast) per image or a large proportion of the cardiac cycle will be used to wait for multiple saturation recoveries. This, combined with the lack of inherent SNR advantage in 3D acquisitions, makes the acceleration required for whole-heart coverage difficult to achieve with multi-slice FPP and the resulting images will lack at least some of the benefits gained with 3D FPP. The remainder of this work will focus on 3D methods (although many of the acceleration techniques presented in this chapter can and have been applied to 2D multi-slice methods).

2.1.2. Requirement for Acceleration in 3D FPP

Extension of FPP to 3D will naturally lead to an increase in shot time due to the addition of partition encoding, causing strong changes in the trade-off between spatial resolution, temporal resolution, LV coverage and SNR. To gain an understanding of the shortfall that an unaccelerated imaging sequence would have in meeting these requirements, timings of a 3D fast

low flip-angle spoiled gradient-echo (FLASH) sequence were calculated to illustrate the potential required 3D shot durations (see Appendix A). Despite using a sequence based on fast timing rather than image quality, this gives an acquisition time of around 2.8s to acquire data of the whole-heart with the proposed desired parameters; this illustrates the scale of the challenge because FPP imaging requires at least alternate-cycle imaging of GBCA distribution, so the usual "segmented" methods for accumulating resolution over multiple cardiac cycles cannot be applied.

Whilst the above estimated timing already prevents adequate temporal resolution of one (or even two) cardiac cycles, the cardiac motion itself further limits the acquisition "window" for FPP to either the mid-diastolic or end-systolic periods of reduced motion (Figure 2.1). Although some formulations exist for predicting these pause times based on the R-R interval [Huang et al., 2014], generally in MRI it is best practice to measure them using cine imaging. For 3D FPP, the end-systolic period has a benefit of the heart being contracted along its long-axis, therefore requiring a smaller 3D partition-direction field-of-view (FOV) which directly reduces the imaging time needed per image. In this phase the myocardium is also transmurally thicker, which has been shown to give greater visualisation of perfusion defects [Motwani et al., 2012]. End-systolic imaging in healthy subjects has been shown in early 3D FPP to produce image quality comparable to diastole [Shin et al., 2010]. Despite this, the short duration of the systolic pause means that a large number of 3D FPP studies to date have been acquired in the diastolic pause. During physiological or pharmacological stress both pauses become shorter, but more particularly at diastole [Ravichandran et al., 2012], and so potential acquisition windows are shortened further. Whilst 3D FPP work has a wide range of stated acquisition windows (Table 2.1), here an ideal time of less than 150ms for the shot duration is used in our estimates. With diastasis durations of 100ms associated with HRs of 70bpm [Chung et al., 2004], even 150ms would be a compromise towards the longer acquisition windows currently being reported in 3D FPP literature.

The potential utility of 3D FPP has driven an improvement in current acceleration techniques, as well as development of entirely novel approaches. Based on the above estimate of a basic 3D FLASH sequence, acceleration factors of around 20 could be required to achieve an acquisition window below 150ms. Acceleration of this magnitude is unlikely to be achieved directly through one method alone. Acceleration methods to date have used

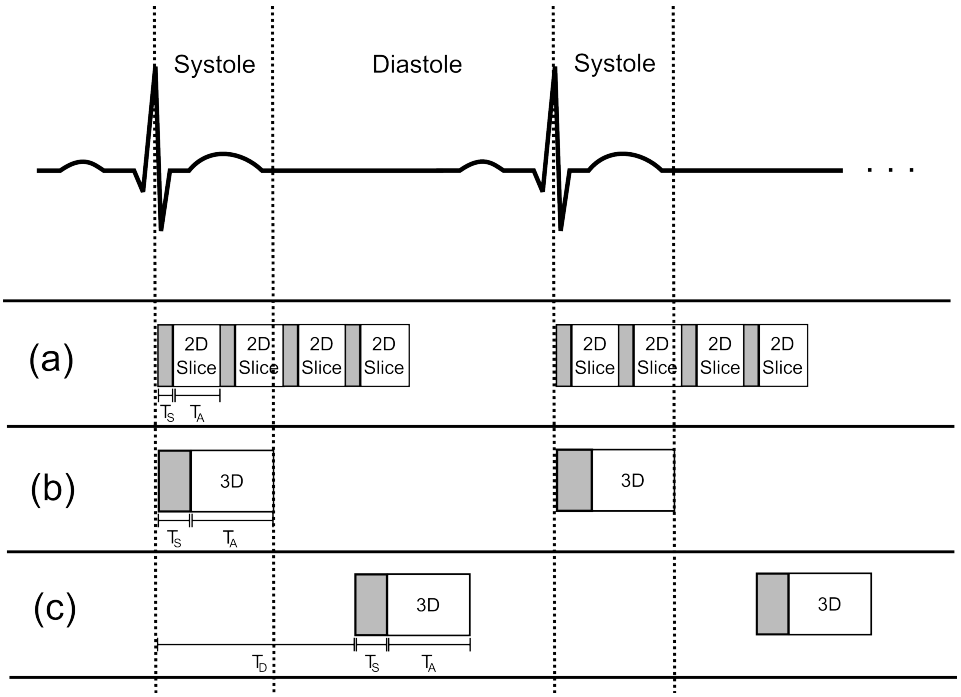

Figure 2.1.: Acquisition timings. Whilst conventional 2D multi-slice FPP is acquired throughout the cycle, typically starting in early systole (a), there are two popular options in 3D FPP. The 3D acquisition can be placed either in mid-systole (b) or mid-diastole (c), although the durations of these periods of minimal motion can be problematic (see text). Trigger delay (TD), saturation time (TS) and acquisition time (TA) are labelled for each in the first cardiac cycle.

a combination of two broad areas: pulse sequence modification (Section 2.2) and sub-Nyquist sampling reconstruction techniques (Section 2.3). This chapter will focus on the current and potential schemes used in these two areas to attain 3D FPP, along with the difficulties arising from their application and discussion on what the future may hold for this rapidly growing field.

2.2. Pulse Sequence Design

Many of the acceleration methods described here can be applied to various MRI pulse sequence types. After a discussion of the basic sequence types available for 3D FPP, an examination of various modifications to increase acceleration will be presented.

2.2.1. Sequence Type

The choice of sequence type for 3D FPP is based on many of the same factors as for 2D FPP (Section 1.5.2). Despite this, almost all previous 3D work has used a SGRE type sequence. One potential reason for this is that with the increasingly complex acceleration techniques used in 3D FPP, a highly robust base sequence is needed. FPP is one application of cardiac MRI where the consensus is fairly clear that it benefits from higher field strengths [Meyer et al., 2008] with the potential SNR loss of high acceleration factors required for 3D further supporting higher field strengths. Previously discussed issues in reliability with h-EPI and bSSFP type sequences at >1.5T are therefore also likely to be a concern.

Despite this, one recent piece of work has applied bSSFP to 3D FPP at 3T, investigating use of dual-source parallel transmit capabilities [Jogiya et al., 2014b]. The application of this technique resulted in bSSFP acquired 3D FPP datasets of similar quality to equivalent 3D SGRE datasets, with predicted increased SNR and CNR, but with increased artefacts (including DRA). An extension to bSSFP specifically for FPP, called Steady-State First-Pass Perfusion (SSFPP), has also been proposed [Giri et al., 2014]. This applied the inherent $\sqrt{T_2/T_1}$ weighting of bSSFP in the setting of short native myocardial T_2 to deliver myocardial T_1-weighting by continuous imaging without saturation pulses. This was presented in 2D FPP as well as showing initial 3D experience.

Earlier 3D work used the SGRE steady-state to eliminate saturation pulses [DiBella et al., 2012] by continuous ungated acquisition, before data with

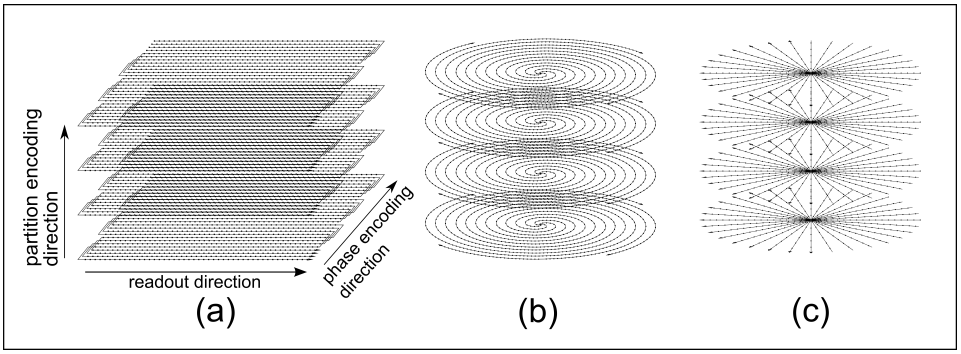

Figure 2.2.: Non-Cartesian trajectories. Examples of three potential alternate trajectories discussed in the text. h-EPI (a) demonstrated with an ETL of 4, a spiral trajectory (b) with 4 interleaves and a radial projection design (c). Partition encoding direction in (b) and (c) is the same as for (a).

similar cardiac phase were identified and reconstructed. The focus of this work was on high SNR and CNR in the myocardium, ignoring effects in the blood pool including inflow artefacts from unsaturated blood, making this implementation of most benefit to non-quantitative FPP. However, for 3D FPP, the acquisition window per 3D image would require even further acceleration before this ungated approach may become realistic.

The majority of previous 3D FPP work has been based on saturation-recovery gated SGRE sequences for the reasons reviewed, and so the primary focus of this chapter will continue with their optimisation.

2.2.2. Alternative K-Space Coverage

As with 2D encoding, coverage of k-space in 3D need not necessarily be Cartesian, and some alternative approaches can accelerate imaging.

EPI, as previously discussed, modifies the way in which it traverses k-space to allow efficiencies in its acquisition. It is geometrically very close to typical Cartesian k-space coverage (Figure 2.2), with some minor modifications to the varying density of k-space sampling when ramp sampling is applied [Bernstein et al., 2004]. h-EPI in 2D FPP typically uses an ETL of around 4 at 1.5 T [Ding et al., 1998] (with no current examples at 3T). An ETL length of 4 would correspond to acceleration factors of approximately 2 compared to the FLASH timings calculated earlier (see Appendix A). Early examples of 2D FPP with extended LV coverage used h-EPI [Ding et al., 1998] [Takase et al., 2004] [Kellman et al., 2004a] but so far 3D EPI imaging has largely

been limited to non-cardiac work.

Other trajectories in k-space gain their efficiency through altering the geometry of their coverage to collect more data after each RF excitation. Spiral imaging [Likes, 1981] [Ljunggren, 1983] collects data while spiralling outward from the k-space centre (Figure 2.2b), replacing the conventional phase-encode and frequency-encode gradients. As with EPI, the multi-shot variants are most commonly used for FPP, due to the relatively large amount of data required and off-resonance effects with long spiral readout durations [Yudilevich and Stark, 1987]. Careful choice of readout duration, flip-angle strategy and other characteristics of a spiral sequence have been shown to compensate for spiral related artefacts in FPP to produce high quality 2D images [Salerno et al., 2011].

Extension of spiral sequences to 3D can in theory provide spherical or elliptical coverage of k-space [Wong and Roos, 1994]. Far more common is a 3D "stack of spiral" approach that uses Fourier encoding in the partition direction to sample a cylindrical distribution. The acceleration achieved with a stack of spiral design for the purpose discussed here is estimated to be similar to that of h-EPI (see Appendix A). The spirals can be produced as uniform density, with a constant sampling interval in the radial direction of k-space, or with variable density which utilises greater sampling density radially in the central region of k-space than is used further out. The variable-density spirals have been shown to improve image quality in 2D FPP [Salerno et al., 2013]. Variable density in the radial direction results in either oversampling the centre of k-space to reduce aliasing artefacts [Tsai and Nishimura, 2000] or to have undersampled edges combined with a Nyquist sampled centre, suitable for combination with parallel imaging (discussed Section 2.3). A 'dual-density' approach, with uniform fully-sampled centre and uniform undersampled edges of the spirals, was applied by Shin *et al.* [Shin et al., 2013] in conjunction with advanced parallel imaging techniques to achieve 3D whole-heart FPP. This gave in-plane resolution of 2.4×2.4mm, and compared favourably with the image quality and dynamics of 2D Cartesian acquisitions, with an acquisition time of 230 ms but was performed only at rest.

Sampling with projections (Figure 2.2c) through the centre of k-space ('projection acquisition' or 'diametrical sampling') is now commonly named radial imaging. For Nyquist sampling at the edges of the acquired k-space, radial trajectories massively oversample the centre, leading to high motion

robustness. This oversampling means that radial trajectories are therefore fundamentally somewhat slower than the conventional phase-encoded approach, but they allow acceleration techniques to be applied efficiently. Even when the edges of raw data are undersampled, the full or oversampled centres naturally support parallel imaging and other acceleration techniques. Likely due to this lower efficiency than phase-encoding, radial imaging has seen less application to 2D FPP, with its limited applications drawing on its suitability to specific purposes (e.g. multiple samples through the centre of k-space to calculate the arterial input function [Kholmovski and DiBella, 2007] and its inherent motion robustness for free-breathing [Ge et al., 2010]). Radial sampling lends itself to combination with compressed sensing methods [Lustig et al., 2007] and as greater numbers of motion sensitive compressed sensing methods emerge it may be applied more to 3D FPP (more discussion in Sections 2.3.4 and 2.4.3). Recently, radial trajectories have been used for 3D whole-heart FPP sequences [DiBella et al., 2012] [Chen et al., 2012] [Wang et al., 2014b], combined with compressed sensing. In all cases, a stack of the 2D radial trajectories formed a 3D cylindrical sampling of k-space, as for the spiral examples. Fully radial 3D trajectories are also possible [Glover et al., 1992] ("kooshball"), with techniques such as Vastly undersampled Isotropic Projection Reconstruction (VIPR) [Barger et al., 2002] utilising the greater tolerance to undersampling, again being well suited to compressed sensing and similar reconstruction techniques [Mistretta, 2009]. Fully radial 3D techniques are less common in cardiac work and with the small number of projections achievable in 3D FPP as well as the lower requirement for isotropic resolution (with coarser sampling typical along the LV long-axis) it is less likely to see application to this topic.

Some of the beneficial properties of the above trajectories can be combined, for example by adding a spiral twist to the ends of radial projections, known as TWIsting Radial Lines (TWIRL) [Jackson et al., 1992] or using a narrow Cartesian grid acquisition rotated through projection angles to cover a disc, named Periodically Rotated Overlapping ParallEL Lines with Enhanced Reconstruction (PROPELLER) [Pipe, 1999]. These have yet to be be applied to even 2D FPP, but are possible considerations for the highly optimised sequences required for 3D FPP.

2.2.3. Other K-Space Efficiencies

To achieve the acceleration required for 3D FPP, further reductions in raw data coverage are often applied in conjunction with many of the methods discussed, although they are incompatible with some of the non-Cartesian methods. These k-space "efficiencies" include methods such as partial Fourier, elliptical "shutters", zero padding and zonal-imaging (see Figure 2.3) and are described in this section. Many of the details of these techniques can be found in textbooks, such as [Bernstein et al., 2004] or [Haacke et al., 1999].

Partial Fourier imaging (Figure 2.3a) is also sometimes known as partial averaging (fractional NEX) or partial echo when applied along phase-encode and frequency-encode directions respectively. If fully implemented, partial Fourier uses the "conjugate symmetry" [Bernstein et al., 2004] of k-space under certain conditions to reconstruct omitted regions. The perfect k-space representation of an object should be Hermitian in nature, meaning that the real and imaginary components are symmetric and antisymmetric respectively in the two halves of k-space, i.e.

$$S(-k_x, -k_y, -k_z) = S^*(k_x, k_y, k_z) \tag{2.2}$$

where S is the signal data and * denotes the complex conjugate.

In reality, phase variations across the image FOV, caused by various factors, break the mathematical conditions supporting this method. In practice therefore, corrections can be made using a low-resolution phase image estimated by extending raw data collection slightly into the omitted half [Feinberg et al., 1986] [Cuppen and van Est, 1987] [Haacke et al., 1991]. A simpler alternative is more often performed, which is not true partial Fourier reconstruction, zero-filling the portions of k-space omitted by the truncated acquisition, for input to the reconstruction by Fourier transformation. However, this usually requires a higher proportion of acquired k-space for acceptable accuracy, and wider Gibbs ringing artefacts are typically provoked by the sudden truncation of sampling nearer central k-space. This process is effectively a filter and consequently reduces spatial resolution. A benefit is that zero-filling allows a truncated acquisition to be applied in multiple directions simultaneously (unlike conjugate synthesis), giving greater acceleration. Cartesian examples of 3D whole-heart FPP have used this principle of zero-filled "partial Fourier" extensively, in 2 [Motwani et al., 2014] [Jogiya et al., 2014a] and all 3 [Schmidt et al., 2014] dimensions.

Another type of zero-filling or "zero-padding" in raw data operates by

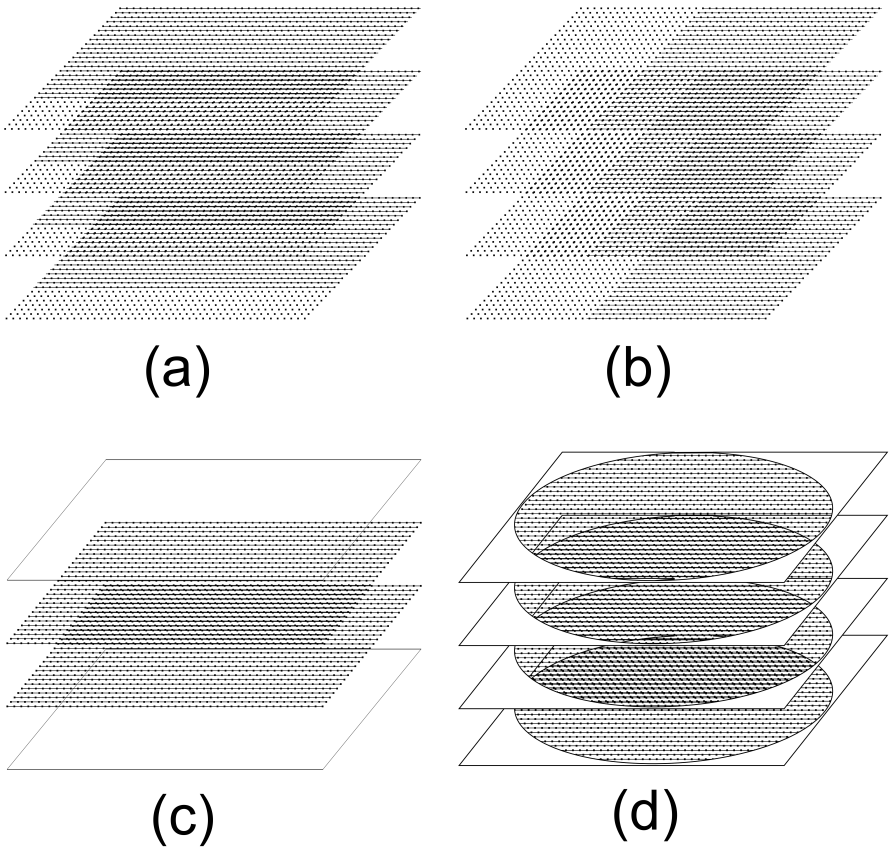

Figure 2.3.: K-space efficiencies. Three k-space acquisition modifications demonstrated for a 3D Cartesian sequence. Representations of partial Fourier in the phase-encoding (a) and readout (partial-echo) (b) directions are shown, with dashed lines denoting data points that are not acquired but later calculated (see text). Zero padding (c) has lines of 'data' filled with zeros added either side of the acquired data before reconstruction, artificially increasing resolution. An elliptical shutter (d) does not acquire the corner regions of k-space, as they are deemed less critical. Each of these methods can be applied in any encoding direction and those chosen here are simply illustrative.

"pads" of extra zero-valued lines added symmetrically to both edges of k-space (Figure 2.3b) before applying the Fourier transform. This synthetically reduces the pixel size of the reconstructed image, without the added time of acquiring extra data. This is virtually equivalent to post-reconstruction interpolation of pixels, but differs regarding consistency of the Gibbs artefact [Ferreira et al., 2009]. Zero-padding is prominently used in the partition direction in 3D FPP imaging due to the significant extension in time needed to increase the acquired data in this direction, but can be applied in any or all directions. Artefacts such as Gibbs ringing are common with this technique, as previously mentioned, with the sharp cut-off in k-space manifesting as ringing artefacts at strong edges in the image. Some filtering can be applied to reduce this ringing at the cost of loss of resolution. Zero-padding is not always explicitly stated in literature, but care needs to be taken with these techniques because Gibbs ringing is a particular issue in DRAs in FPP.

Another possible efficiency gain by omitting regions of k-space is to exclude the acquisition of the corner regions of k-space (Figure 2.3c). This has various names but will here be referred to as an elliptical shutter, due to the typical shape of the acquired k-space. Due to the small genuine signal amplitude in outer regions compared with the uniformity of noise, omitting the corner regions of k-space can improve the SNR. Furthermore, with an apodisation filter to reduce Gibbs ringing typically applied in a radial or elliptical fashion for isotropic resolution, the corners of k-space, even if acquired, are typically filtered to zero before reconstruction. Some scanning efficiency can therefore be gained by omitting acquisition of these corners in the first place. However, combination with other efficiencies makes the effects of this process more complex, because the corners of k-space impact the resolution when applying zero-padding [Bernstein et al., 2001]. The combination of an elliptical shutter and 3-dimensional partial Fourier mentioned in the previous paragraph, on top of other acceleration methods (see Section 2.3.2), enabled a 3D FPP protocol acquiring just 5% of the total k-space data required for the nominal resolution and FOV [Schmidt et al., 2014]. These three types of "zero-filling" k-space efficiency are widely used to further accelerate 3D FPP in addition to the main methods of many papers.

Moving on to an alternative approach, inner-volume [Feinberg et al., 1985], zoomed or zonal-imaging reduces acquisition times by exciting only a narrowed phase-encode FOV over the relevant tissue, therefore reducing the number of required data lines for the same phase-encoding resolution. This

was previously demonstrated in 2D FPP by spin-echo EPI [Gatehouse et al., 2000] [Ferreira et al., 2012], and by two-dimensional spatially selective pulses [Pauly et al., 1989] without spin-echo limitations. The biggest drawback of this latter approach is the complexity and extended duration of zone-selection, which is much slower and less reliable than ordinary slice-excitation. The scanning efficiency gained by zonal-imaging is therefore highly dependent on the application. For 2D FPP, the phase-encode FOV is typically already minimised to the smallest dimension of the patient's thorax in the standard short-axis plane, even permitting phase-encode wraparound if it does not reach the LV myocardium. This, combined with the requirement for rapid repetition of RF excitations, limits zone-selective imaging in 3D FPP, based on simple estimates balancing 2D-selective RF pulse duration, EPI echo train length, SNR and phase-encode FOV reduction. A zonal method, applied in combination with a spiral trajectory, has however recently been applied in 2D multi-slice FPP to gain extended coverage [Yang et al., 2017].

2.3. Acceleration Through Sub-Nyquist Reconstruction

The second broad method of acceleration is with sub-Nyquist reconstruction techniques. As with some of the methods discussed above (Section 2.2.3), these methods also accelerate the acquisition by sampling fewer points in k-space. However, rather than reducing the extent of k-space coverage or traversing it in a more efficient manner, sub-Nyquist methods accelerate through undersampling, defined as increasing the spacing between k-space samples to an extent that would typically cause intolerable FOV aliasing (wraparound) artefacts [Deshmane et al., 2012]. Each technique differs in the way undersampling is performed, and also critically the method used to compensate for missing data and reconstruct an image without FOV aliasing. These methods can achieve high acceleration factors and are an essential component in 3D FPP.

2.3.1. Early Whole-Heart FPP Work Using Parallel Imaging

One of the biggest breakthroughs in MRI, certainly with regards to imaging acceleration, was the creation and improvement of parallel imaging (PI) methods [Carlson, 1987] [Hutchinson and Raff, 1988] [Pruessmann et al., 1999] [Griswold et al., 2002]. The basic premise is to achieve acceleration

by utilising spatial redundancy in multiple receiver coils [Larkman and Nunes, 2007] [Deshmane et al., 2012] and several varieties are standard on commercial scanners. The ability to perform accurate reconstruction with PI acceleration opened the door to the first attempts at whole-heart FPP. With only relatively low acceleration factors achievable due to the SNR losses accompanying PI, the first adaptations to whole heart coverage used multiple time-frames of FPP series data in calculating coil sensitivity (so called temporal PI techniques) to maximise acceleration. General reviews on PI include [Pruessmann, 2006] [Larkman and Nunes, 2007] [Deshmane et al., 2012].

Köstler *et al.* used a verson of SENSE incorporating coil profile information (auto-SENSE) in 2003 to first demonstrate whole-heart coverage every cardiac cycle, with a contiguous stack of 2D slices [Köstler et al., 2003]. Despite achieving full coverage, an undersampling acceleration factor of only 2 was applied and therefore spatial resolution was coarser than the ideal values considered earlier. Kellman *et al.* [Kellman et al., 2004a] extended the use of h-EPI with TSENSE [Kellman et al., 2001] to produce improved quality in extended coverage FPP, potentially whole-heart, but again limited by the parallel imaging performance to an acceleration factor of 2.

These first two works moved towards whole-heart FPP whilst utilising 2D imaging; the step from 2D to 3D requires greater acceleration. Counteracting this is the fact that 3D trajectories allow PI to be spread across the two phase-encoded directions [Weiger et al., 2002]. PI performed in this way is more efficient than the same total acceleration across just one direction because of more moderate increases in the g-factor dependent part of SNR loss (dependent on coil design). Application of SENSE with an undersampling factor of 6 (3x2, phase-encoded and partition-encoded directions respectively) first demonstrated the feasibility of 3D whole-heart FPP [Kellman et al., 2004b]. A more detailed comparison with multi-slice 2D FPP was later made with similar methods but utilising the greater SNR of higher field strengths, and additionally demonstrated the benefit of 3D imaging in estimating perfusion defect size [Shin et al., 2008].

2.3.2. Parallel Imaging Using Joint Spatiotemporal Redundancy

The feasibility of true 3D whole-heart FPP with good SNR, spatial and temporal resolution could not be fully realised until the introduction of a

new type of PI method. These use the joint spatiotemporal redundancy in dynamically acquired datasets i.e. taking advantage of the similarity of large portions of the images during FPP and/or the generally gradual changes in image contrast that occur [Tsao and Kozerke, 2012]. These techniques are collectively referred to here as k-t PI techniques, due to the temporally (t) varying k-space (k) sampling pattern used in these methods. The origins of k-t PI methods can be traced back to the UNFOLD reconstruction algorithm [Madore et al., 1999], which was an extension to the original PI and temporal PI techniques to make simultaneous use of spatial and temporal redundancy. Redundancy in MRI datasets across time (i.e. across the temporal dimension) can be translated as a narrower point spread function (PSF) of the series of images when transformed into representation of the different temporal frequencies in the series. This is known as the x-f domain, where x represents *all* of the spatial dimensions (e.g. an entire image in x-y) and f corresponds to frequency, obtained through a Fourier transform across the images in the time dimension (Figure 2.4). This means, with appropriate sampling patterns and small enough acceleration factors, the leakage of PSF energy due to aliasing can be filtered from the true object signal (Figure 2.5), which is then Fourier-transformed back to make unaliased images. The process, in effect applying a temporal filter, does not directly cause SNR degradation of gradual changes in image contrast, and therein lies its potential. However, this also ties into a limitation that more sudden or dynamic real changes in image contrast can lose SNR locally [Chao et al., 2010], for example if a GBCA bolus remains very compact on arrival in the myocardium.

Whilst UNFOLD and its predecessors uncovered a powerful concept of capitalising on the combined redundancies in spatial and temporal dimensions, its application in cardiac work is mostly limited to acceleration factors of 2 [Tsao, 2002] due to the dynamic region being restricted to a central zone of 50% of the phase-encode FOV. The PSF produced by this dynamic region would overlap at higher acceleration rates and therefore cannot be separated through a simple filter. This minimisation of the dynamic region to only the central FOV enclosing the heart therefore also has a built-in assumption of perfect breath-hold (and negligible other peripheral changes such as vessel pulsatility or contrast agent change), although a method of easing this constraint to improve applicability to free-breathing FPP has been presented [Ablitt et al., 2004].

Alone this would not support the acceleration required for 3D FPP. Ex-

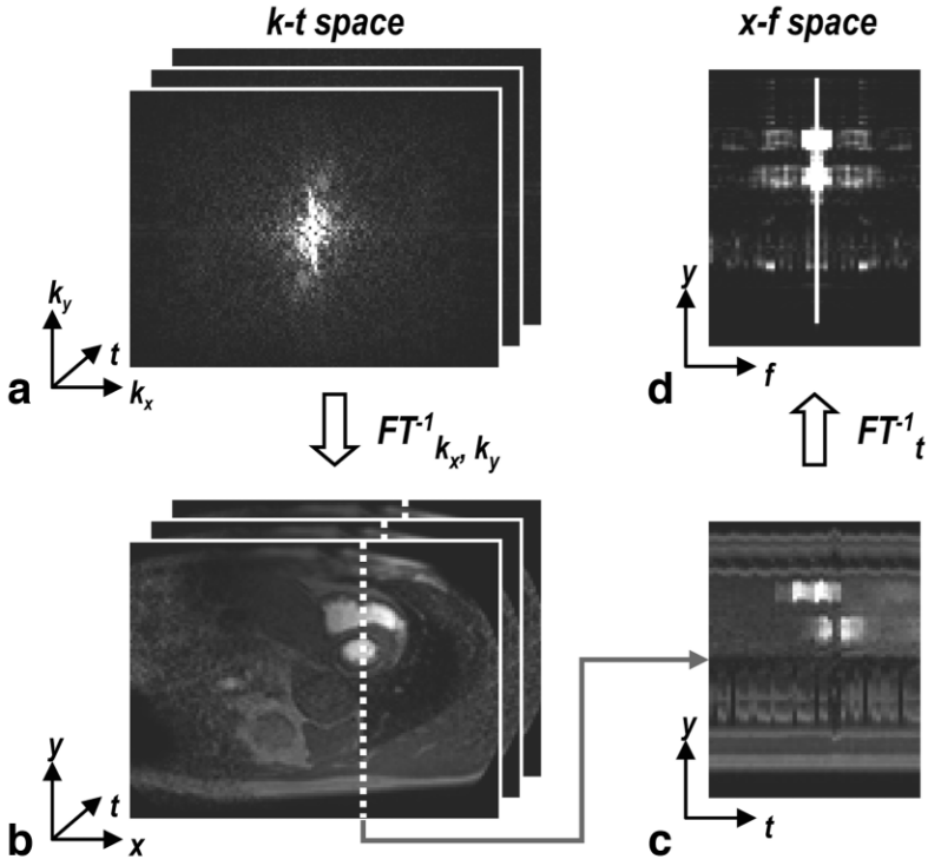

Figure 2.4.: 'Domains' in FPP. Sets of raw data acquired through time are said to be in k-t space (a). Through a Fourier transform in the spatial dimensions this can be converted to a set of dynamic images (b), from which dynamics can be examined by plotting a line at a single image position through time (c) known as x-t space. A Fourier transform of (c) in the temporal dimension then yields x-f space (d). Reproduced from [Pedersen et al., 2009b].

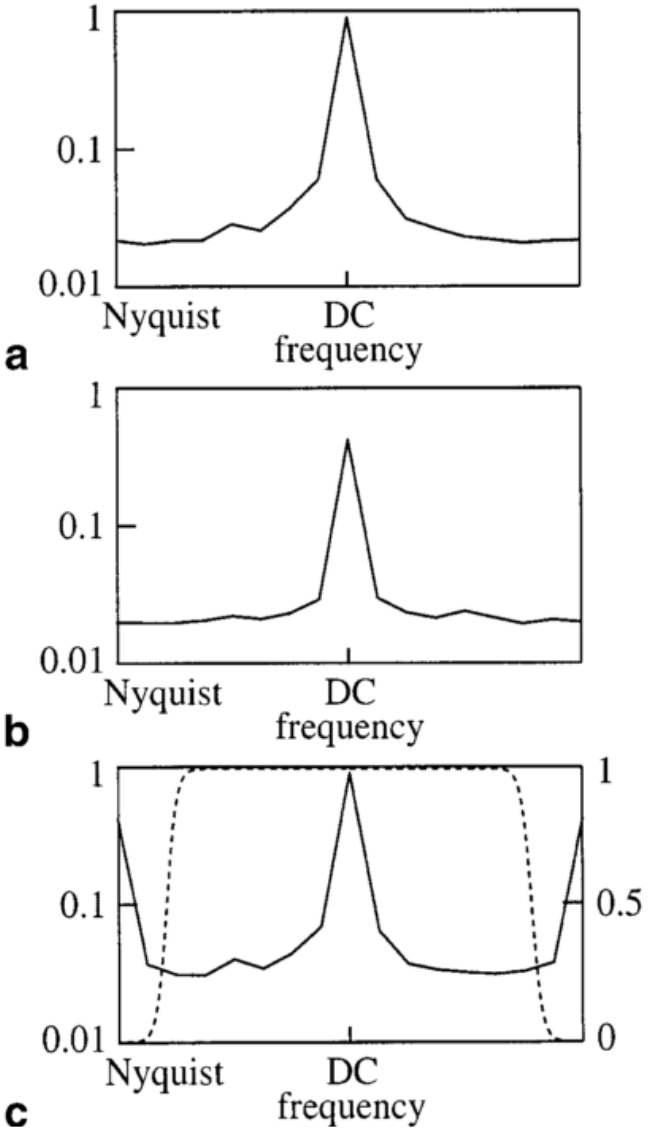

Figure 2.5.: The UNFOLD filter. Example frequency distributions of a more dynamic (a) and less dynamic (b) region of a cardiac dataset. In the cases of undersampling, resulting in aliasing, the small dynamic region and low undersampling factor (i.e. 2) allows the unwanted aliasing induced sidelobes to be removed via a simple filter (c). Reproduced from [Madore et al., 1999].

tension to the concept is made by modelling the expected signal correlations in x-f space using low-resolution unaliased data, known as "training data". This allows accurate separation of the signal in this space, even for the multiple overlaps resulting from high acceleration factors and dynamic contrast (Figure 2.6). This and its enhancement to incorporate parallel imaging are known as k-t BLAST and k-t SENSE respectively [Tsao et al., 2003]. Nominal undersampling factors (undersampling factor, excluding collection of training data) of 5 were demonstrated with k-t SENSE in 2D FPP by Plein *et al.* [Plein et al., 2007], with the recouped time used to increase resolution. Vitanis *et al.* [Vitanis et al., 2009] used SENSE to acquire higher resolution training data, which supported a higher undersampling factor (nominal 8, true 5.8) for k-t SENSE accelerated 2D FPP. In theory, training data can be collected either by a prescan or integrated into the undersampled data itself each cardiac cycle, although this latter case is by far the most popular due to simplicity and greater accuracy during respiratory motion. As the training data resolution is important regarding unwanted temporal filtering effects, an auto-calibrated approach with training data derived from a TSENSE acquisition has also recently been proposed [Ponce et al., 2014] and could be applicable to FPP. k-t BLAST and k-t SENSE have limits in application to FPP due to motion and contrast sensitivity limiting reliability of reconstruction accuracy [Plein et al., 2007][Maredia et al., 2010]. As stated earlier, respiratory motion in FPP causes a further spreading of the signal in the x-f domain, beyond the limited spread due to changing image contrast, and therefore such motion reduces the ability of the reconstruction algorithm to correct the aliased data. Despite this, Manka *et al.* [Manka et al., 2011] successfully applied k-t SENSE in 3D FPP with a true undersampling factor of 6.3 to a fast Cartesian SGRE sequence (including other k-space efficiencies, see Section 2.2.3), achieving an acquisition window of 200ms for a spatial resolution acquisition of 2.3x2.3x10.0. It has also been applied, using a lower total acceleration, in conjunction with a stack-of-spirals sequence design at similar resolution, though with a longer acquisition window of >300ms [Shin et al., 2013].

Transformation of a time-series of images into the x-f domain is the key component of these techniques. Many of the latest techniques aim to accelerate dynamic datasets such as FPP by extending this concept further, with additional or different transformations into mathematical domains that have properties better suiting the reconstruction of the specific dataset

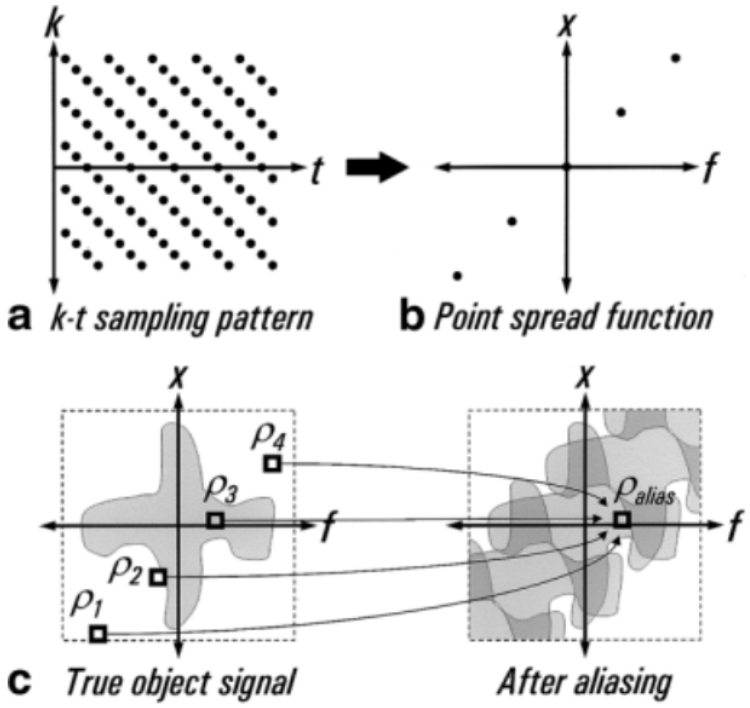

Figure 2.6.: k-t aliasing. With an appropriate undersampling design (a) in a FPP series, the distribution of the point spread function (b) can be predicted. This gives knowledge of how the true object signal in x-f space (c) aliases. Modelling of this predicted overlapping based on acquired training data can allow these signals to be separated and therefore permits greater undersampling factors. Reproduced from [Tsao et al., 2003].

type. The method known as k-t PCA is a prime example of this extension and is currently the sub-Nyquist undersampling technique most commonly implemented in 3D FPP literature (see Table 2.1). As an extension to k-t BLAST (or k-t SENSE), k-t PCA improves the adaptive filter (described above) for removing aliasing while leaving FPP changes unfiltered, by applying principal component analysis (PCA) to the training data used for calculating that filter. This is effectively transforming the images into a new domain of temporal "basis function" components (x-PC) rather than the less suitable temporal pure frequencies as in x-f [Pedersen et al., 2009b]. The advantage of this principal component domain is that it is more sparse, even in the common real-life cases of non-periodic motion such as respiration or misgating. Due to this, the majority of the FPP information is contained within a few principal components, allowing the rest to be discarded. This allows overlapping image space signals to be more easily separated before being converted back into images. Whilst producing large improvements in its ability to cope with motion and contrast changes comparative to k-t SENSE, some artefacts and temporal resolution loss can remain in these situations, particularly at higher acceleration factors [Chao et al., 2010] [Vitanis et al., 2011].

Vitanis *et al.* [Vitanis et al., 2011] was the first work to examine the techniques for 3D whole-heart FPP with k-t PI methods, seen in Figure 2.7. This work used a modified k-t PCA technique designed to support the higher acceleration factors needed for 3D FPP at higher resolutions. A compartment-based model system was added to k-t PCA using automatic identification of compartments of interest (e.g. LV myocardium, LV blood pool, etc). By using an initial higher-resolution reconstruction process, voxels contaminated by partial volume effects in the low resolution training data could be excluded. This correction for partial volume effects is thought to compensate for a large proportion of the errors in the calculation of the temporal basis functions in conventional k-t PCA. Application of this method allowed temporal and spatial resolution to be maintained (1 RR and 2.3x2.3x10.0mm respectively) during whole-heart coverage at 10x nominal (5.6-7.5x true) undersampling factor, combined with additional k-space efficiencies. Later work from the same group employed non-rigid motion correction as part of an iterative version of k-t PCA so as to improve 3D FPP reconstruction in the presence of more severe motion, particularly in the case of failed breath-hold/free-breathing [Schmidt et al., 2014]. Motion

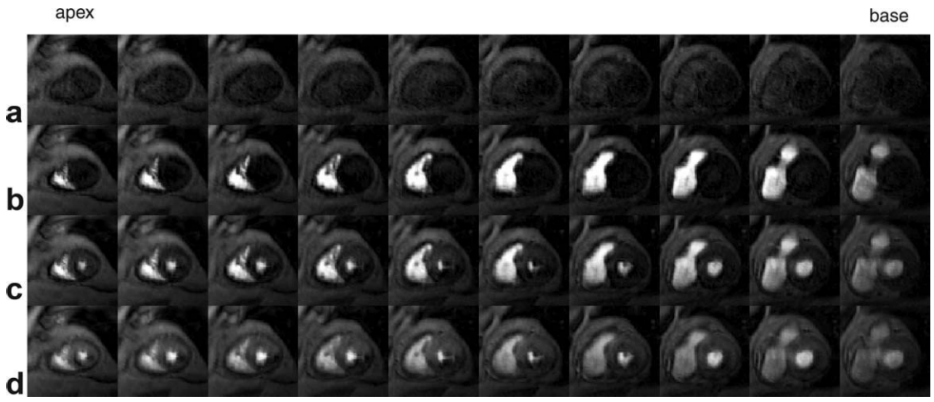

Figure 2.7.: 3D whole-heart FPP dataset. An example 3D whole-heart FPP dataset, showing 10 slices before contrast agent arrival (a), and during RV (b), LV (c) and myocardial (d) contrast enhancement. The technique used a k-t PI reconstruction technique to enable high levels of undersampling. Reproduced from [Vitanis et al., 2011].

correction increases robustness of the reconstruction scheme to free-breathing or breath-hold failure through frame-to-frame warping of the x-PC training data to match a specified reference shape, selected at one phase of the respiratory cycle. Similar acceleration factors and imaging parameters were achieved with this approach, with reported improvement of image quality.

2.3.3. Other Parallel Imaging (PI) Methods

There is a plethora of new PI techniques, based on spatial or spatiotemporal redundancy. While most could in theory be applied to 3D FPP, this chapter does not attempt to cover the entirety of this work, with focus instead on a few PI methods of greatest potential application.

Conventional unaccelerated MRI reconstruction is fundamentally a "linear" process. The term linear, in situations such as this, simply refers to an output that is proportional to an input, for example, with a tissue of twice the brightness in an image corresponding during scanning to twice the strength of its supporting components of the raw data (k-space) values. PI is also fundamentally a linear process as, using coil response profiles, it solves a set of linear equations. Recent PI has focussed on exploiting all available data in the most efficient manner. "Self consistency" is one such approach; optimising together ("joint estimation") the reconstruction of the image and estimation of the coil calibration data, called SPIRiT [Lustig and Pauly,

2010]. When it comes to finding a solution to these types of joint estimation scenarios, the system of equations to be solved no longer linearly connects the raw data to the output images. One way to solve this is non-linear inversion (NLINV), repeated inside an iterative search for the best-fit solution [Uecker et al., 2014]. Such a non-linear scheme with an added variational penalty has demonstrated high quality reconstructions in real time imaging of the heart, with a large acceleration factor [Knoll et al., 2012]. Such non-linear reconstruction may be a possible method for FPP at higher acceleration factors, and therefore for 3D FPP, but is yet to be tested for this application.

Parallel imaging for non-Cartesian trajectories such as radial and spiral can be challenging. The SENSE category of methods, which operate by correcting phase-encode wrap-around in image-space, are more difficult to apply because the effects of non-Cartesian undersampling do not give simple phase-encode FOV wrap-around artefacts as they do in Cartesian undersampling. Methods to solve this exist [Pruessmann et al., 2001], but are not as simple to implement (see Section 2.6.2). The GRAPPA category, where unsampled raw data is calculated from nearby samples in the raw data, depends on the accurate estimation of the "weighting factors" from sampled to unsampled points; for trajectories over the raw data such as radial and spiral sampling, the estimation of the GRAPPA weights is complicated due to non-equidistant spacing between k-space points. Alternative strategies for calculation of the GRAPPA weights have been proposed to rectify this difficulty for GRAPPA [Arunachalam et al., 2007] [Seiberlich et al., 2008] [Codella et al., 2011]. Recently "through-time" calibration techniques for radial GRAPPA [Seiberlich et al., 2011a] and spiral GRAPPA [Seiberlich et al., 2011b] have been developed, which calculate the weights using multiple fully-sampled prescans. Through time radial GRAPPA has been used for breath-held 2D FPP achieving whole-heart coverage with 15 slices [Hamilton et al., 2014] as well as in 3D for non-FPP applications [Wright et al., 2014].

A method called Time resolved angiography With Interleaved Stochastic Trajectories (TWIST), which builds on 'keyhole' techniques that update sections of k-space at different rates, alters the 2D phase-encode pattern. The outer portions of the raw data are collected in a pseudo-random pattern that, combined with multiple time-frames, manipulates the undersampling pattern enabling reconstruction via parallel imaging. Originally designed for angiography, it was adapted in SSFPP [Giri et al., 2014] and used with GRAPPA, as part of a 3D FPP protocol (see Section 2.5.1). By itself the

technique still suffers the same SNR loss and other limitations of traditional PI, albeit with a slightly increased level of allowed acceleration in the outer portions of k-space.

Close analogies can be drawn between some of the qualities exploited with these later techniques, namely non-linear solutions for reconstruction and "random" undersampling patterns, and those used in the final main technique to be discussed - compressed sensing.

2.3.4. Compressed Sensing

This section introduces compressed sensing (CS), followed by examples of application of CS to 2D and 3D FPP.

The mathematical framework of CS [Donoho, 2006] is relatively recent and its potential for application in MRI was almost immediately considered due to the inherent suitability of aspects of MRI data. CS utilises the implicit "sparsity" in MR images, either directly in the image(s) or in a suitable mathematical representation of them (i.e. in a transformed domain via a sparsifying transform, explained later), to reconstruct accelerated acquisitions. The term sparsity is used to describe any matrix, e.g. of image pixels or k-space data, that is predominately zero valued. Such sparseness may exist implicitly in the dataset or more likely after an appropriately chosen transform utilising redundancy in a single image or over a series of related images. Using this property, CS allows accurate reconstruction of undersampled data, with the proviso that the sub-sampling pattern is 'random' and that an appropriate non-linear reconstruction is used [Lustig et al., 2008]. Compression of images using sparsifying transforms is well known [Taubman and Marcellin, 2002] and compressed sensing attempts to implement the same concept from the reverse direction; if images can be compressed accurately, then it may be possible to scan faster by acquiring less k-space data in the first place.

The ability to sample a reduced number of random positions in k-space is essential to realise this idea, with such random subsampling in k-space resulting in incoherent (i.e. noise-like) aliasing artefacts in images. One way to consider this is that strong signals rising above a predetermined threshold can be selected, and the expected interference pattern arising from these signals can be calculated. This interference signal can then be subtracted from the original and the process repeated on the subtracted data, with lowering thresholds, until the true sparse signals have been separated from

the aliased signals [Lustig et al., 2007]. In this simplistic version of CS, the process effectively denoises the incoherent artefacts created by the random undersampling.

In practice, reconstruction of this randomly undersampled data is performed via the solution to an appropriate constrained optimization problem [Lustig et al., 2007], stated in its simplest form as

$$\begin{aligned} &\text{minimise} && ||\psi m||_1 \\ &\text{subject to} && ||F_u m - y||_2 < \varepsilon \end{aligned} \tag{2.3}$$

where the first line, known as the objective function, contains m which is the reconstructed image and ψ which is the operator that performs the chosen sparsifying transform. The second line, the fidelity term, has the undersampled Fourier transform, F_u, which acts on m, and the measured k-space data y. The threshold parameter ε is used for controlling the level of the reconstruction data fidelity to the acquired data. The objective function deals with requirement for sparsity, whilst the fidelity term enforces the consistency of the estimated image with the rawdata.

Practically, different sparsifying operators can be used along with the addition of different penalties to the objective function. Multiple search methods exist for solving these types of problems, finding an estimate of m: interior point methods, projections onto convex sets (POCS) and iterative soft thresholding to name but a limited few [McGibney et al., 1993]. Again, performance is dependent on the choice of several parameters affecting not only the iterative search but also the strength of constraints applied.

In MRI, random sampling is limited to phase-encoded direction(s) but can also vary during a series of images, such as during FPP. CS techniques have accelerated 2D FPP [Otazo et al., 2010] for increased resolution or LV coverage, as with k-t PI. CS has an advantage that it does not require training data which can reduce the overall "true" acceleration. Similar temporal characteristics in the reconstructions are seen at lower acceleration factors for CS and k-t PI methods, with basic variants of both struggling beyond a critical value of $\sim$5 in human FPP [Vitanis et al., 2008]. The increased error for higher accelerations is particularly prominent for CS, limited by insufficient sparsity that is typically achieved in FPP by transformations into other domains, as in k-t PI methods. The x-f domain was popular for early CS work, e.g. k-t SPARSE [Lustig et al., 2006] and k-t FOCUSS [Jung et al.,

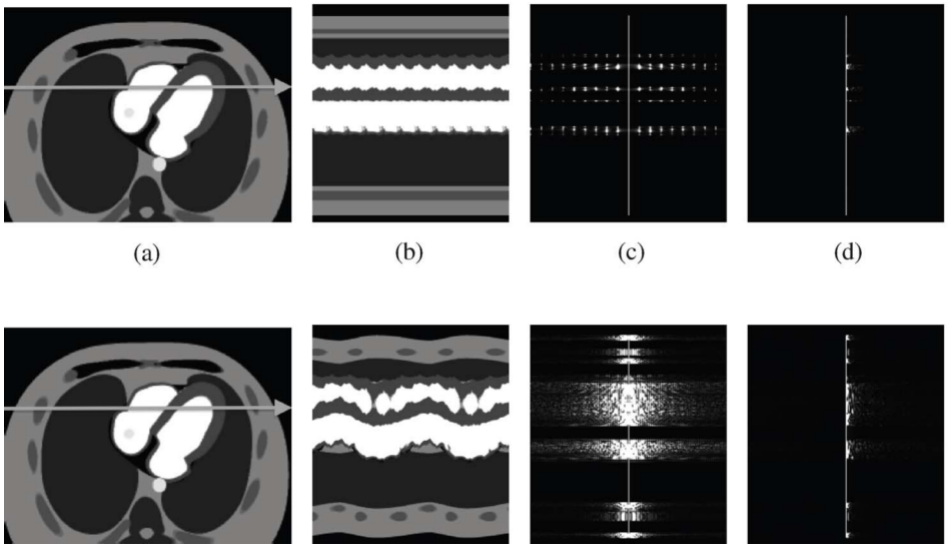

Figure 2.8.: Breath-held and free-breathing sparsity in different domains, including a sparsifying Karhunen-Loève Transform (KLT). The image (a), x-t (b), x-f (c), and x-KLT (d) domains of simulated breath-held (top) and free-breathing (bottom) datasets. The x-f domain (c) is seen to be far more sparse when the patient is breath-holding than when the patient is allowed to breathe. (d) shows the potential for alternate domains to increase sparsity, with improvements in both cases, but of particular importance in the case of free-breathing. KLT is not discussed further here - more information can be found in the references in the text. Reproduced from [Lingala et al., 2011] ©2011 IEEE.

2009]. However, in FPP, due to the changing image contrast with arrival of contrast agent, a wider range of temporal frequencies causes weaker sparsity in this domain, and therefore other domains have been proposed [Lingala et al., 2011] (Figure 2.8).

With potentially high CS acceleration factors under the ideal conditions of good breath-holding and ECG-triggering, work has gone into modifying the standard CS processes to correct for respiratory motion. A technique utilising the Sparsity and Low-Rank properties of the dynamic datasets termed k-t SLR [Lingala et al., 2011] has shown promise in 2D free-breathing FPP in comparison to other CS reconstructions [Lingala et al., 2013], using a transform that provides greater sparsity even in free breathing. Usman *et al.* [Usman et al., 2013] presented free-breathing 2D FPP with more direct motion compensation, improving on methods that adjust for affine deformations (e.g. [Jung et al., 2009]), integrating a general motion correction

technique directly into the CS algorithm. Block LOw-rank Sparsity with Motion-guidance (BLOSM) [Chen et al., 2014b] is a related method for motion correction in CS, designed specifically for FPP, combining similar properties of the above methods, dividing the image into regions that can be tracked over time. This was compared with the previously mentioned CS algorithms in 2D FPP under prominent respiratory motion, as well as recent preliminary work in quantitative 3D FPP [Yang et al., 2014].

Compressed sensing is particularly suited to 3D data and even more so for "4D" data, as in the case of 3D FPP which is a dynamic series of 3D images. The extra dimension(s) and spatial coverage allow greater compressibility of the data. Despite this theoretical advantage, the issues of respiratory motion/ misgating mentioned earlier have limited the application of CS in 3D FPP although its use is increasing. 3D FPP sequences using CS [DiBella et al., 2012] [Chen et al., 2012] [Wang et al., 2014b] used temporal and spatiotemporal constrained reconstruction methods from 2D FPP [Adluru et al., 2009]. The first [DiBella et al., 2012] used this reconstruction with ungated imaging (Section 2.2.1), whilst in [Chen et al., 2012] it was combined with a more typical radial FPP protocol to achieve good quality images in cases of optimised flip angle. [Wang et al., 2014b] applied a similar reconstruction technique but to a Cartesian SGRE sequence, investigating the impact of trajectory ordering strategy choice.

Recently, a CS algorithm using localised spatiotemporal constraints was tested in free-breathing 3D FPP with CS [Akçakaya et al., 2014]. While the compartment based-method for k-t PI [Vitanis et al., 2011] broke the reconstruction process into compartments of interest, here compartments in the PCA-based sparsifying functions were broken down into smaller patches. This allows for overlapping of the patches to improve quality, to similarly compensate for differing physiological characteristics during the FPP series. In addition only a subset of the images in the FPP series are considered when, in effect, reconstructing each image - this was hypothesised to suit free-breathing but has the restriction that only moderate motion is expected over a few consecutive frames. This enabled acceleration to an acquisition window of 250ms at resolution (2.3x2.3x10.0)mm and FOV of (340x340x80)mm during free-breathing, that compared promisingly against other 3D FPP techniques [Akçakaya et al., 2014], although only tested at rest.

Combining parallel imaging with compressed sensing is an intuitive sub-

sequent step and various methods have been proposed [Block et al., 2007] [Liang et al., 2009], as well as CS extensions to joint estimation parallel imaging techniques [Knoll et al., 2012] (see Section 2.3.3). Otazo *et al.* [Otazo et al., 2010] applied a combined parallel imaging and CS reconstruction for 2D FPP, and later showed preliminary work in free-breathing, building the motion directly into the sparsity constraints [Otazo et al., 2011]. It seems likely that more reconstruction strategies combining the two will be seen, including for 3D FPP.

2.4. Motion Challenges

The problems arising from motion in MRI acquisition are well known [van Heeswijk et al., 2012] and FPP is no exception in requiring compensation for cardiac and respiratory induced motion. The necessity for acquiring the data during a quiescent period of the cardiac cycle and the implications of this on the allowed acquisition window were described earlier (Section 2.1.2). The motion susceptibility of many of the proposed sub-Nyquist reconstruction schemes (Section 2.3) can be particularly problematic with regards to respiratory motion. Furthermore, stress FPP, typically performed through intravenous administration of a pharmacological agent such as adenosine, affects both cardiac [Ogilby et al., 1992] and respiratory motion [Watt and Routledge, 1985]. The challenge, addressed next, is that respiratory and cardiac motion both directly affect robustness of acceleration techniques as well as final image quality in 3D FPP.

2.4.1. Cardiac Motion

Whilst short acquisition windows per slice can be used in 2D FPP, aiming to minimise cardiac motion during each single-shot image, 3D acquisitions require extended acquisition windows per cardiac cycle, making this assumption of minimal cardiac motion less valid. The largest impact is the introduction into the images of cardiac blurring and dark-rim artefact (DRA) effects [Storey et al., 2002] [Wang et al., 2014a].

Choosing a maximum appropriate acquisition window is an important trade-off between potential cardiac blurring/reconstruction accuracy and required sequence acceleration. For example, the duration of the typical mid-diastolic quiescence (diastasis) is not only patient specific due to R-R interval, cardiac dysfunctions present, and many other factors, but has been

shown to vary (even when normalised to the R-R interval) between cardiac cycles within the same person [Ravichandran et al., 2012]. The introduction of a pharmacological stressor such as adenosine often increases the heart-rate, especially reducing the duration of diastasis. This all potentially limits the acceptable acquisition window, although there is little literature on this topic in 3D FPP. The stated acquisition windows have varied in 3D FPP literature from 116ms (with low spatial resolution) up to 380ms (see Table 2.1), and many were only performed under resting conditions.

Arrhythmias and ECG triggering unreliability also present challenges, particularly in methods dependent on temporal sparsity (k-t PI and some CS methods), because this assumption is weakened by inter-shot variation in the cardiac phase. This somewhat increases the difficulty of routine clinical application. Some ungated/self-gated methods are beginning to show promise, being less sensitive to irregular cardiac motion, with 2D FPP ungated acquisitions being demonstrated in patients with atrial fibrillation [Harrison et al., 2013].

2.4.2. Respiratory Motion

It is possible to instruct a patient to breath-hold just before the contrast agent bolus arrival in the left-ventricle, and this will usually succeed in providing images of the same myocardial slices during peak enhancement. However, if an acceleration method depends on breath-hold, it may sometimes be unreliable in a routine clinical environment or where some patients under stress are unable to co-operate with breath-hold instructions. Free-breathing has the drawback for 2D FPP slices that different regions may be seen during the respiratory cycle, providing another motivation for 3D FPP imaging.

The assumption of breath-holding greatly widens the range of sub-Nyquist reconstruction techniques that can be applied. Partial breath-holds, timed to coincide with the myocardial arrival of GBCA, or coached breath-holding may be used, with evident possible limitations in clinical work. Furthermore, it is difficult to repeat FPP scans in the case of a failed breath-hold, and free-breathing robust FPP is therefore a topic of interest in clinical MRI.

2.4.3. Motion Correction & Free-Breathing 3D FPP

With the exceptions of Schmidt [Schmidt et al., 2014] and Akçakaya [Akçakaya et al., 2014], there has been limited progress in making 3D FPP robust to free-breathing. This is owing to the severe impact of respiratory motion

when using reconstruction strategies that in any sense share information from multiple cardiac cycles. The ability to perform 3D FPP with free-breathing, given its dependence on some form of sub-Nyquist sampling, necessitates either mathematical modification to k-t PI/CS algorithms, correction to the data as it is collected or reconstruction strategies that make no use of temporal information.

Modifications to k-t PI and CS methods for free-breathing or motion robustness typically correct the data or reconstruction into a state similar to some reference respiratory position. However, this involves a distinct step in complexity beyond the non-rigid image warping applied to conventional 2D FPP images [Li and Sun, 2009] [Xue et al., 2009] or in correcting respiratory drift in a series of single-shot images (as in other applications such as T_1-mapping [Xue et al., 2012]). Such non-rigid "rubber sheet" warping is performed on images that were already completed in separate cardiac cycles, where respiratory motion within the acquired raw data for each image is ignored. However, the modified advanced reconstruction methods must correct respiratory motion during the process of image reconstruction, a much more difficult challenge. This is the case in the "compartmental" and "motion-corrected" k-t PCA methods [Schmidt et al., 2014] [Vitanis et al., 2011] and adapted CS method [Akçakaya et al., 2014] applied to 3D FPP discussed earlier, as well as others applied to 2D FPP, e.g. [Ge et al., 2010] [Usman et al., 2013] [Otazo et al., 2011]. These are currently of interest as they potentially offer the full acceleration of k-t PI and CS methods, assuming that they can be applied robustly.

The challenge with the aforementioned approaches is that they attempt to compensate for raw data that is already corrupted by motion; other potential methods may alternatively attempt to collect the data whilst *prospectively* adjusting its acquisition in real-time in response to the respiratory motion. This can give the additional benefit of correcting through-plane as well as in-plane motion. Diaphragm respiratory position navigators are used in MRI [Ehman and Felmlee, 1989][Scott et al., 2009] for respiratory motion gating or adaptation while scanning. The traditional navigator accept/reject gating cannot be used with FPP because cardiac cycles cannot be omitted. However, the navigator has been used for slice tracking the FPP slices to follow the respiratory motion of the heart. This was first demonstrated in FPP by Pedersen *et al.* [Pedersen et al., 2009a] and improved with application of a navigator-restore pulse to maintain sufficient navigator signal when

combined with the FPP saturation recovery sequence [Basha et al., 2014]. However, as the method has to prospectively shift the slice-excitation based on the navigator information, there will always be concerns over its reliability. Such techniques require a motion-correction model between the position measured by the typical right-hemidiaphragmatic navigator and the targeted position of the short-axis slices, since the heart is non-rigid and this model can include rotations, shears and even hysteresis [Nehrke and Börnert, 2005]; this procedure cannot currently be regarded as clinically routine. A similar technique could in theory be used for 3D FPP where slab tracking might be less sensitive to tracking errors.

Finally, more basic undersampling and reconstruction techniques that do not directly utilise the dynamic nature of FPP series would eliminate inter-frame motion sensitivity. These have lower achievable acceleration factors and still require care to ensure that coil calibration methods, or similar, are not affected by respiratory motion (explored further in Section 4.1). Without using temporal constraints, the challenge shifts for the most part from motion robustness to SNR considerations, a fundamental limitation of parallel imaging algorithms at such high accelerations. This could be, for example, the number of spatially significantly different receiver coils required to prevent an underdetermined PI solution. The high acceleration factors required and the prohibitive SNR losses to achieve successful reconstructions with non-k-t PI techniques make this approach less likely to succeed until new methods of accelerating the sequence or improving SNR are realised. Spatially constrained CS could potentially become more important in this way. Additionally, cardiac-specific coil arrays for optimal performance at high acceleration factors [Ohliger and Sodickson, 2006] would improve high-factor parallel imaging of the LV [Weiger et al., 2001] [Schmitt et al., 2008] [Schuppert et al., 2014]. So far there have been difficulties in the transfer of these designs to a clinical setting, due to high production cost, variable body habitus, discomfort due to weight/shape, or coil fragility in routine clinical use.

2.5. 3D FPP Literature Overview

Much of the current 3D FPP literature was discussed above in the context of the advanced techniques used to realise whole-heart coverage. What follows is a more detailed review of these evolving protocols, comparing and

contrasting the results of these techniques and discussing novelties in their approaches, before taking a look at clinical evaluations to date.

2.5.1. Developmental Research Review

This section should be read with Table 2.1. From this the development of 3D FPP is clear, from early low-resolution images acquired at rest that first demonstrated feasibility, up to the most recent higher resolution, shorter acquisition window protocols applied to populations with CAD.

The early work by Shin *et al.* focussed on demonstrating the feasibility and potential benefits of 3D FPP, first [Shin et al., 2008] comparing with 2D imaging inside an adjustable LV phantom, showing improved accuracy in estimation of defect size, as well as demonstrating *in vivo* 3D use and examination of the time intensity curves. The *in vivo* experiments included a slice by slice measurement of SNR and CNR in the 3D dataset, which exhibited predictable losses in the edge slices due to imperfect slab excitation profile, a reason why many later works discard those acquired edge slices. Also noticed was flickering in the time intensity curves, predicted to be an effect of the calibration method used in the simple temporal version of parallel imaging applied, as well as significant DRAs due to the low spatial resolution - both of which indicated the need for new acceleration techniques in 3D FPP. The second paper by this group [Shin et al., 2010] used similar methods for early comparison between systolic and diastolic acquisitions, proposing end-systolic acquisition for 3D FPP in patients with severe arrhythmia. This was done through analysis of time intensity curves in healthy subjects and showed agreement, though increased DRAs were present at the reduced spatial resolution required to image in the shorter period of myocardial stasis in systole.

The next group of publications made use of k-t PI methods, enabling improvements in many of the protocol parameters. Starting with the clinical application of the sequence [Manka et al., 2011] (Section 2.5.2) and compartment based improvement to the reconstruction [Vitanis et al., 2011], isotropic in-plane spatial resolution of around 2.3mm was first achieved and regularly applied thereafter. Alongside the implementation of the compartmental-based adaptation to k-t PCA (from Section 2.3.2) and comparison with conventional k-t PCA using time intensity curves, this paper also examined the impact on reconstruction performance of the number of k-t PCA training profiles and principal components, and various respiratory motion types.

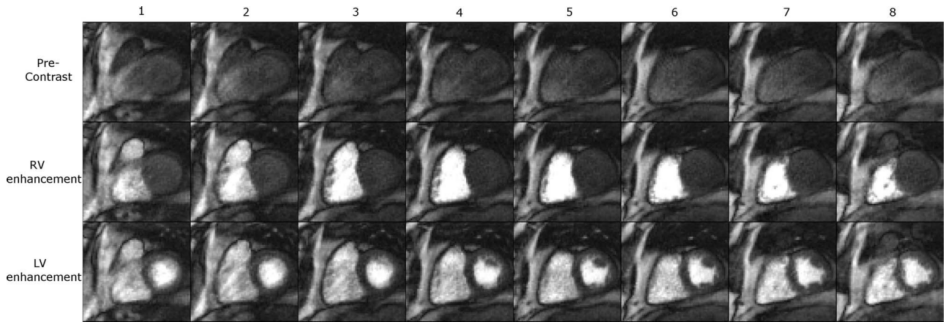

Figure 2.9.: Stack-of-stars 3D FPP dataset. The eight slices of a 'stack-of-stars' 3D radial FPP sequence during 3 stages of contrast arrival. Reproduced from [Chen et al., 2012].

However, protocols during a series of clinical research papers [Motwani et al., 2014] [Manka et al., 2012] [Jogiya et al., 2012] and recent addition of parallel transmit [Jogiya et al., 2014b], continue to use standard k-t PCA without yet including the compartment-based extension. The more recent development of motion-corrected k-t PCA for 3D FPP [Schmidt et al., 2014] may possibly require further work before becoming robust for the clinical routine. Cartesian-based work from other groups have utilised CS algorithms to investigate motion-sensitivity of the technique [Akçakaya et al., 2014] and partition ordering effects [Wang et al., 2014b], as discussed earlier in their respective sections.

Implementations of 3D FPP through non-Cartesian approaches began with the use of radial sequences, first focussing on application of an ungated sequence [DiBella et al., 2012] and later testing the feasibility of radial in a more standard gated approach [Chen et al., 2012] (results in Figure 2.9). Alongside numerical simulations to optimise parameters of the sequence as mentioned in Section 2.2.2, this gated stack-of-stars approach varied the FOV as appropriate, therefore reporting a wider range of resolutions than in other 3D FPP work. With an altered sampling strategy combining higher acceleration and a slightly extended acquisition window, the ungated method gave one of the highest in-plane resolutions to date.

In work examining the optimisation of the first spiral 3D FPP sequence [Shin et al., 2013] (see Figure 2.10), the higher efficiency of this k-space traversal permitted acquisition windows closer to those applied in the k-t clinical studies, at the smallest undersampling factor (5) applied with any CS/k-t PI technique. With the stack-of-spiral acquisition placed during

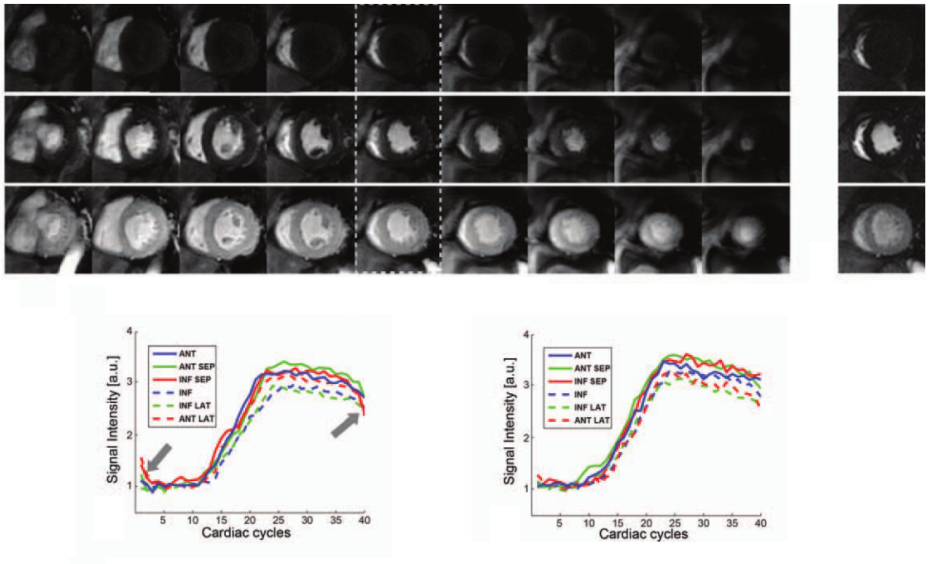

Figure 2.10.: Stack-of-spirals 3D FPP dataset. Illustrative images acquired by a stack-of-spirals protocol during right ventricle blood-pool (top), LV blood-pool (middle) and LV myocardial (bottom) enhancement. Dotted lines indicate the middle slice which was used for comparison with the corresponding single-slice 2D Cartesian acquisition. The myocardial signal-time curves for this and its corresponding 2D slice are shown below, demonstrating good agreement, except for k-t parallel imaging artefacts in the early and late frames. Reproduced from [Shin et al., 2013].

mid-diastole, a 2D single-slice Cartesian acquisition was also acquired each cardiac cycle allowing comparison of this 2D and 3D approach through analysis of the myocardial signal-time curves (Figure 2.10).

Finally, alongside the ungated radial approach just mentioned, one of the more novel attempts was continuous acquisition SSFPP [Giri et al., 2014]. With much of the paper focussing on the SFPP technique in 2D, the 3D initial experience only used a small amount of undersampling and other acceleration techniques, which explains the long acquisition window of 300-380ms, nevertheless providing proof of concept of the contrast mechanism.

2.5.2. Clinical Research Review

With the widening array of acceleration techniques increasing the feasibility of 3D FPP, a small amount of clinical research has begun. Papers that focus on investigating the clinical potential of 3D FPP are examined here in more

detail. Table 2.2 summarises the more clinically relevant aspects of studies containing a population of patients with known or suspected CAD that, among other investigations, compare 3D FPP against a reference standard. The more technical details of the protocols used in these studies can be viewed in their respective entries in Table 2.1.

In 2011, Manka *et al.* [Manka et al., 2011] first investigated the diagnostic ability of 3D FPP, comparing accuracy in identifying significant CAD against quantitative coronary angiography (QCA), as well as demonstrating the potential for volumetry of defect-induced hypointense regions. Compared against QCA, in 146 consecutively recruited patients, the sensitivity, specificity and accuracy were 92%, 74% and 83% respectively, comparing favourably with values in studies using 2D FPP [Schwitter et al., 2008] [Greenwood et al., 2012]. In a subgroup of 48 patients who went on to have coronary stenting, repeat stress 3D FPP was performed within 24 hours of the procedure. It was in these patients that volumetric analysis of the inducible perfusion defects was performed, with comparison of pre and post procedure confirming the predicted large effect of treatment. Further investigations of note, repeated in some of the more recent 3D FPP studies, were on image quality and whole-heart versus 3-slice MRI coverage. Artefacts were split into breathing related, k-t PI reconstruction related and DRA related, which were present in 12%, 10% and 8% respectively. Whilst all images were deemed diagnostic in quality, this relatively high percentage of artefacts, along with their categorisation, highlights many of the problems already discussed in 3D FPP. Examination of 3 slices chosen from the 3D dataset produced a lower sensitivity than for the entire 3D dataset due to an increase in false-negatives. Whilst this agrees with a predicted advantage of 3D FPP over its 2D counterpart, this method of comparison is not a full test of the two as true 2D acquisitions have different properties, as noted in a later study [Jogiya et al., 2014a]. That study [Jogiya et al., 2014a] also included indication of the improved determination of ischaemic burden in 3D over 2D FPP via the same method of using a subset of the 3D dataset's slices.

With the limitation of poor correlation between the haemodynamic effect of a coronary stenosis and QCA [White et al., 1984], Manka *et al.* [Manka et al., 2012] further compared 3D FPP to fractional flow reserve (FFR). The

Table 2.2.: Key parameters of clinical 3D whole-heart first-pass perfusion literature

Lead Author	Year	Patient Number	MRI Centres	MRI Observers	Reference Standards	QCA			FFR		
						Sensitivity	Specificity	Accuracy	Sensitivity	Specificity	Accuracy
Manka	2011	146	Single	Single	QCA	92 CI[85 99]	74 CI[64 85]	83 CI[76 89]	N/A	N/A	N/A
Manka	2012	120	Dual	Single	QCA & FFR	88 CI[77 95]	75 CI[61 83]	81 CI[73 88]	90 CI[82 98]	82 CI[71 94]	87 CI[80 93]
Jogiya	2012	53	Single	Dual*	QCA & FFR	88 CI[71 96]	80 CI[56 93]	85	91 CI[75 98]	90 CI[66 98]	91 CI[83 95]
Jogiya	2014	45	Single	Single	QCA & MPS**	94 CI[71 100]	81 CI[54 95]	88	N/A	N/A	N/A
Manka	2015	150	Five	Multiple	QCA & FFR	77 CI[67 85]	94 CI[84 99]	83 CI[76 88]	85 CI[75 92]	91 CI[81 97]	87 CI[81 92]

*3rd observer used when consensus could not be reached
**For corresponding sensitivity, specificity and accuracy - see text
CI = 95% confidence interval

study was also extended to two centres and included a subgroup undergoing repeat examination for inter-study reproducibility, which resulted in excellent correlation. Sensitivity, specificity and accuracy compared to QCA were similar to that in [Manka et al., 2011], whilst values were improved when using FFR as reference. This trend was also seen in [Jogiya et al., 2012], which provided some of the highest accuracy values, using two observers at a single centre and use of the Duke Jeopardy Score to complement FFR. Most recently [Manka et al., 2015] the dual-centre investigation was extended to multi-centre evaluation of a similar protocol across five (single vendor) European sites. With 155 patients recruited and 150 successfully examined, this is the largest 3D FPP study to date. With all MRI perfusion analysed in a central laboratory, measured image quality remained good and mean specificity compared against QCA and FFR were the highest of all studies in Table 2.2, although there was a decrease in sensitivity against the QCA reference.

Also recently [Jogiya et al., 2014a], the measurement of ischaemic burden by 3D FPP was compared with that by myocardial perfusion scintigraphy (MPS), with sensitivities, specificities and accuracies of the two methods calculated for a subgroup undergoing coronary angiography. These values were 94%, 81% and 88% respectively for MRI 3D FPP and 94%, 63% and 79% for MPS. Comparison of ischaemic burden between the two showed no significant differences. Other clinically focussed work has investigated quantitative 3D FPP, which is of increasing interest [Yang et al., 2014]] [Wissmann et al., 2014a], including a study of 35 patients that estimated myocardial blood flow and myocardial perfusion reserve in systole and diastole [Motwani et al., 2014].

With all of the clinical studies thus far performed at related centres, parameters are understandably similar. In-plane spatial resolution is 2.3x2.3mm in all cases with through-plane resolution being changed from 10mm to 5mm after the first study (likely through zero-padding). The first two studies in Table 2.2 were at 1.5T, whilst the latest three were at 3T and state that images were acquired during systole (cardiac phase not described in the first two). Unlike in [Manka et al., 2011], which used k-t SENSE as the k-t PI reconstruction technique, the latter studies employed k-t PCA. This likely explains at least part of the reduction in number of k-t PI related artefacts in Jogiya ‘12 and Jogiya ‘14. Due to the limited variation in implementation, including protocols, reconstruction methods and breath-hold methods

(not always stated), extrapolation of results to different MRI systems or non-specialist cardiac MRI sites is not yet possible, but these are positive early findings and validate many of the proposed benefits of 3D FPP.

2.6. Future Considerations

Various combinations of acceleration methods that allow total acceleration factors approaching those necessary for 3D FPP have been reviewed. Further acceleration would be desirable as the image acquisition times within each cardiac cycle remain too long, requiring some care in setup, and current spatial resolutions are also known to be vulnerable to partial volume and Gibbs artefacts. Clear evidence for clinical advantages of 3D FPP over 2D would be beneficial before proceeding to expensive large multi-centre, multi-vendor trials. Some of the reviewed 3D FPP methods require improved reliability and computational efficiency (i.e. faster image reconstruction) before they would be suitable for clinical trials.

2.6.1. Reliability & Accuracy

The highly accelerated dynamic acquisition for 3D FPP is a particularly difficult problem. Some issues that can lower the reliability were mentioned for techniques reviewed above, and are addressed further in this section.

Non-Cartesian trajectories are a potentially efficient sampling approach for 3D FPP sequences, but despite a long period of development there is a distinct scarcity in their routine clinical usage. This can be largely attributed to their reliability depending on extra complications (e.g. requirement of field-map off-resonance corrections, scanner-specific adjustments of sequence timings, and more complex reconstructions) in comparison to what is currently realistic in a more routine clinical environment. Furthermore, where a long readout is used after each RF excitation, as in EPI and spiral methods, the nominal spatial resolution can be impacted by cumulative off-resonance and motion-induced phase errors during the readout [Gatehouse, 1999]. The non-Cartesian work so far has been developmental, applied at rest may and require some evaluation or improvement for stress before approaching clinical utility.

Similarly, slice-tracking and other prospective motion-correction algorithms can be unreliable and damage irreparably an acquisition which might otherwise have been of clinically usable quality even if suboptimal. The

majority of such techniques are in their early research stages and so the consistency of their routine clinical performance is as yet uncertain. The use of dynamic information to support sub-Nyquist sampling reconstruction schemes has delivered clear improvement in performance. However, study is required on more subtle temporal effects that may arise with these techniques. Temporal smoothing is known in some PI methods that use temporal calibration of coil sensitivity data as well as k-t PI techniques [Maredia et al., 2010], though methods to improve these issues have been proposed [Blaimer et al., 2011]. It is suggested more recent algorithms have shown less of this temporal smoothing effect in FPP [Pedersen et al., 2009b], but careful examination of the effect on dynamic regions of the image in particular may be important in techniques utilising temporal sparsity, even when all of the supporting conditions are perfectly satisfied.

The availability of 3T, although sometimes of controversial benefit in clinical cardiac MRI compared to 1.5T, is likely to be important for 3D FPP. As many of the acceleration methods sample fewer raw data points, which directly reduces SNR, the potentially greater SNR at increased field strength becomes desirable. This SNR gain is not always delivered in a straightforward manner by 3T for cardiac applications [Gerber et al., 2008] [Hinton et al., 2003]. However, at low flip-angles and short sampling trajectories after each RF pulse, as in the spoiled GRE often used in 3D FPP, some SNR enhancement is predictable, especially at peak contrast-agent reduction of T_1 (as most GBCA relaxivities are not greatly reduced at 3T vs 1.5T [Sharma et al., 2006]). With traditional PI reducing SNR proportionally to the square root of the acceleration, the increased SNR of higher field strengths can partially compensate. In addition, the coil sensitivity profiles at the higher frequencies of increased field strengths may improve parallel imaging performance (up to a typical "critical limit" of approximately rate 4 acceleration) although this improvement only becomes strongly significant at field strengths typically referred to as "ultra-high field" [Wiesinger et al., 2006], i.e. $\geq$7T. Issues with higher field strengths are well known, with increased main field inhomogeneities of particular pertinence for longer readouts after each RF pulse in cardiac imaging near the B_0 distortion associated with relatively empty lungs and with epicardial veins [Niendorf et al., 2010][Niendorf et al., 2013]. These inhomogeneities exacerbate some of the unreliability of non-Cartesian trajectories, requiring shorter sampling path duration after each RF (which limits achievable acceleration through

sequence efficiency), and are responsible for increased artefacts even in standard sequence designs [Bernstein et al., 2006]. A comparison of FPP in 2D between 1.5T and 3T, using Cartesian SGRE k-t SENSE and other acceleration methods to achieve high spatial resolution acquisitions, showed similar artefacts and diagnostic quality between images acquired at the two field strengths, with an increase in SNR at 3T [Plein et al., 2008b].

As with all 3D MRI the slab profile must be optimised to minimise contamination of the edge partitions ("partition aliasing") while also exciting sufficient signal towards the edges of the slab (Figure 2.11). A common issue in other 3D cardiac MRI techniques, this problem is exacerbated for FPP because of the fast repeat time of RF excitations, and is commonly concealed by clinical MRI protocols not displaying the edge slices. The 1D-selective slab-excitation RF pulse can potentially be "truncated", enabling a shorter acquisition window within each cardiac cycle by the shorter T_E and hence T_R of the pulse sequence, as used in [Akçakaya et al., 2014], but this can also potentially adversely affect the slab profile.

For assessing the clinical reliability of sequences utilising these techniques, large scale clinical trials have shown promise, with good results in large consecutive patient studies (Section 2.5.2). Further studies, including larger multi-vendor, multi-centre trials, are still required.

2.6.2. Computational Efficiency

Virtually immediate reconstruction of images acquired with standard MRI protocols has become the expectation in the clinical environment. However, the acceleration methods required for 3D FPP demand greatly increased computation for reconstruction, and meeting this expectation of near-immediate results becomes a strong challenge.

Whilst the original parallel imaging and k-t PI methods have an analytical solution for image reconstruction, this does not apply to PI methods that involve non-linear components, CS, and some methods modified for motion correction or improved performance. Fundamentally, these methods require a computationally demanding iterative search for some optimised fitted estimate for the solution. Further to the choices of search method, of what variables are searched over, and of exactly what types of "constraint" are applied, there are generally also weights controlling how strongly the constraints are enforced, and a stopping criterion for when the search is allowed to conclude (which may in some implementations simply be after

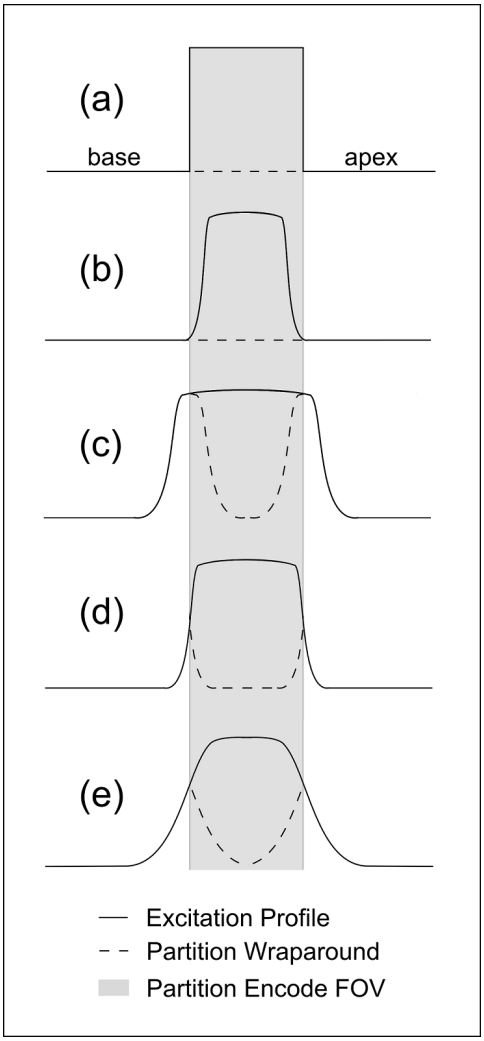

Figure 2.11.: Partition-encoding aliasing in 3D imaging. Demonstration of partition-encoding aliasing (or "wraparound") due to slab excitation profile imperfections. An ideal but impracticable excitation profile would be as in (a), exactly matching the FOV in the slab direction. Using a narrower excitation pulse (b) loses SNR in the edge partitions, whilst in (c) exciting signal outside the FOV leads to wraparound contamination of many more partitions. A more realistic ideal scenario than (a) is shown in (d) whereby only the outermost partitions are affected by wraparound and these are usually not displayed. Due to timing constraints in 3D FPP, and therefore the short RF pulses used, avoiding results such as (e) is a distinct challenge.

a fixed number of iterations). These sometimes unpublished parameters are clearly crucial to the implementation, affecting quality and reliability of output images as well as reconstruction times.

Using non-Cartesian trajectories, regardless of other applied acceleration techniques, also increases the complexity of the reconstruction and with it the computational workload. Gridding prior to fast Fourier transform (FFT), for which various techniques of differing accuracy and complexity exist (very popular is the so called non-uniform FFT (NUFFT) [Fessler and Sutton, 2003]), is required due to non-uniform spacing of data points in k-space. Trade-offs must often be made between reconstruction accuracy and computational cost, but accurate reconstructions can typically be achieved in reasonable times. When combined with sub-Nyquist methods the reconstructions are further complicated and again require iterative solutions as above. This computational strain of advanced reconstructions is especially pertinent for multi-frame 3D FPP sequences with numerous coil channels. For many methods, the reconstruction remains too slow for the images to be viewed while the patient stays in the scanner. Although there may sometimes be little prospect of re-acquiring FPP for other reasons, such slow reconstructions are undesirable and potentially obstructive if a result is poor (an improved re-acquisition is sometimes feasible, e.g. applying stress again and omitting the resting perfusion).

Many reconstruction algorithms used in 3D FPP are implemented only in prototype software that requires raw data to be exported from the scanner's standard clinical software reconstruction system. Such algorithms may be written in MATLAB (MathWorks, Natwick, MA) or similar and are far from optimised in terms of reconstruction time. Whilst this may be acceptable for initial "proof-of-concept" studies, improvements would be required for clinical application, and may be enabled by open-source reconstruction frameworks such as the Gadgetron [Hansen and Sørensen, 2013], at least until manufacturers have implemented the more successful approaches.

Many attempts have been made to improve reconstruction times of advanced acceleration algorithms [Murphy et al., 2012] [Smith et al., 2012] [Cauley et al., 2015] and making more efficient use of available hardware such as graphical processing units (GPUs) can reduce reconstruction times [Stone et al., 2008]. This has been shown for non-Cartesian reconstructions [Sørensen et al., 2008] and PI/k-t PI techniques [Hansen et al., 2008], but depends on specialised programming to optimise GPU performance.

2.7. Conclusions

While the clinical utility of 3D FPP is yet to be fully validated and challenges still remain in its implementation, advances in acceleration methods have opened up the feasibility of achieving 3D whole-heart coverage in FPP. The vast amount of data required within the short acquisition window of each cardiac cycle has necessitated the application of multiple techniques, involving both the sequence and reconstruction. The novelty of many of these methods requires further testing of their properties, both individually and combined, and only some 3D FPP methods are anywhere near routine clinical application. Challenges with respiratory and cardiac motion remain a real concern, as do reliability and reconstruction times. However, there is much promise in 3D FPP and with future improvements and careful evaluation of the effects of the applied acceleration techniques, robust 3D FPP may reach the levels required for clinical utility.

3. A 3D "Stack-of-Stars" Sequence Method

This chapter introduces the MRI pulse sequence design selected and developed for this thesis work, to enable 3D whole-heart first-pass perfusion. This includes the motivation for this sequence choice, the development of the sequence, the various parameter choices, and detailed investigations intended to optimise the sequence further. This acts as technical development that is critical in producing a reliable sequence for use in the future investigations of this thesis.

3.1. Motivation

The primary aim of this thesis was to develop whole-heart myocardial perfusion imaging with realistic potential for full clinical utility. Previous research has developed the performance of 3D FPP techniques (Chapter 2) but their discussed limitations may restrict their implementation into the clinical routine. For a whole-heart perfusion sequence to have the greatest chance of being adopted into the clinical work-flow, it should ideally have the following facets:

- Imaging parameters of a similar level to those currently accepted as standard in 2D multi-slice FPP.
- A short enough shot duration to be feasible under stress conditions.
- Reasonable tolerance to all forms of motion including, ideally, respiratory motion.
- Reliability of application regarding artefacts, with those occurring being predictable and identifiable.

Following the review of available approaches (Chapter 2), with the aim of best achieving these above combined features, a combined radial and

Cartesian "stack-of-stars" 3D first pass-perfusion approach (defined fully in the next section) was chosen as a basis for this work for the following primary reasons.

Radial sequences maintain reasonable performance in their reconstruction even after high levels of undersampling. It is hoped this undersampling robustness, combined with its natural affinity with compressed sensing methods, will allow the selected method to achieve the acceleration necessary for short shot duration. The stack-of-stars radial approach was chosen as, by sampling in a Cartesian pattern in the k_z plane where resolution is typically coarser, the inefficiency of radial sampling in 3D can be avoided.

Radial acquisitions are also well-known for their tolerance to intra-shot motion [Rasche et al., 1997][Uecker et al., 2012][Pflugi et al., 2015]. This should therefore assist the sequence's robustness to cardiac motion and any intra-shot respiratory motion. In addition, radial acquisitions have also been shown to potentially reduce the prevalence and extent of dark-rim artefacts [Sharif et al., 2014].

3.2. Stack-of-Stars Design

3.2.1. Trajectory

A stack-of-stars (SOS) trajectory is defined here as any traversal of k-space encompassing a radial in-plane design combined with Cartesian k_z encoding. Within this SOS approach, flexibility is available, for example regarding ordering, angle distribution and temporal variation of the angular distribution. Each of these factors could impact on final image quality.

In its simplest form a SOS design is equivalent to a standard volumetric Cartesian acquisition with in-plane phase-encoding steps removed and modification to the physical axis rotation matrix to apply an in-plane angular rotation to the readout. The choice of angular change per readout is typically either a small, constant, increment designed to sequentially cover π or 2π, or alternatively a fixed larger angle, such as the golden angle [Winkelmann et al., 2007], that provides approximately equal angular distribution of coverage for any reasonably large number of rays (known as "ray number"). For the angle θ of ray index n (of total ray number N), the rotation angle is either

$$\theta_n = \frac{(2\times)\pi \times n}{N} \tag{3.1}$$

or

$$\theta_n = \frac{111.25 \times \pi \times n}{180} \tag{3.2}$$

for "sequential" and "golden angle" varieties respectively (Figure 3.1). The $0 \rightarrow \pi$ coverage is more common than $0 \rightarrow 2\pi$ as by virtue of diametrical sampling, full, equiangular, coverage of k-space is still achieved by the former but at half the number of rays.

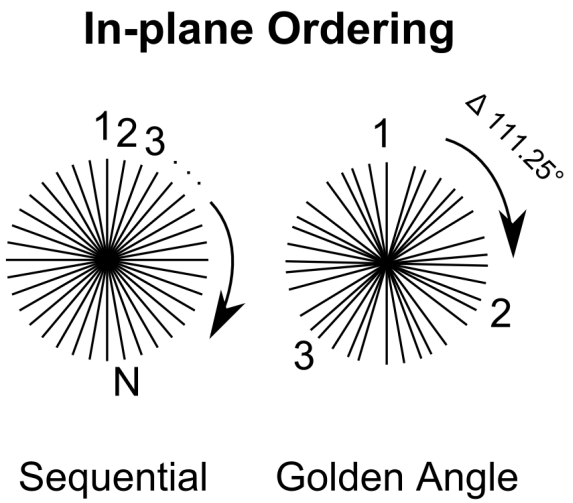

Figure 3.1.: In-plane radial trajectory ordering. Two options for the order of ray acquisitions in radial sequences are sequential and golden angle (see text for definitions).

Each temporal repetition of a SOS FPP sequence could in theory maintain identical parameters. However, as discussed in Section 2.3.2, current advanced reconstruction techniques utilise sparsity in the temporal domain. Compressed sensing in particular benefits from frame-to-frame variation in acquisition to differently distribute aliasing artefacts, making the artefacts appear more 'noise-like' across time. For this reason slight modification in angular ordering (Figure 3.2) between frames should bring benefits in image quality after full reconstruction. A small incremental offset to the starting angle can be applied, rotating the set of acquired angles and therefore the angular undersampling aliasing artefacts of a frame compared to its neighbouring frames in time. Depending on the size of the incremental offset and the size of the angular spacing, particularly for sequential ordering of ray angles, the starting angle will repeat after a set number of acquisitions but should still give a suitable distribution. Alternatively, for golden angle

acquisitions, the starting angle can continue on from the angle of the last acquisition in the previous frame. This continues to give a distribution that is effective for CS across time whilst being independent of the number of frames.

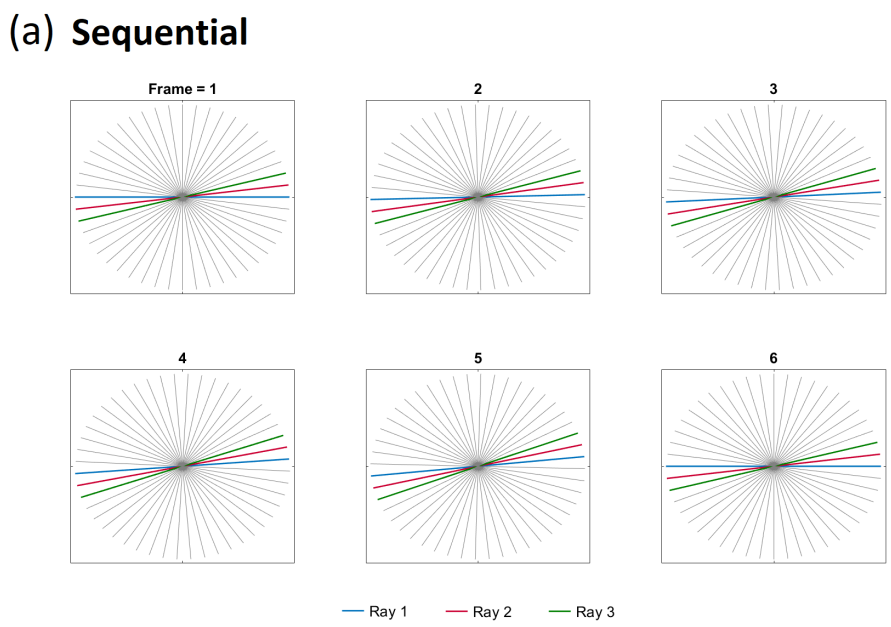

Figure 3.2.: Temporal variation of acquisition scheme. An offset to the starting angle between each acquisition can help improve frame-to-frame aliasing variation across time. Sequential ordering (a) applies a small incremental offset, in this case resetting after every fifth [n.b. the small changes in the diagrams]. For golden angle ordering (b) the golden angle increment continues on for the first ray of the new frame from the angle of the last ray in the previous frame.

With these potential alternative methods in mind, a flexible SOS pulse sequence program was developed using the IDEA (Siemens) pulse program-

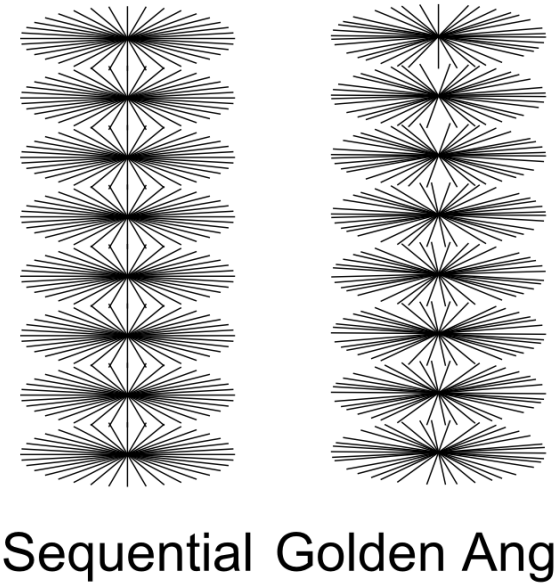

Figure 3.3.: Stack-of-stars trajectory. A single SOS sequence program was designed so as to allow modification of in-plane ordering. k_z partition encoding is along the vertical direction.

ming environment. This was created entirely from scratch, and allowed simple switching between sequential or golden angle in-plane ray ordering (Figure 3.3). For the k_z (partition) ordering, a complete set of rays were collected for one partition at a time, starting from one edge partition and collecting each complete partition across the k_z direction in a 'linear' order. So called 'centric' k_z ordering, which first collects the central k_z partition before alternating outwards, was not studied here. Temporal variation per cardiac cycle was provided by a small initial angle offset for sequential ordering, set so as to repeat every five frames as previously published [Chen et al., 2012], and as golden angle temporal variation for the golden angle acquisition type.

3.2.2. Fast Spoiled Gradient-Echo (SGRE)

A standard saturation recovery spoiled gradient-echo (SGRE) sequence type was applied in support of the SOS trajectory design. The waveforms are shown in Figure 3.4.

All gradient pulse amplitudes, durations and ramp slew-rates were designed to be optimal in speed subject to two different limiting criteria: hardware

Figure 3.4.: SOS sequence diagram. The gradient waveforms for a single readout of a SGRE SOS sequence, demonstrating the overlapping waveforms on the three axes for minimised timings. G_Z: slab selection, G_Y,G_Y: in-plane axes.

performance and peripheral nerve stimulation.

Hardware performance refers to the peak current (i.e. peak gradient strength) and peak voltage (i.e. peak gradient rate of change, since the gradient coils have significant inductance) available from the three channels of gradient amplifiers into the three independent gradient field coils G_X, G_Y and G_Z.

Nerve stimulation by the gradient waveforms also limits the applied performance level on the fastest systems (capable of 40mT.m^{-1} per axis at over 180T.m^{-1}s^{-1} switching rate, or "slew-rate"). Depending on the level of caution against any perceived effects that is selected in the operating software (based on a concealed model built by the manufacturer using healthy volunteer tests), this will prevent sequence parameters that require combinations of fast slew-rate and strong gradient pulses in rapid succession. Since the nerve stimulation is highly dependent on the image plane orientation, it will vary greatly during a cardiac examination, and software handling of this is usually be based on predictions from gradient waveform simulations rather than real-time measurements which occur too late.

For rapid imaging sequences such as FPP, it is typically the gradient slew-rate rather than maximum amplitude that is the limiting factor in reducing the total duration of a gradient pulse. This dominant dependence on ramp times is exacerbated by the need to run gradient pulses on slice-selection

and in-plane imaging directions "overlapped" in time, to achieve the fastest sequence operation. Such overlapping gradient pulses combined with the varying double-oblique acquisitions could demand very high slew-rates on a single physical axis. For maximum flexibility on scanning orientation as required for the highly variable cardiac orientation, this difficulty was compensated for here with an allowed slew rate of $\frac{SR_{max}}{\sqrt{2}} and \frac{SR_{max}}{\sqrt{3}}$ for two and three overlapping gradients respectively, where the total maximum slew-rate (SR_{max}) of 180T.m^{-1}s^{-1} was used.

For the data sampling during the echo, another fundamental trade-off exists between shorter T_R and the increased random noise of the wider range of frequencies sampled using a stronger gradient for the same radial resolution. Relatively large readout bandwidths were selected, in the range of (550 - 850)Hz.pixel^{-1}. This accepts an SNR penalty in exchange for a faster readout duration, allowing a shorter T_R.

Saturation of M_z was performed before each shot for FPP for maximum sensitivity. Two distinct approaches were tested: an adiabatic BIR-4 RF pulse and a 3-pulse "composite saturation" method. Exact saturation is more important for perfusion quantification, which is outside the range of this thesis, and initial work that tested both types of saturation found similar performance. This is as predicted within the less stringent needs of the non-quantitative work being performed here. The composite RF saturation method was finally selected because its RF energy deposition into the patient results in a lower specific absorption rate (SAR, discussed in Section 3.3.1). The reduced SAR became slightly more relevant during the investigation of bSSFP 3D perfusion in Section 5.2.

3.2.3. Choice of k-Space Efficiencies

In order to achieve the greatest possible sequence acceleration without further angular undersampling, a combination of k-space efficiencies (as introduced in Section 2.2.3) were implemented.

"Readout partial Fourier" (rPF) was employed to reduce the duration of the readout gradient. Earlier formation of the gradient echo along each ray also enabled a shorter pre-echo dephasing gradient time, which were both effective factors in reducing T_R. The high spatial frequencies no longer sampled were instead filled with zero values.

In the partition ('slice') phase-encoding direction, a similar omission of high spatial frequencies from one side of the origin was employed, labelled as

"slice partial Fourier" (sPF). These missing partitions were again replaced with zero values. While this does not reduce the sequence T_R, it reduced the total number of rays required per shot and was effective in reducing the total 3D shot duration.

After initial testing in phantoms (Section 3.2.7), both rPF and sPF were set as "75%" (i.e. omitting $-k_{max}$ to $-k_{max}/2$ and sampling only $-k_{max}/2$ to $+k_{max}$) for the remainder of the work; this degree of partial acquisition is commonly used in zero-filled partial Fourier applications (see Table 2.1). Reasonable accuracy can usually be achieved with the zero-filled method at this degree of acquisition [Haacke et al., 1999], albeit with increased Gibbs ringing due to the sudden truncation of acquired frequencies. Application of a windowing function to reduce this truncation effect is possible, but with a potential consequence of reduced image resolution.

3.2.4. Variable Undersampling

A further reduction in the shot duration was gained through so-called variable undersampling (VU) of the number of rays per partition. This technique maintained the number of rays in the central k_z partition, instead shortening the shot duration by lowering ('undersampling') the number of rays acquired in the outer partitions. The undersampling was increased for higher k_z i.e. with increased k-space distance from $k_z = 0$.

The VU scheme tested is shown in Figure 3.5. Starting with 20 rays in the central partition, as before, a consistent drop-off of two rays per partition from the centre was used. With a 75% slice partial Fourier acquisition, the rays acquired can therefore be written as (12-14-16-18-20-18-0-0). This equates to a reduction of acquired rays by 22, which for a T_R=2ms would be a 44ms reduction of the shot duration.

The variable undersampling would be expected to generate additional artefacts compared to non-VU implementations (i.e. a fixed number of 20 rays/partition). By focussing the sampling towards the centre of k-space, VU aims to combine an important reduction in shot duration with minimising the associated reduction in image quality.

3.2.5. Flip Angle Considerations

The slab excitation flip angle programmed in the initial sequence was 12°, based on the following estimations and well-known approximations.

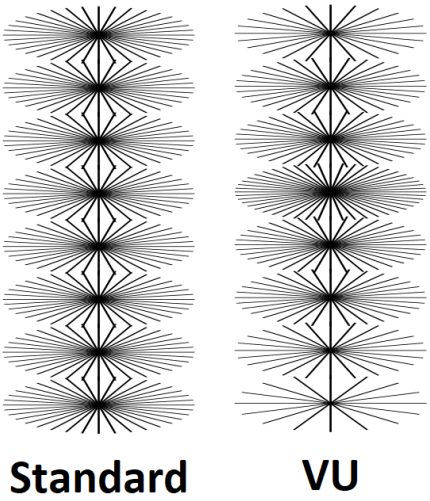

Figure 3.5.: Standard and Variable Undersampling (VU) SOS trajectories.

The Ernst angle [Ernst and Anderson, 1966] is frequently used in trying to select a flip angle that will provide maximal SNR for a given T_R and tissue T_1. The Ernst angle is given by

$$\theta_E = cos^{-1}(e^{-\frac{T_R}{T_1}}) \tag{3.3}$$

For 3D imaging, since most of the slab thickness is unaffected by cardiac motion that might bring fully magnetized tissue into the slab during the shot, and as there is also a reasonably constant flip angle over the central region of the slab profile, the Ernst angle may be more relevant than for cardiac 2D SGRE imaging.

Under the bolus injection conditions used in this work, the peak myocardial concentration of GBCA (although highly subject-dependent) is around 1-3mM (Section 1.5.3). During the first-pass of GBCA, the myocardial T_1 will consequently drop from its native ∼1300ms at 3T, down to ∼110ms (estimated range: 65ms [3mM at r_1=5s^{-1}.mM^{-1}] to 260ms [1mM at r_1=3s^{-1}.mM^{-1}]). The Ernst angles across this estimated range of T_1 values and for a range of T_R times are shown in Figure 3.6. For T_R=2.0ms, the calculated Ernst angle at T_1=110ms would be 10.9°.

The B_1 field can be highly non-uniform over the heart, particularly at 3T, where it is known to typically reach ±20% around the B_1 at the centre of the left ventricle (Figure 3.7). This non-uniformity is subject-dependent and is also likely to change with respiratory position. Any programmed value of

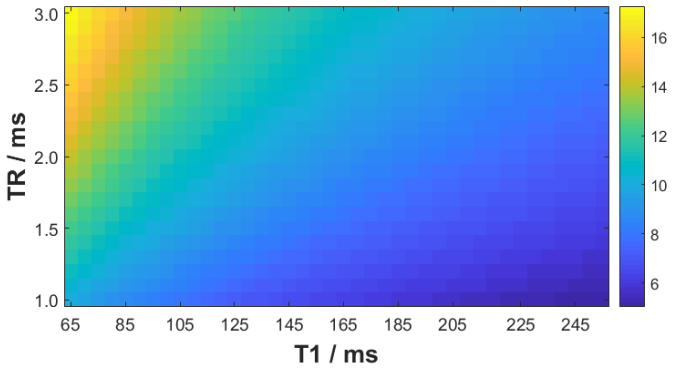

Figure 3.6.: Ernst angle plot for varying T_1 and T_R values.

the excitation flip-angle is therefore quite imprecise and the pulse sequence physics in any reliable method cannot depend on its precision.

The Ernst angle calculation contains a further assumption that possibly invalidates it for use with single-shot imaging. Since data for FPP is acquired while the dynamic equilibrium of M_z is being established between recovery and partial saturation by the imaging RF pulses, the calculated Ernst angle may be lower than actually optimal in these scenarios.

Considering these factors, a slightly higher flip angle of 12° was chosen. This is in keeping with values in previously published 3D FPP SGRE literature [Chen et al., 2012][Jogiya et al., 2014a], and so enables consistency in comparison with these approaches.

3.2.6. Initial 3D SOS FPP Pulse Sequence Parameters

While the exact pulse sequence parameters varied, as will be explained for each experiment, the following "default" set of parameters acted as a starting point from which modifications were made. These were chosen using some initial phantom work to test previously reported values in the literature (Table 2.1).

Frequency-encoded ADC sampling along each ray acquired 144 samples with a gradient strength calculated to give 300mm field-of-view along each radius. With no penalty in timing, it was possible to acquire 288 samples by doubling the ADC sampling-rate, known as oversampling, which at least nominally extends the diametrical FOV. On the assumption of sufficient angular sampling, this provided a nominal isotropic in-plane resolution of ∼2.1mm as a baseline for the following work on acceleration of this sequence.

Six partition-encodings were acquired through the slab excitation, extended

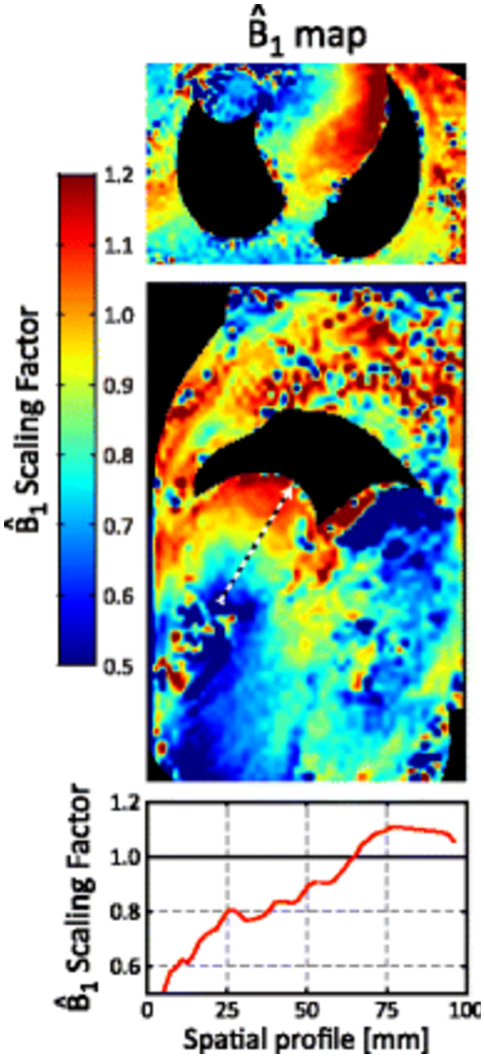

Figure 3.7.: *in vivo* B_1 variation. B_1 scale factor (ratio of actual to nominal radiofrequency field strength) for a representative human volunteer. A line profile is shown for the SAX image. Reproduced from [Chow et al., 2015].

to eight with two zero-filled points by the sPF explained above. The partition-encoding gradient pulses were calculated to acquire 10mm resolution over a slab thickness of 80mm. T_R was approximately 2ms after application of 75% rPF and other discussed sequence optimisation.

The initial setup was based on 20 rays per partition, as utilised in the previous example of 3D SOS FPP [Chen et al., 2012]. For the 6 acquired partitions, this required a total of 120 rays per shot in initial work. For the T_R of 2ms this gave a shot time of 240ms. The VU implementation described earlier reduced the number of rays to 98, thereby reducing shot duration to 196ms.

The saturation recovery time (SRT) was defined for this work as being from the centre of the last composite saturation RF pulse to halfway through the number of rays sampled for the central k_z partition. The SRT was chosen as 150ms. While this SRT is longer than in most 2D clinical perfusion setups for "eyeballing", a large part of this is not free recovery time as it is affected by the SGRE sequence in progress.

3.2.7. Initial Phantom Testing

Early testing of the sequence was performed using MRI phantoms, to examine initial image quality prior to any *in vivo* acquisitions. Further optimisation is performed in Section 5.3. The imaging phantoms and reconstruction method used throughout this chapter are described here, as well as example 3D SOS acquisitions for different sequence parameters.

Various vendor provided phantoms were used throughout the developmental work, primarily the three shown in Figure 3.8. Phantom A was a uniform oil-filled spherical phantom of 24cm diameter with a measured T_1/T_2 of 180/120ms. Phantom B was a smaller uniform cylindrical phantom of 11.7cm diameter and 17cm length with a nickel-sulphate solution of measured T_1/T_2 of 300/270ms. Finally, Phantom C was a cylindrical phantom (19cm diameter, 17cm length) containing internal perspex block patterns that varied in-plane and through-plane, and contained a copper-sulphate solution with measured T_1/T_2 of 285/240ms. Exact phantom T_1 and T_2 values were not deemed important for their application in this work but the measured values provided confidence of approximately valid values in the myocardium during first-pass.

Phantom acquisitions were performed using the scanner's built-in whole-body cylindrical "bird-cage" transmit/receive coil, which gives a more uni-

Figure 3.8.: Three phantom objects (A-C) used for test imaging throughout the project. See text for details.

form coil-weighting coverage compared to the use of surface coils, at the expense of reduced SNR. This gave grater confidence that any variations in image signal intensity were due to the pulse sequence or reconstruction, as well as enabling greater repeatability between experiments (i.e. without concerns over changes in surface coil positions).

Reconstructions were performed using a pre-interpolation gridding algorithm, further described later, in Section 4.2.2. The gridded reconstruction provided a fast, simple reconstruction that does not attempt to compensate for undersampling aliasing. This enabled examination of image quality without effects potentially caused by more advanced reconstructions.

Example images acquired on Phantom C are shown in Figure 3.9. A "base parameter set" was defined with the parameters stated in Section 3.2.6, but without the additional k-space efficiencies (Section 3.2.3). Acquisitions were performed with this base set and were repeated with single variations in either trajectory ordering or k-space efficiency.

A single central slice is shown for the images in Figure 3.9a, while the complete set of eight slices is shown for a single set of parameters in Figure 3.9b. A single time-frame is demonstrated in each case due to the static nature of the phantom. Defining background signal as the amount of radial "streaking" artefact over the empty image regions, the base set had the lowest background signal of all the undersampled acquisitions. Read (rPF) and slice partial Fourier (sPF) added only minor increases in the background signal, although sPF was seen to additionally degrade the through-plane resolution (Figure 3.9b), as visible by the more gradual edges of the oblique segment of the fluid in the phantom (within the central rectangle of solid plastic). Golden angle orderings had a more noticeable increase in background signal compared to the mean phantom intensity. The impact of the high level of

undersampling was examined by comparison with the fully acquired example.

Phantom images were also acquired with and without the VU scheme (Figure 3.10). Acting as a basic initial test, good visual agreement is seen between the datasets, across all slices. This technique is investigated further in Section 5.3.1.

Further modifications to the 3D FPP SOS sequence were made during *in vivo* testing and for the different investigations described in later chapters.

The following sections describe two techniques investigated during the sequence development, with the purpose of shortening T_R to attain a minimal FPP shot duration. These are examined with their impact on image quality to allow selection of a setup with a suitable trade-off between acceleration and artefacts.

3.3. RF Excitation Pulse Optimisation

3.3.1. Introduction

With optimised partition and frequency encoding gradients, and fast ADC sampling times, the duration of the slab-selective excitation RF pulse can potentially be a large proportion of the T_R. Most vendor-provided RF pulse designs are tailored for their specific application, and it is therefore to be expected that these pulses can be adjusted for optimal performance in the 3D FPP application. For this work, with shot duration the strongest constraint, the duration of the RF pulse could likely be shortened which is examined next.

Whilst shortening an excitation pulse, care needs to be taken that a short pulse duration is not overly detrimental to other features related to the excitation and so a compromise is often required. RF pulse design typically has the following considerations:

- Pulse duration. This is the key parameter that, for rapid imaging, should ideally be minimised subject to other constraints.
- Flip angle. In the SGRE approach used for SOS, only a low flip angle is needed. This is a key to optimising the design, as for this work the pulse will not be required to deliver more than 12° nutation, as explained previously.

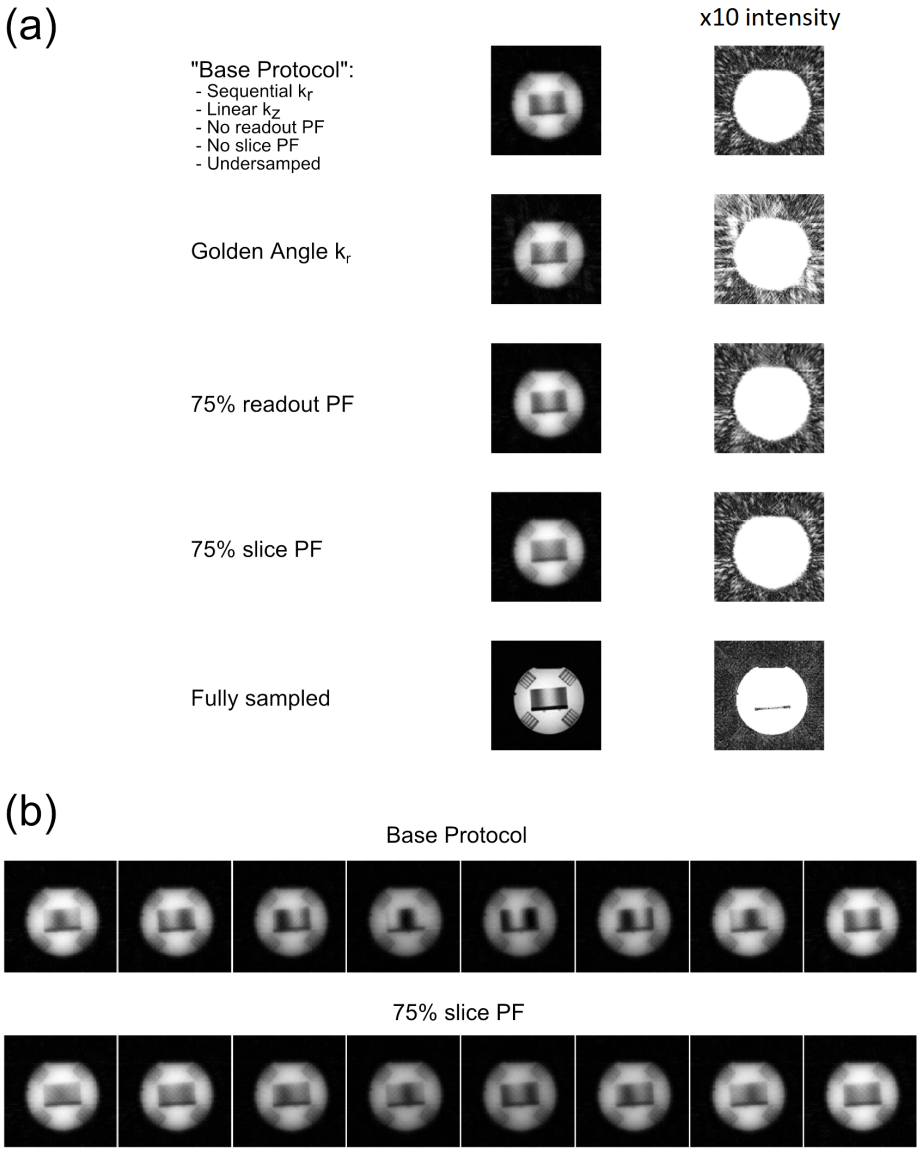

Figure 3.9.: Example sequence acquisitions in a phantom. Single central slice example images (a) for the default sequence and with individual parameter modifications (with 10x intensity also displayed to show background signal). All eight slices (b) are shown for the default sequence and for a sequence with a zero-filled slice partial Fourier acquisition. All images were reconstructed by a gridding process.

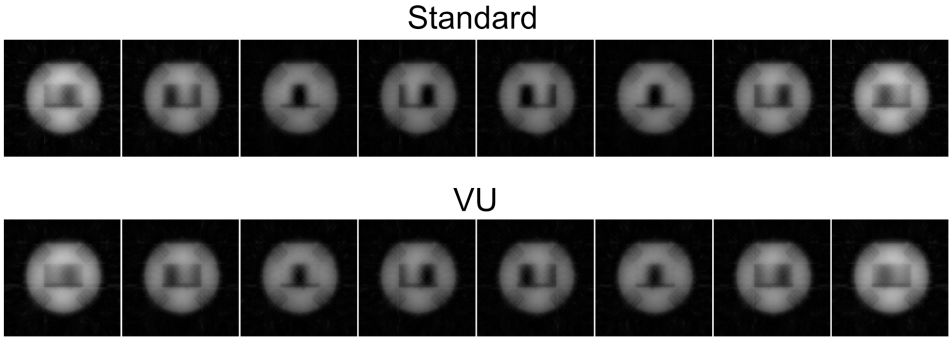

Figure 3.10.: Phantom acquisition with and without variable undersampling. All eight image slices are shown for a phantom acquired with the 'Base Protocol' parameters, as in Figure 3.9, without variable undersampling (standard) and with variable undersampling (VU).

- Pulse bandwidth & excitation profile. The bandwidth of an RF pulse and its slab excitation profile are intrinsically linked. For flip angles $\ll 90°$ the profile is well approximated by the frequency-domain Fourier transform of the RF pulse temporal waveform. Sinc pulses are typically used for excitation, as an infinite sinc pulse would produce a perfect rectangular slab profile. The degree to which the sinc pulse is truncated requires consideration as it will cause imperfections in the slab profile. This is particularly important in 3D imaging with the challenge of aliasing along the partition-encoded FOV arising from an imperfect slab excitation profile (Section 2.6.1).

- Peak RF voltage. This is the highest voltage required out of the RF power amplifier into the whole-body RF transmitter "birdcage coil" to generate the B_1 field in a patient for the designed RF pulse. The peak is typically at the central lobe of a sinc pulse, and is determined by the pulse bandwidth (i.e. its slab thickness along the accompanying selection gradient), duration and flip angle. Along with hardware limits, the peak RF voltage available is affected by the "RF load" imposed by the patient within the birdcage coil (i.e. how much RF power they absorb as heat).

- Energy Deposition. The rate at which energy from an RF field is absorbed by a body is described by the specific absorption rate (SAR). SAR is given by

$$SAR = \frac{1}{V}\int \frac{\sigma(\mathbf{r})|\mathbf{E}(\mathbf{r})|^2}{\rho(\mathbf{r})}d\mathbf{r} \tag{3.4}$$

where σ is the conductivity, $\mathbf{E}$ is the electric field, ρ the density and V the volume. The units are typically in W.kg^{-1}. SAR is therefore dependent on flip angle and increases quadratically with frequency. Whilst a major area of consideration for much RF pulse design, for this low flip-angle work using intermittent operation, SAR is unlikely to be of major impact.

In this section, the above features were investigated to adjust the compromise between RF pulse minimisation and preservation of the other described properties, to optimise the 3D FPP sequence.

Three separate components were required for this analysis to account for the various interdependencies: a framework for calculation of sinc waveforms of varying bandwidth, a simulation of the produced slab profile and corresponding peak voltage at varying durations and flip-angles, and analysis of achievable peak voltages based on a survey of previous patient scans.

3.3.2. Sinc Waveform Generation

A framework was created to enable generation of various RF waveforms.

A time-dependent RF waveform is given by

$$B_1(t) = \begin{cases} W \times A \times t_0 \frac{sin(\pi t/t_0)}{\pi t} & -(N/2) \times t_0 \leq t \leq (N/2) \times t_0 \\ 0 & \textbf{elsewhere} \end{cases} \tag{3.5}$$

where N is the number of sinc zero-crossings (defined including the zero-touchings at either end of the pulse), A is the amplitude and W is the windowing function, described by

$$W = (1-\alpha) + \alpha \times cos\frac{\pi t}{N t_0} \tag{3.6}$$

Windowing compensates (through smoothing) for the sudden truncation of the sinc function and is commonly one of two variants. Setting $\alpha = 0.46$ produces a Hamming window, whereas $\alpha = 0.5$ forms a Hanning window[1] [Bernstein et al., 2004].

[1] More accurately known as a "Hann" window, it is now often referred to as Hanning because of its similarity with the Hamming function.

The value of N chosen for the pulse is equivalent to the bandwidth-time product (BWTP)

$$BWTP = T\Delta f = N \tag{3.7}$$

which is a dimensionless descriptor often used in MRI RF pulse design, and related to the selectivity sharpness of the corresponding slab profile. This is an important metric but clearly only partially characterises the profile shape.

RF pulses were generated for a range of BWTP values from 1 to 8 for the two windowing functions. For initial work, to limit the increasing number of different pulse tests required, it was decided to trial only integer values of BWTP. Analysis of the corresponding slab profiles was then performed through the Fourier transform approximation.

3.3.3. Slab Profile Analysis

To introduce this analysis, the key components of a slab selective profile are shown in Figure 3.11.

For a defined partition-encoded FOV, the regions of the slab profile excited outside of the FOV will alias (or "wrap") into partitions from the opposite edge of the partition-FOV (see Section 2.6.1). The z-positions of the (FWHM) at each side of the simulated slab profile, $FWHM_-$ and $FWHM_+$, were calculated and used to define the partition-encoded FOV. By use of the FWHM values as the z-positions of the partition-FOV limits, a good balance should be achieved between partition-encoding wraparound and insufficient signal excitation in the partitions at the profile edges.

The regions of the slab profile that fall outside the FWHM (partition-FOV) limits, and that therefore cause partition aliasing, can be analysed for any given pulse. If a limit of the allowed partition aliasing is set as a fraction of the peak intensity of the slab profile (accepted aliasing, AA), then the z-position limits along the partition-FOV at which these aliasing levels occur can be defined as $lim(AA)_-$ and $lim(AA)_+$.

From these values, the fraction along z of the excited slab profile that contained unacceptable aliasing (i.e. >AA), defined as ξ, was calculated as

$$\xi(AA) = \xi(AA)_+ + \xi(AA)_- \tag{3.8}$$

where

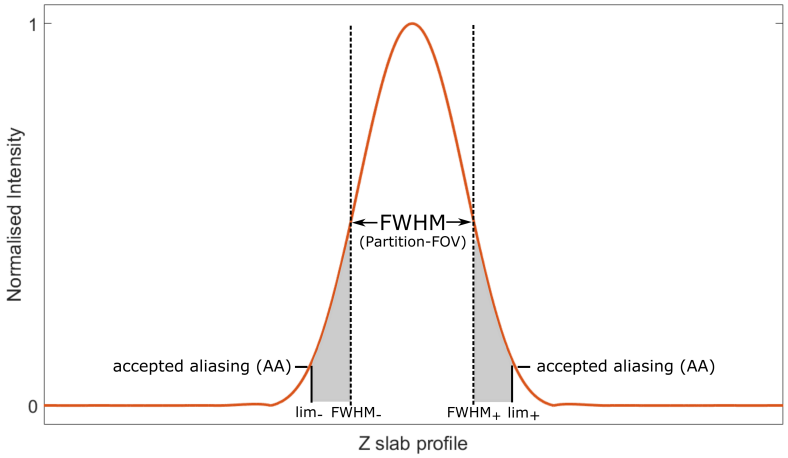

Figure 3.11.: Components of a slab selection profile. The regions of aliasing above the accepted aliasing (AA) value are shown shaded as grey. A poor slab profile is demonstrated for clarity of labelling.

$$\xi(AA)_+ = \frac{lim(AA)_+ - FWHM_+}{FWHM_+ - FWHM_-} \tag{3.9}$$

and

$$\xi(AA)_- = \frac{FWHM_- - lim(AA)_-}{FWHM_+ - FWHM_-} \tag{3.10}$$

For a total number of partitions, N_{total}, the number of partitions that are at least partially[2] contaminated by this level of aliasing, N_{alias}, is given by

$$N_{alias} = \lceil N_{total} \times \xi_+ \rceil + \lceil N_{total} \times \xi_- \rceil \tag{3.11}$$

where $\lceil\ \rceil$ is the mathematical representation of a ceiling operation. This value can therefore reasonably be assumed to be the number of edge slices that would have to be discarded after reconstruction.

For this work N_{total} was set at 8, as defined in the default parameters (Section 3.2.6) and the maximum accepted aliasing, AA, was set at 0.1. There is little literature on the ideal value for AA, because the tolerable level *in vivo* would be dependent on the source of the aliasing. For these evaluations the 10% value was decided as a reasonable compromise: a reasonably low value is required *in vivo*, for example because of bright subcutaneous fat

[2]The "partial contamination" approach is approximate but can be justified in view of the smoothly-varying slab profile.

signal near surface coils, while attempts to impose a smaller AA value would give unnecessarily high suppression considering the constraints of the highly rapid volumetric acquisition.

This analysis was performed for all of the examined RF pulse profiles.

3.3.4. Peak RF Voltage Investigation

In order to determine realistically usable pulse designs, examination is also required of the peak voltage of these pulses at various potential pulse durations and flip angles, as exceeding the peak voltage would prevent their correct function.

The peak RF voltage demanded by an RF pulse is dependent not only on the RF pulse BWTP, duration and flip angle, but also on a calibration of the B_1 field accounting for the RF absorption "load" of the patient inside the RF transmitter coil, known in this work as the transmitter calibration or reference voltage.

The term "reference voltage" is specific to Siemens systems. It is defined as the RF power amplifier output voltage into the whole-body transmit birdcage coil to achieve a 180° nutation with a 1ms rectangular ('boxcar') pulse shape, assuming on-resonance application. This calibration is performed by the scanner every time the patient table is moved within the bore, using a series of dual flip-angle transverse 50mm slab excitations. The calibrated RF power amplifier output voltage required for any RF pulse is calculated by the time-integral of that pulse relative to the 1ms reference pulse, scaled further by the requested flip-angle comparative to the 180° in the reference.

This calibration procedure complicates the peak voltage calculations for the waveforms generated in Section 3.3.2 as, even when all the other parameters have been decided upon, the reference voltage is subject specific.

To enable the design of RF pulses that would perform as fully intended in the overall majority of patient scans, an examination of previous reference voltages used in patient scans was performed. This was done for clinical scans that had taken place on the same scanner for which the SOS sequence work was planned because the calibration is dependent on the RF birdcage coil size and design[3] as well as the field strength.

A MATLAB program was written that searched through the hospital MRI DICOM files to extract cardiac images that had been obtained using

[3]This affects the efficiency in converting RF power into the B_1 field, with some power lost in the coil and its external RF shielding as heat.

the scanner of interest for this thesis work, and that had been marked as performed by a clinical operator. The 200 most recent adult (age≥18) patient datasets that satisfied the above criteria were selected from this search. The transmitter calibration voltage was extracted from the header of a single image from each patient, deemed suitable as the calibration is performed at the start of a scan and the reference voltage typically remains constant unless the patient is moved.

The results of this search gave the distribution of typical reference voltages on the scanner, so that a maximum reference voltage, $V_{ref,max}$, that would likely be encountered could be estimated in support of the 3D FPP design.

The different RF pulse designs mentioned above (with differing BWTPs and windowing functions) were transferred to the scanner and, based on the $V_{ref,max}$, the peak voltages required by the different pulse designs for various flip angles and durations were recorded. The required flip angle for the 3D FPP sequence was estimated earlier in this thesis (Section 3.2.5), enabling a suitable range of flip angle values to be tested on the scanner to determine the minimum RF pulse duration, subject to a satisfactory slab profile.

Overall, the work in these sections (3.3.2 - 3.3.4) therefore aimed to provide the 3D FPP work with practical and reliable RF pulse designs that would support the majority of patient studies, in terms of slab profile as well as the durations and flip angles at which they would perform as requested.

3.3.5. Scanner Validation of RF Pulse Designs

Confirmation of slab profile simulations was performed on the scanner using the calculated RF pulses applied in a modified pulse sequence. Additionally, the effects of exceeding the peak RF voltage were examined.

To enable a test of slab profiles, a simple 2D Cartesian SGRE pulse sequence was modified so that the frequency-encoding gradient waveform was instead applied in the same direction as the slice-selection gradient. By using the RF pulse of interest for the slice-selection, its slab profile performance could therefore be imaged. Applying such a sequence to a phantom which is thin in the unresolved direction (along which this is a projection image), an image was reconstructed whereby the intensity plotted as a line profile along the frequency-encode direction should give a reasonable approximation of the slab-select profile. To avoid saturation-related distortion of the slab-select profile, a low flip-angle and long repetition time compared to the phantom

T_1 were used.

A low flip-angle 2D Cartesian SGRE sequence was used with a T_R of 100ms, 1.2x1.2mm resolution, flip angle 12°. Three pulses were chosen to be investigated: a low BWTP pulse (N=1), a high BWTP pulse (N=8) and the pulse design that was finally selected based on the results of the other investigations (Sections 3.3.2 - 3.3.4). By testing the validity of the simulations at each extreme of the range of RF pulse designs, as well as for the chosen pulse, reasonable confidence in their correct design could be gained.

Data was exported from the MRI scanner for reconstruction and further analysis in MATLAB. Reconstructions were performed with a 2D fast Fourier transform (FFT). To improve the SNR (which was low due to the thin-phantom requirement), averaging was performed across 20 sequential lines in the phase-encode direction. This produced the final representations of the slab-selection profiles achieved by the scanner, which were compared with their Fourier transform approximations.

The investigation of peak RF voltage (Section 3.3.4) aimed to verify that the RF pulse would achieve the programmed flip-angle in the majority of patients. In the following practical work, two steps were investigated to handle situations where the limit of the scanner peak RF voltage was still exceeded.

An alert was included in the 3D FPP SOS sequence to give a warning if the peak RF voltage was exceeded, using a programming function that checked whether the peak voltage requested was achieved (vendor designed ".wasClipped()" function). Before proceeding with work depending on this, confirmation was sought about two aspects of the function: first that the alert was functioning correctly and second that if the peak voltage was not achieved, exactly what happened to the RF pulse waveform. If the RF pulse design and the parameters requested from it exceeded the peak RF voltage available, there were two potential outcomes. This could cause a "clipped" top of the RF pulse modulation waveform, thereby severely distorting the excitation profile. Alternatively, if managed more benignly by hidden levels of the MRI system software, it could reduce the amplitude of the entire pulse (delivering a reduced flip angle but preserving the slab profile).

An oscilloscope with sufficient frequency response was positioned outside the magnet room and connected to a long co-axial cable that ended with an

approx 4cm diameter wire loop. This loop was placed in the magnet bore to pick up the B_1 field. The amplitude calibration of the received signal was unimportant provided it was held the same throughout each series of RF pulse tests, i.e. nothing in the scanner bore nor the cable was moved.

To examine these RF waveforms, a triangular RF pulse waveform was inserted into the pulse sequence. The pulse sequence used was the 3D SOS sequence, although as only the RF pulse was being investigated this should not have an impact on this study. The triangular RF pulse was selected so that any potential changes in this shape would be more easily identifiable. The sequence was initially applied with both low (3°) and high (90°) flip-angles to test for the basic function of the alert, and also to compare the "clipped" RF waveform shape at 90° against that at 3°. Next, the sequence was repeated at increasing flip-angles, starting from the low-flip angle and using increments of 1°. Note was made of the transmitter voltage in each case. When the transmitter voltage did not change after incrementing from one flip angle to the next this was assumed to be the peak RF voltage and therefore a clipped pulse. The presence of the clipping alert was also recorded at each flip angle for comparison and indication of correct performance.

3.3.6. Results & Discussion

The findings from the methods presented earlier in Sections 3.3.3 - 3.3.5 have interlinked consequences, as their results guided certain aspects of the later methods, and therefore the results and discussion for these three sections are presented together in this section.

Simulated slab profile examples of low and high BWTP RF pulses are shown with their aliasing depth values, ξ, in Figure 3.12. An overview of the ξ values (with the corresponding number of aliased slices, N_{alias} provided in brackets) is compiled in Table 3.1. Undesirably high N_{alias} values are shaded in greyscale; values higher than 2 were deemed unacceptable due to the acquisition time required to acquire each partition and the relatively low overall number of partitions. From this, the cut-off point of pulses with $N_{alias} \leq 2$ was identified as $BWTP \geq 4$.

Across the range of BWTPs, Hamming filters appeared to marginally outperform Hanning filters, particularly at higher BWTPs, as can be seen in Figure 3.13. However, the magnitude of this difference was small and therefore the selection of this filter appeared not to be important for further

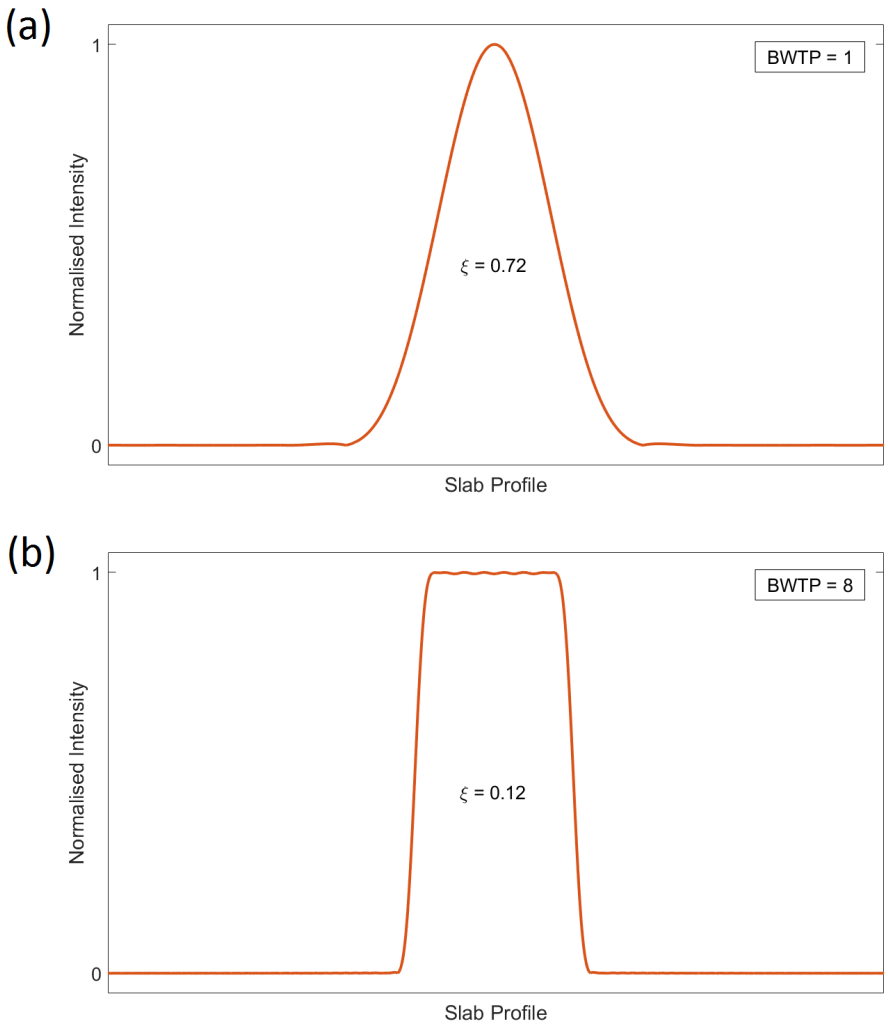

Figure 3.12.: Example simulated slab profiles. Simulated profiles with a low BWTP=1 (a) and a high BWTP=8 (b) and their corresponding ξ values.

Table 3.1.: Aliasing values for simulated slab profiles

BWTP	Hamming	Hanning
1	0.72 (6)	0.70 (6)
2	0.46 (4)	0.51 (6)
3	0.31 (4)	0.33 (4)
4	0.23 (2)	0.25 (2)
5	0.18 (2)	0.20 (2)
6	0.15 (2)	0.17 (2)
7	0.13 (2)	0.14 (2)
8	0.12 (2)	0.12 (2)

investigation; Hamming filters were applied for the rest of this investigation.

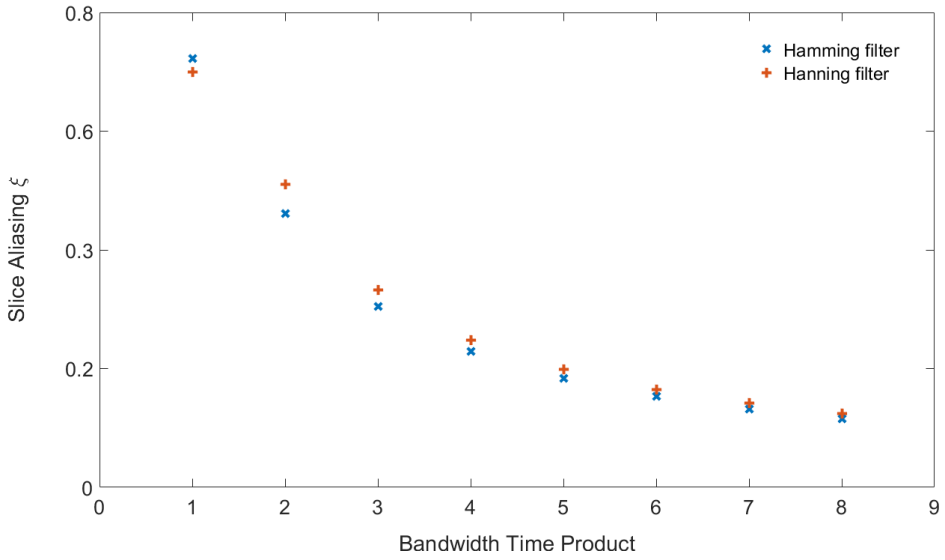

Figure 3.13.: Slice aliasing plot. Slice aliasing values ξ plotted for sinc pulses of different BWTP values and different filters, from Table 3.1.

For the peak RF voltage investigation (Section 3.3.4) a histogram of the scanner transmitter calibration reference voltages is shown in Figure 3.14. The upper limit of the 95% confidence interval of the distribution was at 660V. For all subsequent work, this was selected as the highest reference voltage likely to be required, $V_{ref,max}$.

The peak transmitter voltage results for the RF pulses (selected based on the acceptable N_{alias} results in Table 3.1), using the previously explained

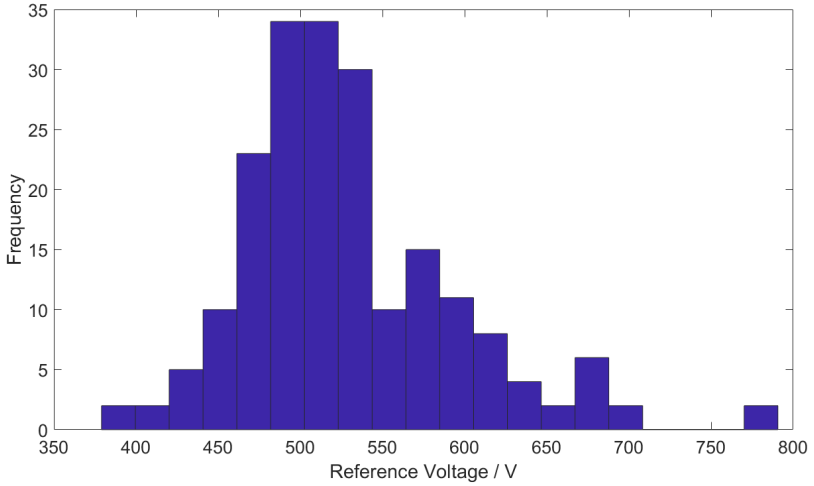

Figure 3.14.: Scanner transmitter reference voltages. A histogram of reference voltages for 200 previous adult patients on the scanner.

660V calibration reference, are shown in Table 3.2. Considering the $\alpha = 12°$ flip angle intended for application of the RF pulses, Table 3.2 showed that the minimum duration for these RF pulses ranged from 512-1024μs.

The results were sufficiently "slowly-varying" with BWTP that the decision in (Section 3.3.3) to test only integer values of BWTP appeared sufficient and no further investigation on a finer level of changes in BWTP was considered necessary.

As the RF pulses investigated all met the requirements for the slab profile, minimised duration (subject to the other conditions investigated) was the aim for this section of the work. Therefore the lower BWTP RF pulses at 12°, BWTP=4 at 512μs or BWTP=5 at 640μs, were decided to be the most suitable.

Both BWTPs 4 and 5 had the same number of aliased slices, N_{alias}, within the chosen criterion, subject to the correctness of the initially postulated AA valued of 0.1. However, the reduction in ξ using 5 instead of 4 was considered potentially important considering some likely challenges of *in vivo* conditions. Therefore, the RF pulse design at BWTP=5 applied at 640μs was chosen for future work. The increase of RF pulse duration by 128μs required for the higher BWTP was judged to be a compromise acceptable in the need for minimal slab-profile aliasing.

Following the above results and discussion which selected particular de-

Table 3.2.: Transmit voltages of Hamming sinc RF pulses using a 660V reference

$\alpha = 9°$

Duration / μs	BWTP=4	BWTP=5	BWTP=6	BWTP=7	BWTP=8
1024	258	321	388	450	516
896	295	367	443	514	590
768	345	429	517	600	689
640	414	514	620	720	763
512	517	643	763	763	763
384	689	763	763	763	763

$\alpha = 12°$

Duration / μs	BWTP=4	BWTP=5	BWTP=6	BWTP=7	BWTP=8
1024	345	429	517	600	689
896	394	490	591	686	763
768	460	571	689	763	763
640	551	686	763	763	763
512	689	763	763	763	763
384	763	763	763	763	763

$\alpha = 15°$

Duration / μs	BWTP=4	BWTP=5	BWTP=6	BWTP=7	BWTP=8
1024	431	536	646	750	763
896	492	612	738	763	763
768	574	713	763	763	763
640	689	763	763	763	763
512	763	763	763	763	763
384	763	763	763	763	763

The grey values exceeded peak RF voltage

signs for further work, the methods in Section 3.3.5 proceeded to validate the simulated slab profiles on the scanner. Results are shown in Figure 3.15 for BWTPs at the low (1) and high (8) ends of the range, as well as the final selected BWTP=5. The measured profile shape was in good agreement with the simulated approximation in all three cases.

Finally, results from the testing of the MRI system when requesting excessive peak voltage are presented. Oscilloscope measurement of the triangular RF pulse was successfully performed in the scanner. An oscilloscope trace is shown in Figure 3.16.

For the initial test, the software clipping alert included in the sequence on the scanner was triggered by requesting a 90° flip-angle but not at 3°. Notably, the "90°" scan ran with no other warnings shown by the standard scanner software. A large amplitude difference was easily observable between the two; however, the triangular test shape remained consistent, with no observed truncation of the peak. During the incremental increases in flip angle, the transmitter voltage was observed to increase until the 15° increment, at transmitter voltage 763V. The "clipping" pulse alert was confirmed as functioning correctly, first activated at this 15° level and subsequently for each increased flip angle. The flip-angle achieved by this triangular pulse shape was itself of no interest, and was only for evaluation of the concealed scanner technology behind excessive peak RF voltage requests.

3.3.7. RF Excitation Pulse Conclusions

The importance of optimising the RF excitation pulses for the required specific flip-angle and slab-selection profile quality was demonstrated. Unnecessarily stringent demands on the RF excitation parameters would have prevented adequate shortening of the slab-selective RF for 3D FPP. This work enabled a very short slab-selective RF pulse time to be achieved and applied in the future 3D FPP SOS investigations. This short RF pulse duration aided in meeting one of the primary challenges of 3D FPP - ensuring a reasonably short acquisition shot duration within each cardiac cycle.

Following this investigation, the future experiments could also proceed with reasonable confidence that the scanner hardware was delivering the requested flip-angle. In the small proportion of patients where this requested flip-angle might not quite be delivered, this section of the work also gave clear confirmation that the peak of the RF pulse would not be "clipped" and

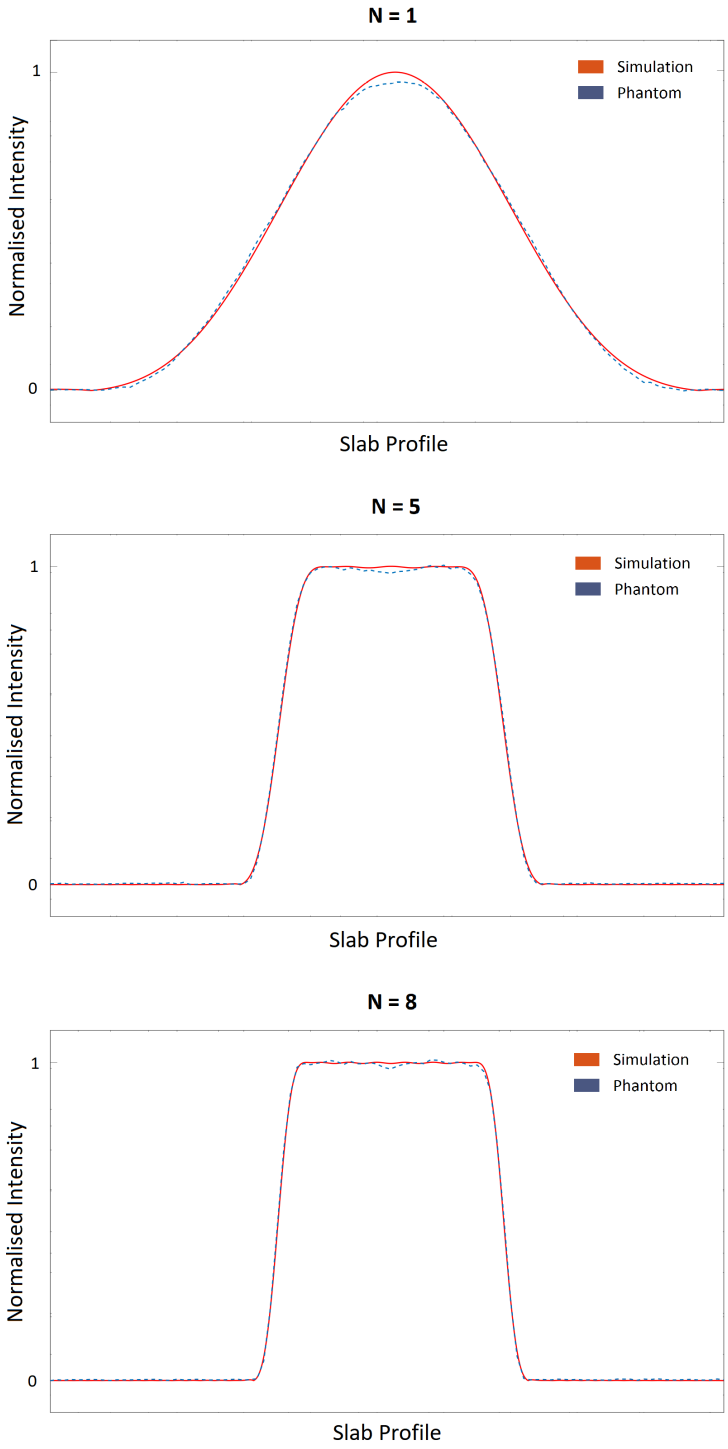

Figure 3.15.: Slab profile validation. Comparison of the simulated and phantom-acquired slab profiles for three BWTPs.

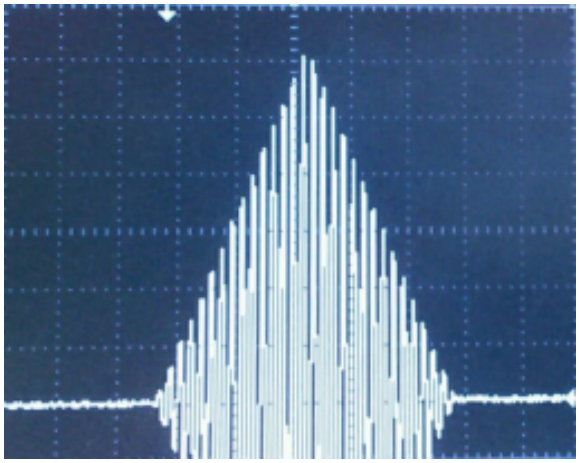

Figure 3.16.: Oscilloscope trace. The triangular RF pulse, detected on the scanner, for investigation of any 'clipping' effects. The apparent cycles are a digital scope artefact, not real RF cycles.

therefore that the slab profile would not be distorted, only reduced equally.

3.4. Spoiling Investigation

3.4.1. Spoiling with Minimised T_R

SGRE sequences, by definition (Section 1.5.2), require the residual transverse magnetisation of each T_R to be spoiled. Spoiling methods are especially important in 3D FPP SOS because of the extreme need to minimise shot duration, and therefore to reduce T_R as much as possible. This section describes an investigation into a method for adequately dephasing the transverse magnetisation in the SOS sequence without extending T_R. As with the slab-selective RF work, this section forms part of the "technical setup" of the sequence to be utilised in later investigations.

Early examples of SGRE methods achieved spoiling of transverse signal coherences by the addition of post-readout "spoiling" gradients, at the cost of extending the minimal possible T_R. The use of RF spoiling [Crawley et al., 1988] is a potential alternative strategy, which uses a varied transmit and receive phase each T_R to create a pathway for destructive interference in a steady-state gradient echo sequence. Such a spoiling scheme necessitates that all magnetisation components acquire a constant gradient-related phase change during each T_R, and therefore in practice requires addition of phase-encode rewinding gradients; for radial imaging this requires rewinding of the

rotated readout gradient within each T_R. These additional gradient pulses extend the T_R and even then the technique does not guarantee idealised spoiling.

Alternatively, [Lin and Song, 2009] proposed a random RF phase change each T_R combined with large spoiler gradients of random size for efficient spoiling in radial acquisitions. This technique uses the diffuse distribution of artefacts produced by radial sampling to improve spoiling comparative to conventional RF methods. Roeloffs *et al.* [Roeloffs et al., 2016] extended this work to investigate the feasibility of spoiling radial SGRE with use of random RF phase but without any additional gradient pulses after each ADC. The Roeloffs method would clearly be strongly relevant for 3D SOS FPP, provided it performs adequately in this particular sequence, as it would enable a direct reduction in the T_R.

The Roeloffs work, which was performed for 2D radial imaging, compared three spoiling methods: a "gold standard" sequence employing rewinding and spoiler gradients with conventional RF spoiling, an intermediate sequence that had no additional gradients but conventional RF spoiling phase changes, and a newly proposed sequence that performed spoiling only though implementation of a random RF phase change. The new method, randomised RF spoiling without additional gradient pulses, performed well in the Roeloffs work. This randomised method removed residual spoiling artefacts that were present in the intermediate sequence and it had only small, noise-like (i.e. randomly distributed), artefacts visible comparative to the gold standard sequence.

This randomised RF phase spoiling technique would clearly be ideal for the proposed SOS sequence, as it minimises T_R whilst also reducing residual signal artefacts. However, certain parameters tested in the original Roeloffs work vary from those in the 3D SOS FPP sequences proposed here (Section 3.2.6), most particularly in its requirement for application to 3D. The three proposed spoiling methods from the Roeloffs work were therefore added to the proposed 3D FPP SOS sequence, to examine their performance and potential benefits, as preliminary work in establishing an optimal 3D FPP SOS sequence.

3.4.2. Methods

The SOS sequence was adapted to allow switching between three spoiling variants. These are labelled Type A, B and C, matching those in the Roeloffs

work.

Type A was taken as the gold standard regarding spoiling quality, employing conventional RF spoiling combined with spoiling gradients, which thereby extended the minimal possible T_R. Type A applied a constant gradient dephasing per T_R and therefore fully rewound the radial frequency-encode gradient before applying in-plane and through-plane dephasing gradients. These were applied so as to achieve a constant dephasing of π over the radially resolved pixel size, simultaneously for each axis of the imaging sequence. The spoiling gradients were applied with maximised slew rate, as was also applied to the other gradient waveform designs. The gradient spoiling was combined with a quadratic increase in absolute RF phase each T_R of 117°, i.e. an *increasing* transmit and receive phase increment each T_R.

Type B had neither rewinding of the radial frequency-encode nor any added spoiling gradients, and therefore caused a varying gradient dephasing per T_R. The sequence therefore relied entirely on the quadratic RF phase change to spoil residual transverse magnetisation. Although Type B diverged from the formal requirements of spoiling theory, it had the advantage of the shortest possible T_R duration.

Type C is the proposed new variant by Roeloffs *et al.*, with no radial rewinding or additional spoiling gradient pulses (as for Type B), so that the T_R remained minimal. Instead of the quadratic increase in phase, Type C used a randomised RF phase change. The phase angle increment was randomly chosen from a uniform distribution each T_R. This random RF phase change was hypothesised to improve the spoiling ability compared with sequence B.

Initial validation of the three spoiling types (A-C) was performed in a 2D variant of the SOS sequence, with parameters chosen to be close to those of the Roeloffs work. Frequency-encoded (radial) resolution: 128 samples, FOV: (256x256)mm, T_R: 4ms, N_{rays}: 128, flip-angle: 12°, ADC sampling bandwidth: 1540Hz/Px. Imaging was performed in Phantom C for all three sequence types, using both the sequential and golden angle (111.25° angular step) ray orderings.

Next the performance of the three spoiling techniques implemented in the 3D SOS version of the sequence was examined. These sequences were applied with minimised gradient waveform timings, enabling operation at a T_R of 3.2ms for Type A and 2.1ms for Types B and C. Other sequence parameters were as described in the default setup in Section 3.2.6. Sequential and golden

angle in-plane orderings were tested.

Spoiling in 3D SOS requires an extra consideration comparative to 2D radial sequences due to the inclusion of k_z partition encoding. The partition-encoding gradient has the potential to rephase the signal along k_z, leaving residual transverse magnetisation in 3D sequences that do not include additional spoiling gradients. This could feasibly weaken the spoiling effectiveness of Types B and C when applied in 3D SOS. To isolate and examine the impact of this effect, rephasing along k_z was artificially induced in the 2D fully-spoiled radial sequence by introduction of a pre-phasing gradient on the slice-select axis, prior to slice selection. This balances the signal dephasing through the slice-thickness, generating a transverse steady-state unless the in-plane radial gradients apply sufficient dephasing. Acquisitions using this sequence were compared with those from a 2D radial sequence that was identical apart from an absence of the pre-phasing gradient. Both sequences employed the Type C spoiling method and used the sequence parameters from the validation methods.

3.4.3. Results

Initial validation of the three methods in 2D radial sequences showed good correspondence with the work by Roeloffs *et al.*. Figure 3.17 demonstrates images acquired with Types A, B and C, as well as the magnified difference images, for sequential and golden angle trajectory ordering. A distinctive ringing-like artefact emanating from a point source is visible for the intermediate Type B sequence, more prominently for the golden angle trajectory, which is eradicated in Type C. This is in good agreement with the types of artefacts seen in the original publication, and how they vary for the different sequences, giving confidence that the spoiling methods have been accurately reproduced.

In their application to the 3D SOS FPP sequence, the three spoiling types presented with a similar pattern to that seen in 2D. Figure 3.18a shows a central slice image from Types A, B and C applied with a sequential ordering. The Type B image had artefacts not present with the fully-spoiled Type A method. These artefacts appeared to arise from the sharp edges of the phantom and, whilst of a relatively low level, they had a clear structure. The Type C image did not present with such characteristic edge-related artefacts and was of marginally improved overall quality, although some residual signal clearly still impacted the image comparative with the fully

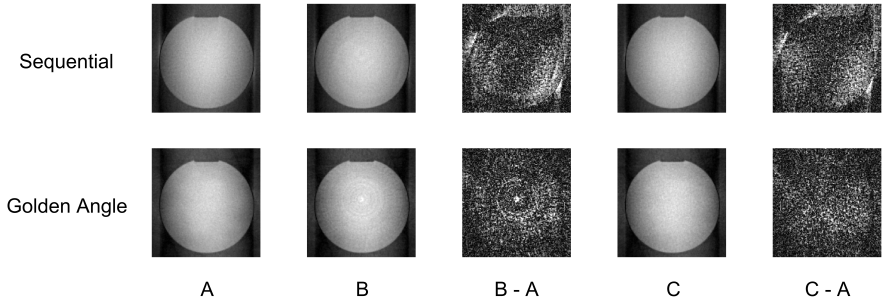

Figure 3.17.: Spoiling results: 2D acquisitions. Phantom acquisitions with the Type A (reference standard), Type B and Type C spoiling methods, and their difference images. Sequential and golden angle ray orderings were compared.

spoiled method.

In Figure 3.18b the corresponding images in a golden angle ordered sequence can be seen. Whilst the Type A full spoiling image was again of high quality, as it was for the sequential ordering, the Type B and C images showed a far more apparent degradation in quality. From examination of the difference images, this can be seen to be due to the residual signal appearing with a stronger, noise-like distribution with the golden angle trajectory. This appeared in both of the RF phase-only spoiling methods, although Type B additionally had the "ring" artefact similar to that in the 2D validation work (Figure 3.17), which was absent from the Type C image.

Comparison of the "balanced" fully-spoiled 2D radial sequence, which included the additional re-phasing gradient, against its unbalanced standard equivalent enabled the assessment of the extent to which the z-axis rephasing effect impacted the Type C RF phase-only spoiling method in 3D. Figure 3.19 shows a small but visible difference in the phantom image acquired with these two sequences. For sequential ordering (a), balancing the slice-select axis produced mild artefacts, similar to those in the corresponding Type C 3D datasets, arising from high spatial frequencies in the test object. For golden angle ordering (b) the balanced sequence introduced an increased noise-like signal, again matching with the Type C 3D SOS equivalent. The standard 2D sequence with golden-angle ordering does still contain a slight noise-like appearance, suggesting that some residual signal also remains due to improper in-plane spoiling in both golden-angle versions.

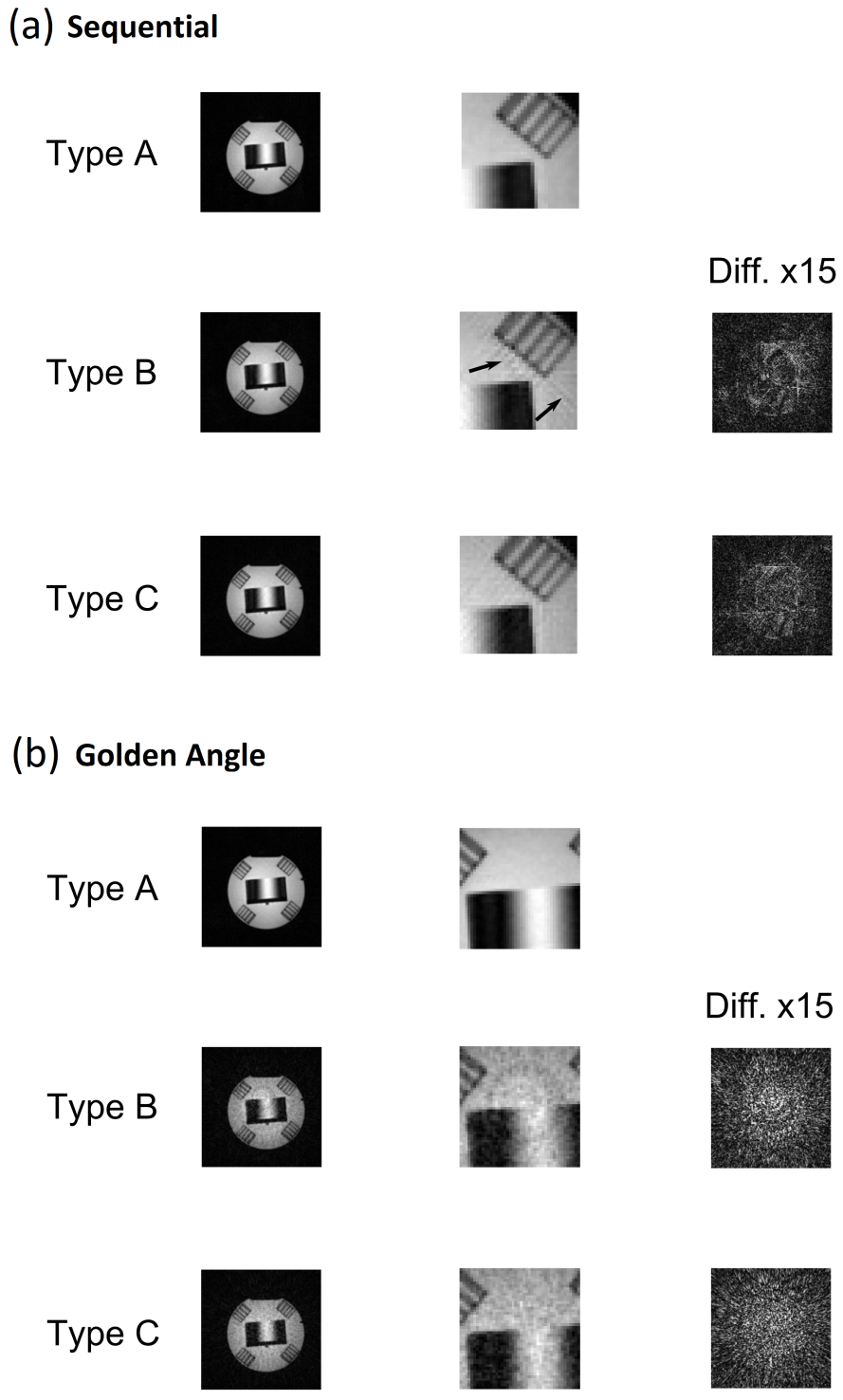

Figure 3.18.: Spoiling results: 3D acquisitions. Example central slice images for the three spoiling types applied with 3D SOS. Zoomed and enhanced difference images highlight the changes between the images.

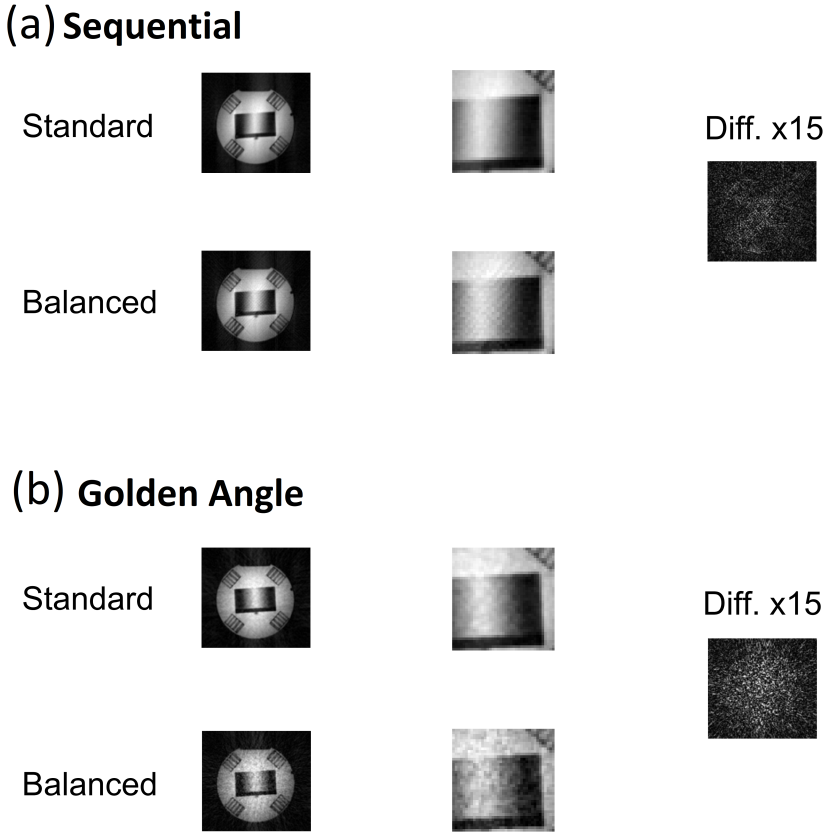

Figure 3.19.: Rephasing effects. Images are shown that were acquired with full spoiling using a 2D sequence that was unmodified (standard) and a 2D sequence that had an additional prephasing gradient applied on the slice-select axis (balanced), to mimic potential kz rephasing effects with Type C spoiling in 3D. Images are shown acquired with sequential ordering (a) and golden angle ordering (b), with zoomed and enhanced difference images.

3.4.4. Discussion of Spoiling Choice

Randomised RF spoiling without the addition of time consuming gradients has been shown to perform to a reasonable standard in the 3D SOS sequence. Rephasing along the slab-select direction caused by the partition encoding gradient has been found to weaken this method of spoiling when applied to a 3D sequence, such as SOS. Randomised RF phase spoiling still outperforms a traditional quadratic phase-only method, and provides relatively little difference to a perfectly spoiled sequence. Trajectory order plays a role in the effectiveness of the randomised RF spoiling method, as in the original work. The method is less successful with the golden angle ordering, suggesting gradient spoiling may be necessary in SOS sequences that use golden angle.

Minimising the T_R of the 3D SOS FPP sequence is of critical importance. The additional gradients required to fully spoil these sequences corresponds to an increase in T_R of >1.0ms, which for 100 rays/shot would cause an intolerable increase in shot duration. Whilst some imperfections in spoiling occur without the use of gradient dephasing, the randomised RF phase spoiling method reduces these effects and enables reasonable imaging quality, particularly for sequential acquisition order.

3.5. Further Sequence Considerations

What follows is discussion and examination of other considerations that can potentially affect a radial imaging sequence. These considerations include effects arising from imperfect timing of the MR hardware, as well as effects that can broadly be grouped as causing off-resonance phase-errors. These affect all imaging sequences, with characteristic impacts on those utilising a radial trajectory. These issues are well known for Cartesian and non-Cartesian trajectories alike, and so only a brief examination is made here of their impact on the 3D SOS FPP sequence.

3.5.1. Timing Delays

For non-Cartesian imaging, gradient-induced phase shifts should obviously correspond to the k-space locations used in the regridding operation onto a non-Cartesian path. This implies that the timing of gradient waveforms in relation to the ADC sampled MRI receiver data must be precisely controlled, and must furthermore be stable regarding factors such as long-term drift,

gradient heating and hidden scanner recalibrations [Aldefeld and Börnert, 1998][Brodsky et al., 2009].

In support of this thesis work, a short undergraduate research opportunity (UROP) student (Mr Arjun Khetia) was asked to measure these timings and their stability on the 3T Skyra system used. The method was based on FIDs of thin test objects. The objects were chosen to be thin along the applied gradient, so that their dephasing was sufficiently gradual to allow capture of the gradient pulse start by its impact on the phase of the free induction decay. A standard deviation of 0.05μs was obtained by repeated testing. This work showed that the gradient pulse arrival times differed by less than 0.9μs, tested over the range $\pm$100mm from the isocentre on all three axes. The variation in these timings caused by intense scanner activity did not exceed the standard deviation.

The outcome of this work was supportive for non-Cartesian imaging on the Skyra scanner used for this work[4], in that no corrections for gradient pulse direction were required as initially under consideration early in the thesis work.

However, as for all non-Cartesian imaging, the synchronisation of the sampled ADC with the regridding operation required the optimisation of a single timing parameter, which can be expressed as a number of ADC samples to discard from each echo before commencing the gridding of that echo. The number may be fractional requiring a simple interpolation between the stored ADC values to obtain the required intermediate delay.

The optimisation of this timing parameter between ADC sampling and gridding location was performed by analysis of phantom acquisitions. Phantom A datasets were acquired using the default 3D SOS sequence in the three standard perpendicular planes (i.e. transverse, sagittal and coronal). The datasets underwent gridded reconstruction after application of a shift along each rawdata echo. The reconstructions were repeated with this shift varied from -1.0 to $+1.0$ in 0.1 ADC sample intervals. As the incorrect placement of the k-space centre during regridding leads to a 'smearing' effect of the object signal across the entire FOV, the quality of each image repetition after each shift was measured by its background signal. This was performed in MATLAB by segmenting the object from the background and calculating the mean background signal, normalised by the mean object signal. This normalised background error is plotted for the three orientations in Figure

[4]These timings were found to be approximately three times worse on the older Siemens Avanto hardware.

3.20.

Over the three datasets, an ADC shift of +0.4 ADC samples was found to minimise the background error most successfully and was applied to correct for the sequence delay retrospectively (during the gridding process) in all future acquisitions. In-plane FOV offsets of non-Cartesian rawdata can be extremely sensitive to timing errors and were not used in the project.

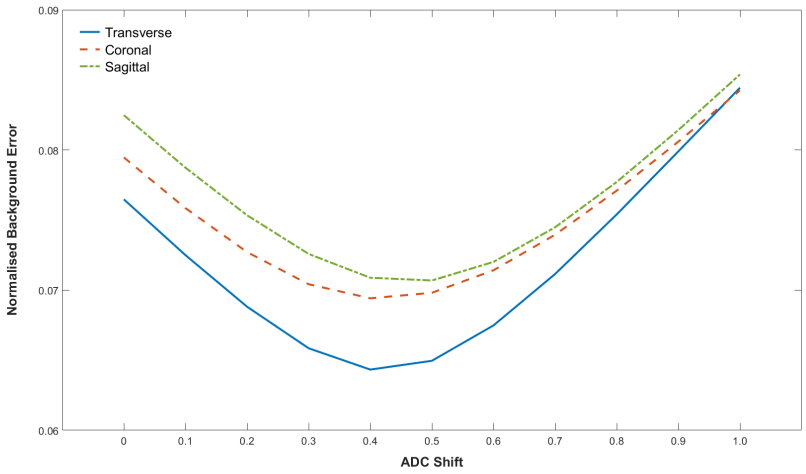

Figure 3.20.: ADC timing error correction. A normalised background error measurement at varying ADC shifts, for three perpendicular imaging planes.

3.5.2. B_0 Field Inhomogeneities

Producing a perfectly homogeneous B_0 field across the heart *in vivo* is impracticable in MRI systems. Most normal tissues are diamagnetic, creating a field that opposes the main-field, whereas the lung space around the heart is relatively empty and therefore far less diamagnetic than the heart. This variation in magnetic susceptibility creates local field distortions around the myocardium of the heart due to the differences in diamagnetism [Ferreira et al., 2013]. A partial, low-order correction can be made by acquiring 3D field plots which measure the frequency at each point by the phase-difference between two echo times. From this the best-fit spatial harmonics can be calculated and the currents in the coils that generate those spatial terms across the patient can be adjusted. This process requires slightly more experienced operators and localised, high-order, variations are likely to still remain uncorrected.

B_0 field inhomogeneities offset the local resonant frequency from the scanner reference ('centre') frequency, referred to as "off-resonance", which generates phase errors in the precessing transverse magnetisation. The effects caused by such phase-errors vary by sequence types. A strong advantage of Cartesian imaging is its tolerance to such phase errors compared to other types of sequence. Relatively little has been done to examine the off-resonance impact on radial trajectories, although some correction methods for radial imaging have been proposed [Cui et al., 2012].

Phantom B was used to investigate the robustness of the designed 3D SOS sequence to off-resonance effects. Great care was taken to shim the main field as accurately as possible over the volume of the phantom before commencing the following work. Images were then acquired using the various parameter options (Section 3.2.6), initially at "on-resonance", i.e. 0Hz off-resonance. With identical sequence parameters used each time, the acquisitions were repeated with centre frequency shifts of 100Hz, 250Hz and 500Hz applied to the scanner, corresponding to off-resonance frequency errors of 0.8ppm, 2.0ppm and 3.9ppm.

Examples of images at the central slice of the partitions are shown for each acquisition type, at 0Hz, 250Hz and 500Hz shifts, as well as a (500Hz-0Hz) difference image with an increased magnitude scale factor (Figure 3.21). The imaging sequence appears robust to large off-resonance errors, for all sequence types. A larger impact, and change in distribution of the artefact caused by off-resonance phase accumulation, occurs for the golden angle trajectory. This is in keeping with theory that suggests a different impact from off-resonance effects in golden angle trajectories compared to radial orderings that only complete a 0 to π coverage [Block, 2005].

Overall the SGRE 3D SOS FPP sequence was shown to perform robustly for off-resonance errors up to 500Hz, corresponding to a frequency error of 3.9ppm.

3.6. Stack-of-Stars Sequence Design Conclusions

An SGRE 3D radial stack-of-stars sequence was designed and optimised with regards to its shot duration. Various sequence parameters were selected and the sequence underwent initial testing in phantoms. A randomised RF-only method of spoiling was examined to maintain the short T_R, and shown to work to an acceptable level for sequential ray ordering. This spoiling

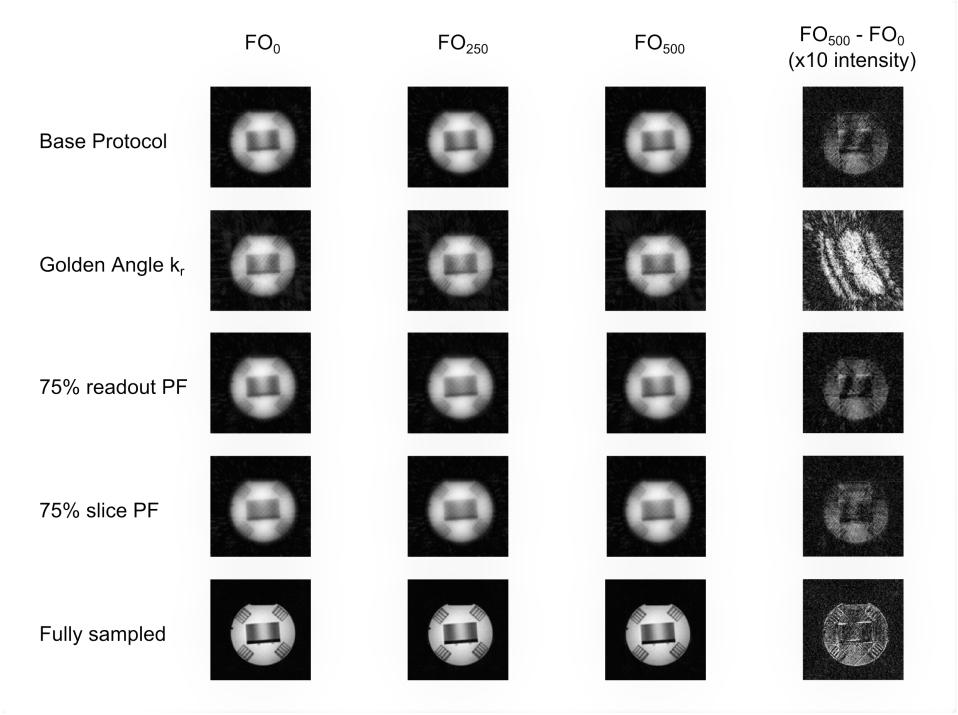

Figure 3.21.: Impact of increasing off-resonance error. Phantom acquisitions, as for Figure 3.9, with increasing centre frequency offsets (FO). A difference image between the 500Hz and 0Hz FO images is shown with increased magnitude.

method was therefore combined with sequential ordering in all future work. Other considerations that may affect the sequence were examined, and a required correction factor to the ADC timing was identified, which was then automatically implemented in future reconstructions.

4. Advanced Reconstruction & Motion Tolerance in FPP

Concurrent with the design of a pulse sequence for 3D FPP, consideration is required of the reconstruction method to be applied. The chosen reconstruction method will influence not only achievable acceleration/undersampling but also the sequence design.

In this chapter, traditional parallel imaging techniques are examined first, with the introduction of a novel method for improving their robustness to respiratory motion (Section 4.1), in keeping with the stated free-breathing aim of this thesis. Later, the focus shifts to an approach centred on compressed sensing (Section 4.2), to enable the extra required sequence acceleration for 3D FPP. The implementation of this technique is based upon previous work provided for this project under a collaboration with Professor Edward DiBella, University of Utah[1]. A brief overview of the technique's theory is presented before its configuration for this thesis work is described. The tolerance of this compressed sensing technique to motion is briefly examined, along with a technique to potentially improve its temporal fidelity (Section 4.3).

4.1. Free-breathing FPP using Parallel Imaging

As reviewed earlier, FPP methods have so far typically employed parallel imaging (PI) techniques to achieve sequence acceleration. Limits of feasible acceleration exist for these PI techniques due to SNR degradation and intolerance of the techniques to motion. What follows is an investigation into these limits for standard versions of PI techniques, as well as a proposed method for improved reconstruction based on modification to the coil response calibration technique. This aimed to enable higher acceleration factors in free-breathing FPP datasets.

[1]Utah Center for Advanced Imaging Research, University of Utah, Salt Lake City, USA

4.1.1. Coil Response Calibration in Parallel Imaging

The potential benefits from accelerating dynamic MRI sequences [Tsao and Kozerke, 2012] have driven a proliferation of different parallel imaging acceleration techniques. Alongside many novel PI methods of producing improved single-image reconstructions (e.g. [Uecker et al., 2008] [Lustig and Pauly, 2010]), there has been significant literature on making use of the dynamic nature of the series to support the reconstruction process [Tsao et al., 2003] [Pedersen et al., 2009b], as previously described (Section 2.3.2). Independent of the precise method, knowledge of the coils' spatial response is a fundamental requirement of PI. With the exception of a small number of computationally expensive "calibration free" PI methods [Chen et al., 2013] [Shin et al., 2014], coil calibration data is typically acquired in dynamic PI through one of three main methods (Figure 4.1)s: separate calibration acquisitions ('prescan') [Sodickson and Manning, 1997], variable density acquisitions that fully sample low resolution data ('integrated') [Jakob et al., 1998] or, assuming adapted undersampling patterns, calculation through filtering of consecutive frames of the accelerated data ('temporal') [Kellman et al., 2001].

Of these methods for collecting coil response data, integrated techniques provide the most faithful coil calibration information but reduce the achieved acceleration, whilst the prescan method conversely allows full acceleration but can cause large artefacts in the reconstructed image in cases of respiratory motion. With the ever increasing requirement to maximise achievable acceleration, temporal methods are therefore desirable in many free-breathing protocols. Acting through a filter of the undersampled data in the image or k-space domain, auto-calibration of the coil data through these methods can tolerate reasonable respiratory motion during the accelerated dynamic acquisition. However, there is less certainty about their ability to cope with more extreme breathing motion, for instance during pharmacologically-induced stress as in FPP, and this limitation has been recognised in previous PI work [Ding et al., 2011].

Popular PI methods using these temporal calibration techniques include TSENSE [Kellman et al., 2001], which typically employs a low-pass temporal filter, and its k-space domain equivalent TGRAPPA [Breuer et al., 2005], often using a moving average (MA) or average all (AA) filter of raw data. These are also applied in PI methods that make use of joint spatiotemporal redundancy [Tsao et al., 2003] [Huang et al., 2005]. A different approach

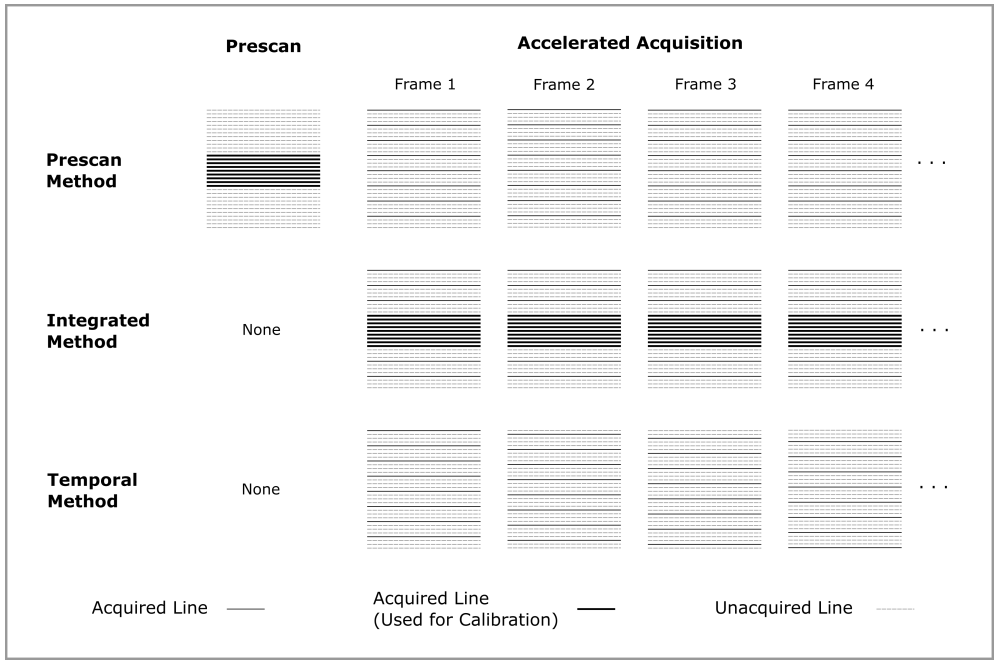

Figure 4.1.: Common methods of coil profile calibration in dynamic imaging. The Prescan method (top) acquires a separate full-FOV acquisition for calibration, prior to the accelerated acquisitions. The Integrated method (middle) acquires additional lines during the accelerated scan itself, to provide a central full-FOV region of k-space from which calibration can be performed. Temporal methods (bottom) do not acquire additional information for calibration purposes, instead altering the undersampling order from one frame to another to allow generation of calibration data through a temporal filtering process (different techniques are described in the text). R=4 undersampling is used for this example.

to 'temporal' calibration has previously been presented for non-Cartesian data, termed through-time radial/spiral GRAPPA [Seiberlich et al., 2011a] [Seiberlich et al., 2011b], which collects extended prescan data to allow calibration of the GRAPPA kernels across time despite non-equi-distant k-space sampling.

It has been shown that the application of a low-pass filter leads to nulls in the temporal frequency spectra of the reconstructed images, corresponding to temporal filtering [Madore, 2004] [Blaimer et al., 2011]. Whilst a method has been proposed to correct for these signal nulls by applying an additional filter, reduced signal-to-noise ratio (SNR) is a possible consequence, along with increasing the complexity of the algorithm [Blaimer et al., 2011]. Techniques in the k-space domain tend to avoid this effect, but may still suffer with sudden inter-frame motion. Combination of interleaved k-space data produces ghosting in the resulting reference data during such inter-frame motion, causing errors in the calibration. This is particularly true in the use of MA filtering. Applying a Karhunen-Loève (KL) filter across the temporally combined raw data has been suggested to improve accuracy of the calibration for free-breathing datasets, although it is accepted it cannot correct for such ghosting in the calibration data [Ding et al., 2011]. Using an AA approach is now the most common implementation for TGRAPPA, which reduces such ghosting through increased averaging, but at a cost of reduced SNR in the reconstructed images [Ding et al., 2015] and inevitably still including some coil reference data from incorrect respiratory positions. A simple yet robust method for producing calibration data that more accurately combines the advantages of both prescan and integrated methods would be of potential benefit.

In this section it is proposed that a new multiple free-breathing prescans (MFP) method can be utilised to give reference data that has accurate coil information for each respiratory position, without slowing down the main acquisition. It is hypothesised that this can be achieved with relative simplicity by having the prescan continually acquire over an extended period, similar to through-time non-Cartesian methods, capturing data over a similar respiratory range to that expected to occur during the main scan. As a technique appropriate for single-shot imaging acquired during free breathing, where each frame has a distinct respiratory phase, the performance of this method in producing accurate reconstructions is examined in free-breathing FPP datasets. This is performed comparative to prescan, integrated and,

in particular, temporal calibrations. Preliminary investigations are made through retrospective subsampling of fully-acquired datasets for quantitative analysis of image quality, in order to guide the methods of the prospectively accelerated acquisitions. The prospective investigations used visual analysis for investigation of different temporal techniques.

4.1.2. Methods

Experiments were performed on a Skyra 3 Tesla whole-body scanner (Siemens, Erlangen, Germany). An 18-channel anterior surface receiver coil and in-bed spine receiver coils were used, with appropriate array elements selected for cardiac coverage at the operator's discretion. A standard linear phase-encode ordered Cartesian Fast Low-Angle Shot (FLASH) sequence with saturation recovery was used for all scans, providing 48 measurements (after exclusion of initial proton density maps) of 3 slices each (T_E: 1.49ms, T_R: 2.98ms, SRT: 140ms, α=12°). The acquired resolution was typically ∼(2.6x2.6x10.0)mm, which for rate 4 acceleration gave an acquisition window of approximately 179ms/slice. Alterations to phase-encode FOVs and slice orientation were patient dependent, whilst the other parameters were kept the same for consistency across the subjects.

Informed consent to the use of power-injection and extra image acquisitions was gained from all patients, who were undergoing contrast-enhanced MRI for clinical purposes, with permission granted by the organisation's ethics committee for performing these scans at rest. To simulate potential increased breathing motion during stress imaging (as for hyperpnoea associated with adenosine [Watt and Routledge, 1985] or post physical exercise [Pflugi et al., 2015]), an attempt was made to intensify the volunteers' breathing motion. Therefore the volunteers were asked to use a "slow and deep" breathing motion throughout the acquisition process, and this instruction was repeated for both the MFP and FPP scans.

The PI reconstruction method chosen for this research was a GRAPPA implementation [Griswold et al., 2002], with a kernel size of 2 x 7 (ky x kx). The kernel size was chosen from testing on separate initial datasets (not shown). For all calibration techniques investigated, the entirety of the collected reference data was used for calibration. Care was taken to make sure during comparisons that the core GRAPPA method was kept identical, with only the coil calibration differing. The GRAPPA algorithm was modelled on the k-space-based 2D-neighbourhood implementation described by Brau

et al. [Brau et al., 2008], with no regularisation applied, and was performed in MATLAB. The reconstructed coil images were combined using the root sum-of-squares method.

Multiple Free-breathing Prescans (MFP) Method

The requirement was to produce prescan reference data that could give accurate coil response information for a series of free-breathing frames. By acquiring multiple prescans over the entire respiratory cycle, this would allow matching of coil response profiles obtained at a highly similar respiratory position to each undersampled data frame, prior to PI reconstruction (see Figure 4.2).

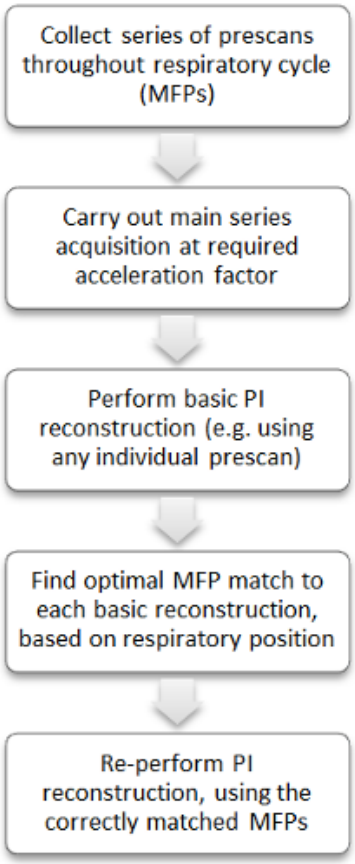

Figure 4.2.: An overview of the MFP reconstruction process.

The proposed method acquired the MFP prescan data as for the main FPP sequence except without cardiac gating and without saturation, which aimed to improve the sampling of breathing motion covered and increase

the SNR in the MFP respectively. The prescans in this case were therefore acquired at the same resolution as the main perfusion images. The main, undersampled, images were then acquired as normal for FPP, at the desired acceleration rate.

Matching of the optimal prescan to each undersampled frame was required prior to their application in PI reconstruction. This requires some initial reconstruction of the undersampled data to allow a comparison of respiratory positions in each prescan to each frame, to determine the appropriate prescan to use for calibration in the MFP calibrated PI reconstruction. The matching algorithm implemented was a fully-automatic combined high-pass filter cross-correlation technique. An initial PI reconstruction of the undersampled FPP data was performed using either a single Prescan or the Temporal calibration technique, dependent on the type of undersampling pattern applied to the data. A Sobel gradient operator was applied both to the prescan (MFP) images and a frame of the FPP initial PI reconstruction. The filtered MFP images underwent thresholding, to leave the top 5% pixels by intensity (i.e. primarily regions of subcutaneous fat adjacent to the receiver coils), thereby excluding regions where cardiac motion or contrast change between prescan and FPP frame might affect comparison. Each prescan then underwent a 2D-correlation calculation with the FPP frame,

$$r = \frac{\sum_x \sum_y (MFP_{xy} - \overline{MFP})(FPP_{xy} - \overline{FPP})}{\sqrt{\sum_x \sum_y (MFP_{xy} - \overline{MFP})^2 (FPP_{xy} - \overline{FPP})^2}} \tag{4.1}$$

where MFP and FPP are the respective images of the frames being compared and the bar denotes the 2D image mean. This allowed indexing of the most appropriate prescan via the highest r coefficient value. An example of this process is demonstrated in Figure 4.3. This matching process was repeated for each FPP frame and slice independently before a final reconstruction of the dataset was performed using the selected prescans as calibration data.

The proposed MFP method was evaluated in two separate groups of experiments: retrospective subsampling of fully acquired rawdata and analysis of reconstructions from accelerated acquisitions. As it is impracticable to quantitatively measure the severity of aliasing artefacts without knowledge of the true unaliased images, the preliminary retrospective work was performed to investigate the performance of MFP, including the effect of different acceleration factors and for comparison with the main categories of calibration methods. This acted as a guide to the methods adopted for the

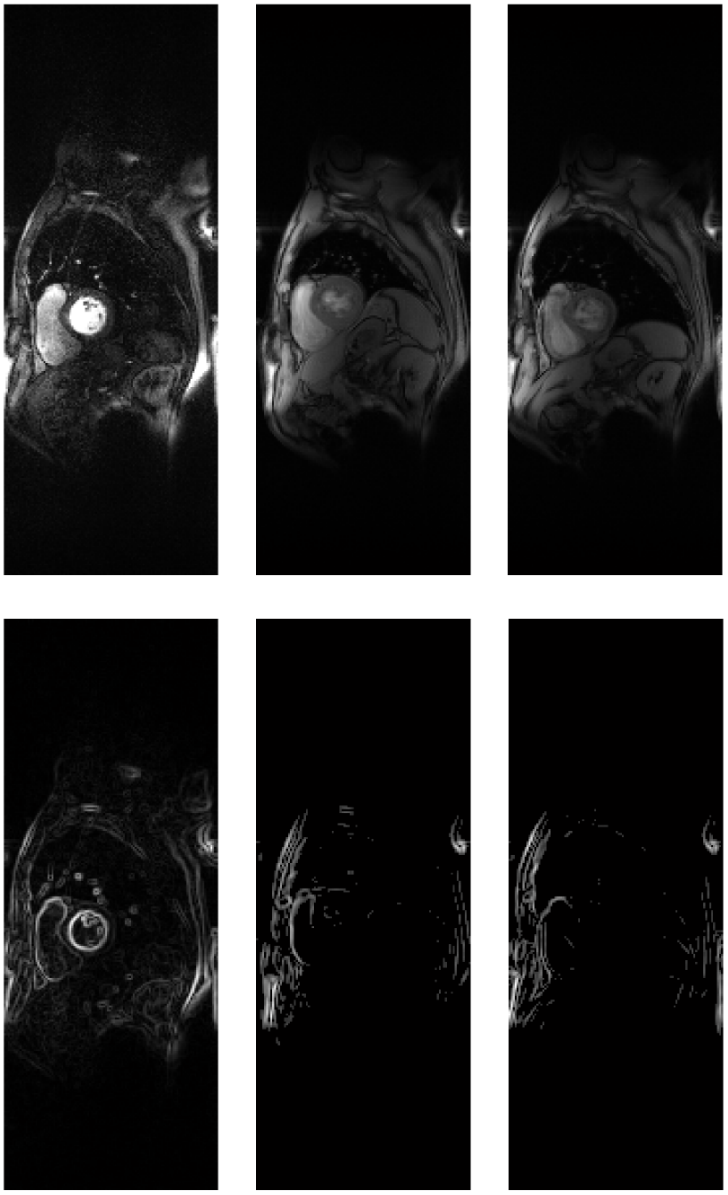

Figure 4.3.: Demonstration of the MFP matching process. An FPP frame (top left) undergoes edge-detection (bottom left). Each MFP frame (e.g., top middle) also goes through edge-detection as well as additional intensity filtering (bottom middle). Each MFP edge map is correlated with that of the FPP; the MFP edge map providing the highest correlation value (bottom right) is used to select the appropriate MFP frame (top right) for the FPP frame. This is repeated independently for all FPP frames and slices.

later prospectively-accelerated acquisition study.

In vivo Retrospective Study

Fully sampled data was acquired and then retrospectively subsampled prior to the reconstruction processes. Full k-space sampling increased the image acquisition duration, beyond that previously stated. To maintain image acquisition every cardiac cycle, the number of slices was reduced to one. The expected cardiac blurring caused by this long image time was considered immaterial to the purpose of this section of the work. This methodology enabled a numerical comparison of the PI reconstructions against the fully sampled images as a reference, primarily through use of Relative Root-Mean-Square Error (RRMSE) [Wang and Fernndez-Seara, 2006] over all N pixels,

$$RRMSE = \sqrt{\frac{\sum_{i=1}^{N} ||I_i^{reference}| - |I_i^{recon}||^2}{\sum_{i=1}^{N} ||I_i^{reference}||^2}} \tag{4.2}$$

Six fully-sampled datasets were acquired for this section of the work, each consisting of 48 images during the first-pass injection of contrast agent. The undersampled rawdata for each image was reconstructed with the Temporal (AA) and MFP methods at different acceleration factors, as well as with their equivalent Prescan and Integrated methods at rate 4 undersampling, for the comparison between these methods. AA was chosen as the representative temporal method, due to it being a common implementation. The significance of any differences was evaluated using a Wilcoxon signed rank test due to the limited sample size. The rawdata for Prescan, Integrated and MFP methods was subsampled in a regular pattern, i.e. the same for each cardiac cycle. A time-interleaved undersampling pattern was used for the data to be reconstructed by the Temporal method, as is typical for acquisitions using this PI type. The number of reference lines, N_{ref}, for Prescan, Temporal and MFP was kept the same size for each, utilising all available data (i.e. N_{ref} = number of phase-encodes). Defining R* as the nominal undersampling rate that does not take into account acquired reference lines, and R the true undersampling rate (or "acceleration factor"), the Integrated method was performed using an R* and N_{ref} chosen such that the true acceleration factor R was identical to the R of the other methods. As usual for integrated methods, the reference data was included in its final reconstruction.

In vivo Prospectively Accelerated Acquisitions

Based on the results of the retrospectively subsampled study, the following prospectively accelerated acquisition work was performed in 20 patients. The MFP method was applied to reconstruct undersampled FPP images acquired by an accelerated sequence for a direct comparison with temporal calibration methods. Imaging parameters were as previously stated, with an R=4 time-interleaved sampling scheme as used in the retrospectively subsampled study.

Quantitative comparison against a fully sampled image was no longer possible for the prospectively accelerated datasets, so a blinded visual observer scoring system was utilised. Twenty patient FPP datasets were acquired and reconstructed using the three temporal calibration techniques (defined earlier) and the newly proposed method; the four methods were labelled MA-TGRAPPA, KL-TGRAPPA, AA-TGRAPPA and MFP-GRAPPA respectively. The KL filter was set so as to retain three eigenmodes and the MA sliding window was set to a width of three fully-sampled k-space frames (i.e. a moving average of 12 frames for rate 4 undersampling), as applied in their original implementations [Ding et al., 2011] [Breuer et al., 2005].

The visual observer scoring system allowed relative assessment of respiratory PI artefacts between the various methods, while avoiding the influence of other factors affecting image quality. The reconstructed sets were anonymised and sorted into 80 randomly ordered image sessions, each containing the 3 slices per patient reconstruction. Two independent observers with experience examining FPP datasets performed aliasing artefact scoring on the sets. The datasets were assessed, purely on the basis of aliasing artefacts, on a scale of 0 (none) – 4 (severe) (see Table 4.1 for full definitions of each level, as given to the scorers). The agreement between observers was measured using a Cohen's Kappa coefficient [Cohen, 1960] (with interpretation using the work of Fleiss [Fleiss, 1981]), before final consensus scoring was performed. Assessment of agreement was also applied to repeated scoring of a subset of the methods (AA-TGRAPPA and MFP-GRAPPA), performed by the same scorers separated by a large time gap (>3 months), as further validation of the accuracy of the method. The statistical significance between the scores of each method was measured using a two-tailed paired Student's t-test.

The image SNR was also assessed for each of the four methods. A pseudo multiple replica method [Robson et al., 2008] was applied to a single frame (40th) part way after the LV first-pass, for each of the 80 datasets (20

Table 4.1.: Parallel imaging artefact scoring definitions during the blinded observer study

Score	Definition
4	Strong; *has potential to cause uncertainty or non-diagnostic quality for assessment of the myocardial perfusion.*
3	Moderate; *average level of difficulty in assessing the myocardial perfusion.*
2	Weak; *artefact visible with little impact on myocardial perfusion.*
1	Insignificant; *artefact visible but would have negligible impact on myocardial perfusion assessment.*
0	No artefact is visible.

patients, 4 methods) using 150 replicates in each case, maintaining an identical reconstruction process. In addition, for a subgroup of five datasets reconstructed with each of the four methods, each frame underwent an SNR calculation to investigate possible differences in SNR variation in time with the frame number. This was performed so as to investigate any possible increased temporal fluctuation in image SNR caused by the calculation of different GRAPPA kernels throughout the perfusion series in MFP, in comparison to the other techniques examined.

4.1.3. Results

In vivo Retrospective Study

An example frame, reconstructed using each of the Prescan, Integrated, Temporal and MFP calibration methods at R=4, is shown in Figure 4.4 as an illustration of the new technique. The corresponding RRMSEs are 0.265, 0.254, 0.155 and 0.114. Figure 4.5 shows the RRMSE in each of the 48 reconstructed frames of the same FPP example, for each method. Spikes in the error, corresponding to a mismatch between the coil profile in the prescan and reconstruction frame, are clearly visible for the Prescan method. The spikes are smoothed out over time in the Integrated example; however, an increased baseline error is present with Integrated calibration, corresponding to the SNR caused by higher R*. The Temporal calibration method shows a compromise between these two, with reduced mean and variation of RRMSE comparative to the previous two methods. As hypothesised, the MFP method shows a low error across all frames regardless of respiratory motion with a low baseline error, suggested to be mostly due to PI SNR reduction, slightly below that of the Temporal method.

The results averaged across all six FPP datasets are summarised in Table 4.2. Along with a higher mean RRMSE than MFP reconstructions, the Prescan method has a far greater mean inter-frame standard deviation than all other methods, corresponding to the changing accuracy of the coil information with respiratory motions throughout the 48-cardiac cycle FPP acquisition. The Integrated method instead has lower standard deviation but a significantly increased RRMSE due to the higher R* required to achieve the equivalent R as commented on previously. The Temporal method was the closest in overall accuracy to the MFP method, showing only slightly, though still significantly ($p<0.05$), larger errors overall. For this reason, which supported the known benefits of Temporal calibration over the Prescan

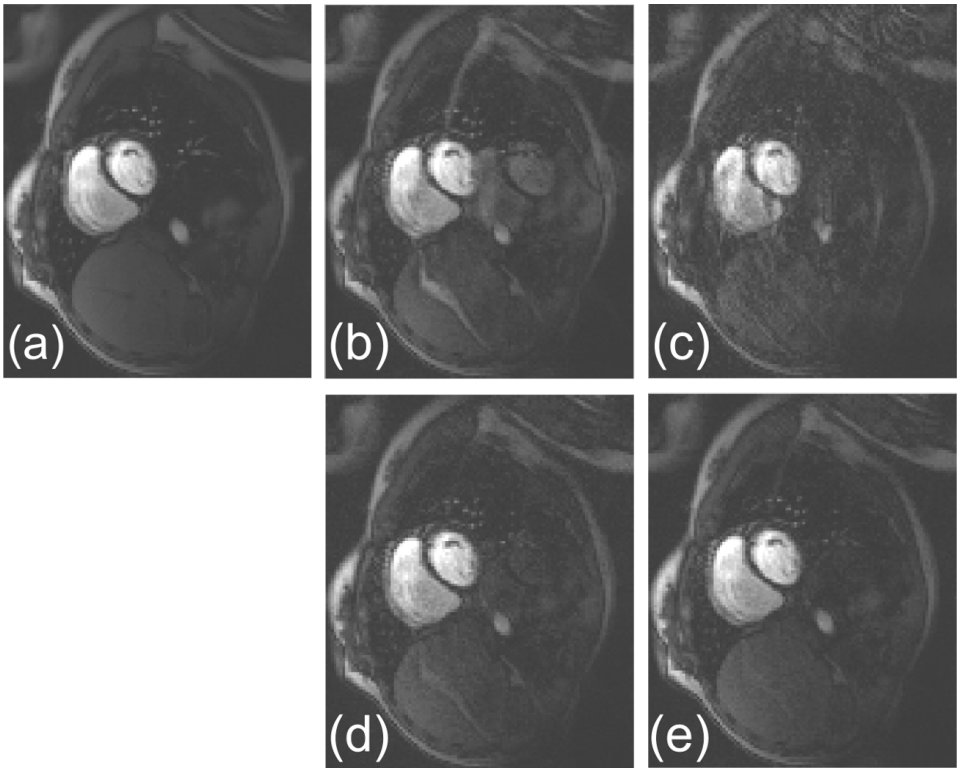

Figure 4.4.: Reconstruction of a single frame from a fully acquired perfusion dataset (a) and the corresponding PI reconstructions after rate 4 undersampling, using prescan (b), integrated (c), temporal (d), and MFP (e) calibration methods.

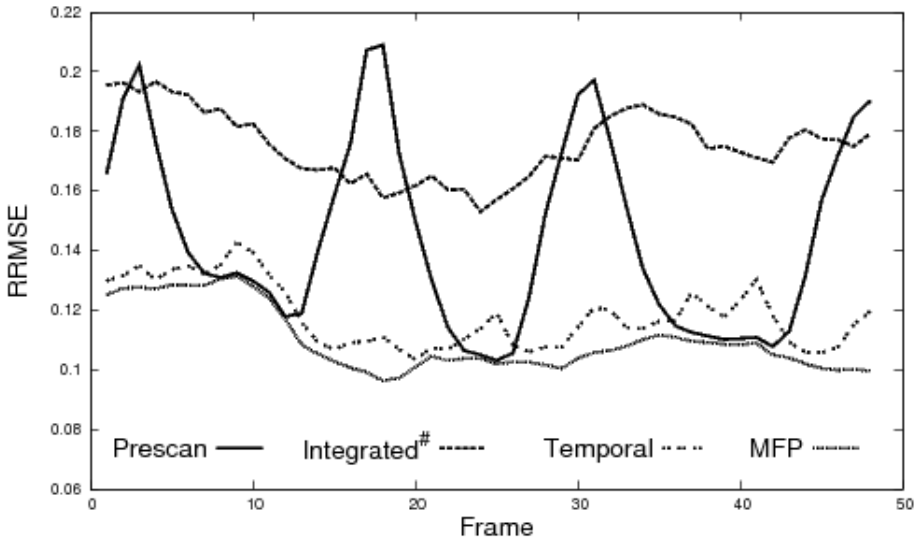

Figure 4.5.: Relative root-mean-square error for each frame of the same perfusion dataset undersampled at rate 4, using the prescan, integrated, temporal (average-all) and MFP calibration methods. The differing characteristics of the various methods are clearly visible. #Integrated method had R* and N_{ref} chosen to have an R value as close as possible to the other methods.

and Integrated methods during free-breathing, investigation of MFP from this point onwards focussed on comparison with the Temporal techniques in more detail.

Table 4.2.: Summary of retrospective study results

Calibration Method	Mean RRMSE†	S.D. RRMSE†
Prescan	0.160 ± 0.006	0.027 ± 0.005
Integrated	0.208 ± 0.017	0.016 ± 0.003
Temporal	0.145 ± 0.008	0.017 ± 0.003
MFP	0.138 ± 0.009	0.017 ± 0.003

†averaged across six patients

In order to estimate a suitable R to use for the prospectively accelerated *in vivo* acquisitions, the retrospectively subsampled datasets were reconstructed at increasing acceleration factors using the Temporal and MFP methods. Figure 4.6 shows a representative frame reconstructed in this manner. Aliasing artefacts in both methods were barely visible at the lower acceleration factors, but increased in strength with increasing acceleration factor. Whilst the SNR worsened for higher R values in both cases, as expected, the MFP method appeared to consistently suppress the PI artefacts for all acceleration factors. The mean RRMSE, which is the mean of the RRMSE over all 48 frames, was further averaged over all six FPP datasets, each reconstructed across acceleration factors 2-6. Shown in Figure 4.7, an increasing error with acceleration factor is visible for both methods, as well as an increasing divergence between the errors for each method. The increasing error values at higher accelerations, combined with concerns about lower SNR, supported the choice of R=4 as a reasonable compromise for the prospectively accelerated acquisition investigation.

In vivo Prospectively Accelerated Acquisitions

Scoring for the reconstructed datasets showed fair agreement between observers (κ=0.48) and good agreement in repetition (κ=0.62). Consensus scoring gave mean artefact values of 3.1±0.6 for MA-TGRAPPA, 3.6±0.4 for KL-TGRAPPA, 2.5±0.6 for AA-TGRAPPA and 0.8±0.4 for MFP-GRAPPA. All differences were significant ($p<0.001$), except between MA-TGRAPPA and KL-TGRAPPA. Figure 4.8 plots these results for each dataset, while Figure 4.9 shows individual example images: one where all of the methods reconstructed without significant PI artefacts, as well as a case where the Temporal calibration reconstructions showed detrimental artefacts that were cleared by the use of MFP-GRAPPA. In all of the datasets, the use of MFP produced the lowest artefact scores and left no residual artefacts that were scored as causing a significant impact on perfusion assessment, despite the sometimes extreme respiratory motion; none were judged above level 2 ("weak"), as opposed to over half of the AA-TGRAPPA reconstructed FPP series and 80% of those by the other two methods.

The mean SNR over all datasets was calculated as 26.1±0.5, 20.6±0.4, 22.9±0.4 and 25.2±0.5 for the MA-, KL-, AA- and MFP-GRAPPA methods respectively. The differences in SNR were significant between every reconstruction type ($p<0.01$). In the group of five datasets tested for temporal

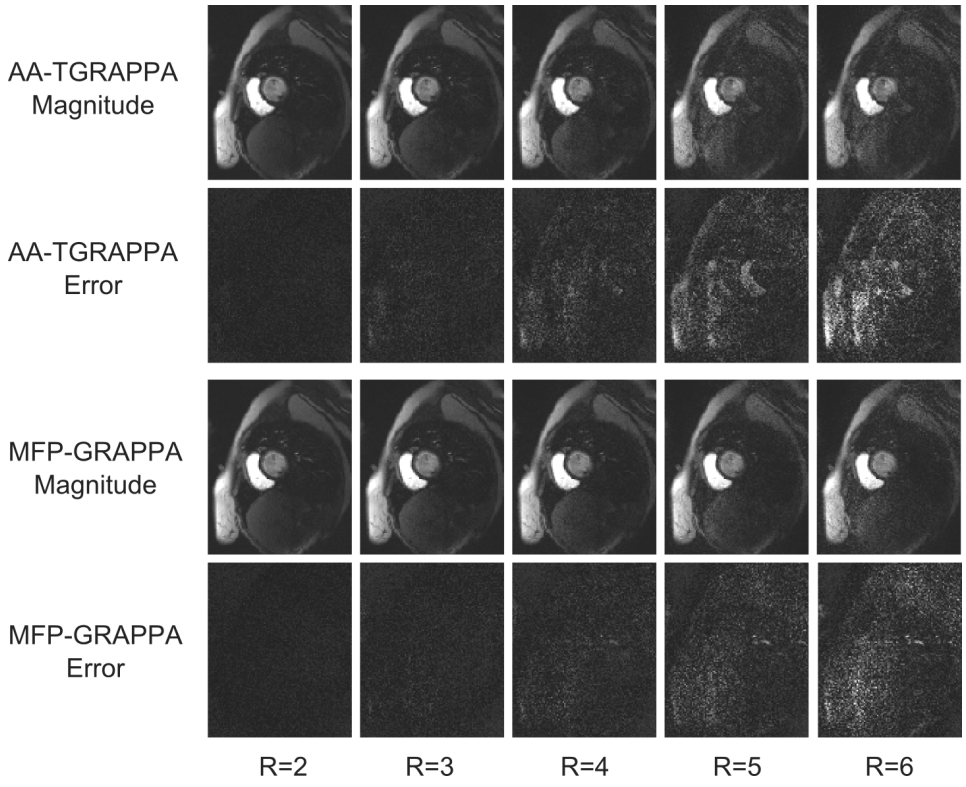

Figure 4.6.: Retrospectively subsampled AA-TGRAPPA (temporal) and MFP-GRAPPA reconstructions of a single frame at increasing acceleration factors (2−6) and their corresponding error maps in comparison to the fully sampled images. With higher R, both show expected increasing noise levels, however, MFP appears to more successfully remove aliasing errors. Intensity level of error images x4 of magnitude.

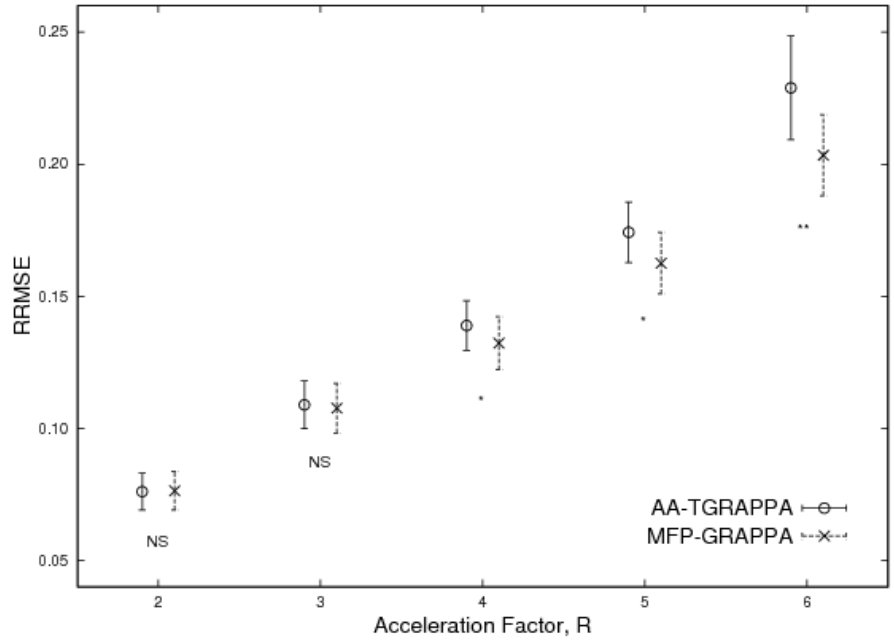

Figure 4.7.: Mean relative root-mean-square error over six 48-frame datasets, for acceleration factors 2 to 6. NS not significant. *P < 0.05. **P < 0.01 (Wilcoxon signed rank, n = 6).

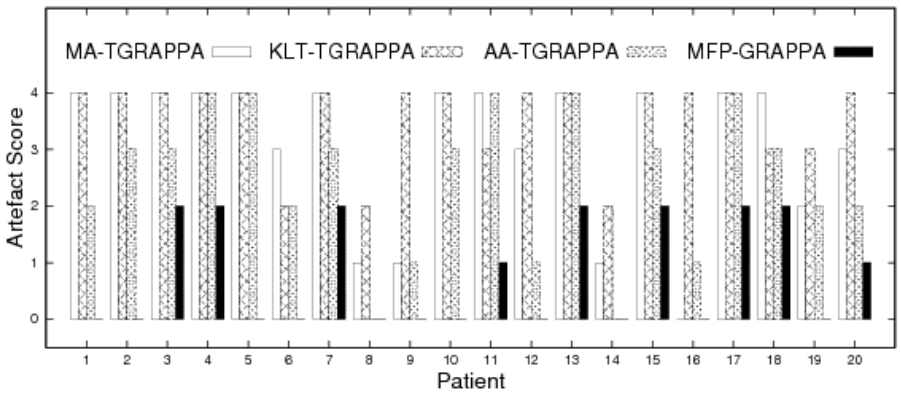

Figure 4.8.: Comparison of consensus visual observer scores of parallel imaging induced artefacts (ranging from 0 to 4) in prospectively accelerated FPP datasets reconstructed with MA-TGRAPPA, KL-TGRAPPA, AA-TGRAPPA, and MFP-GRAPPA.

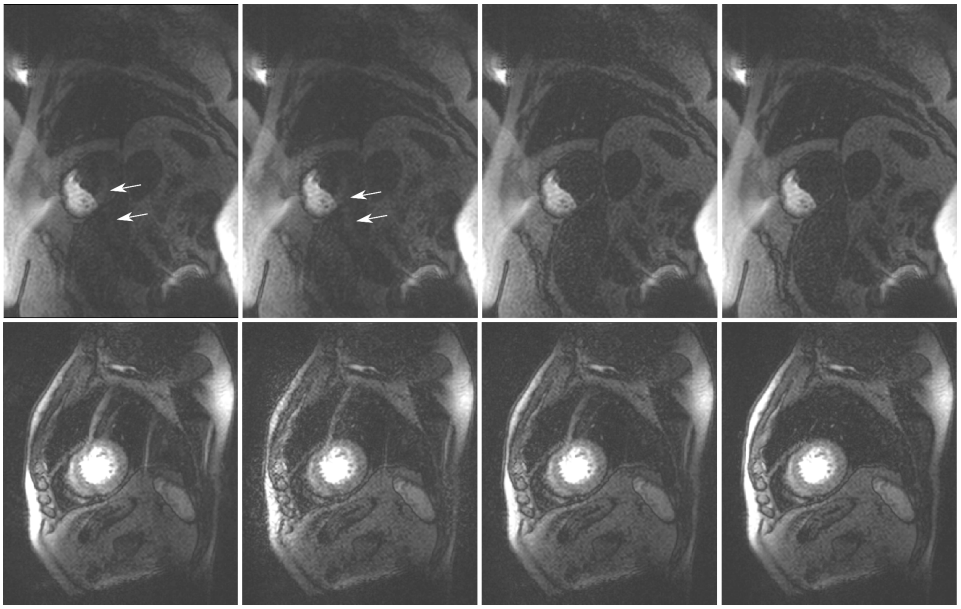

Figure 4.9.: Example FPP frames from two datasets, reconstructed with (from left to right) MA-TGRAPPA, KL-TGRAPPA, AA-TGRAPPA, and MFP-GRAPPA. The top row gives an example from a dataset where all reconstructions performed to a high standard, with only minor artefacts, indicated by arrows (patient number 14 from Figure 4.8). In the bottom row (patient 5), the implementations of TGRAPPA show an artefact, passing through the heart, which was cleared by the use of MFP-GRAPPA.

variation in SNR, the standard deviation of the SNR over the frames was 1.54±0.35, 1.37±0.35, 0.99±0.28 and 1.16±0.31 as ordered previously.

4.1.4. Discussion

The first set of results based on retrospectively subsampled datasets confirmed the potential of the MFP idea and confirmed the prediction that, of the established techniques, the use of temporal calibration was the best compromise between accurate coil information and preservation of SNR .

The second stage, with prospectively accelerated datasets, showed the improved performance of the MFP method in comparison to a range of temporal calibration techniques. The AA method performed best out of the temporal methods investigated, with insignificant differences between KL and MA, as measured by the applied scoring system. The SNR performance of the temporal methods matched expected relationships (KL<MA [Ding et al., 2011] and AA<MA [Ding et al., 2015]). For this setup (acquisition of MFPs at full resolution, etc) the MFP method appeared to maintain SNR in comparison with the temporal methods, alongside its improved artefact suppression performance. A potential explanation for this is that artefacts due to motion in the reference data from temporal averaging can lead to additional noise enhancement in the reconstructed images [Blaimer et al., 2011], which was avoided through use of prescans as in MFP. Only minor differences were found, within error, in the variation of SNR across the frames for MFP in comparison to other methods; potential frame-to-frame variable SNR arising from variation in the GRAPPA kernel in the MFP method, appeared to be insignificant in this work in comparison to the temporal methods.

There are a few points to consider regarding the implementation of the MFP technique in this work, suggesting required adaptation or potential limitations in more general settings. The use of a SGRE sequence gives a reliably bright anterior chest wall signal and the matching algorithm utilises this feature. Different sequence types (such as bSSFP with frequent off-resonance "dark-banding" in the chest wall fat) may require modification to the thresholding value used or remodelling of the algorithm to maintain accuracy, and this has not been investigated. Finally, with regards to edge detection methods, a Sobel filter was chosen as it is a simple, computationally cheap method that gave robust results in this implementation. Investigation of other filters may be worthwhile if reduced accuracy is observed during

application to other scenarios.

A practical disadvantage of the MFP method is the requirement for an additional preceding scan, of reasonable duration, for the collection of the MFP reference data. An optimal duration for this prescan was not explored, which would likely consist of a compromise between capturing a sufficiently large respiratory range and unnecessarily extending the total MR examination time. It is proposed that future work could establish the effect that the number of respiratory cycles covered by the prescans has on the reconstruction accuracy, as this work perhaps used an unnecessarily long duration to collect the MFPs (i.e. 48 images / slice, which was chosen to be the same as for the FPP run for simplicity).

Among the potential limitations of the method, the most vulnerable assumption is that there will always be a prescan at a similar enough respiratory position to provide accurate coil information for each frame of the main scan. This requires the patient's breathing during the main scan to not extend past the extremes of inhalation or exhalation covered during the acquisition of the MFPs. This could be invalidated by unexpected changes in breathing, and also by bulk motion of the patient between MFPs and the main scan. In general though, as long as the same conditions are present in both scans, e.g. the inducement of stress, reasonably similar ranges would be expected. As the breathing pattern itself need not be similar as long as the respiratory range of the undersampled acquisitions is covered in the prescans, the increased range could be artificially induced if required, i.e. requested from a co-operative patient before the stress scan began.

On the aspect of computational efficiency, the matching method also required the images to be first reconstructed through a standard PI method. The reconstruction time in this instance is therefore approximately increased by a factor of 2, plus the duration of the matching algorithm, which with a non-optimised implementation for this work was in the order of a couple of seconds. With the computationally fast basic PI methods currently available, it is therefore believed using this method would not require excessively long reconstruction times. Incorporation into more advanced PI techniques that already have long reconstruction times might require alteration to use a more efficient initial reconstruction for use in the matching step. It is worth noting that many recent PI algorithms already make use of initial or multiple reconstructions (e.g. [Lustig and Pauly, 2010] [Chang et al., 2012]) and so this method could potentially be combined efficiently with such techniques.

Reliability is important in FPP; due to studying the first-pass of a contrast agent, repetition of this scan would require at least a 20 minute delay for contrast-agent washout, and may also reach the maximum permitted total dose in the short-term, which would require rescheduling of the patient's perfusion test. The breathing instructions provided to the volunteers were an attempt to mimic the breathing response likely in stress-induced patients, in order to test the robustness of the MFP method. Such deep breathing may not occur in all stress FPP patients but was a reasonably realistic model of a common side-effect of adenosine stress. If in any patient breathing motion were to occur as in the extremes of this study, there would probably be difficulty reporting all acquired myocardial segments with high confidence when using the temporal methods, especially at increased acceleration factors, which was improved by the use of MFP. In this work, a large variation in patient response to the breathing instructions was seen, giving a wide range in artefact levels for Temporal reconstructions, as observed in the scoring study. It is suggested this variation of voluntary response is a reasonable reflection of the variation in patient breathing seen under pharmaceutical stress.

Examination of the 'temporal' calibration techniques in this work was restricted to the k-space based implementations; this was due to the potential temporal-smoothing effects of the low-pass filter mentioned previously, which would complicate analysis of comparative performance. The use of a low-pass filter method is not expected to perform significantly better in either reducing parallel imaging artefacts or retaining SNR [Ding et al., 2011]. The reconstruction algorithm was also limited to a GRAPPA implementation, chosen as a common PI technique that avoids any unintentional bias arising from the method of coil sensitivity map generation, though MFP could theoretically be equally applicable to image-domain techniques. The aim here was a first demonstration of the ability of this technique to provide accurate coil profile information for calibration.

Improved calibration appears to allow increased acceleration factors for free-breathing FPP, however SNR still causes loss in image quality at acceleration factors $\sim>4$.

4.1.5. Conclusions

In conclusion, an alternative method has been proposed for compensating against the effect of anterior coil movement due to free-breathing on parallel

imaging coil calibration. It was suggested that, by extension of prescan acquisitions to cover the entire respiratory cycle, improved coil information via a matching process could be used to reduce parallel imaging aliasing errors in reconstructions. A method for achieving this was presented and applied across short-axis myocardial first-pass perfusion datasets with successful reduction in respiratory-related aliasing artefacts during deep breathing without reduction in SNR or temporal resolution, and even potentially enabling higher acceleration factors. Whilst robustness to free-breathing is improved at higher acceleration factors using this technique, SNR loss is an inevitable consequence of standard PI methods and SNR degradation of the images is very high for the higher acceleration factors examined.

The MFP approach was investigated as a potential method that might be extended for application to 3D FPP. However, with the choice of SOS as the sequence trajectory and from later work in the thesis indicating that many other factors in the optimisation of 3D SOS and its reconstruction required more investigation, the potential of MFP was not explored further.

4.2. A Compressed Sensing Reconstruction Method

To enable reconstruction of the highly accelerated pulse sequence required for 3D FPP, a compressed sensing method for combination with the SOS sequence design was necessary.

Through a collaboration with the University of Utah, access was gained to a MATLAB implementation of one such type of reconstruction. Variations on this implementation are also currently in the public domain[2]. A brief overview is given next of this technique in general, followed by its application in 3D FPP SOS.

4.2.1. Spatio-temporally Constrained Reconstruction (STCR)

As detailed in Section 2.3.4, early 3D whole-heart FPP investigations included the use of compressed sensing reconstructions by Adluru *et al.* [Adluru et al., 2009][Chen et al., 2012][Wang et al., 2014b]. The method can be implemented using a single temporal constraint, known as a temporally constrained

[2]https://github.com/edibella/Reconstruction [Tian et al., 2017]

reconstruction (TCR), or with both spatial and temporal weighting - a spatio-temporally constrained reconstruction (STCR).

Reconstruction is performed by an iterative search operation seeking minimisation of the cost function, C, defined as

$$C = \phi(\tilde{m}) + \psi(\tilde{m}) \tag{4.3}$$

where ϕ and ψ are the data fidelity and constraint terms respectively, with $\tilde{m}$ the estimated image data. The fidelity term is

$$\phi(\tilde{m}) = \| WF\tilde{m} - \tilde{d} \|_2 \tag{4.4}$$

as described previously (Section 2.3.4), with F being the Fourier transform, W the undersampling pattern and $\tilde{d}$ the acquired k-space data. The constraint term for the STCR implementation[3] is given by

$$\psi(\tilde{m}) = \alpha\times \| \sqrt{\nabla_t \tilde{m}^2 + \varepsilon} \|_1 + \beta\times \| \sqrt{\nabla_x \tilde{m}^2 + \nabla_y \tilde{m}^2 + \varepsilon} \|_1 \tag{4.5}$$

where ∇_t is the temporal gradient operator, and ∇_x and ∇_y are spatial gradients in the x and y direction respectively (the in-plane image axes). α and β are separate weighting factors for the temporal and spatial components of the constraint. ε is a small positive constant to avoid singularities in the calculation [Acar and Vogel, 1994]. This minimisation of the cost function is equivalent to Equation 2.3 for compressed sensing, with the gradient operators, sometimes referred to as total variation operators, acting as the sparsifying transform for this reconstruction.

Methods for solving such minimisation problems are complex and beyond the scope of this thesis. [Samsonov et al., 2004] describes the Projections Onto Convex Sets(POCS)-based technique that was used in this implementation. POCS is an iterative approach, starting with an initial estimate for the image and performing updates on the image each iteration whilst applying the chosen constraints. In the POCSENSE technique [Samsonov et al., 2004] used here, information on the coil sensitivities is also applied during this process, in effect combining some parallel imaging capabilities into the reconstruction process.

[3]The constraint term for TCR is the same, but with spatial terms set to zero.

4.2.2. Application of STCR for 3D SOS

Various types of spatio-temporally constrained reconstructions have previously been applied to FPP using both 2D radial [Adluru et al., 2009] and 3D SOS [Chen et al., 2012] acquisition sequences. This gave some initial confidence in its general applicability for whole-heart FPP project. Differences in the exact implementation of STCR and of the sequence to which it is being applied still need to be considered, and are discussed next.

The iterative reconstruction procedure involves the repetitive forward and inverse Fourier transform of the data. For non-Cartesian data, such as that arising from the SOS sequence, traditional FFT techniques cannot be used directly (as discussed in Section 2.6.2). The non-uniform fast-Fourier transform (NUFFT) [Fessler and Sutton, 2003] and its inverse can be used, which combines a gridding interpolation and FFT each time it is applied. Alternatively pre-interpolation of the data can be performed prior to the start of the iterative process, allowing the faster rectilinear FFT and iFFT to instead be used during each iteration. Various pre-interpolation methods exist, which have been shown to accelerate the iterative reconstruction time by a factor of $\sim$6 comparative to use of NUFFT (for a 2D dataset with fixed parameters) [Tian et al., 2017]. The NUFFT and '3-point' pre-interpolation method (described in [Tian et al., 2017]) were each used at different stages of this thesis.

The inclusion of coil sensitivities into the STCR framework is a relatively recent addition, with its only previous application in 2D ungated FPP [Likhite et al., 2016]. The use of a radial sequence design avoids some of the previously described issues in acquiring calibration data for coil sensitivity information (Section 4.1.1), because low resolution data with reduced and diffuse aliasing can be generated by extracting the central region of radially acquired subsampled k-space data. Using the coil images produced through a basic reconstruction of this low resolution data, the coil sensitivity information can be extracted - in this case using the "Walsh" method [Walsh et al., 2000]. This is a possible area where the MFP method previously described (Section 4.1.2) could feasibly be included into the reconstruction in future work.

New to this particular implementation was the addition of an optional total variation constraint in the through-plane (slice) direction, similar to those used in-plane. As there are only relatively gradual changes (e.g. of the myocardium) in this direction, the differences in this direction could

potentially be small enough to act as a constraint to assist the reconstruction. By applying a further constraint in this direction with its own weighting factor, γ, a complete 4D spatio-temporally constrained reconstruction was achieved.

The weights of these separate constraints varied in this thesis depending on the precise topic under investigation. Weights were chosen either through experimental approximation based on visual analysis, or through more advanced methods (see Section 5.3.2). Previous literature shows that weightings tend to remain fairly consistent over different subjects for a given application [Adluru et al., 2009].

Likewise, the number of iterations used varied throughout the project, with initial work using a high number to ensure good convergence of the solution. An example 3D SOS FPP *in vivo* image is shown in Figure 4.10 after varying numbers of STCR iterations at fixed weight values. Initial iterations appear "blurred" due to the high degree of angular undersampling, which is slowly compensated for by the reconstruction process. For this particular weighting factor, little difference is seen between the image reconstructed after 100 iterations and that reconstructed after 200 iterations, potentially suggesting that the process could have been terminated at an earlier stage (see further examination of this in Section 5.3.2).

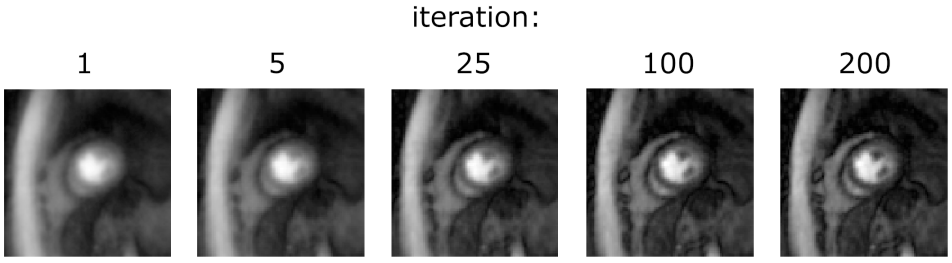

Figure 4.10.: Effect of iteration number on STCR reconstruction. An example slice of a 3D SOS FPP *in vivo* dataset, reconstructed with increasing number of iterations.

4.3. Motion Tolerance in Compressed Sensing

4.3.1. The Impact of Motion on STCR

Compressed sensing techniques that utilise constraints across time rely on the ability to extract sparsity in this dimension (see Section 2.4). The total variation (TV) constraint produces this sparsity by, in effect, taking the

difference across images in time. Local variations in image intensity with time due to first-pass arrival of the GBCA are unavoidable in FPP methods. Furthermore, for the aim of free-breathing acquisitions, respiratory motion has a strong impact on the global TV sparsity.

The initial 3D SOS FPP investigations in this thesis (Sections 5.1 & 5.2) applied STCR as part of a "breath-held" protocol, requesting that the subject should hold their breath for GBCA arrival followed by gentle breathing when the breath-hold can no longer be maintained. As free-breathing 3D FPP acquisitions are a stated aim of the thesis, this section examines the potential impact of motion on the STCR reconstruction.

First, consideration is made of the effects of motion and sudden changes in image contrast on the TV constrained STCR method, before a technique is tested that has previously been proposed to aid the reconstruction in such situations where the temporal sparsity is reduced.

4.3.2. Temporal Variation Effects: a "Step Test" Illustration of Temporal Constraints

For readability, the methods and results of this brief demonstration are included together within this section, rather than with a formal division.

A method was developed to test the ability of STCR to cope with a simple, clear intensity change. A dataset was acquired that would allow the effects of a single sudden change in global object intensity to be examined.

A small modification was made to the SOS sequence so that the saturation pulse would only be applied to the first 20 image acquisitions, after which the acquisitions would continue as previously but without any saturation. A uniform phantom (Phantom B) was scanned using this SOS sequence, with other parameters kept as their default values (Section 3.2.6). 40 measurements were acquired in total.

The sudden saturation change aimed to provide a dataset with a consistent low object image intensity for half of the acquisitions, before immediately switching to a new higher intensity for the remaining acquisitions. A plot of this intensity with time should therefore produce a step-like response. This intensity change is similar to sudden changes that could be expected from contrast agent arrival, but could also represent sudden pixel intensity changes due to respiratory motion shifting the location of bright signal within the image.

Reconstruction of the dataset was performed using three methods: pre-interpolation 'gridding' without STCR, STCR with a standard temporal weighting (3×10^{-4}), and STCR with a stronger temporal weighting (3×10^{-2}). These weightings were chosen based on reconstructions of separate *in vivo* datasets, selected so as to give reconstructions that were deemed to give reasonable suppression of undersampling aliasing but without obvious effects on the temporal dynamics (standard weighting) and reconstructions that gave an exaggerated effect on the temporal dynamics (strong weighting). The gridded reconstruction should show accurate temporal fidelity, against which the STCR reconstructions could be compared. The pixel mean was calculated for an ROI in the centre of the phantom of each reconstruction, to produce frame-by-frame intensity plots. The averaging over pixels within the ROI was performed to compensate for small in-plane signal variations caused by the rotating angular undersampling.

Figure 4.11 shows these plots for the three reconstructions. The step response of the image intensity appears in the gridded reconstructions as expected (Figure 4.11a). For STCR with weaker temporal constraint (Figure 4.11b) the temporal response matches closely to the gridded case, with only small deviations away from the baseline intensity levels visible for a few frames either side of the step. With the stronger temporal weighting (Figure 4.11c) a far more pronounced effect is seen. The corners of the step are partially clipped and frame-to-frame ringing appears to be created either side of the step.

This case is an extreme test of the reconstruction's ability to retain temporal dynamics, as the "input" is a perfect step change. The fact that a reasonable response is demonstrated with a weak temporal weighting factor is reassuring for the use of STCR in the application of 3D FPP, when applied cautiously. The distorted response at a stronger weighting factor perhaps gives an insight for the possibility of detrimental temporal effects with this method and serves as a warning to ensure a reasonable choice of temporal constraint weighting for *in vivo* work.

A method for potentially reducing these effects is introduced next, examined alongside investigation of temporal effects of STCR *in vivo*.

4.3.3. Constraint Reordering Theory

A method, referred to here as 'constraint reordering', has previously been proposed for reconstruction methods that employ total variational (TV)

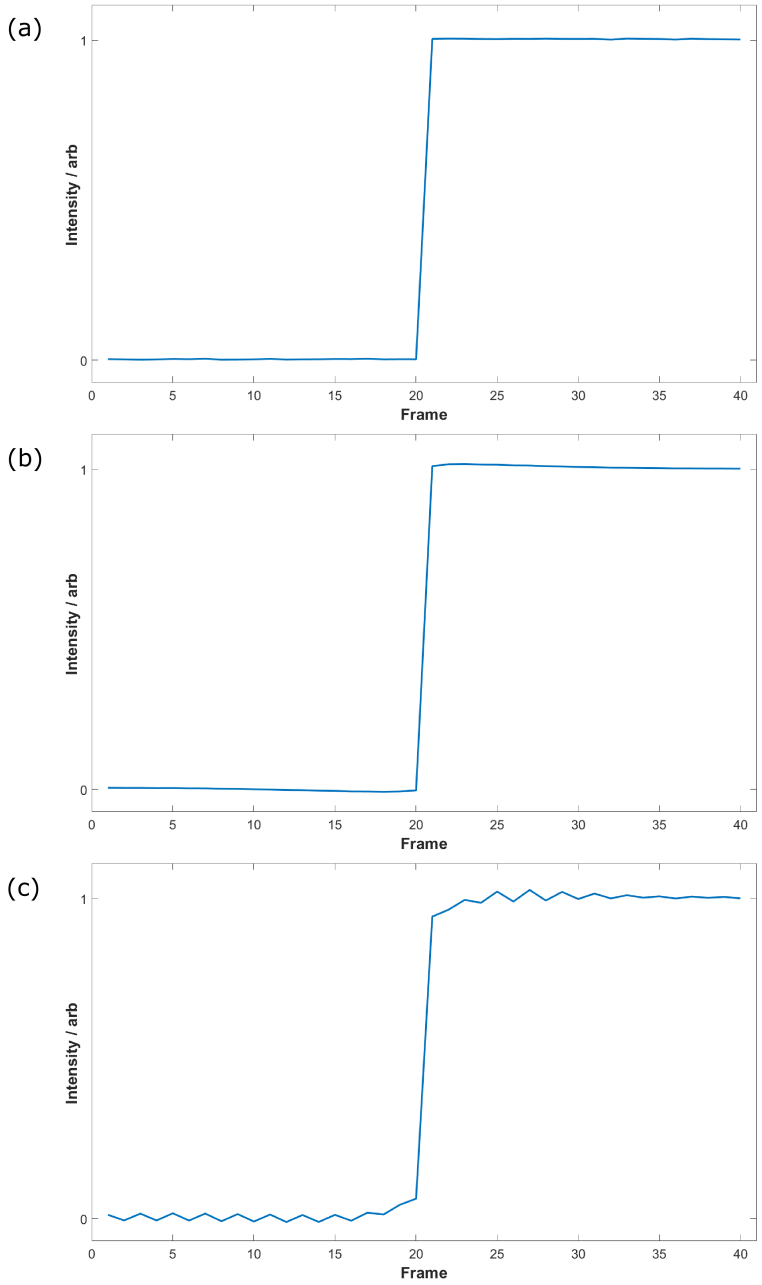

Figure 4.11.: Temporal response 'step-test'. The changing mean signal intensity in a phantom imaged across 40 frames, with a sudden change in the saturation after 20 frames. The dataset is reconstructed with gridding (a), STCR with a typical temporal weighting (b) and STCR with a strong temporal weighting (c). Changes in the intensity step-response can be seen to be dependent on the STCR temporal weighting.

constraints such as STCR [Adluru and DiBella, 2008]. It aims to improve the reconstruction process in the presence of motion or some other non-smooth temporal intensity change. This method was investigated here for its application to 3D SOS FPP, with the aim of improving image quality and robustness to free-breathing motion.

TV-constrained reconstruction methods have been shown to perform with a very high level of accuracy in idealised scenarios, whereby the image set contains signals that vary smoothly across the direction of the constraint or that can be described as "piece-wise constant" [Candes et al., 2006]. MR images in general do not fit this latter definition and both the GBCA arrival and respiratory motion in FPP datasets reduce the smooth variation of the signal across time. The constraint reordering method (CRM) proposes modification to the data order during the calculation of the TV constraint, with the aim of making the data monotonic and smoothly varying (Figure 4.12). By reordering of the data for the calculation of the constraint, the reconstruction should operate on data which is closer to satisfying the ideal conditions for STCR, and therefore improve final image quality, particularly in datasets that include large amounts of motion.

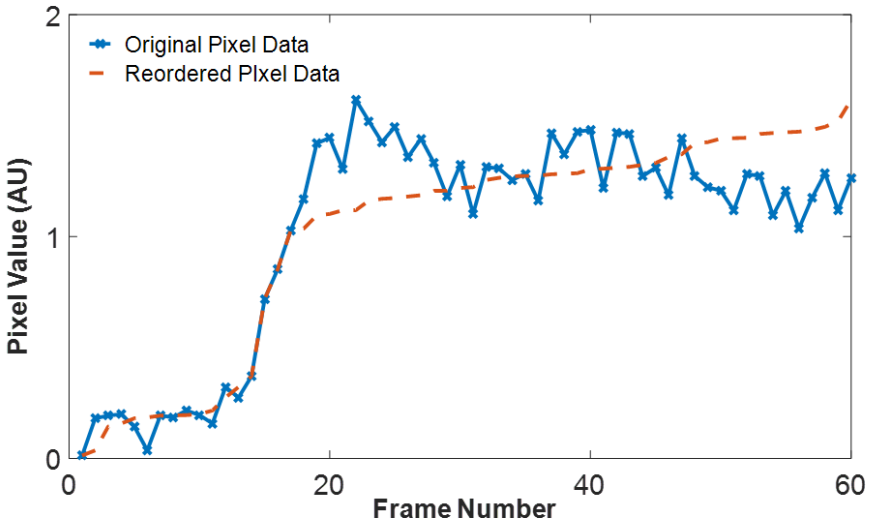

Figure 4.12.: Pixel value reordering. An example of how the reordering of a pixel value, here selected in the LV myocardium, across time can make the signal values more smoothly varying and monotonic. This reordering principle can be applied independently to all image-domain pixels prior to the application of a temporal constraint.

The implementation of the CRM can be represented by the introduction of a reordering matrix, P, which is a permutation matrix (i.e. a square matrix with a single 1 value in each row and column, with 0 values in all other locations). The constraint term of the cost function to be minimised can then be modified from the version in Equation 4.5:

$$\psi(\tilde{m}) = \| \sqrt{\nabla \tilde{m}^2 + \varepsilon} \|_1 \tag{4.6}$$

to

$$\psi(\tilde{m}) = \| \sqrt{\nabla (P\tilde{m})^2 + \varepsilon} \|_1 \tag{4.7}$$

with these equations generalised for any dimension(s).

This reordering method has previously been demonstrated for 2D Cartesian multi-slice FPP datasets that were retrospectively subsampled from fully-sampled acquisitions [Adluru and DiBella, 2008]. Figure 4.13 demonstrates the potential for constraint reordering from that work. A TV-constrained reconstruction is demonstrated in both an ideal simulated piece-wise constant dataset and in a retrospectively subsampled *in vivo* dataset, where the constrained reconstruction is non-ideal. The potential for constraint reordering to improve the reconstruction is then shown.

Calculation of P in the original publication [Adluru and DiBella, 2008] was taken from the pixel value order in the fully sampled images, to provide a best case scenario, that would not be available in a real application of undersampled acquisition. Whilst investigation of the effect of random perturbations on this ordering showed reasonable robustness to incorrect ordering, the ability to adequately estimate P using undersampled data has not previously been tested.

Therefore this thesis work continued by investigating a version of the CRM for use with the 3D SOS FPP undersampled acquisitions.

4.3.4. 3D SOS FPP Constraint Reordering: Methods

Modification was made to the pre-interpolation '3-point' implementation of STCR for inclusion of constraint reordering along the temporal dimension. The temporal dimension was chosen for investigation because respiratory motion most strongly reduces the sparsity of the data in this direction.

The 'gridded' aliased image data, $\tilde{m}$, was reordered prior to the total variation calculation in the POCS-based algorithm, with the resulting image

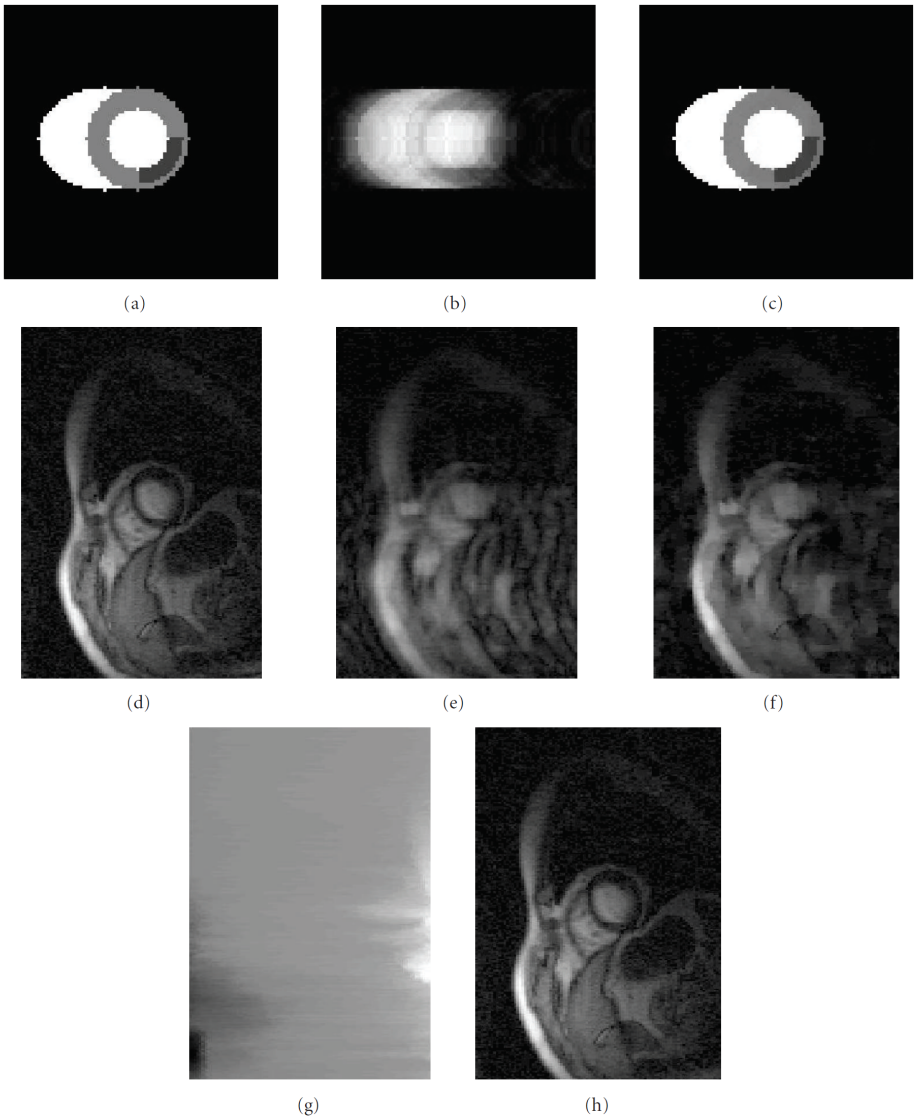

Figure 4.13.: Constrained reconstruction with and without optimised constraint reordering. A piece-wise constant dataset is shown in the top row, reconstructed by FFT from fully-sampled data (a), reconstructed by FFT from subsampled data (b) and reconstructed by a TV spatially-constrained reconstruction from subsampled data (c). The corresponding reconstructions for *in vivo* data are shown (d-f). Whilst the CS reconstruction was able to accurately reconstruct the simulated data, poorer quality is seen in the reconstruction of the *in vivo* dataset. By applying a row-reordering scheme (see [Adluru and DiBella, 2008] for details) (g), an improved spatially-constrained reconstruction was achieved (h). Reproduced from [Adluru and DiBella, 2008].

update term then returned to its original temporal ordering. As $\tilde{m}$ is complex, this reordering (and the application of the constraint) was applied separately for the real and imaginary components. Estimation of the correct temporal ordering for each pixel was performed using a coil combination of the initial gridded images as a prior, from which the pixel value ordering could be calculated.

Five free-breathing 3D SOS FPP datasets that had been acquired as part of a separate investigation (Section 5.3) were used for this study.

An initial test compared the standard STCR implementation with a STCR+CRM that used an identity matrix for reordering (i.e. no reordering), to confirm the equivalence of these two methods. These two reconstructions should be the same, with re-ordering set to simply copy the original order of pixels, and was performed as a basic test of the new implementation.

STCR reconstructions both with and without the additional constraint reordering step were performed on the five datasets for comparison of the two reconstructions. Reconstructions were performed with both 'standard' ($\alpha = 3 \times 10^{-4}$) and 'strong' ($\alpha = 3 \times 10^{-2}$) temporal weightings, as applied in Section 4.3.2. Other parameters were held consistent throughout: N=200 iterations and spatial weightings (β and γ) = 0, to isolate temporal effects.

Analysis of image quality, particularly with respect to temporal dynamics, was complicated by the inability to compare the images with those from fully acquired datasets, which is the most common technique for analysing reconstruction methods. However, as stated before in this thesis, such fully sampled data is not possible for 3D FPP as it would require an acquisition duration of almost an entire cardiac cycle per frame. As the only practicable option, reconstructions with strong and moderate (standard) temporal weightings were hoped to separately provide an estimate of reasonable reduction of undersampling artefact and maintenance of accurate temporal dynamics respectively. The image quality of individual frames were compared for the introduction or reduction of any obvious artefacts by visual analysis. Temporal dynamics were investigated by examining the change in a line profile across time (so called "x-t" space) for a single spatial slice of each reconstructed image set. The in-plane (x) position of the line profile was manually chosen so as to cut through regions of interest that would be expected to undergo respiratory motion and prominent contrast-agent variations (e.g. chest-wall, LV-myocardium, etc).

4.3.5. Constraint Reordering Results

Firstly, the results of differing temporal weightings without any re-ordering are described: The two STCR weightings were chosen so as to provide examples of a standard and a strong temporal constraint in the non-reordered reconstructions, which were seen in the corresponding output image sets (Figure 4.14). By visual inspection, both of these STCR reconstructions provided clearly improved in-plane image quality over the gridded reconstruction, as expected, but with the strong weighting cases demonstrating a noticeable alteration in the temporal characteristics. The chest wall and organs that undergo motion due to respiration appear more static in the strong STCR reconstructions. With closer inspection, the standard weighting STCR reconstructions also showed this effect compared to the gridded non-STCR reconstructio, although to a reduced extent. By plotting a line through the chest-wall in the datasets and examining its variation over time, this motion suppression effect can most clearly be displayed (Figure 4.14).

The reordered reconstruction with use of an identity matrix for reordering provided identical reconstructions to those produced by the original non-reordered STCR algorithm, which verified the equivalence of the two implementations.

The reordered reconstructions that used the estimated reordering matrix P enabled the signal intensity to vary monotonically with "reordered time" (Figure 4.15), which would be expected to reduce the temporal contribution to the total variational (TV) cost calculation (i.e. produce a higher degree of sparsity).

The images produced by the reordered reconstruction were of similar in-plane quality to those of the non-reordered reconstructions. Consistency between the reconstructed datasets varied, dependent partly on the degree of respiratory motion. In some cases, mild improvement to apparent motion blurring could be seen (Figure 4.16), but was only visible in a small number of the datasets. An increase in artefacts was also sometimes visible with reordering, particularly in frames that varied with sudden motion from the surrounding frames (e.g. Figure 4.17).

The temporal dynamics of the reconstructed datasets most clearly demonstrated the potential changes delivered by the reordered reconstructions (Figure 4.18). Examination of a line profile across time, (x-t) space, showed the deviation of the temporal dynamics in the various STCR reconstructions comparative to the gridded reconstruction. For the gridded reconstruction,

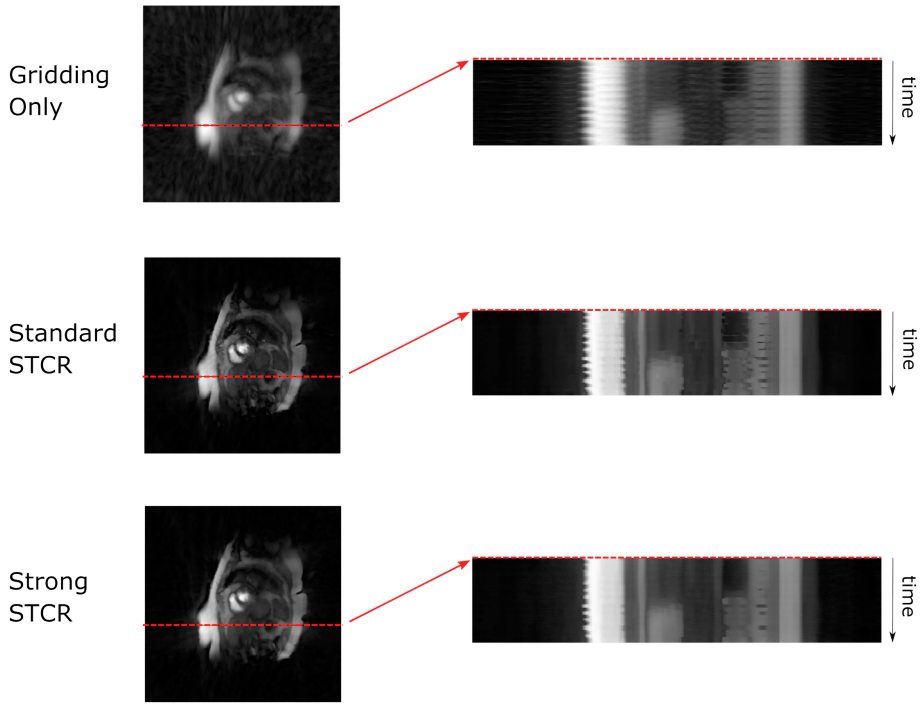

Figure 4.14.: Motion suppression with STCR. Demonstration of observed apparent motion suppression with the STCR algorithm, shown for the 'standard' and 'strong' temporal weight values. A single slice and frame of the reconstruction is shown on the left, with a line profile across the chest wall for each image at the same spatial position (red line). The temporal variation in this profile is plotted for the series of frames, on the right. This shows the "suppression" of motion by strong temporal weights.

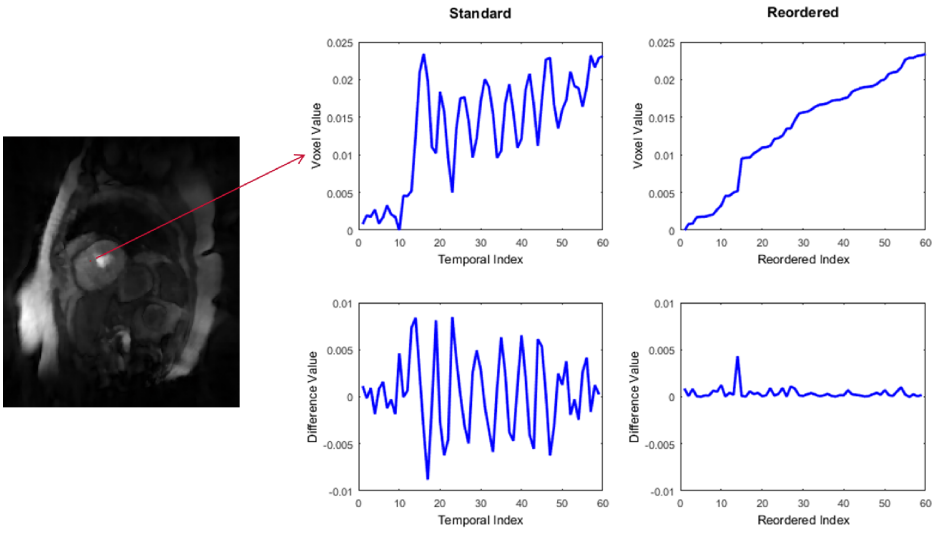

Figure 4.15.: Pixel reordering in a free-breathing dataset. The effect of respiratory motion on a pixel value within the myocardium, and on the sparsity of the temporal difference is demonstrated for a standard method (left). With application of reordering (right) there is potential to greatly smoothen this variation, which corresponds to an increase in the sparsity of the difference calculation.

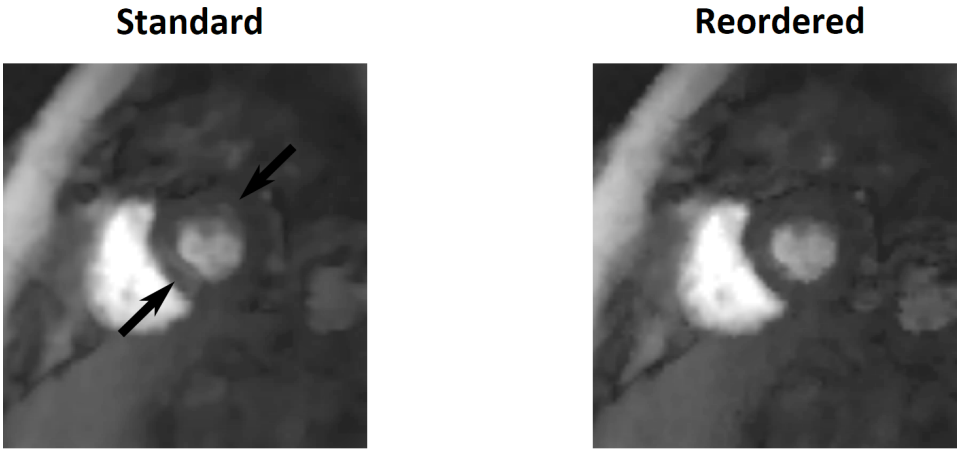

Figure 4.16.: Example of improvement with CRM. Artefacts in the myocardium of a slice reconstructed with a standard implementation of STCR are seen to be improved in this example by the application of the reconstruction with inclusion of CRM.

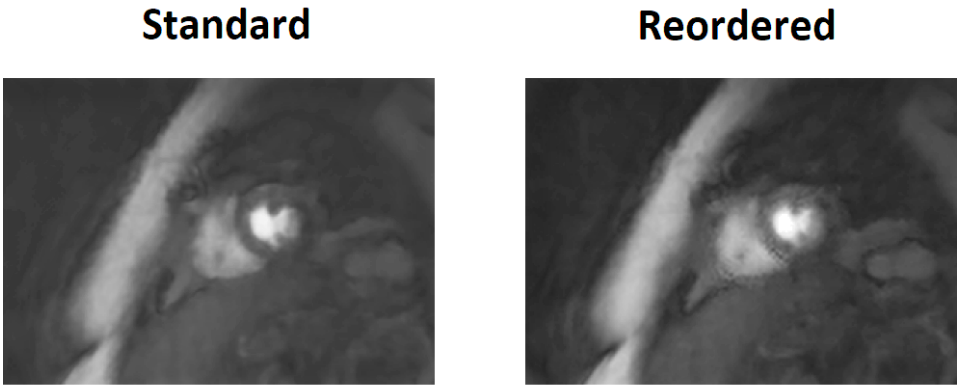

Figure 4.17.: Example of artefacts with CRM. A degradation in image quality is seen in this example with application of CRM compared with the standard STCR implementation.

respiratory-induced temporal variation of the signal was clearly visible. In both non-reordered STCR reconstructions (standard and strong TV weighting), this variation was reduced; the signal variation was still somewhat present for the "standard" weighting but almost entirely smoothed with the "strong" temporal weighting. The intensity variations in separate spatial regions corresponding to different tissues (e.g. blood-pool, myocardium) across the profile also seemed to be smoothed with the strong weighting. The reordered implementation of these reconstructions showed respiratory variation patterns of greater similarity to the gridded dataset, but with the sharpened boundaries between separate tissue regions being preserved following the reordered STCR reconstructions. This is the case with both the standard and strong temporal weights for the reordered reconstructions. Such changes in the temporal profiles for the various reconstruction methods were relatively consistent across the five different FPP datasets analysed in this section, although smaller differences between the two methods were sometimes present.

4.3.6. Discussion and Conclusion of the Constraint-Reordering Method

The suppression of motion that is seen in the non-reordered STCR reconstruction at stronger temporal-constraint weighting is clearly an artificial effect. Such strong modification of the true motion between frames is not intended nor necessarily desired. Unlike the deliberate motion correction

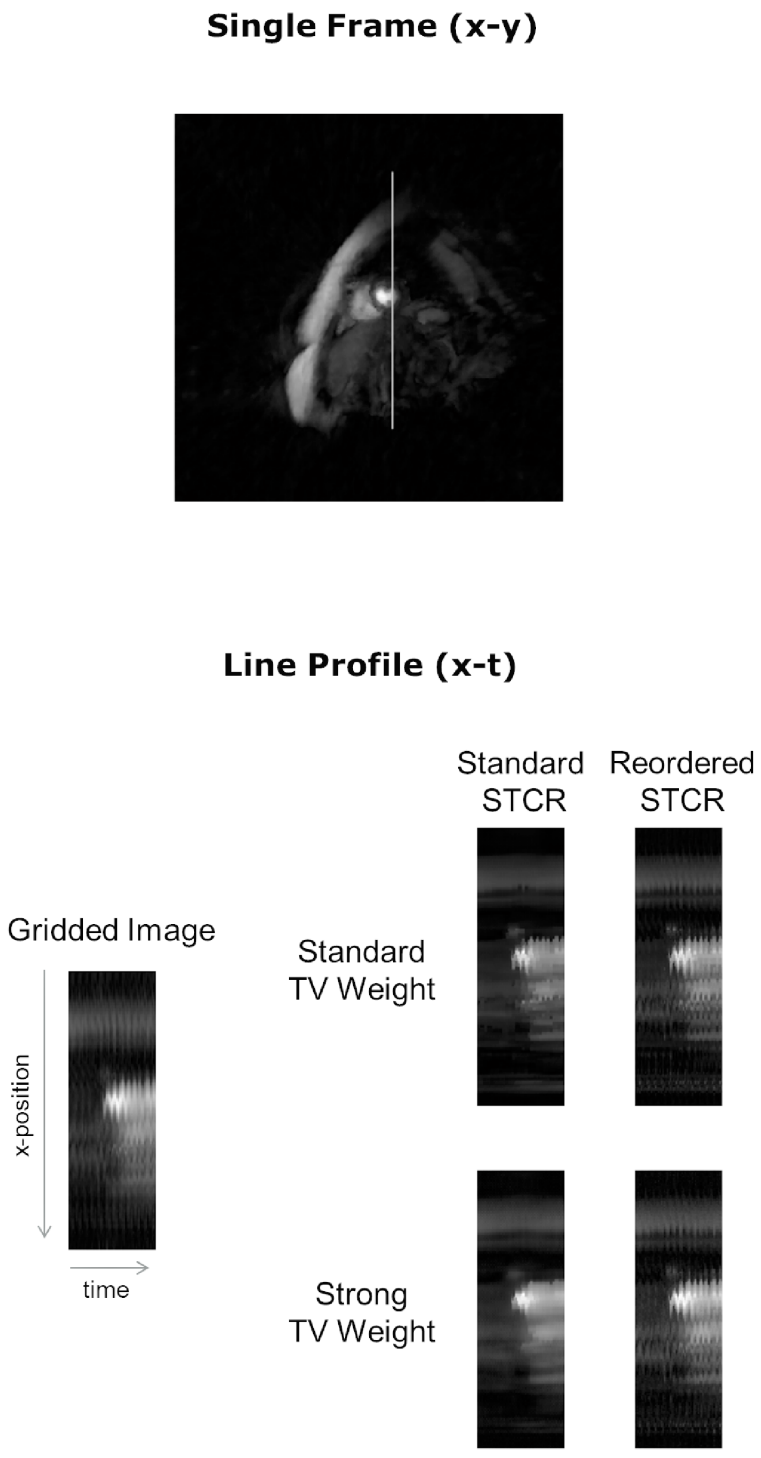

Figure 4.18.: Temporal dynamics of STCR reconstructed datasets. A line profile in a single frame is shown, along which x-t images are produced over all frames of the FPP series, for each combination of reordering and temporal weighting. The differences in the temporal profiles of the STCR reconstructions were compared with that of the gridded reconstruction (see text).

applied as part of some other algorithms [Chen et al., 2014b], the motion suppression here is the consequence of overly strong temporal filtering and could potentially mask genuine diagnostic information such as perfusion defects.

Similarly, the smoothing of signal intensity variation across time, seen in the more strongly weighted non-reordered reconstructions, is also of concern. Whilst TV-constrained reconstructions are intended to preserve edge information, if such temporal smoothing becomes too strong there is potential that this could impact upon the visibility of rapidly filling defects.

The importance of choosing appropriate weightings for the reconstruction is highlighted by differences between the standard and strong temporal weights when applied to the non-reordered STCR reconstruction; this result prompted a more in-depth investigation into the choice of the different weight values (Section 5.3.2).

The reordered reconstructions were effective in restoring the correct temporal dynamics of the reconstruction. However, the introduction of new artefacts somewhat offsets the benefit of this method in its current form. As these artefacts occur in the frames of concern, i.e. those containing sudden motion or sharp changes in image contrast, and tend to impact areas such as the myocardium, they are particularly troublesome. It is worth considering though that motion effects are possibly already affecting these frames and that they are simply being artificially smoothed by the use of standard STCR.

A possible cause of the new in-plane artefacts, which did not occur in the original publication (that utilised completely sampled data for its ground-truth guidance of the P-matrix calculation), is the inevitably inaccurate estimation of the reordering matrix P. Such use of an incorrect prior from which to estimate the reordering could result in regions of sub-optimal reordering, particularly near object edges. The original publication warns against use of an initial reconstruction as a prior [Adluru and DiBella, 2008], although constraint reordering in other algorithms have applied this successfully [Adluru et al., 2015]. Use of an initial gridded image is also of limited accuracy due to those images containing undersampling aliasing. Both attempts were briefly examined during preliminary work and the gridded prior was found to perform better in this implementation. Other, improved, priors may be possible.

The CRM has not, as far as it is known, previously been applied to

non-Cartesian datasets. The reordering method should in theory be a good match, by improving the inter-shot motion robustness in combination with the intra-shot robustness of radial imaging. However, the use of radial sampling may explain the difficulty in acquiring an adequate prior. While radial imaging has the advantage that unaliased, low-resolution, data can be extracted from a central region of the undersampled k-space itself, the high degree of angular undersampling employed in this work makes this feasible only if very low resolutions are extracted. Such low-resolution information is markedly insufficient for the pixel-wise reordering estimation. The angular undersampling also means that use of the gridded reconstruction as the prior provides a blurred estimate of the pixel values; the most crucial pixels of the image are those in the myocardium adjoining the LV blood and are missed by such a reconstruction, leading to a strong difficulty for this method without some new development.

The CRM has been demonstrated and evaluated in this thesis section, applied for the first time in prospectively acquired 3D SOS FPP, where it showed improvements to the temporal fidelity of the reconstructed datasets. The improvements were relatively modest however, and the potential for inducement of artefacts, especially in the subendocardial myocardium, made the benefit of this technique in its current form questionable. Nevertheless, with some improved prior estimation to guide the reordering, the reordering method might provide some benefits if temporal blurring becomes of concern in an STCR reconstruction.

4.4. Reconstruction Methods Conclusions

The MFP work enabled higher acceleration factors in free-breathing 2D FPP than previously possible without the risk of PI artefacts caused by respiratory misregistration. However, there was still intolerable SNR loss with high acceleration rates. During the MFP work, it was recognised that the PI methods were shown to be too limited by SNR for use at the acceleration factors that would be required for fully-sampled 3D FPP.

Application of a compressed sensing algorithm (STCR) to the SOS sequence was therefore explored, which used spatial and temporal constraints to enable reconstruction of 3D FPP datasets. Potential negative temporal effects of the reconstruction were examined alongside a constraint reordering

method that it was hoped might reduce these issues.

The STCR algorithm was chosen as the method to reconstruct the 3D SOS FPP datasets acquired during this project. The importance of choosing the correct weighting factors was highlighted in this chapter and is explored further later (Section 5.3.2). The constraint reordering method has been shown to potentially aid in the improvement of the reconstruction temporal fidelity, if required, however in its current implementation this can come at the cost of increased artefacts that risk impact of clinically relevant regions of the images.

Some possible avenues for future work are stated in the final chapter of the thesis (Section 8.3).

5. Novel 3D myocardial perfusion sequences

Following the development of an optimised SOS sequence (Chapter 3) in combination with the STCR reconstruction (Chapter 4) to enable 3D FPP acquisition, some novel variations on this initial sequence are investigated next.

Firstly, a method is presented that sacrifices the temporal resolution of the acquisition for improvements in spatial resolutions and to potentially enable improved artefact detection. Secondly, a section of work investigates the modification of the sequence to produce and evaluate a bSSFP 3D SOS FPP sequence aiming for improved robustness to artefacts. Lastly, modification and set-up of the default SGRE 3D SOS FPP sequence and its reconstruction is performed to focus on providing reliable application in the clinical environment.

5.1. An alternate-cycle sequence interchanging high-resolution and isotropic imaging

5.1.1. Introduction

Simultaneous improvement of parameters such as left ventricular coverage, image resolution and shot duration for a 3D FPP sequence is currently not feasible, as attaining "whole-heart" coverage already stretches current acceleration capabilities. It is accepted that compromises in the acquisition are required, as previously discussed (Section 2.1.2), and for a fixed shot duration this sacrifice typically occurs in the spatial resolution or coverage.

The need for higher in-plane resolutions in FPP is well understood, with previously discussed benefits being shown in 2D that include reduction in artefacts [Plein et al., 2008a]. The impact of through-plane resolution on the diagnostic confidence of 3D FPP datasets is not well understood, with a very limited range of through-plane resolutions reported (Table 2.1). Without

extending the shot duration, there is difficulty in improving these resolutions to examine the relative importance of through-plane and in-plane limitations.

Some reduction in the acceleration requirements has previously been achieved in 2D multi-slice FPP by distributing the slices over two cardiac cycles [Bertschinger et al., 2001][Schwitter et al., 2001], known as alternate-cycle acquisition, which was shown to maintain high diagnostic ability but remains a topic of some debate. Splitting up each 3D acquisition over two cycles has not been performed for 3D FPP, likely due to the potential for strong inconsistencies in the raw data across the two cycles (discussed in Section 1.5.6). However, the idea of modifying the single-shot acquisitions in alternate cardiac cycles has previously been performed; a 3D FPP sequence acquired different cardiac phases in alternate cardiac cycles [Motwani et al., 2014], in order to examine differences in quantitative 3D FPP between systole and diastole, with all its other imaging parameters otherwise held constant.

In this work it is proposed that a sequence could be switched between two 3D FPP strategies with different desired parameters in alternate cycles. By applying differently improved parameters in each of the alternate cycles, it is proposed that together the acquisitions could move towards capturing the full range of desired 3D FPP properties. This idea was examined by alternating between a short-axis (SAX) higher in-plane resolution acquisition with potentially reduced base-to-apex coverage, and a long-axis (LAX) isotropic (but lower in-plane) resolution acquisition of the whole LV. This new approach also aimed to provide a "repeated acquire" confirmation against artefacts, by imaging the same myocardium with two different interleaved 3D scans.

5.1.2. Methods

The SGRE 3D SOS sequence program was modified to enable fully independent settings of FOV, spatial resolution and slab position on alternate cardiac cycles. This dual configuration for alternate cycles is referred to as a "dual-slab" method in the following work. Imaging was performed on the Skyra 3 Tesla system, with an 18 channel anterior chest array and 12 channel posterior array, as for most other experiments in this thesis.

After optimisation in volunteer subjects (N=3), rest first-pass perfusion using the dual-slab method was acquired in 10 patients. Short-axis (SAX) images at higher in-plane resolution were acquired on odd cardiac cycles and lower in-plane, higher through-plane, resolution long-axis (LAX) images were acquired on even cycles (Figure 5.1).

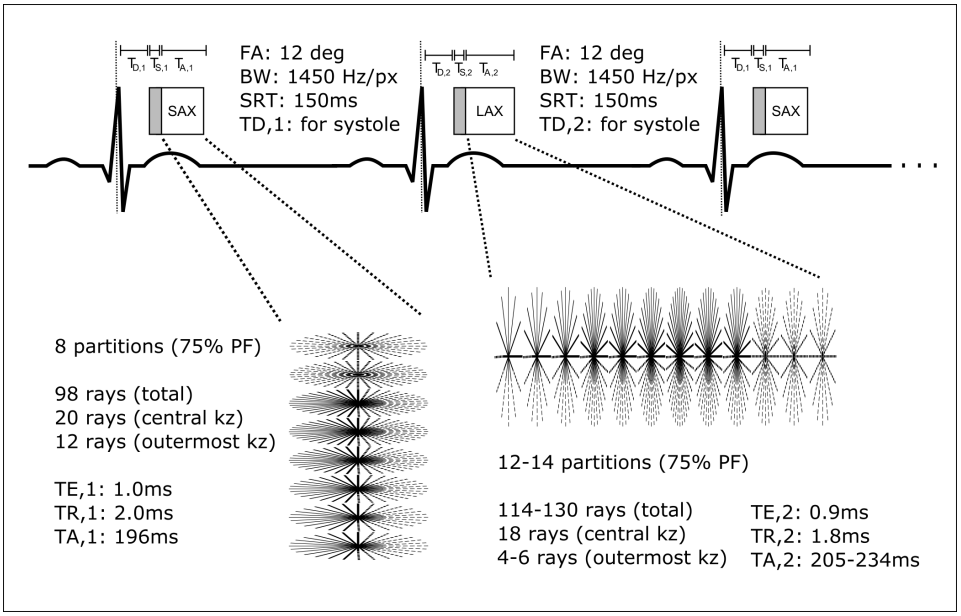

Figure 5.1.: The alternate-cycle 3D FPP protocol. Higher in-plane resolution SAX data was acquired on odd numbered cardiac cycles, with fewer acquired k_z partitions along the LV. On even cycles, the LAX orientation and systolic acquisition combined to minimise the FOV required by partition encoding across a short-axis of the LV, enabling higher through-plane and lower in-plane resolution, towards isotropic acquired voxel size. Rays per partition gradually reduced at higher k_z for further acceleration.

The SAX cycles collected 6 partitions (of the 8 reconstructed with zero-filled 75% slice-PF) requiring a total of 98 rays (Variable Undersampling (VU): 12-14-16-18-20-18-0-0). Along each ray, 144 points were sampled with a T_E/T_R of 1.3/2.0ms, which enabled a shot duration of 196ms. The FOV was 300x300x80mm, which therefore allowed 6 wrap-free slices to be reconstructed to 1.1 x 1.1 x 10.0mm voxels, after additional 2x zero padding in-plane.

For the LAX cycles, the number of partitions was adapted dependent on the end-systolic diameter of the LV, selected as either 12 or 14 partitions (which required 9 or 11 partitions to be acquired respectively for zero-filled 75% slice-PF). The lower in-plane resolution requirements in the LAX acquisitions allowed fewer rays to be collected per partition for approximately the same amount of undersampling. A modified VU scheme was used, with the same rate of drop-off in the number of rays per partition, to collect either 114 rays (6-8-10-12-14-16-18-16-14-0-0-0) or 130 rays (4-6-8-10-12-14-16-18-16-14-12-0-0-0). Significantly, the lower in-plane resolution also enabled the T_R to be reduced to 1.8ms so that the shot durations of 205-234ms were not excessively long. The FOV for the LAX acquisitions was 300x300x(72-84)mm, enabling 20-24 usable slices to be reconstructed at 3.0 x 3.0 x 3.0mm isotropic resolution, after 2x through-plane zero padding.

The SAX and LAX acquisitions were both timed to acquire central k-space in mid-systole, and maintained other imaging parameters as previously described (Section 3.2.6): α=12°, BW=1450Hz/Px, SRT=150ms. To ease the burden on the reconstruction algorithm for investigation of these novel applications, breath-holds were requested from the patients during the acquisition, for a duration as long as the patient could comfortably manage. 50 frames were acquired (25 SAX, 25 LAX).

The NUFFT-based STCR algorithm was used for reconstruction, modified so as to split the data from the alternate-cycles and perform the reconstructions of the two orientations separately. The reconstructions were performed in MATLAB and used a temporal weighting = 0.7[1] and a stopping criterion of 100 iterations. β and γ were set to zero, effectively making this a TCR reconstruction.

For the 10 subjects imaged, the effectiveness of the two interleaved shot locations was assessed with particular attention to: ventricular coverage, spatial resolution and differences in artefacts. Images were inspected for

[1]Weighting values are not comparable between the different STCR implementations (NUFFT-based and pre-interpolation).

dark-rim artefacts (DRAs), with a dataset adjudged to contain a DRA if an artefact with a clear, characteristic appearance (Section 1.5.6) was present in multiple slices of the dataset. Other artefacts and degradation of the image quality in different ways were also noted during this analysis. Comparison was made of these results between the SAX and LAX datasets.

5.1.3. Results

All 10 patients were successfully imaged. An example single frame image of the central slice is presented for all 10 datasets in Figure 5.2 (SAX) and Figure 5.3 (LAX). Image quality varies over the 10 datasets, particularly with regard to endocardial border clarity, but the myocardium is clearly distinguishable in all cases. The complete set of slices are shown for two of the datasets: one of a higher representative image quality with regards to border clarity (Figure 5.4) and one of a lower representative image quality (Figure 5.5).

Six of the patients required the 84mm through-plane FOV for the LAX acquisitions to completely cover the LV myocardium, which corresponded to the longer 234ms shot duration, while four of the patients were acquired with the 72mm FOV. In one patient incomplete coverage of the LV was obtained, caused by incorrect placement of the slab during planning of the acquisition. In the other nine patients, successful coverage of the LV was achieved in the LAX acquisitions.

By the definition laid out in the methods, DRAs were identified in three of the SAX datasets and six of the LAX datasets. In no datasets were the presence of DRAs found in the SAX frames but not in the LAX frames. The width of the SAX DRAs appeared smaller than in the LAX images and did not necessarily correspond to the same regions of the myocardium. Residual streaking was present in almost all datasets but did not noticeably affect myocardial visibility. However, a dark transient artefact was often visible in both orientations during the arrival of contrast agent into the myocardium (Figure 5.6).

5.1.4. Discussion

Higher spatial resolutions have been achieved alternatively in-plane and through-plane at end-systolic shot durations, by separating them across two interleaved acquisitions on alternate cardiac cycles. These acquisitions are at improved in-plane and through-plane resolutions than have previously been

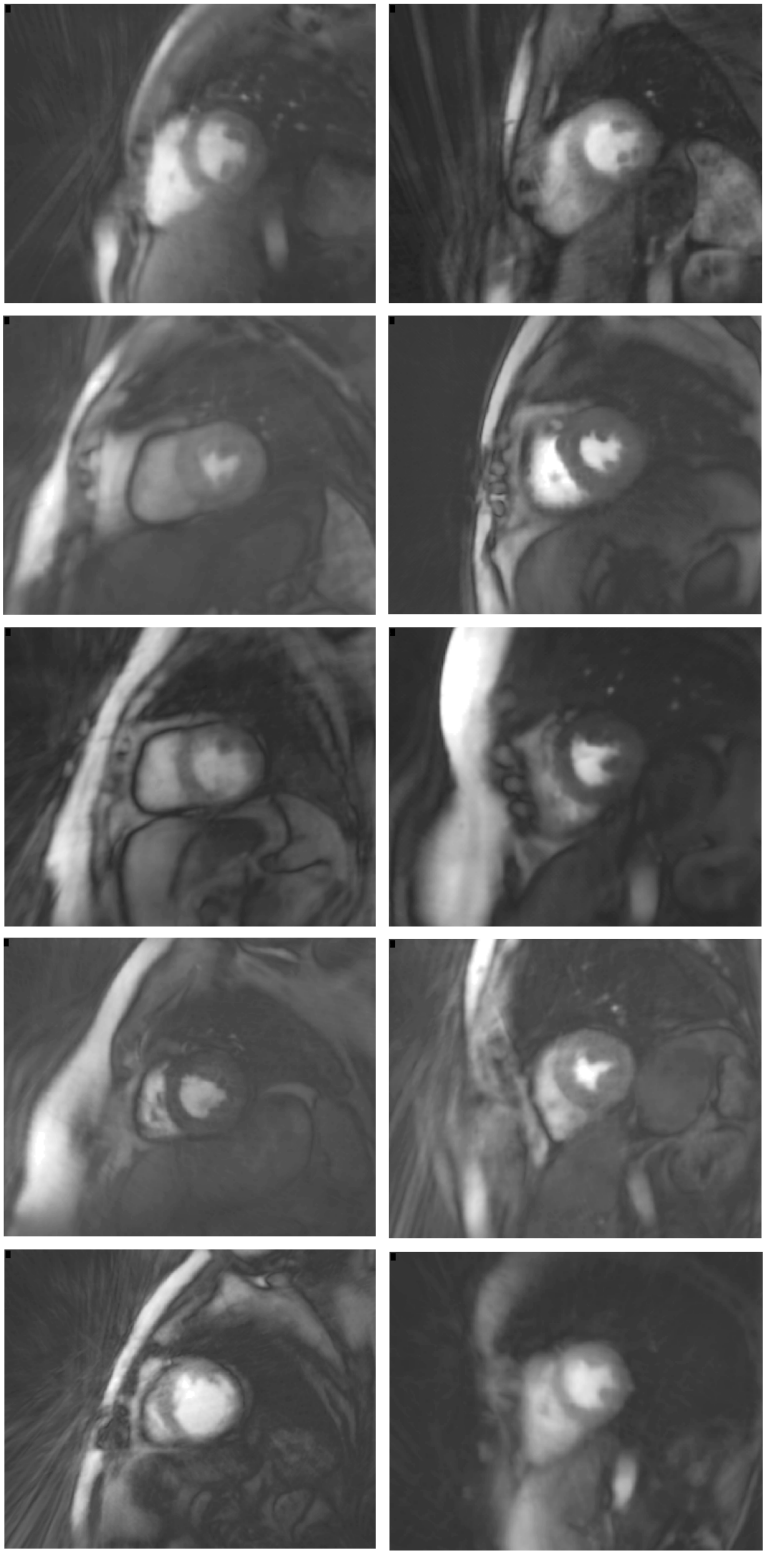

Figure 5.2.: Overview of the SAX acquisitions. A single slice and frame is demonstrated for all 10 patients.

Figure 5.3.: Overview of the LAX acquisitions. A single slice and frame is demonstrated for all 10 patients. Anterior chest wall is to the right, with the exception of the two top-right images where it is to the bottom (due to acquisition orientation).

Figure 5.4.: Alternate-cycles example dataset 1. Alternate-cycle images captured from a single patient, showing 6 slices of the higher in-plane resolution SAX frame (top) and 24 slices of an isotropic lower-resolution LAX frame (bottom) acquired during the same first pass. The endocardial border is clearly shown, and the myocardial tissue signal is clear and with good uniformity.

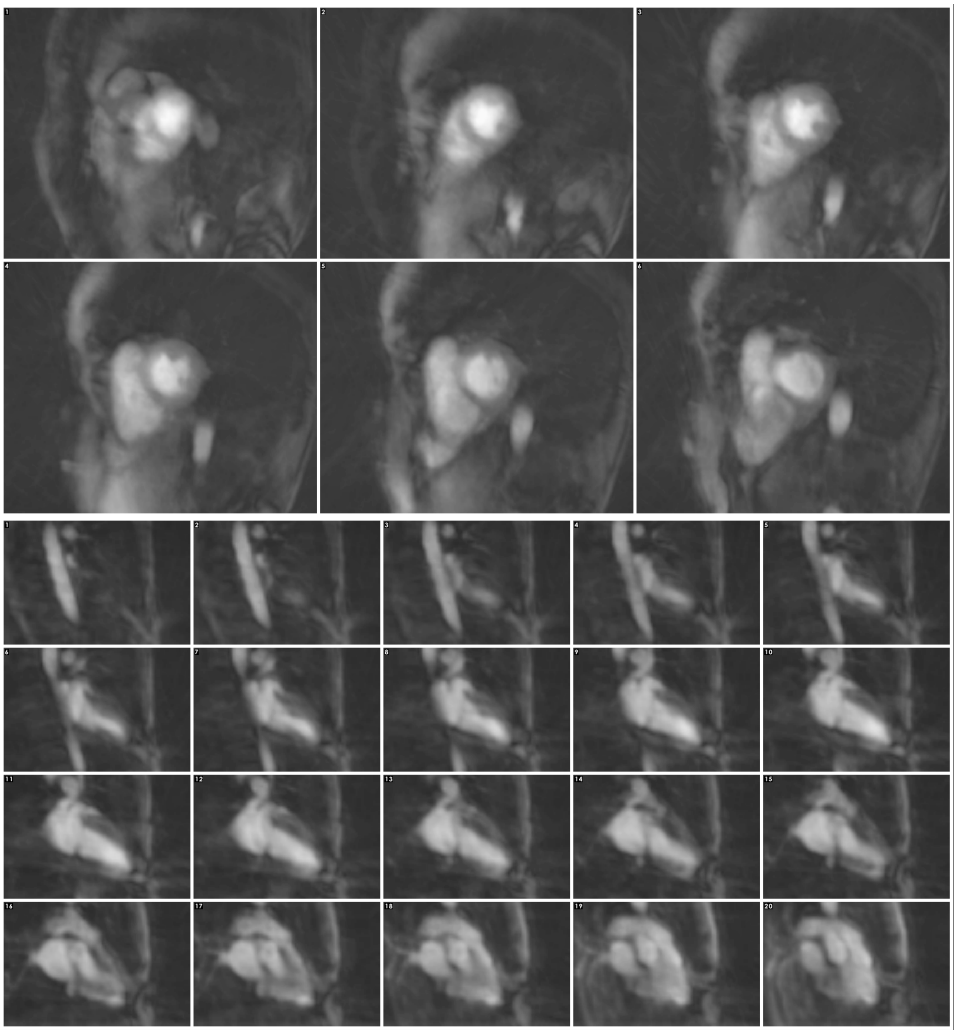

Figure 5.5.: Alternate-cycles example dataset 2. As for Figure 5.4, SAX and LAX frames acquired during the same first-pass, this time for a patient dataset with lower image quality. Both orientations have unclear endocardial boundaries and dark regions can be seen in the myocardium, particularly in the LAX view.

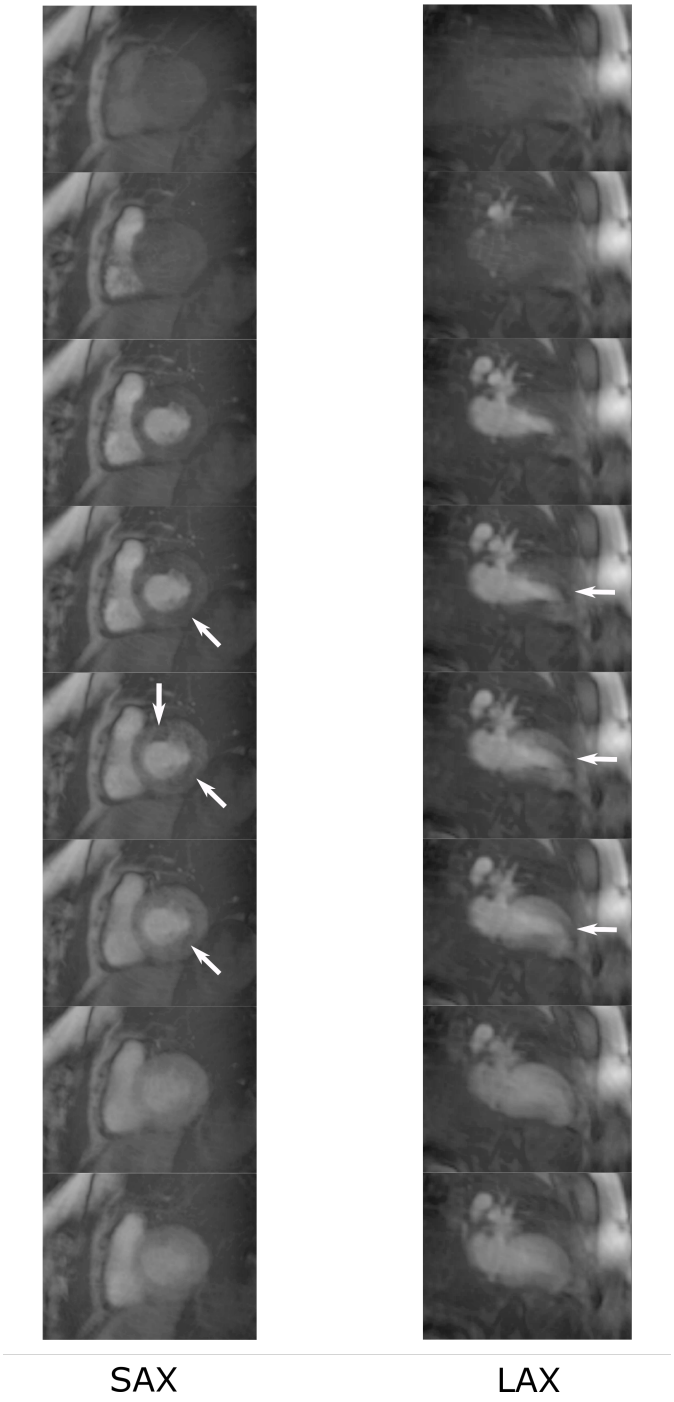

Figure 5.6.: Example dynamics of the alternate-cycle acquisition. For a single patient, multiple frames during the first-pass (top to bottom) are shown for central slices of the SAX (left) and LAX (right) acquisitions. Both of these sets were captured during the same first-pass, on alternate cardiac cycles. White arrows mark the presence of unexplained transient dark regions in the myocardium.

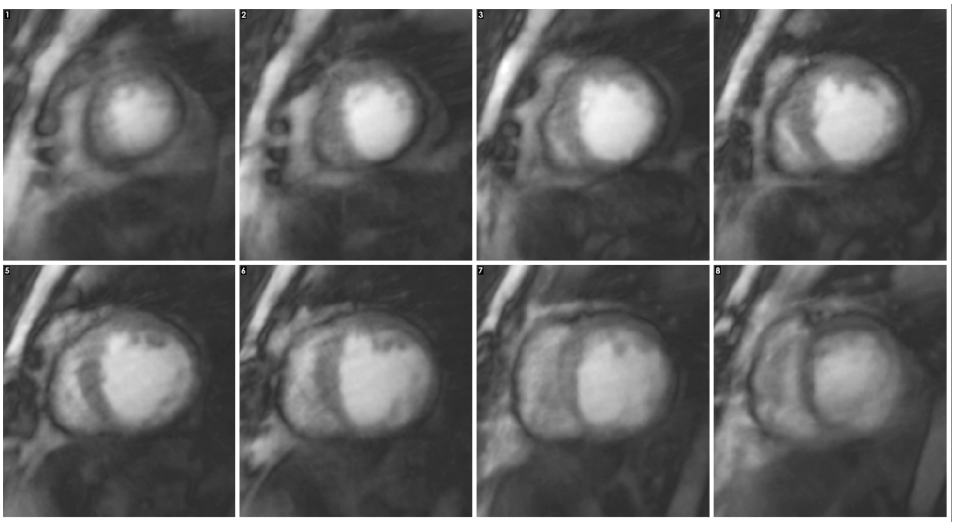

Figure 5.7.: Example (apex to base) resting perfusion images from a single patient (with dilated-cardiomyopathy and inferolateral infarction) with a thin myocardial wall, even during systole, demonstrating the potential benefit of the higher in-plane resolution obtained on the odd cardiac cycles.

realistically achieved by 3D FPP. The higher in-plane resolution acquisitions were acquired in the SAX orientation most typically used for FPP. The LAX orientation was used for higher through-plane resolution acquisitions at coarser in-plane resolution, enabling the partition FOV to cover the systolic LV diameter. This method for acquiring interleaved datasets in these two alternating configurations during the same first-pass is distinct from simply reformatting a single 3D FPP scan, due to their difference in acquisition parameters. A similar strategy for confirmation of disease is often used in cardiovascular magnetic resonance, for example by repetition of a slice with swapped phase-encode direction in late-enhancement imaging.

The acquisitions in the SAX orientation on the odd cardiac cycles produced higher quality images, approaching the resolution of some multi-slice 2D FPP protocols, but with additional benefits of contiguous coverage of the myocardium, and most particularly with all slices being acquired at the same cardiac phase. An example dataset for a patient with dilated cardiomyopathy (Figure 5.7) gives an example case where the higher in-plane resolution might potentially be important in distinguishing the thinned myocardium from adjoining blood and fat.

The LAX (even cycle) images would provide the clinical reader with a second viewpoint of the first-pass, and the altered motion and resolution

characteristics compared to the odd cycles might aid in making a judgement on a potential artefact. Image quality in the LAX acquisitions was reduced by the coarser in-plane resolution, but the improved through-plane resolution of the LAX was considered a successful first attempt at moving 3D FPP towards a more isotropic resolution. Additional information is potentially captured in these LAX acquisitions, with their aim to be used in addition to the more conventional SAX acquisition. The isotropically reconstructed voxel size was more consistent with enabling the reformatting of the dataset into any plane if required (Figure 5.8), for example to assist clinicians with inspection of the spatial distribution of a perfusion defect or artefact. The quality of the LAX scans due to their lowered in-plane resolution somewhat limits the information that can currently be gained from them, including any potential benefit from their improved through-plane resolution.

Dark-rim artefacts were visible in many of the datasets, as is often the case for FPP acquisitions. The visibility of the DRAs was reduced for the datasets with higher in-plane resolution, as would be expected from in-plane Gibbs contributions to these artefacts. The observation that the DRA location in the myocardium did not typically match between the two datasets lends some support to the dual-acquisition approach providing improved artefact differentiation. Of more concern in these datasets were the presence of dark transient artefacts that also occurred during the key FPP frames, appearing as dark transmural regions in the myocardium that filled in over a few frames. Whilst it might be possible to distinguish them from true perfusion defects, as for DRAs, their greater transmurality is of concern, as is the uncertainty in their cause.

The perfusion scans in this study were performed at rest, however, the shot durations achieved were comparable with those used in previous 3D FPP literature (Table 2.1) and are realistically short durations that would not prevent application at stress. This was a consistent aim of the project, that it should be consistent with real-world clinical stress applications. For the LAX acquisitions, the coarser in-plane resolution permitted the reduction of the number of rays per partition as well as a faster T_R, so that the shot duration remained reasonably short; however, the duration was still extended, particularly in cases where the LV diameter required a larger k_z FOV. This work highlighted a difficulty in extending the number of acquired partitions to improve through-plane resolution in 3D FPP.

Systole was chosen for the reasons previously discussed, including that the

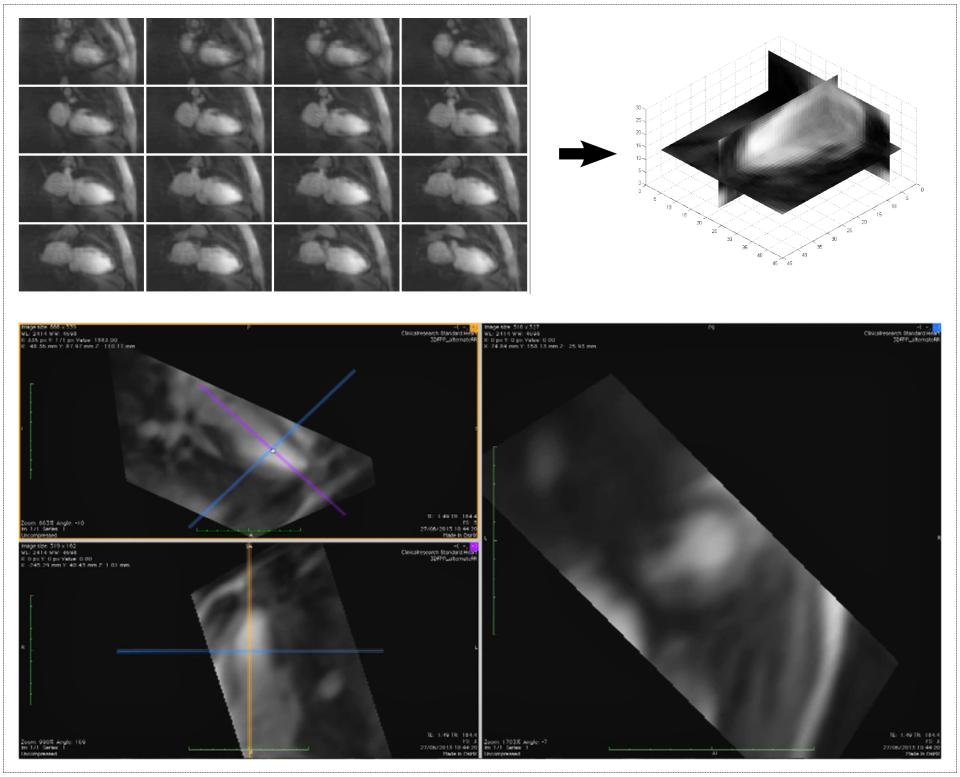

Figure 5.8.: Example reformatted transverse, coronal and sagittal slices from an LAX acquisition are combined (top), demonstrating the 3D isotropic nature of the LAX shot. Isotropic voxels also help support double-oblique reformatting for any frame, demonstrated in a different dataset (bottom). This could potentially help further examine the full spatial distributions of possible artefacts or perfusion defects.

thickened myocardium contains more voxels and also that the contracted LV helps to minimise the required FOV. It could instead be potentially feasible to capture both of these SAX and LAX acquisitions, with their altered sequence parameters, within each cardiac cycle (capturing one in systole followed the other in diastole). The different cardiac phase between the two datasets in such an acquisition scheme could again alter artefact characteristics, possibly aiding their identification, while the cardiac phase of the images within each individual 3D dataset would still remain self-consistent. Potential issues would arise in reliably fitting both acquisitions, including their saturation recovery times, within each cardiac cycle, and this approach was not considered further.

Zero padding (as well as partial Fourier zero-filling) of the k-space matrices prior to reconstruction was used extensively in this work. The use of rawdata zero-filling cannot realistically be used as a key component to meeting the acceleration challenges faced in 3D FPP. The zero-padding in this work was used simply to enable a first examination of isotropically reconstructed 3D FPP datasets. The effects of zero-padding, combined with the low acquired spatial resolution, is likely to impact on the quality of the reformatted "isotropic" images.

While comparisons of the 3D dual-slab method with some other FPP resting images would be highly desirable, this work was extremely limited by the availability of patients or volunteers. Furthermore, a test approach of giving two contrast agent doses was not permissible by ethical considerations, and would be weakened technically by the complication of incomplete washout of GBCA before the second dose.

5.1.5. Conclusions

The feasibility was presented of alternate-cycle separate 3D acquisitions, with differing optimisations, acquired during the same first-pass. This was shown to be capable of acquiring datasets that stretch current limits of both in-plane and through-plane resolutions (but with other compromised parameters). This idea aimed to deliver two independently optimised acquisitions of the same first-pass for potentially improving clinical confidence. While a more closely isotropic acquisition of 3D FPP data has been demonstrated for the first time, the lowered in-plane resolution and the reliance on zero-padding was considered to somewhat limit the possible diagnostic use of this overall method. Dark regions of myocardial signal, present in both views but

particularly prevalent in the LAX, were also identified as an area of concern.

5.2. A Balanced Steady-State Free Precession (bSSFP) 3D FPP Sequence

5.2.1. Introduction

Spoiled gradient-echo (SGRE) and balanced steady-state free precession (bSSFP) are both common sequence types utilised in myocardial first-pass perfusion (FPP). As reviewed earlier (Section 1.5.2), the refocusing and typically higher flip-angles used in bSSFP increase SNR compared to SGRE, making it particularly suited to FPP. The benefit of this SNR increase could be important in the case of 3D FPP, where the high undersampling rates greatly reduce the intrinsic SNR, potentially undermining the advantage conferred by the partition-encoding of 3D.

3D FPP literature has been dominated by sequences using SGRE based readouts, with only two exceptions to date that employed bSSFP. The first of these employed dual-channel transmission for use with bSSFP [Jogiya et al., 2014b], hardware that is non-standard on clinical scanners. The second of these exceptions was a method that used a balanced SSFP sequence as part of a continuous acquisition scheme [Giri et al., 2014]. Both of these methods used bSSFP to support rectilinear k-space acquisition methods.

A bSSFP sequence is naturally sensitive to off-resonance phase-accumulation during the T_R between RF pulses. Even small off-resonance errors, that are well within bSSFP limits of $\pm\pi$ radians, can perturb the initial stabilisation of the precessing magnetisation which is needed before the start of bSSFP data acquisition [Scheffler and Lehnhardt, 2003]. This sensitivity is exacerbated by the typically longer T_R required for a bSSFP sequence comparative to its SGRE equivalent, which is the consequence of additional gradient pulses being required for rewinding. While bSSFP is quite widely used in 2D FPP ([Kramer et al., 2013][Kellman et al., 2017]), the slab-selective RF excitation of 3D imaging is generally slower than for slice-selection, leading to an even slower comparative T_R. With bSSFP it is also well known that large changes in gradient waveforms from one T_R to the next, such as in-between partitions with the SOS trajectory, can also cause artefacts [Bieri et al., 2005]. Finally, off-resonance phase-accumulation occurs more rapidly at the higher field strength (3T) used in this project, whereas the patient nerve-stimulation still limits gradient waveform speed, as for lower main field strengths.

This work aimed to investigate and optimise the performance of bSSFP with the 3D FPP SOS trajectory, including modifications to the sequence that aimed to reduce off-resonance artefacts. The first *in vivo* demonstrations of bSSFP 3D SOS feasibility are presented.

5.2.2. Methods

The 3D SOS sequence program was modified for bSSFP by the inclusion of balancing gradients, the removal of spoiling, and the addition of appropriate RF phase-alternation. The trajectory, sequence parameters (where possible) and k-space efficiencies were kept the same as for the SAX acquisitions in Section 5.1. Linearly incremental flip-angles were applied over 10 startup T_R cycles [Nishimura and Vasanawala, 2000] without acquisition, used to establish the precessing magnetisation towards a steady-state before data acquisition began.

The RF pulse was modified from that described in Section 3.3, because the low flip-angle assumption in the SGRE work was no longer valid. Instead, a sinc pulse with lower BWTP (3.0) was applied over an extended duration (768μs), designed to achieve a flip-angle of 30°. Reductions enforced by the SAR regulation systems and the presence of any 'RF clipping alerts' related to limited RF transmitter voltage (Section 3.3) were recorded as part of the results.

With the inclusion of the necessary additional rephasing sequence gradients, the T_E and T_R were extended to 1.3 and 2.8ms respectively. The inclusion of the startup cycles for stabilisation of bSSFP required extension of the saturation recovery time to 190ms (from saturation to acquisition of central k-space). The total data acquisition shot duration, i.e. excluding the startup T_R cycles, was 270ms. For the *in vivo* datasets, 2x k_z zero-padding was added prior to reconstruction to produce ∼12 usable slices (after discarding of edge slices, as for the SGRE sequence) with reconstructed voxel size 2.1x2.1x5.0mm.

The known issue of sudden large changes in movement through k-space with bSSFP led to the investigation of two different trajectory patterns (Figure 5.9), which altered the transitions between k_z partitions. The first is a standard $0 \rightarrow \pi$ radian coverage for each partition, as implemented in the SGRE SOS work. The proposed new pattern instead added a $+\pi$ starting angle shift on alternate partitions. This provided a smoother transition of the gradient waveforms between partitions and was hypothesised to cause

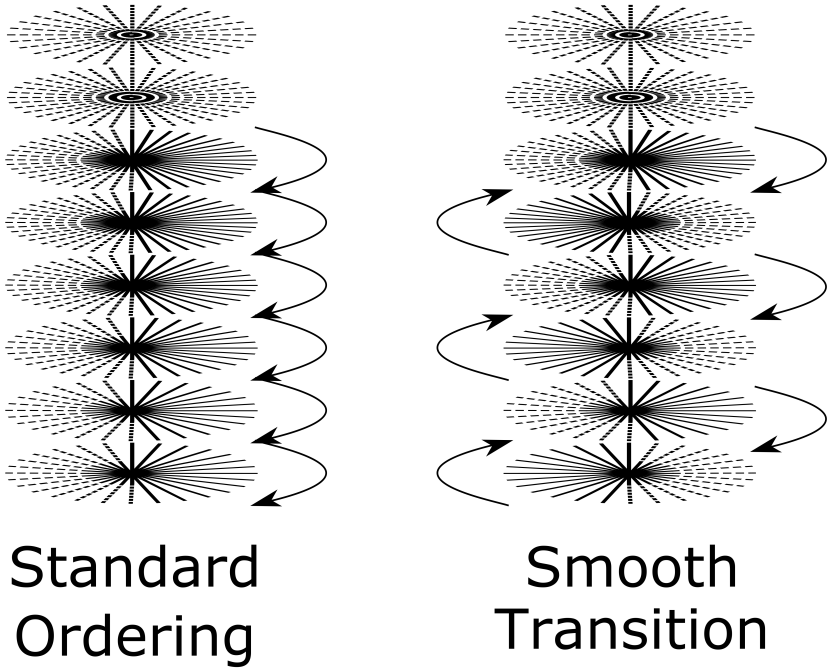

Figure 5.9.: The investigated bSSFP SOS trajectories. Standard ordering (left) collected all rays within each partition rotating from 0 to π. A transition-corrected ordering (right) added $+\pi$ to the starting angle on alternate partitions. This correction was hypothesised to be potentially advantageous because of a smoother change in the gradient waveforms between partitions.

fewer transient bSSFP instabilities, which are known to be exacerbated by off-resonance [Bieri et al., 2005].

The SNR of bSSFP was compared with the SGRE-based variant of the SOS sequence, using a 100-fold multiple acquisition approach [Reeder et al., 2005] in Phantom A. This phantom was chosen because its T_1=180ms was a reasonable approximation for the myocardium at peak GBCA perfusion. Phantom acquisitions were also performed with the standard and smooth transition trajectories in Phantom C, which was selected so as to provide a test that contained image features. As was performed for the SGRE off-resonance test (Section 3.5.2), these images were first acquired after careful shimming of the main field, and then repeated with increasing centre frequency shifts (to represent off-resonance errors). Phantom reconstructions were reconstructed by use of an NUFFT, with no undersampling compensation applied.

Following the phantom evaluations, the finalised sequence was run at

rest in five patients that had been clinically referred for late-enhancement imaging, who agreed to volunteer for the additional acquisitions under ethical approval. Cardiac 3D-FOV shimming of the B_0 field was applied before each acquisition using a prescribed, consistent procedure as would be necessary for routine clinical use. 40 measurements were acquired during the first-pass. Experiments were performed at 3T, with the experimental setup, including the *in vivo* reconstruction methods, kept the same as for Section 5.1.

For the *in vivo* analysis, image evaluation in the five patients could again only be performed through subjective visual inspection, because rigorous comparison against other "baseline" perfusion methods was not possible due to ethical and medical limitations associated with GBCA injections. The images were inspected for overall quality as well as for the presence of bSSFP-related and other imaging artefacts.

5.2.3. Results

The phantom studies demonstrated the feasibility of bSSFP 3D SOS, showing image quality subjectively similar to those produced by the SGRE sequence, and a 44% increase in SNR was measured.

A reduction of image artefacts was also demonstrated in the phantom images acquired with the smooth transition ordering compared against the standard transition ordering, and this difference became more pronounced with increasing off-resonance (Figure 5.10). Therefore this smooth transition ordering was adopted for the *in vivo* acquisitions.

The 3D bSSFP SOS method was successfully run in all of the five patients, achieving flip-angles $\alpha \geq 22°$, without RF pulse voltage clipping in any subject. An example slice and frame from each of the five patients is shown in Figure 5.11, with a complete set of slices shown for one of the patients in Figure 5.12.

bSSFP-related off-resonance dark-band artefacts were detected in the LV myocardium in two out of the five patients (example, anterior segment of LV in top right Figure 5.11). In one of these cases, only one slice was strongly affected. However, in all the patients, at an average of 4 out of 6 slices, the myocardial visibility was at least partially impacted by dark transmural regions during the GBCA arrival (arrows on Fig 5.12), notably similar to those seen in Section 5.1 with SGRE.

However, in general there was little observed impact on bSSFP stability caused by the arrival of the bolus of the contrast agent bolus (Figure 5.13).

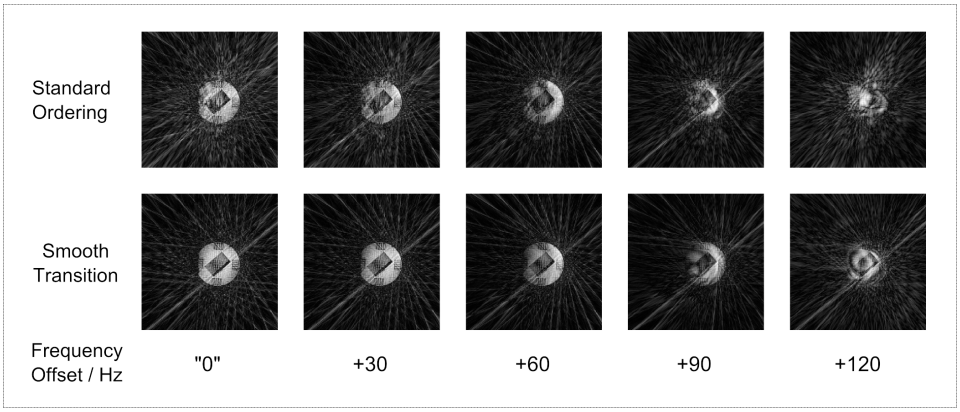

Figure 5.10.: Comparison of undersampled phantom acquisitions using the two different bSSFP SOS trajectory patterns. Increased streaking artefacts appeared to be associated with the angular jump at partition steps (standard ordering), with the artefacts reduced by the smooth transition ordering. Furthermore, the impact of frequency offsets appears more severe for standard ordering than for smooth transition.

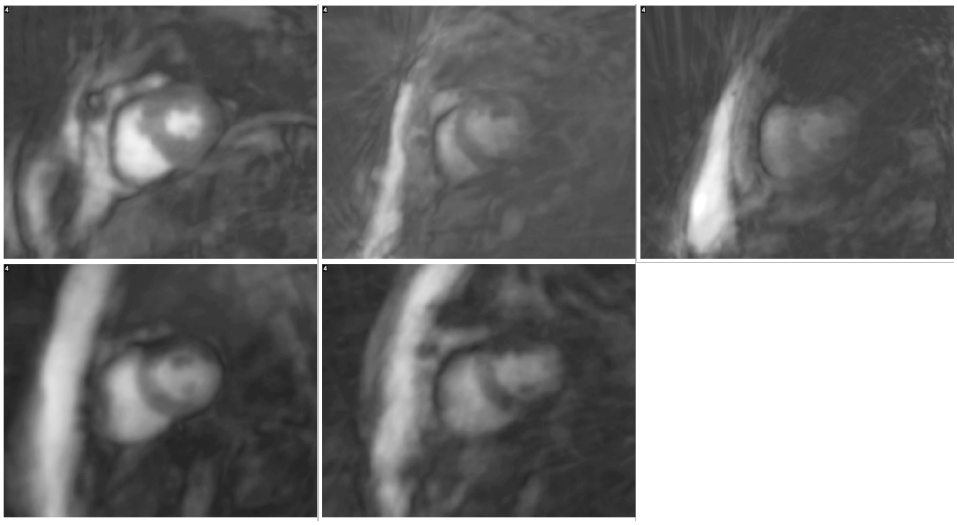

Figure 5.11.: Overview of the bSSFP acquisitions. A single slice and frame is demonstrated for all five patients. Myocardial intensity was often impaired by dark regions that did not appear to be simply bSSFP off-resonance banding and were not explained. The dark regions occurred mainly in the superior and inferior myocardial segments.

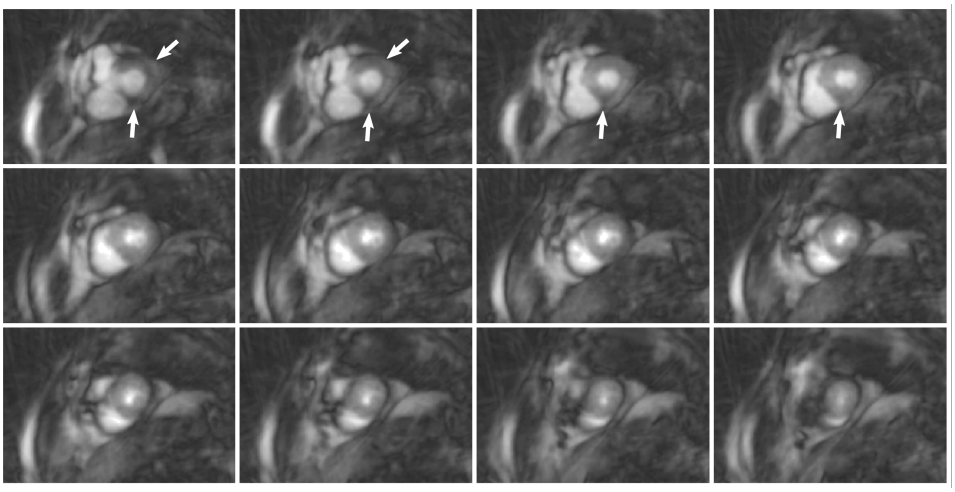

Figure 5.12.: Example bSSFP dataset. 12 slices of a single FPP time-frame, acquired using the smooth-transition 3D bSSFP SOS sequence. Arrows indicate unexplained dark transmural regions which appeared mostly in the more basal slices of the LV (see Discussion), as was typical for most acquisitions as shown in Figure 5.11. The images were relatively free of bSSFP off-resonance artefacts.

The image quality remained consistent, even during peak RV blood pool enhancement by the magnetic susceptibility of the more concentrated RV GBCA, when off-resonance effects could be expected to be at their most severe.

5.2.4. Discussion

The initial phantom tests demonstrated a clear benefit of the novel idea to improve the smoothness of the changes in gradient waveforms across partition-encoding steps. With the limited availability of patient testing, only the improved new method for 3D bSSFP SOS was taken further for *in vivo* evaluation.

Most of the *in vivo* images showed relatively few bSSFP off-resonance (dark band) artefacts, especially considering the higher Larmor frequency at 3T and the extended 3D bSSFP T_R. However, the presence of bSSFP off-resonance artefacts in some of the cases was still detrimental to the clinical feasibility of such a sequence. Rigorous attention to shimming of the B_0 field over the heart and reference frequency adjustment would be important in reliable use of this sequence. Sequences that use bSSFP are

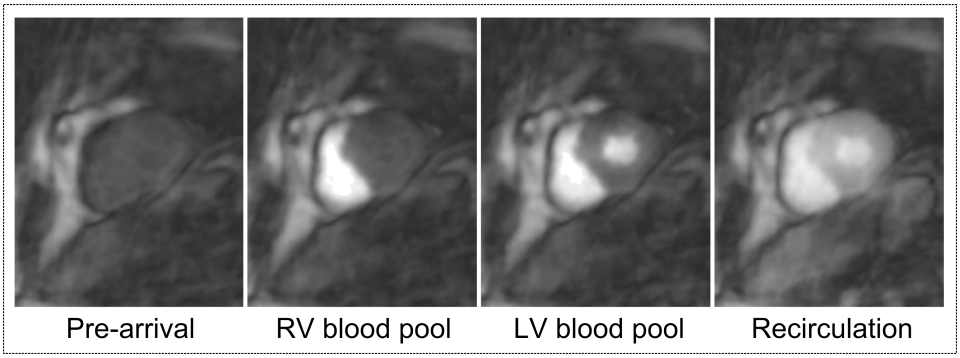

Figure 5.13.: Multiple time-frames from a single slice during the first-pass of GBCA. The image quality remained consistent, even during RV blood-pool GBCA bolus arrival, when off-resonance effects could be expected to be at their most severe.

widely used for 2D multi-slice stress FPP, with high reliability at 3T; the extended T_R (2.8ms) that was required for the 3D slab-selective RF pulse in 3D bSSFP clearly impacted the reliability of the sequence.

The results noted the frequent presence of dark transmural artefacts. These regions were not at locations that could have potentially shown fixed perfusion defects; such a correlation was excluded by examination of the clinically acquired late-enhancment images. The possible reasons for these dark transmural regions require further investigation. The resolution was not coarse enough that Gibbs effects would be transmural, and no clear reasons for these effects could be found. One possibility which would explain their predominant appearance in more basal slices is through plane cardiac motion, which is greatest for the basal planes. The 270ms shot duration for this sequence was longer than that achieved with the SGRE sequences in this project, and is a possible explanation for the increased prevalence of these artefacts seen in the bSSFP datasets.

The SNR measured *in vitro* gave only an indication of the improved SNR available in 3D SOS with the bSSFP sequence compared to SGRE. For *in vivo* acquisitions, this improved SNR may not translate directly and the compressed sensing reconstruction method used for *in vivo* acquisitions greatly complicates evaluation of the final image SNR. Improving the image quality and in particular the reliability may have greater importance for an FPP sequence. However, the potential to increase the acquired SNR in 3D FPP by using bSSFP is still believed to be a worthwhile investigation. The comparison of the SNR for 3D bSSFP and SGRE *in vivo* would require

multiple contrast agent injections, or potentially interleaving of bSSFP with SGRE on alternating frames. Comparison of *in vivo* SNR would also require more sophisticated and computationally expensive SNR measurement methods [Robson et al., 2008].

Future work would ideally focus on decreasing T_R to further shorten the shot duration. This could potentially involve methods to reduce the RF pulse duration, such as the use of asymmetric RF pulses, but investigations into the effect on slab profile accuracy would be required. A shorter shot duration is also essential to reduce cardiac motion during the shot, and would additionally help to reduce the currently long SRT. Other methods to shorten the SRT potentially include shortening of the steady-state startup procedure.

5.2.5. Conclusions

A radial stack-of-stars bSSFP 3D imaging approach during high-dose fast-injection of GBCA FPP was demonstrated for the first time. The *in vivo* imaging was not severely disrupted by artefacts even at the high angular undersampling required to minimise 3D shot duration, which potentially remained too long at 270ms. Factors essential in the reduction of artefacts, such as a novel modification of the angular ordering for stability of the bSSFP, were highlighted and investigated.

Overall, the *in vivo* image performance of this 3D bSSFP method for FPP required further optimisation, particularly regarding the observed dark regions of myocardium; however, the potential of bSSFP was shown for the first time by this work in 3D SOS FPP.

5.3. Towards a Clinically Robust Sequence

The previous two sections have examined novel potential implementations of the SOS sequence and STCR reconstruction for 3D FPP, testing new acquisitions by pushing at the currently achievable limits. The focus in this section moves towards creating a 3D FPP sequence that was considered to have the best possible chance of clinical adoption, i.e. in terms of robustness and ease of use, in order to fully meet the aims of this project.

5.3.1. Sequence Modification

Variable Undersampling Modification

Previous literature [Chen et al., 2012] showed that 20 angular rays per partition was a reasonable lower limit of the angular undersampling for SOS acquisitions. A variable undersampling (VU) method was introduced in Section 3.2.4 to modulate a compromise between maintaining this lower limit of rays per partition and of reducing the total numbers of rays acquired (to reduce the shot duration). Variable undersampling was initially introduced as a method that maintained the number of rays in the central k_z-partitions while reducing the ray numbers in higher k_z partitions. Alternatively, it is also possible to increase the number of rays in the central k_z partition, and reduce more sharply the numbers of rays per partition towards the edges of k_z, in sum obtaining a similar total number of rays as the original VU method.

Here, three potential VU methods were compared. This included the original VU scheme, as well as two versions that utilised an increased number of central k_z rays combined with faster drop-off towards the edge partitions. The three VU schemes, implemented with 75% slice-PF, were: VU(1)=(12-14-16-18-20-18-0-0), VU(2)=(8-12-16-20-24-20-0-0) and VU(3)=(4-10-16-22-28-22-0-0). The total number of rays for these three methods were therefore 98, 100 and 102 - resulting in a relatively consistent 3D SOS shot duration (difference $<$ 8ms).

The three VU methods implemented in the SOS sequence, along with the non-VU equivalent (20-20-20-20-20-20-0-0), were tested in Phantom C. The resulting images across all the slices are shown in Figure 5.14. The image quality remained fairly consistent between those acquired with the non-VU sequence and those acquired with all three of the VU methods. A slight improvement of in-plane sharpness is visible with increasing central ray number. However, against that benefit a drawback was noted. Examination of a line profile drawn horizontally through the central region of the phantom[2] demonstrated the negative impact on the partition-encoding fidelity (Figure 5.15). This was caused by the sharper drop-offs in ray numbers that are required because of the increased central ray number.

The outcome of these tests of the variable undersampling strategy was as follows: With a greater number of rays in the central partitions of k-space,

[2]This contained an oblique wedge of fluid signal that provides some indication of the partition-encoding fidelity. See Section 3.2.7 for phantom details.

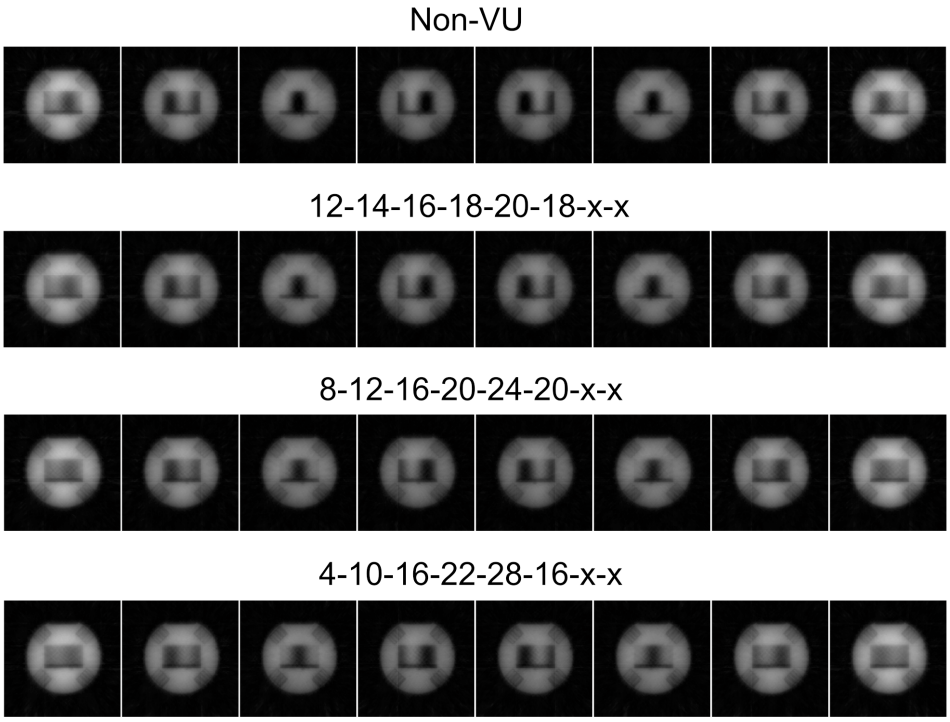

Figure 5.14.: All eight slices of a phantom dataset acquired with the three variable undersampling (VU) methods, as well as the non-VU method.

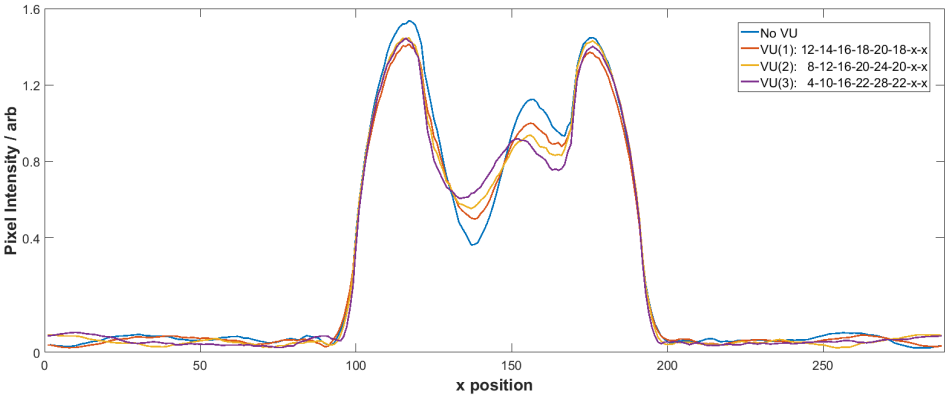

Figure 5.15.: Variable undersampling line profiles. A horizontal central line profile taken from the centre slice of the phantom images in Figure 5.14, plotted for each of the variable undersampling methods. With increased VU the line profile begins to smooth the oblique wedge variation, due to degraded partition voxel sharpness.

structures in the phantom that did not vary along the partition-direction showed an improved sharpness. However, the central "tilted wedge" of signal showed clearly that the partition-encoding was losing fidelity when applied with a steeper drop in ray-numbers. Therefore, the VU(2) scheme was selected as the compromise between providing clearer in-plane results and maintaining the partition-encoding accuracy. The application of the VU(2) scheme reduced the shot duration by 16.7% compared to the Non-VU scheme.

5.3.2. Reconstruction Modification

Optimisation of Reconstruction Weighting

Many iterative reconstruction methods require the selection of at least one weighting value, which "trades off" the measured data consistency against the introduction of other information in some form. This is the case with STCR, which minimises a total cost term that consists of a balance between the data fidelity and the satisfaction of various spatial and temporal constraints. Different weighting values can be applied to each of these constraints to control their relative impacts on the reconstructed images. The choice of the weighting value applied to a constraint is an issue due to its dependence not only on the reconstruction algorithm but also on its precise application. This requires the optimal weightings to be considered for every new sequence and application.

In the project work so far, weighting values had been chosen by visual inspection of reconstructions that were performed with different values. As the computational duration of each reconstruction was long (see *Reduction in Reconstruction Time* section, next), only a limited selection of potential weighting values could be studied. It was therefore quite possible that there was some uncertain deviation from the optimal weighting values. Earlier work (Section 4.3) demonstrated the potential for detrimental spatiotemporal effects of reconstruction with non-optimal weightings.

Most of the published work on the optimisation of reconstruction methods typically makes use of retrospectively subsampled data. This allows the root-mean square error of tested reconstructions to be compared with the reconstruction of the "ground-truth" data, that had been obtained by complete k-space sampling. Such a method could be applied in order to choose optimum weighting values for STCR, with the weights selected as those that minimised the total error. However, for this project, such ground

truth 3D FPP data clearly cannot be acquired at the temporal resolution required during FPP. Any attempt to do so would produce images with such different characteristics that any notionally optimal weights derived would likely no longer be applicable for the prospectively undersampled acquisitions. Therefore, this approach to optimising the weights was not adopted in this work.

Instead, the L-curve method [Hansen, 2000] is a technique for finding a weighting value that provides the best compromise between the terms being minimised, without the requirement for ground-truth data. The "L-curve" is a description of the parametric log-log plot of the two costs involved in the reconstruction method, where a point is plotted for each reconstruction that uses a different weighting value. The term L-curve is used due to the typical distribution of these points on the plot (Figure 5.16), with an elbow in the curve occurring around a certain weighting value. The weighting that yields the best compromise between the two costs is therefore near this corner, where both cost values remain low. The L-curve method has often been used for parallel imaging methods that employ regularisation, to explore the best compromise between the regularisation of the data and its fit to the original data [Ying et al., 2004]. For STCR, the L-curve method can be performed to find the best compromise between the terms in its cost function (Equation 4.3): the sparsity constraint (L_1-norm[3] cost term) and the data fidelity (L_2-norm cost term) [Adluru and DiBella, 2008].

For three *in vivo* datasets that had been acquired with the finalised 3D FPP SOS sequence (presented later, Section 5.3.3), reconstructions were performed with different weighting factors to produce L-curve plots. To optimise the temporal constraint weight value, the spatial constraint weights were set to zero, and a range of 15 temporal weights, α, were used. An initial series of temporal weights was chosen to give equal coverage over a large range, based on experience with the weights in earlier reconstruction of 3D SOS FPP datasets. Following the results from the initial series, more weights were then chosen in the segment of most interest along the curve, i.e. traversing the corner. The same final set of weights were used to reconstruct all three datasets.

Figure 5.17 shows the L-curves for the three datasets, using the same axes. The values of the norms can be seen to vary between the datasets, but the location of the "elbow" in the L-curve was in a relatively consistent

[3]The L symbols used for defining norms are unrelated to the "L" in the L-curve name.

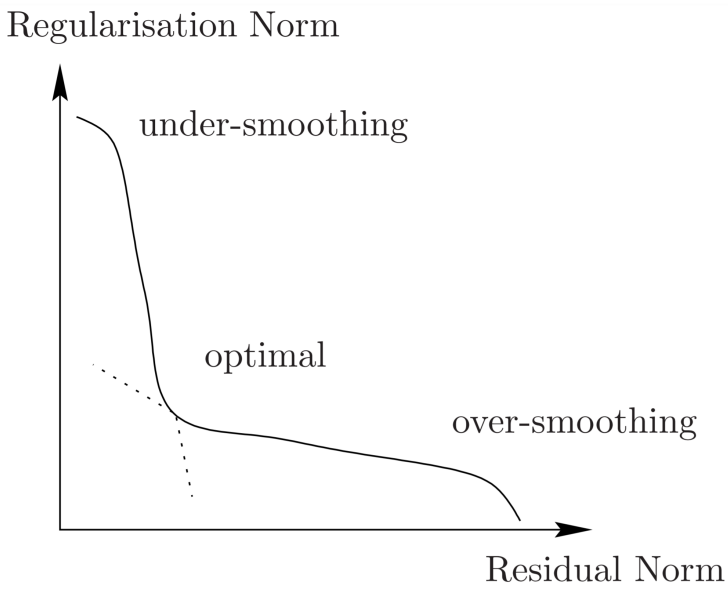

Figure 5.16.: The L-curve appearance. An L-curve, as often used in regularised parallel imaging, will typically follow the above pattern. An optimal weight value will produce a point in the 'corner' region of the curve. This provides a compromise between fitting to the original data (data fidelity) and to some other information (regularisation, or for STCR - spatio-temporal constraints). Reproduced from [Pullan et al., 2010].

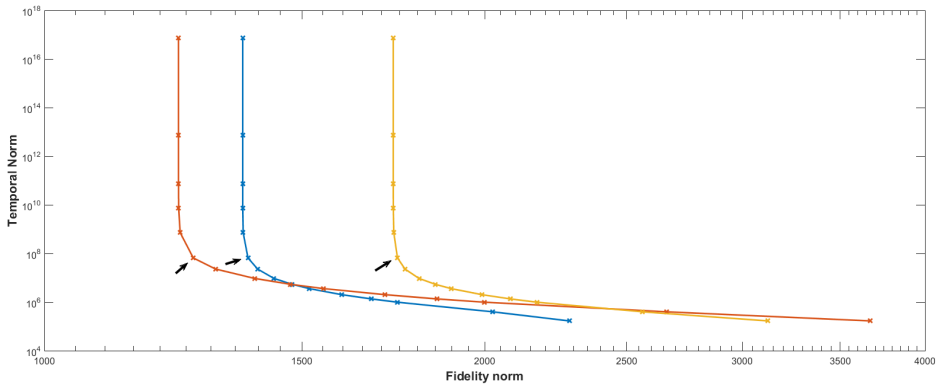

Figure 5.17.: L-curves for 3D SOS FPP *in vivo* datasets with STCR. The α weight values used to produce each point on the curve (from top-left to bottom-right) were: 1.0×10^{-13}, 1.0×10^{-9}, 1.0×10^{-7}, 1.0×10^{-6}, 1.0×10^{-5}, 1.0×10^{-4}, 2.5×10^{-4}, 5.0×10^{-4}, 7.5×10^{-4}, 1.0×10^{-3}, 1.5×10^{-3}, 2.0×10^{-3}, 2.5×10^{-3}, 7.5×10^{-3}, 1.0×10^{-2}. $\alpha = 1.0 \times 10^{-4}$ was selected as the final weighting value, marked on each curve by an arrow.

temporal weight range. Both $\alpha = 1.0 \times 10^{-4}$ and 2.5×10^{-4} appear in this corner region for each case. Mathematical methods exist to accurately determine the weighting value at the corner of such curves, technically the point of maximal curvature [Hansen, 2000], but a manual selection was considered sufficient for this work. The temporal constraint weight was chosen as 1.0×10^{-4}. The points with this weight for all 3 datasets are shown with arrows.

Spatial constraints (both in-plane and through-plane) were now also planned for inclusion in the STCR method, which had not been used up to this point in the project. After setting of $\alpha = 1.0 \times 10^{-4}$, the entire L-curve plotting process was repeated first for the in-plane spatial constraint weight (β) and then the through-plane spatial constraint weight (γ). From those L-curves (not shown), the weights were set as $\beta = 7.5 \times 10^{-5}$ and $\gamma = 5 \times 10^{-5}$.

As explained above, the L-curves were only examined for three patient datasets. A complete reconstruction with a large number of iterations is required for the calculation of each data point on the curve, and so the generation of the L-curve plots was time intensive. In addition, a fixed choice of the weighting values was desired as early as possible in the *in vivo* testing (Section 5.3.3), to give consistency of reconstruction effects whilst sequence-related variations in the datasets were being examined. The

literature has previously suggested that the optimised weighting values are robust for a given application [Adluru et al., 2007][Adluru et al., 2009], and the good agreement between the corner weight values for three curves in the three datasets examined here gave confidence that the appropriate values had been identified.

Reduction in Reconstruction Time

The total reconstruction time for a full *in vivo* 3D dataset with STCR had, up to this point, been prohibitively long for guaranteed same day viewing. The potential for reduction in reconstruction time was therefore seen as particularly important for the move towards clinical testing.

A large number of receiver channels (typically 18-34) were acquired with the coil arrays used for the *in vivo* imaging work in this project. While a larger number of channels is generally seen as beneficial, as they can potentially generate improved SNR and aid in PI techniques, not all of the information contained within the full set of channels is necessarily useful. In addition, a large number of channels, particularly when combined with already large datatsets, significantly increases the duration and computational memory requirement of the reconstruction. "Channel compression" methods have therefore previously been proposed [Buehrer et al., 2007], that reduce the number of effective channels (or "virtual channels") that are used in the reconstruction process. Principal component analysis (PCA) has been suggested as one such channel-reduction method, which can compress the data into a preset number of principal components to be used as the new virtual channels [Huang et al., 2008]. Such a method has previously been demonstrated to be effective for the STCR reconstruction with 2D FPP data [Adluru and DiBella, 2012], and was implemented in this project from this point forwards, with a reduction of the data to 8 'channels'.

For use with STCR, the "pre-interpolation" method (discussed in Chapter 4) was also implemented from this point forwards, rather than the repetitive use of NUFFT for each iteration. Pre-interpolation slowed down the initial stages of the reconstruction but dramatically sped up each iteration, leading to a sharply reduced total reconstruction time. With inclusion of the channel-reduction method, approximate STCR reconstruction times[4] for a 60 frame 3D FPP dataset were: 3mins for initialisation + 2.0mins/iteration (NUFFT interpolated STCR), and 15mins for initialisation + 0.17mins/iteration

[4]On a workstation with a 10-core Intel Xeon (3.0GHz) processor and 64GB RAM.

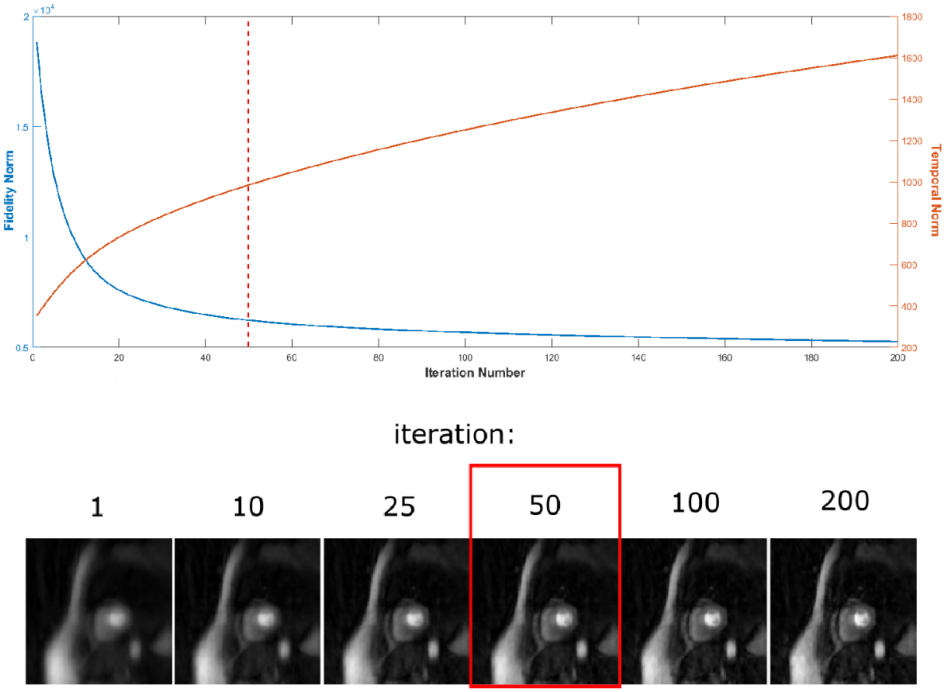

Figure 5.18.: Reconstruction variation with iteration number. For the final selected weight values, the fidelity norm can be seen to reach a stable level after relatively small number of iteration, while the temporal norm continues to rise. An example image is shown at various iteration numbers, including the selected 50 iteration case.

(gridding pre-interpolated STCR).

From the investigation of the weighting optimisation (Section 5.3.2) it was also decided that the number of iterations used for each reconstruction could be reduced. For the investigated datasets reconstructed with the chosen weighting values, the temporal and fidelity norm costs could also be plotted at each iteration (Figure 5.18). The stabilisation of the fidelity norm as the iterations progressed was consistent across the datasets and suggested that the reconstruction process could be terminated after 50 iterations without significant impact on the image appearance. Examples of an *in vivo* dataset reconstructed with the selected weights (Section 5.3.2) are shown for different STCR iteration numbers in Figure 5.18.

A typical total reconstruction time for the *in vivo* 3D SOS FPP datasets with these above factors was <25 minutes.

5.3.3. A Finalised 3D FPP Method

Summary of Parameters

The 3D SGRE stack-of-stars sequence was now held constant for subsequent *in vivo* acquisitions, with the parameters as described in this section. Sequential acquisitions of the rays were performed for SOS coverage, employing asymmetric echo (75%), slice partial Fourier (75%), and other previously described methods to enable a T_E of 0.98ms and T_R of 1.88ms. With the selected partition-dependent VU method (8-12-16-20-24-20-0-0), the total shot duration was 188ms. The saturation recovery time was kept at 150ms and the flip-angle was 12°. The nominal acquired resolution with these parameters was 2.1x2.1x10.0mm.

Reconstruction of the FPP datasets used the pre-interpolated STCR algorithm, using PCA-based channel reduction to eight 'coils', with weightings: $\alpha = 1.0 \times 10^{-4}$, $\beta = 7.5^{-5}$ and $\gamma = 5.0 \times 10^{-5}$. This was performed for a fixed $N_{iterations} = 50$.

After STCR reconstruction, zero-padding was performed in k-space for the partition-encoding direction, to double the number of viewable slices.

In vivo Testing

Throughout the development of the sequence for this project, extensive *in vivo* testing was performed. This enabled examination of the quality of the sequence while modifications to the trajectory and other sequence considerations were implemented.

The majority of these tests were in patients who were under clinical care to monitor myocardial tissue health and cardiac function during treatment for cancer, who had been referred to MRI for clinical LGE without other perfusion or angiography scans. All patient tests were only conducted after the patient was asked by the PhD candidate for informed consent to have the additional research MRI scans performed during the GBCA injection and for the use of power-injection. The availability of such successful recruitment was highly variable, sometimes extending the time period required to perform the desired number of *in vivo* tests. In total, 42 3D FPP *in vivo* acquisitions were performed for the development of the sequence, excluding those described elsewhere in this thesis.

Five additional patients were recruited in this manner to test this finalised sequence, with no adjustments made to the sequence, reconstruction or

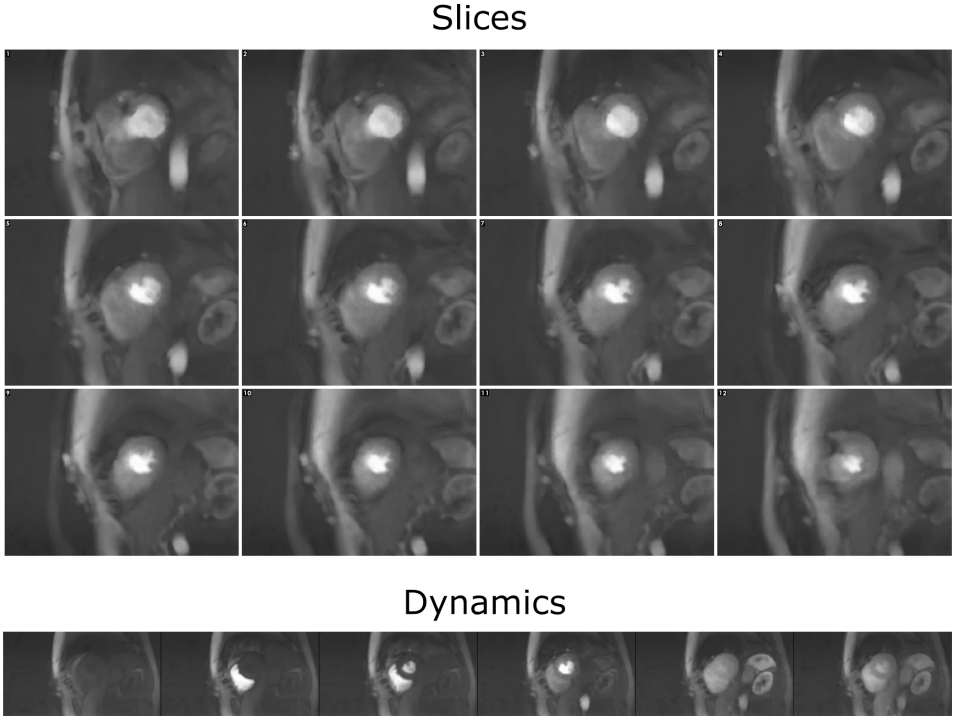

Figure 5.19.: Example *in vivo* dataset with the final selected sequence and reconstruction parameters. On the top, 12 reconstructed slices (base to apex) are shown for a single frame. Below a single slice is shown at different frames during the first-pass.

acquisition method. This was to enable the robustness and typical imaging quality of the finalised method to be determined before acquisitions at stress were scheduled to begin, for which subjects were even more difficult to recruit.

An example acquisition is shown in Figure 5.19, which demonstrates 12 reconstructed slices of a single perfusion frame for one of the patients. The image quality remained consistent across the five datasets, which supported the continuation to testing at stress. The transient dark artefacts, that had been encountered in earlier *in vivo* work, were notably still present in some of these resting datasets.

6. Clinical Validation

Various methods for extending myocardial first-pass perfusion (FPP) to whole-heart coverage with 3D imaging have been demonstrated earlier in this thesis (Chapter 5). As well as examination of novel acquisition strategies, attention has been given to optimisation of the quality and robustness of the sequence. Minimisation of the shot duration has been given particular focus because one of the biggest challenges in implementing 3D FPP is believed to be the substantial increase in this duration comparative to 2D FPP. However, until *in vivo* testing at stress is performed it is difficult to know how these acquisitions will cope with increased heart-rates and respiratory motion. Likewise, while imaging quality and reconstruction effects have been investigated, the diagnostic capabilities of these techniques cannot be certain until testing is performed in clinical populations against established diagnostic methods.

This chapter takes the sequence and reconstruction methods that were developed over the thesis and finalised at the end of the previous chapter (Section 5.3.3), and investigates their application at stress in both healthy and diseased subjects.

6.1. Introduction

To investigate the true capability of the 3D SOS FPP sequence, clinical testing is required at stress and in patient populations with known or suspected CAD. 3D radial sequences have yet to be tested at stress for FPP, and so assessment needs to be made of factors such as their respiratory and cardiac motion robustness. Similarly, compressed sensing has yet to be used in 3D FPP in clinical populations, where previous studies utilised the k-t class of methods in Cartesian modes, and so this work will also be important in determining the ability of compressed sensing to identify induced perfusion defects in highly undersampled datasets. The introduction of free-breathing is another development in this work which has not previously been explored in a clinical scenario for 3D FPP.

As reviewed in Chapters 1 and 2, the clinical validity of FPP has previously been tested with 2D multi-slice acquisitions in many large studies [Schwitter et al., 2012][Greenwood et al., 2012], against diagnostic reference standards including CXA, SPECT and PET (Section 1.5.4). The k-t SENSE/PCA approaches to Cartesian 3D FPP have begun to undergo clinical testing, primarily using CXA measures as well as a recent study also containing SPECT myocardial perfusion scintigraphy (MPS) (Section 2.5.2). The choice of diagnostic method for comparison with MRI can be difficult and is sometimes ultimately driven by availability. CXA is the gold-standard in terms of interventional decision making, but does not examine perfusion limitations in the same way as FPP. CXA also has the further complication of potentially biasing the recruited patient population towards those with stronger perfusion defects, if it is used as a required reference standard for a comparison study. MPS is possibly the most comparable method to FPP, in that both directly image myocardial perfusion, but it has shown only equal or lower diagnostic performance in predicting CAD comparative to traditional 2D multi-slice FPP [Chen et al., 2014a], so some caution is required when using this as a reference standard.

In this work, the 3D SOS FPP sequence was used to acquire datasets at stress and rest in both healthy volunteers and patients with suspected CAD. The latter also underwent a standard clinical stress and rest protocol with SPECT MPS, which acted as a reference for comparison of potentially detected induced perfusion defects.

6.2. Methods

6.2.1. Experimental Design

A stress MRI protocol was designed for consistent scanning of each subject with the 3D SOS FPP sequence, based upon the typical procedures described in Section 1.5.3.

After initial "scout" acquisitions, where the patient table was moved so that the mid-LV was at the isocentre plane (z=0), typical LV cines were acquired. The stress 3D FPP acquisitions were planned from these cines with the LV centred in the volume to be imaged, and a trigger delay was set so as to aim the timing of the central k-space acquisition optimally against LV myocardium motion (during the mid-systolic pause).

A trial run of the planned 3D FPP sequence was acquired and reconstructed

to ensure correct planning (e.g. position and coil selections), and that no gradient system errors or nerve stimulation warnings occurred, as these can be dependent on cardiac orientation. The trial run was also used to confirm that the 3D FPP cardiac gating was performing satisfactorily during sequence operation, as a good basic trigger strength was essential to withstand any extra stress-related challenges to the ECG-detection system. To enable a fast check of the trial run images, their reconstruction was made only by gridding, without STCR.

Following an acceptable 3D FPP trial result, administration of adenosine (140μg/kg/min) was started, during which the subject's cardiac rhythm, heart-rate, blood pressure and symptoms (such as breathlessness and angina) were monitored by a clinician. Approximately six minutes was used as the expected duration required to achieve the appropriate effect, although the subject's physiological response was also taken into consideration in determining when this had been reached. At approximately half the time to this full effect, a mid-LV SAX cine was acquired, modified to acquire during free-breathing by taking highly accelerated multiple averages of the cine over 12 cardiac cycles. Final modifications could then be made to the 3D FPP trigger delay, based on changes in the time to systole observed from the cine images. The FPP sequence was applied during free-breathing with the continued infusion of adenosine, capturing the first-pass of 0.1mmol/kg antecubital power-injected Gadobutrol at 3ml/s, with 20ml saline flush at 5ml/s. Adenosine infusion was then halted and the subject was checked for the dissipation of the effects. After 10 minutes, acquisition of an LV stack of late gadolinium enhancement (LGE) images commenced. After >20 minutes post-injection of the first dose of gadolinium, the FPP sequence was repeated exactly as before, but without the inducement of stress, to provide the "rest" dataset.

The 3D stack-of-stars sequence (Figure 6.1) was used for the FPP acquisitions. The sequence and reconstruction parameters were as previously described (Section 5.3.3).

6.2.2. Healthy Volunteers

Four volunteers with no suspected CAD or other cardiac conditions were recruited for the stress/rest 3D FPP protocol. These acquisitions aimed to provide initial validation of the sequence acquisition under stress, and were performed using an identical procedure as planned for the patients with

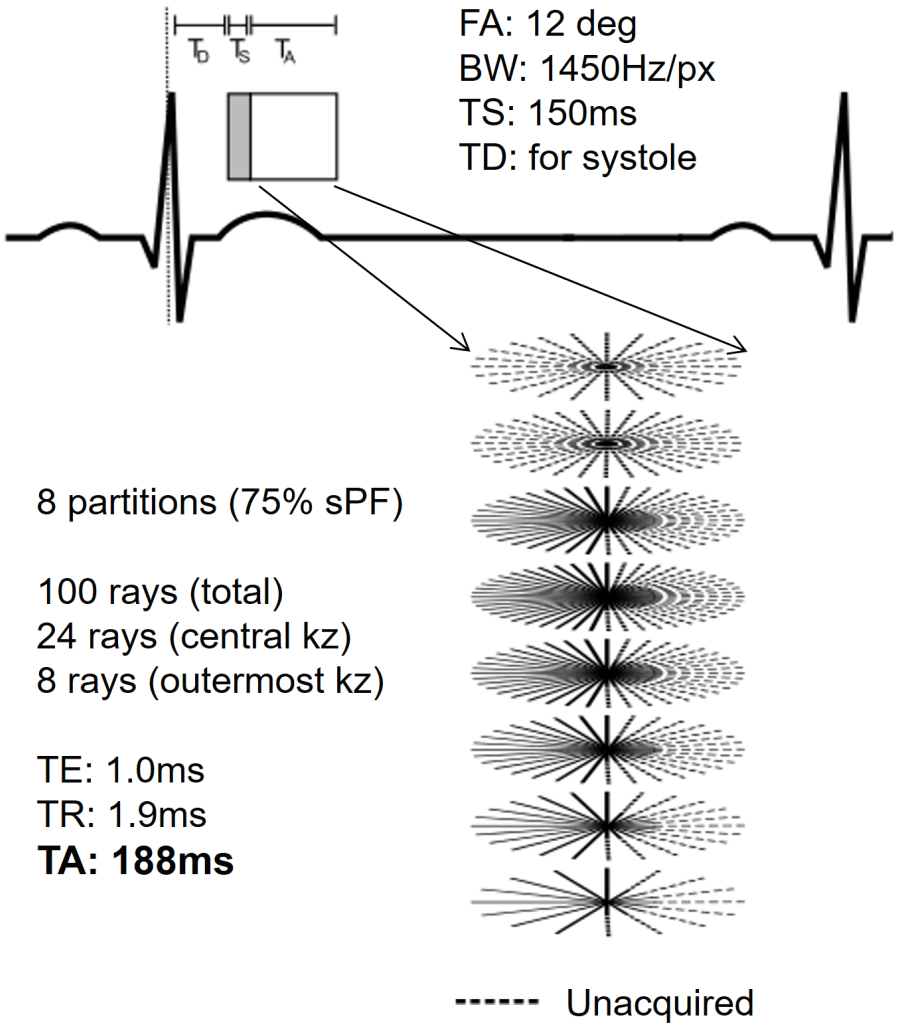

Figure 6.1.: Finalised 3D SOS FPP sequence. A full description of the sequence parameters can be found in Section 5.3.3.

suspected CAD.

6.2.3. CAD Patients

Patient Recruitment

Five patients were recruited for the stress/rest 3D FPP protocol. The patients were selected after their clinical referral for an MPS scan, and were chosen so as to explore a range of severities of coronary artery disease. This was in order to test the response range of 3D SOS FPP compared to MPS. Exclusion criteria prior to invitation to participate in the MRI research scan included arrhythmia, and other contraindications to MRI, adenosine or GBCA. The MRI was scheduled so as to be $\leq$6 weeks after the MPS scan.

The patient history and information was available and reviewed by a clinician to check for the suitability of participation. Additional information, such as any other relevant recent imaging tests if available, was identified at this point.

Informed consent was requested subject to the research ethical approval, using the materials in Appendix B.

SPECT Acquisitions

Technicium-99m tetrofosmin (Myoview, GE Healthcare, USA) SPECT MPS was performed on the patients with the standard clinical protocol. Four patients were scanned on a D-SPECT (Spectrum Dynamics, Israel) solid-state gamma camera and one patient was scanned on a CardioMD (Phillips, Netherlands) conventional gamma camera.

All patients were imaged with a 1-day stress and rest protocol, using a 250MBq dose at stress and a 750MBq dose at rest. Adenosine or regadenson was used as the primary vasodilator (depending on clinical indication) and the Technicium-99m tetrofosmin was injected three minutes into the infusion of adenosine, or 90 seconds after the regadenoson injection. Image acquisition was started 60 minutes after the injection of the tracer and at least three hours were left between the tracer injections for the stress and rest acquisitions.

On the D-SPECT camera dual supine and upright stationary acquisitions were acquired[1], which lasted for approximately six minutes at stress and three minutes at rest. The CardioMD scanner, equipped with an all-purpose collimator, acquired 64 projections over 180° while the patient was supine,

[1]Dual acquisition approach used to aid artefact detection.

which lasted approximately 20 minutes. A 20% symmetrical energy window was used at 140keV. Attenuation correction was applied.

6.2.4. Analysis Methods

The difficulty in subject recruitment for stress FPP meant that only a small number of datasets could be acquired in the >12 months that recruitment was attempted, both for the healthy volunteers and the suspected CAD patients. With such a small population size, there is little benefit in applying tests for statistical significance for any quantitative measures of induced perfusion defects made from the images (e.g. between 3D SOS FPP and MPS). In general, definitive conclusions about either the success or failure of the method are unlikely to be possible at this novel stage of sequence acquisition with the limited number of volunteering patients. Nevertheless, these acquisitions provide the first trials to detect inducible myocardial perfusion defects with the sequence and reconstruction methods of this type and it was hoped that some insights could be gained into the clinical feasibility of this technique.

Therefore, examination is made in this chapter on a case-by-case basis with visual analysis performed for each FPP dataset to identify potential perfusion defects and artefacts, or in healthy subjects artefacts alone. In the case of the CAD patients, the 3D FPP datasets were also compared with the MPS results, and any other available clinical imaging test results.

The MPS datasets were viewed using the Quantitative Perfusion SPECT (QPS) software (Cedar-Sinai, USA). The software generated automatic estimation of induced defect size, previously shown to have good accuracy [Slomka et al., 2005], which was used to categorise the severity of suspected CAD. Severe ischaemia is classified as a total volume >10%, moderate ischaemia as 5-10%, and mild ischaemia <5% [Task Force Members et al., 2013].

6.3. Results

6.3.1. Healthy Volunteer Results

All four subjects were successfully scanned (Figure 6.2), with reconstructions tolerating the wide range of respiratory motions in both rest and stress. At stress imaging the heart rates reached up to 97bpm. Good coverage of the LV myocardium was achieved in all cases (for example, Figure 6.3).

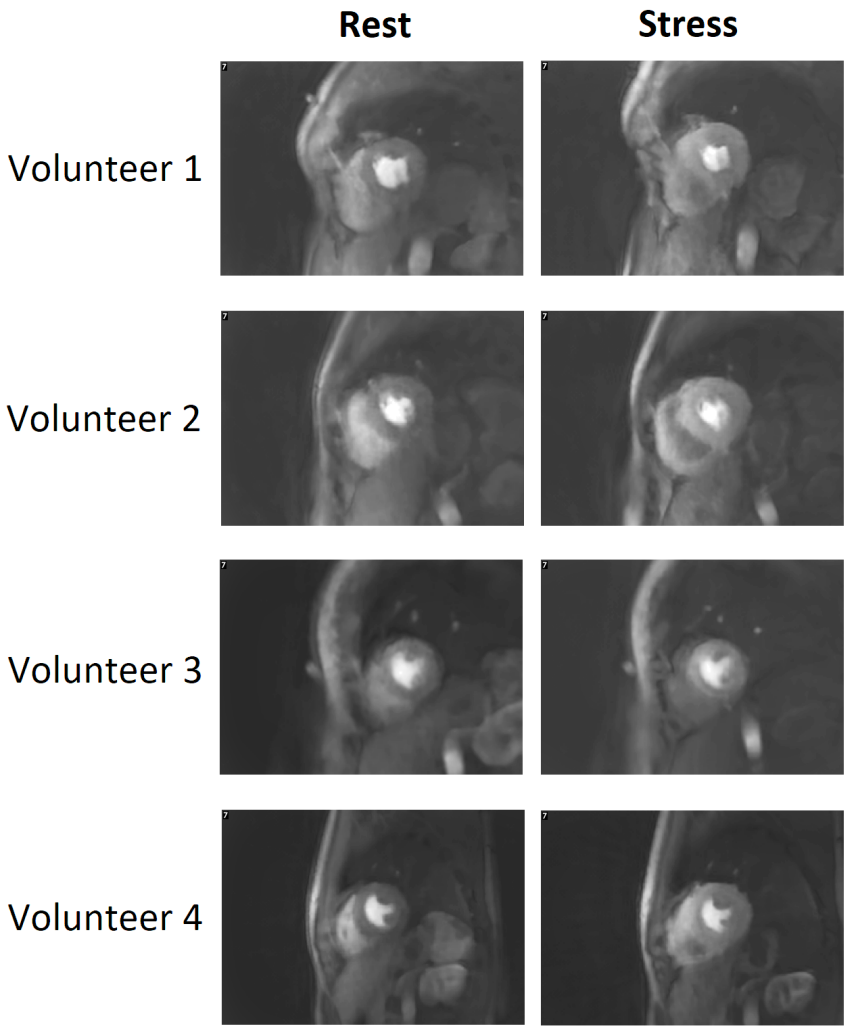

Figure 6.2.: An overview of the four healthy volunteer subjects, demonstrating a single central slice at a single time point for each, at both rest (left) and stress (right).

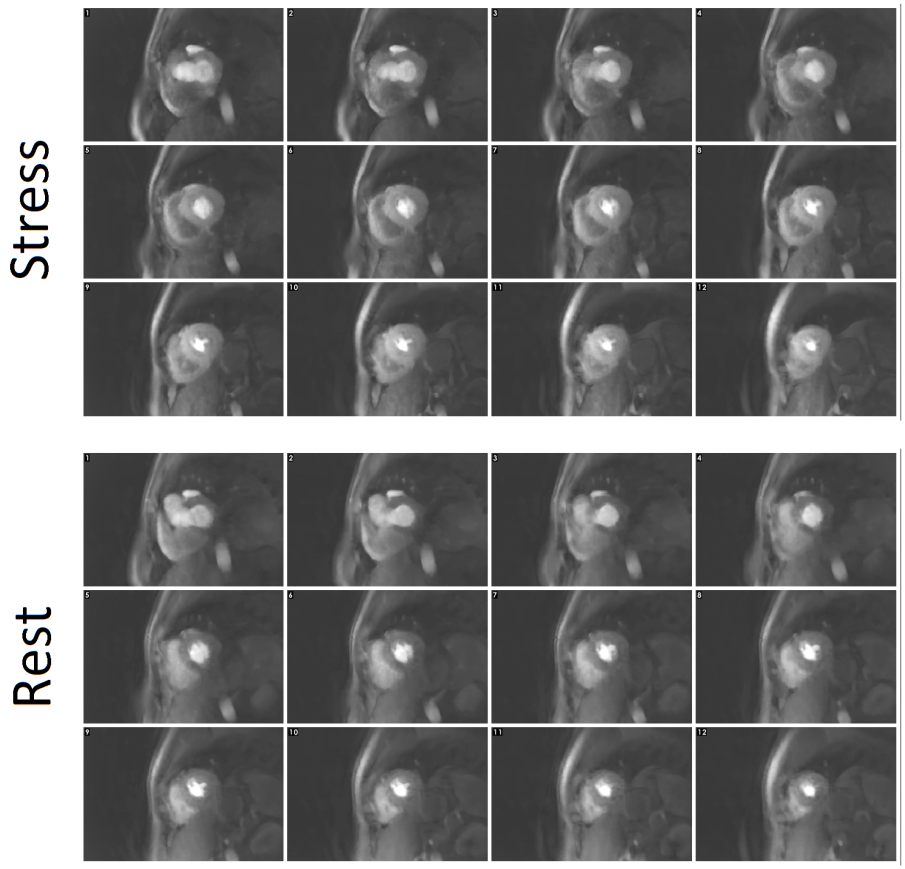

Figure 6.3.: Example healthy volunteer dataset showing 12 reconstructed 5mm slices from base (top left) to apex (lower right) of a single frame at stress (top) and rest (bottom).

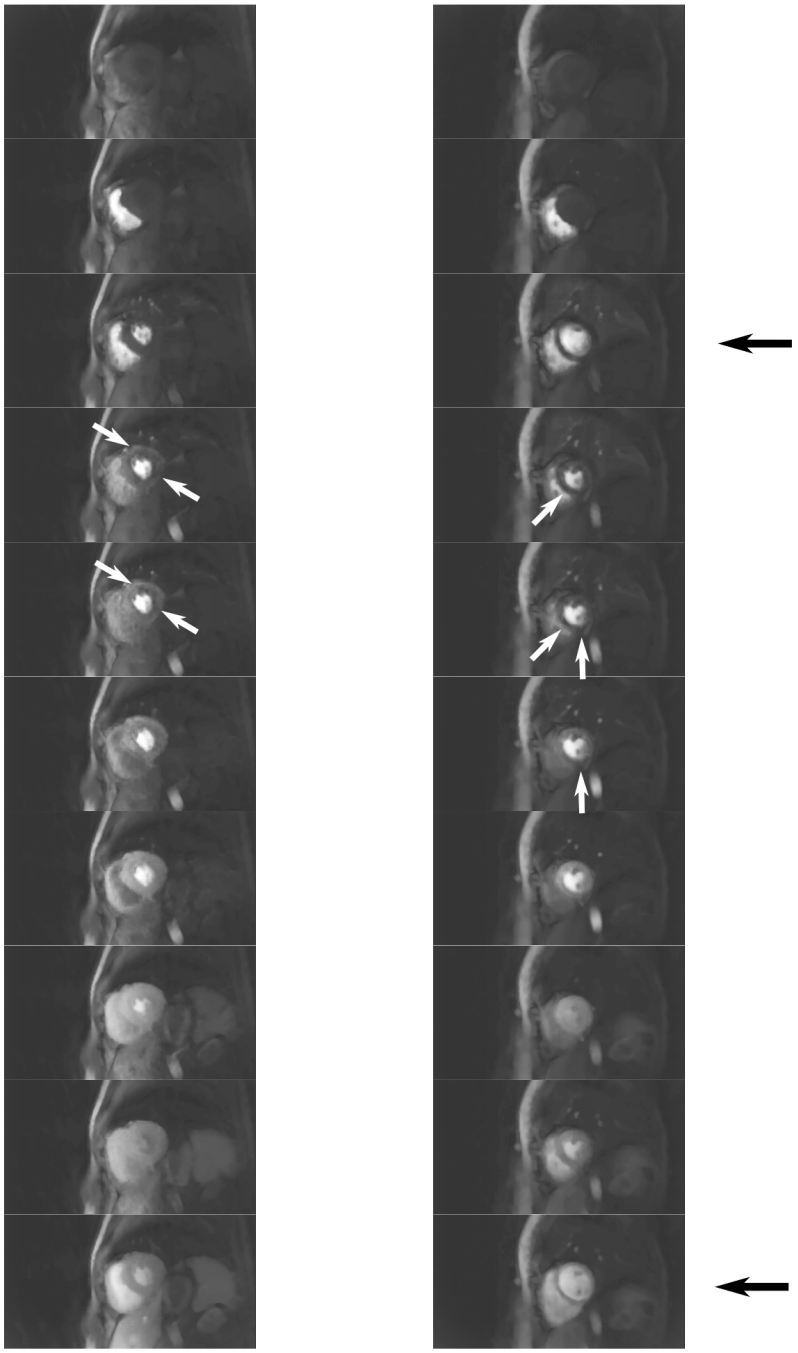

Figure 6.4.: GBCA arrival dynamics in healthy volunteers. Selected frames to demonstrate the arrival of the GBCA (top to bottom) in two healthy volunteers, at stress. Both datasets demonstrate artefacts with a dark-patch appearance (white arrows), which occur during the arrival of the GBCA into the LV myocardium but quickly dissipate, apparently as the myocardium brightens. The dataset on the right also contains frames where mis-triggering has occurred (black arrows).

Myocardial dark artefacts can be seen in 2 of the datasets during the arrival on the GBCA into the LV myocardium (Figure 6.4). The artefacts match those previously seen at rest with the 3D SOS FPP sequence, remaining for 2-3 frames before dissipating as the myocardial intensity becomes brighter with more GBCA perfusing into the myocardium. In addition, one of these datasets suffered from poor ECG-triggering at stress (Figure 6.4), likely due to the connection of the ECG leads. This sensitivity to ECG placement observed during the volunteer scans guided subject preparation and careful setup for the suspected CAD patients.

Following satisfactory performance on volunteers, it was decided to continue into patient tests.

6.3.2. CAD Patient Results

Four out of the five patients completed the stress protocol successfully. One patient had an adverse reaction to adenosine which led to immediate termination of the adenosine infusion and abandonment of the protocol, prior to initiating the FPP acquisitions.

The four successfully imaged patients were classified by their MPS results as having mild, moderate or severe stress-induced ischaemia, based upon the description in the methods. The four patients are labelled as Patient 1-4, in the order they are presented[2].

Severe Ischaemia Detection

One patient scanned was classified by MPS as having severe stress-induced ischaemia (Patient 1). The MPS images at stress (Figure 6.5) showed a strong septal/infero-septal defect basally and a milder infero-lateral defect apically, that did not occur at rest.

The stress FPP images showed clear, persistent hypointense regions, closely matching with the MPS regions of interest, which were not present in the rest dataset (Figure 6.6).

The strength and persistence of the hypointense regions can clearly be seen in the dynamics of the dataset (Figure 6.7). Some additional hypointense regions, which occurred during the first arrival of the GBCA into the LV

[2]Every effort has been made to present the FPP dynamics clearly, but owing to its particular importance in these datasets, movie files have also been made available in Appendix C.

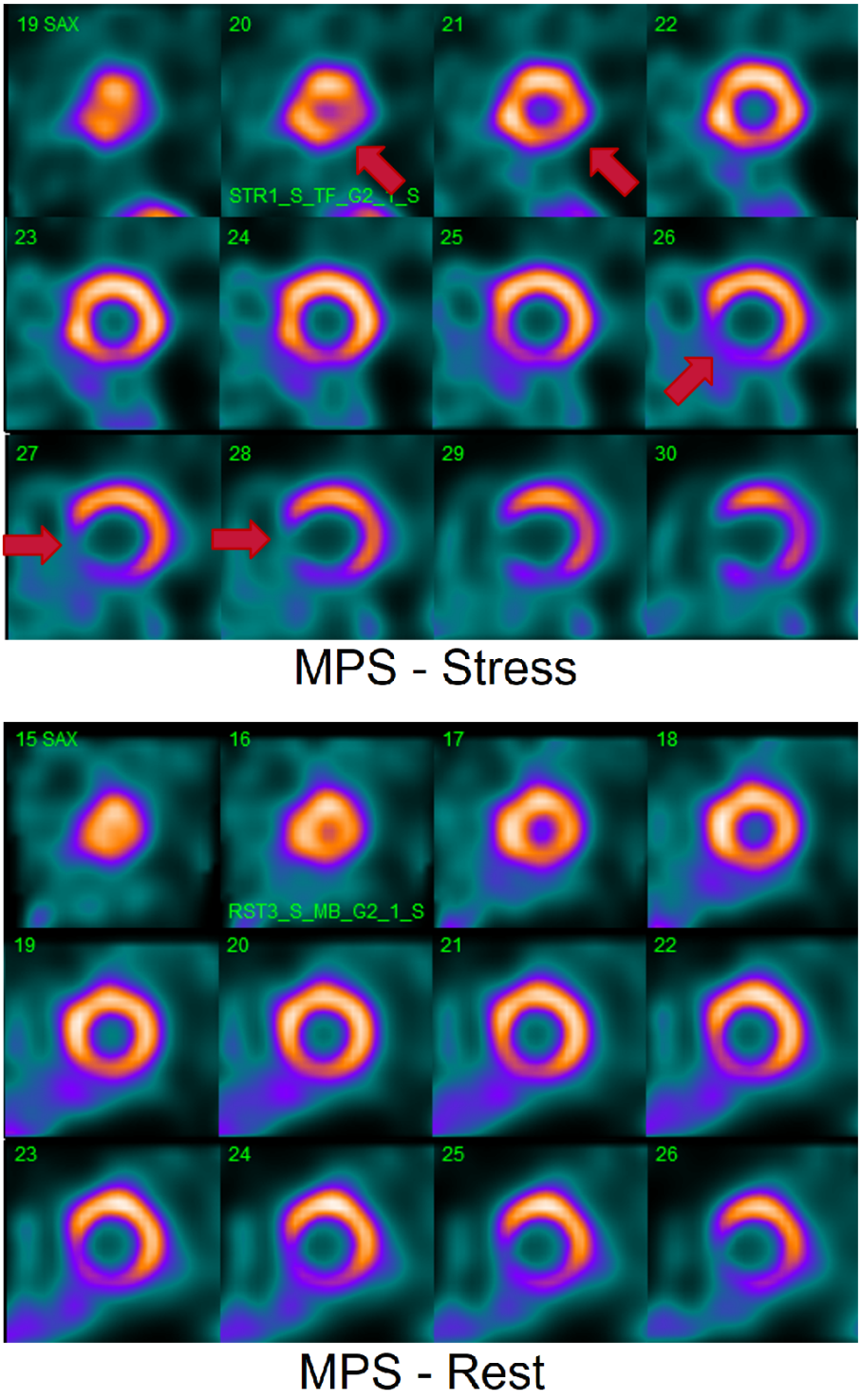

Figure 6.5.: MPS images for Patient 1. The stress (top) and rest (bottom) MPS images for a patient, judged to have severe inducible ischaemia. A strong septal/infero-septal defect can be seen in the base-to-mid slices, as well as a milder infero-septal defect in the apical slices.

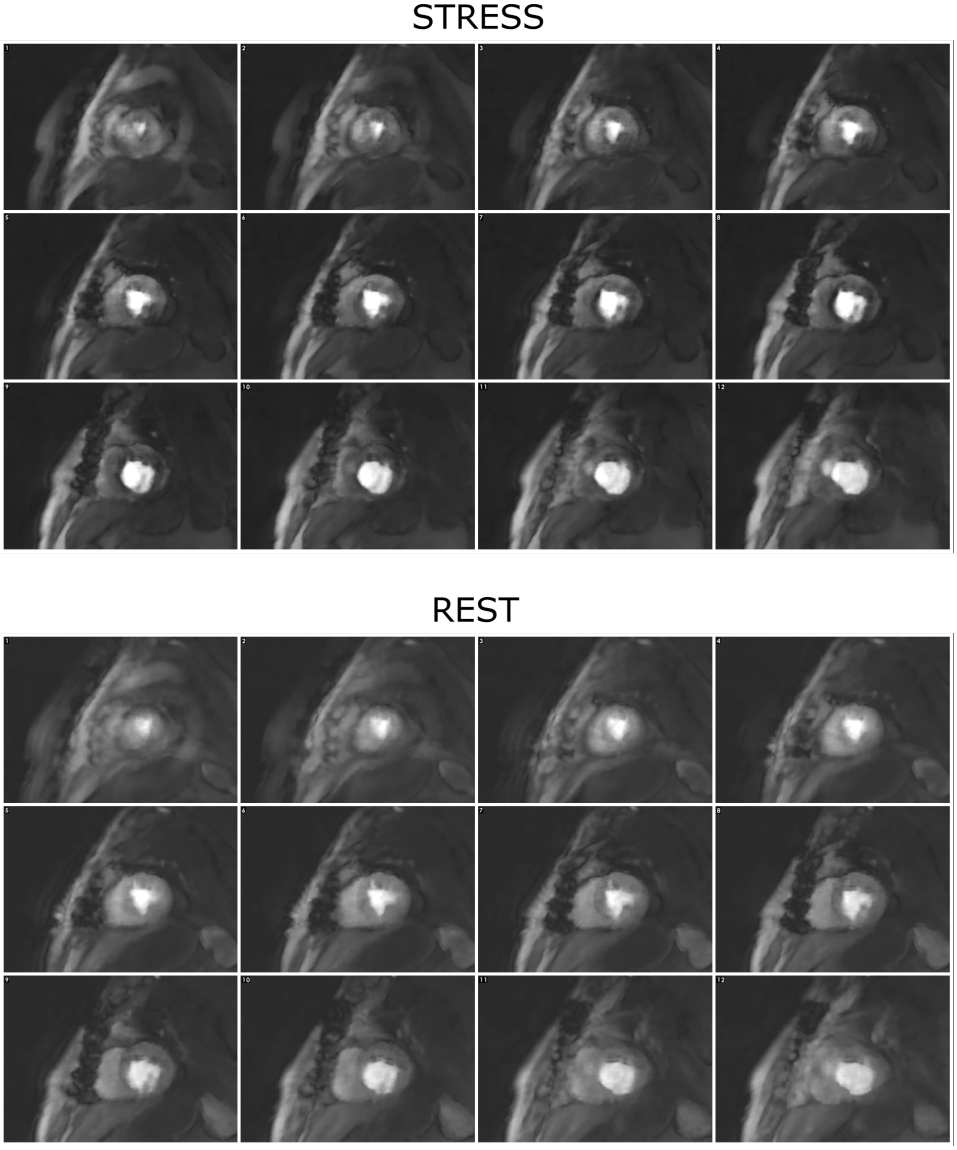

Figure 6.6.: FPP images for Patient 1. The stress (top) and rest (bottom) 3D SOS FPP slices, for one perfusion frame. These are ordered so as to be as close as possible to their MPS equivalent (Figure 6.5). Hypointense myocardial regions can be seen, including in locations that match with the MPS data. Examination of the temporal dynamics (Figure 6.7 and Appendix C) is required to identify the persistence of these hypointense regions.

myocardium before rapidly dissipating, were similar in appearance to the artefacts identified in the healthy volunteer datasets.

This patient had also undergone recent CXA, which was able to confirm that the patient had substrates for ischaemia in all three coronary territories (Figures 6.8 - 6.10). This is in agreement with the FPP images.

Moderate/Mild Ischaemia Detection

From the MPS definitions, one patient was classed as moderate, while the other two were classed as mild.

The moderate CAD patient (Patient 2) showed an apparent inferior/infero-lateral defect in the basal to mid-ventricular images, which matched well with the MPS scan (Figure 6.11). Again, transient myocardial artefacts were visible during the contrast arrival (Figure 6.12), however this hypointensity was only persistent in regions of the myocardium that matched spatially with the MPS defects.

In the first mild CAD patient (Patient 3), agreement was not found between the stress FPP and MPS images (Figure 6.13). The stress FPP dataset showed a smooth, consistent uptake of GBCA quite uniformly over the LV (Figure 6.14), with no obvious hypointense regions to match the antero-septal defect suggested by the MPS.

The second mild CAD patient (Patient 4), had images of a poor visual quality comparative to the other datasets, partly due to mistriggering at stress. The very mild (1%) defect demonstrated by MPS was not clearly visible on the stress FPP (Figure 6.15), with increased artefacts during contrast arrival (Figure 6.16).

6.4. Clinical Validation Discussion

6.4.1. Diagnostic Capability

In this small sample size of four, the overall performance in comparison to MPS appeared to be mixed.

The severe CAD case was, unsurprisingly, the easiest in which to determine the presence of a perfusion defect and inspection of the MRI datasets showed good agreement with MPS and CXA. The longer persistence in time of the stress-induced defects in this case helped with their identification. This and the transmurality of the defects in this severe case enabled easy differentiation from image artefacts.

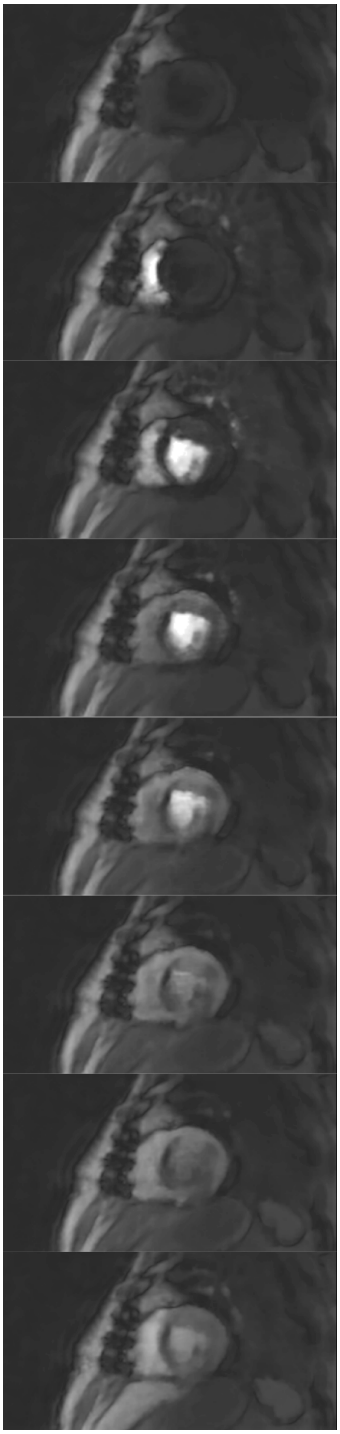

Figure 6.7.: Temporal dynamics of the FPP: Patient 1. For a single slice of the Patient 1 stress FPP, multiple frames of the first-pass of the GBCA are displayed.

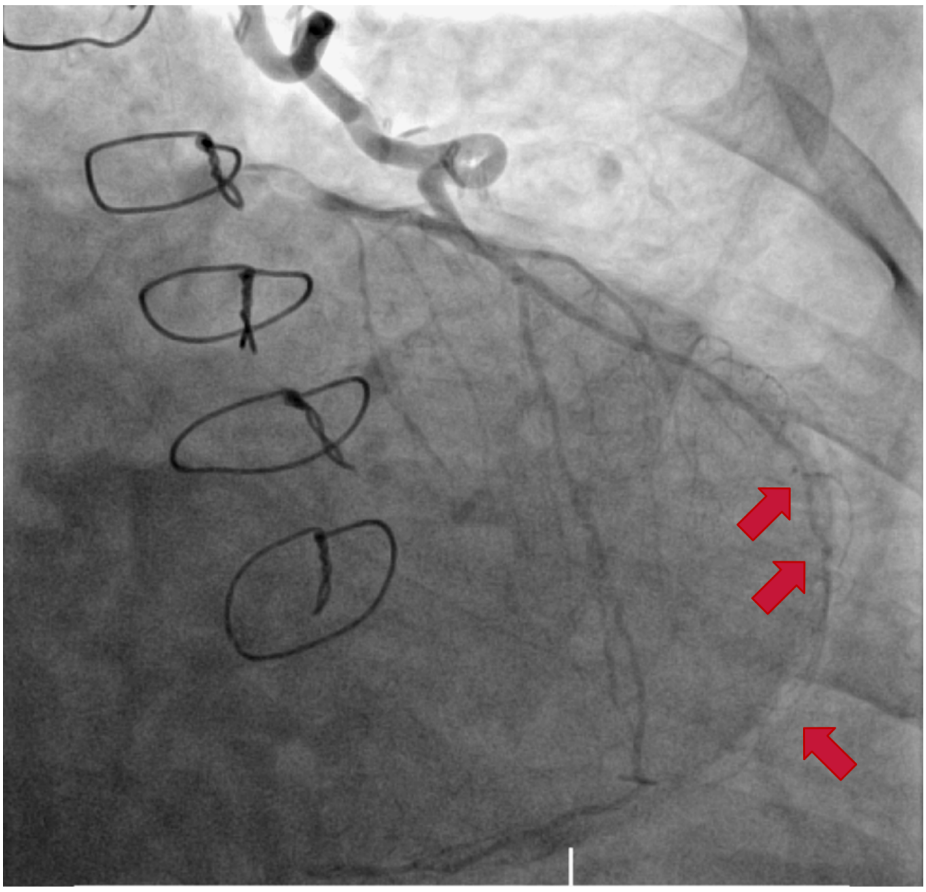

Figure 6.8.: CXA of the left anterior descending coronary artery for Patient 1. Examples of the diffuse disease of the vessels are marked by red arrows. Sternal wire loops are visible, which did not disrupt the SGRE 3D SOS FPP method.

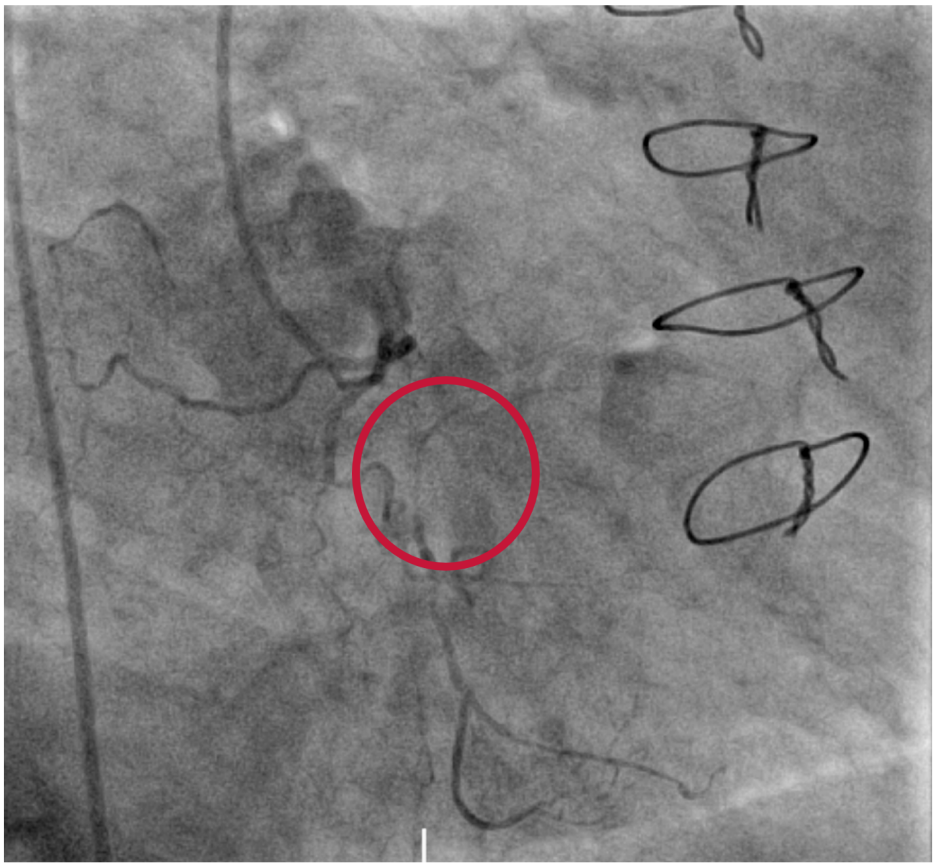

Figure 6.9.: CXA of the right coronary artery for Patient 1. An area of occlusion is marked by the red circle.

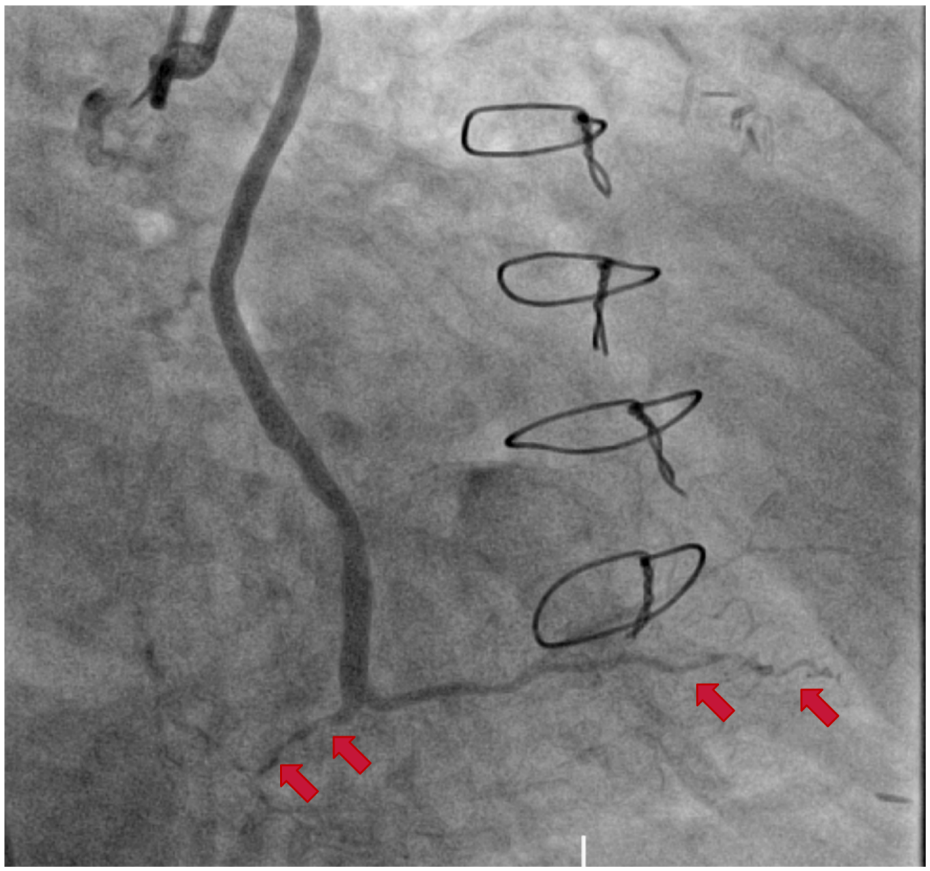

Figure 6.10.: CXA of the left circumflex artery for Patient 1. Examples of distal disease of the vessel are marked by red arrows.

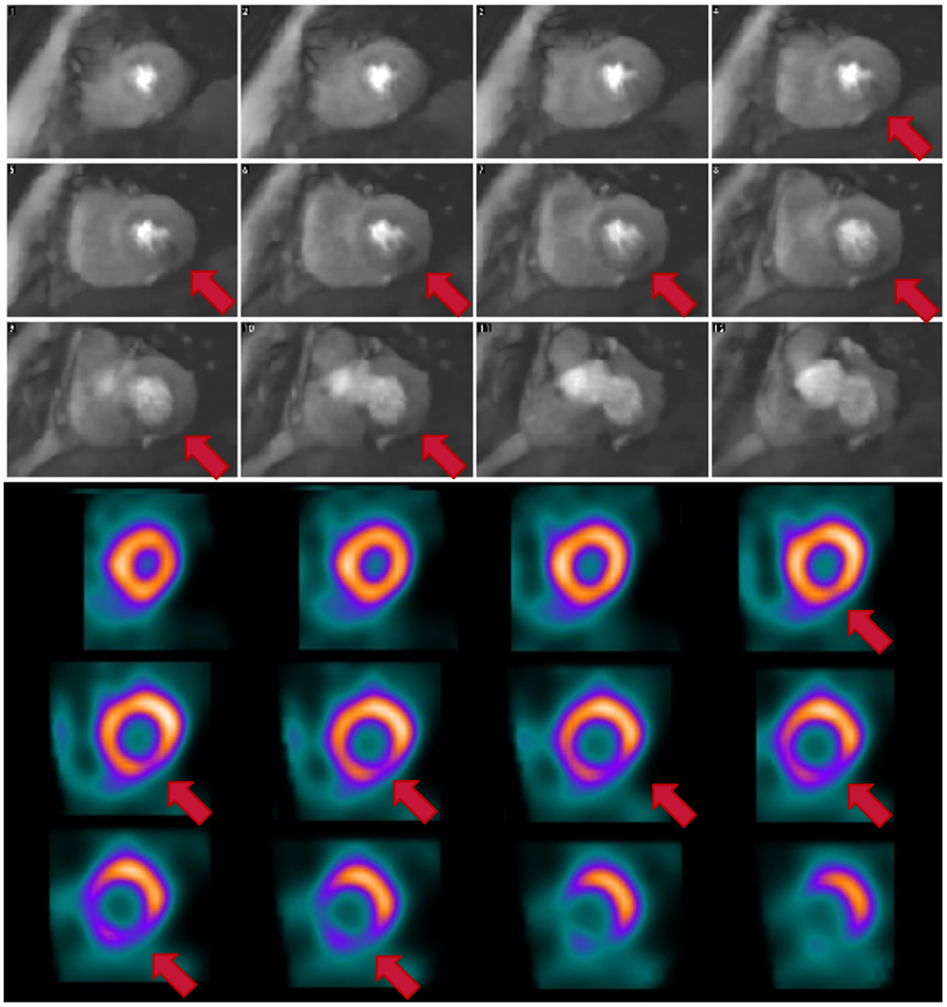

Figure 6.11.: FPP and MPS images for Patient 2. Stress FPP (top) and stress MPS (bottom) are shown for Patient 2. Red arrows mark potential defects in both datasets.

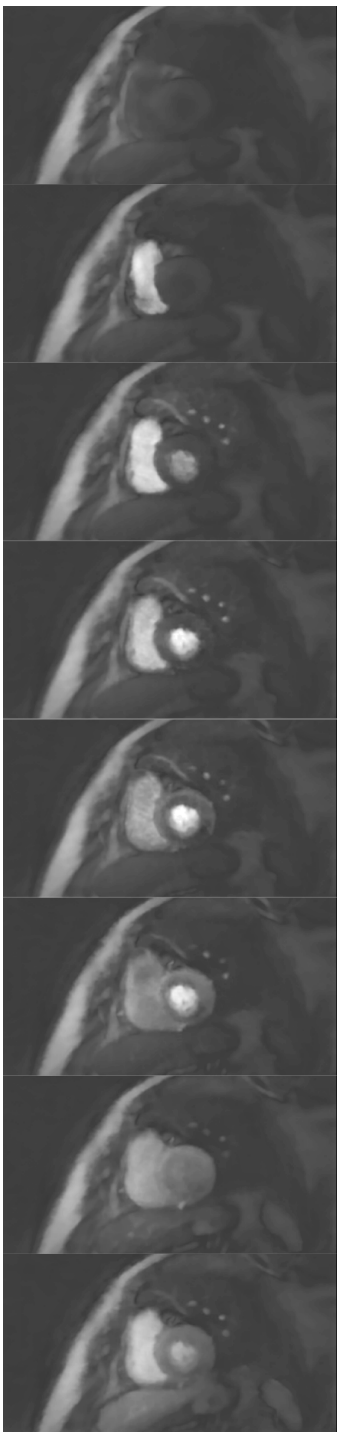

Figure 6.12.: Temporal dynamics of the FPP: Patient 2. For a single slice of the Patient 2 stress FPP, multiple frames for the first-pass of the GBCA are displayed.

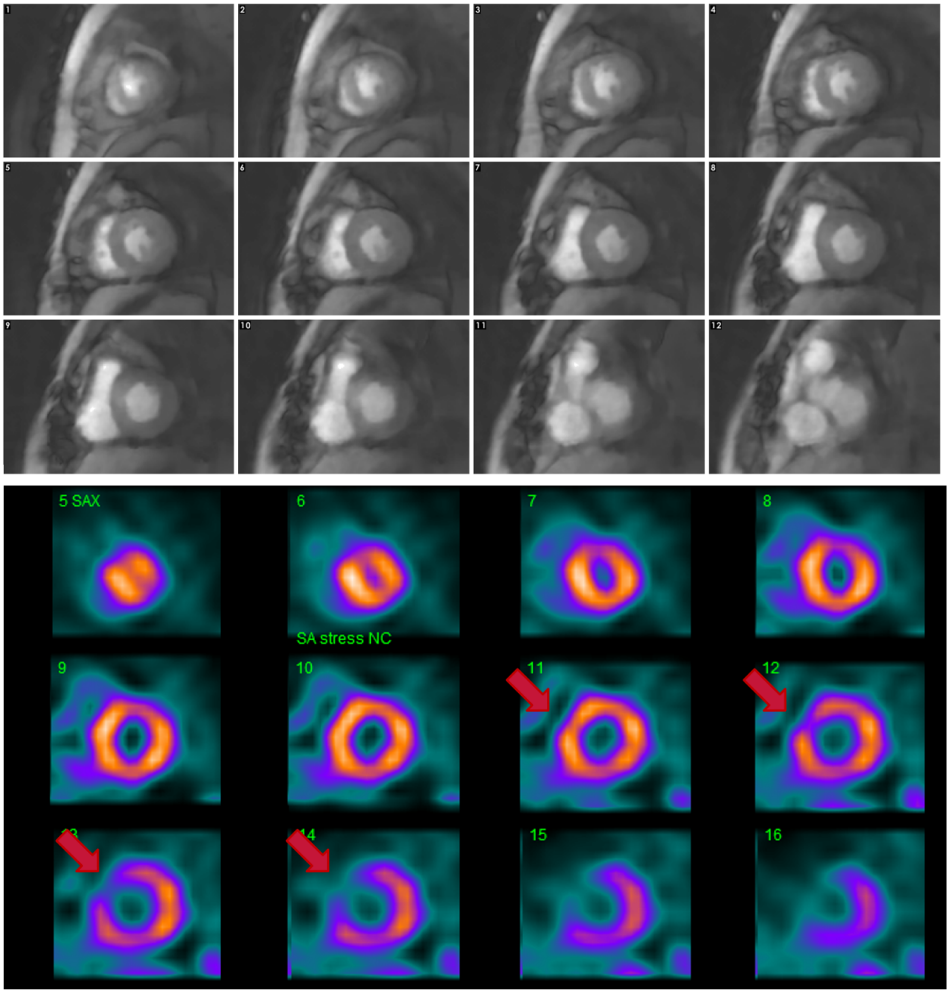

Figure 6.13.: FPP and MPS images for Patient 3. Stress FPP (top) and stress MPS (bottom) are shown for Patient 3. Red arrows mark potential defects in the MPS dataset.

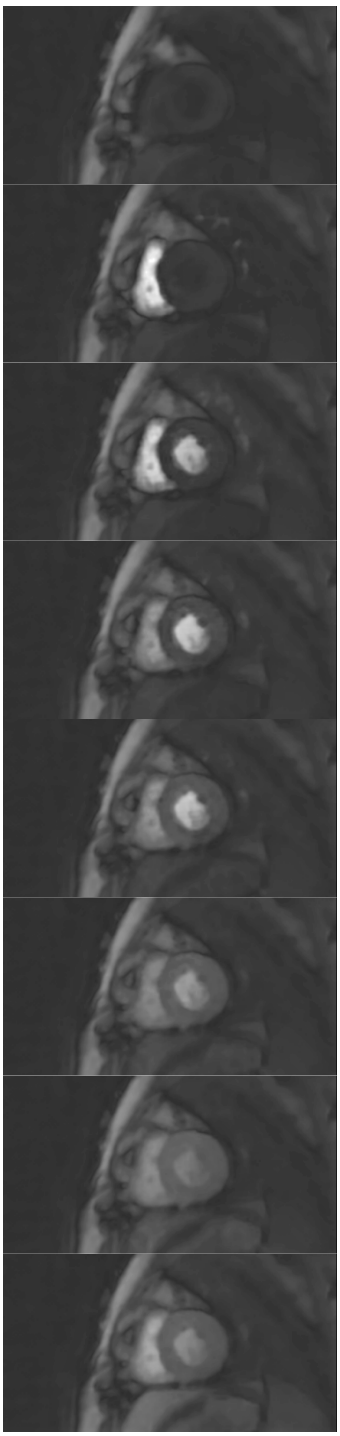

Figure 6.14.: Temporal dynamics of the FPP: Patient 3. For a single slice of the Patient 3 stress FPP, multiple frames for the first-pass of the GBCA are displayed. No persistent FPP stress defect could be seen.

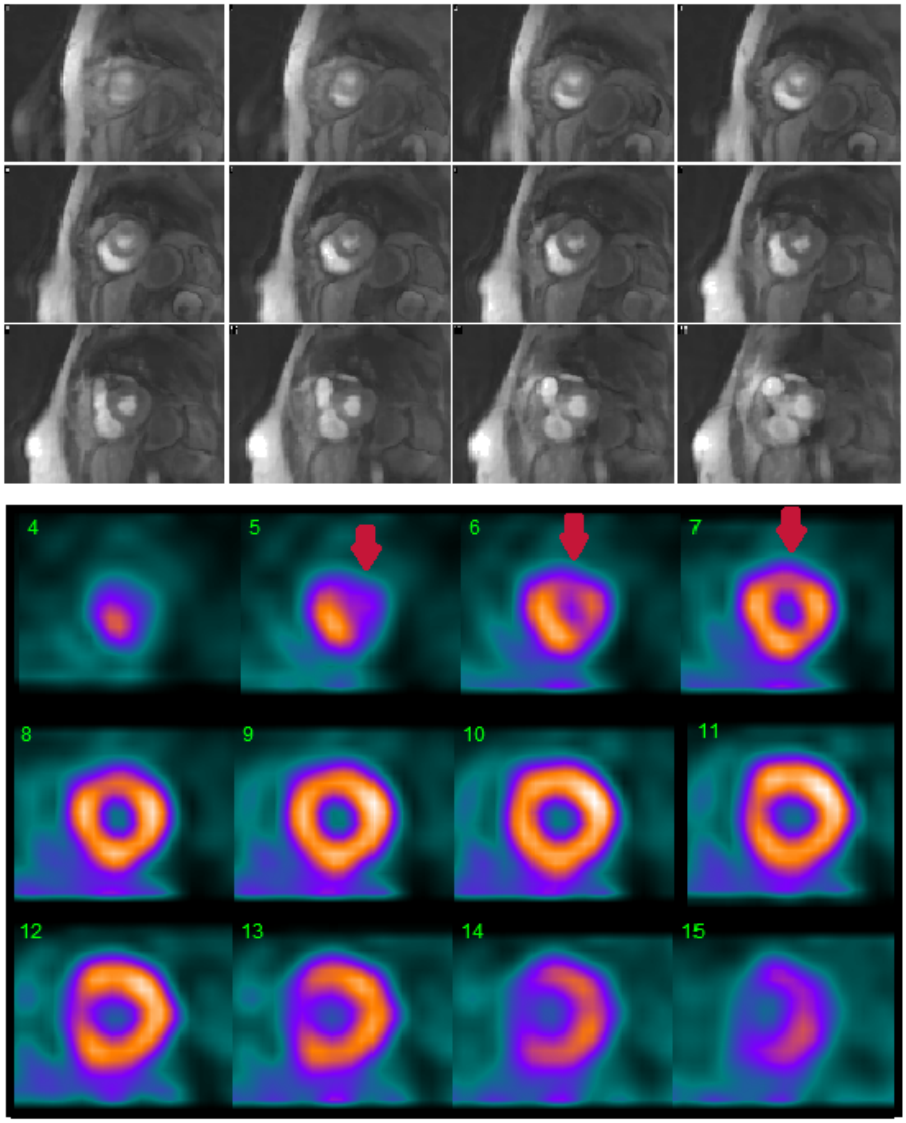

Figure 6.15.: FPP and MPS images for Patient 4. Stress FPP (top) and stress MPS (bottom) are shown for Patient 4. Red arrows mark potential defects in the MPS dataset.

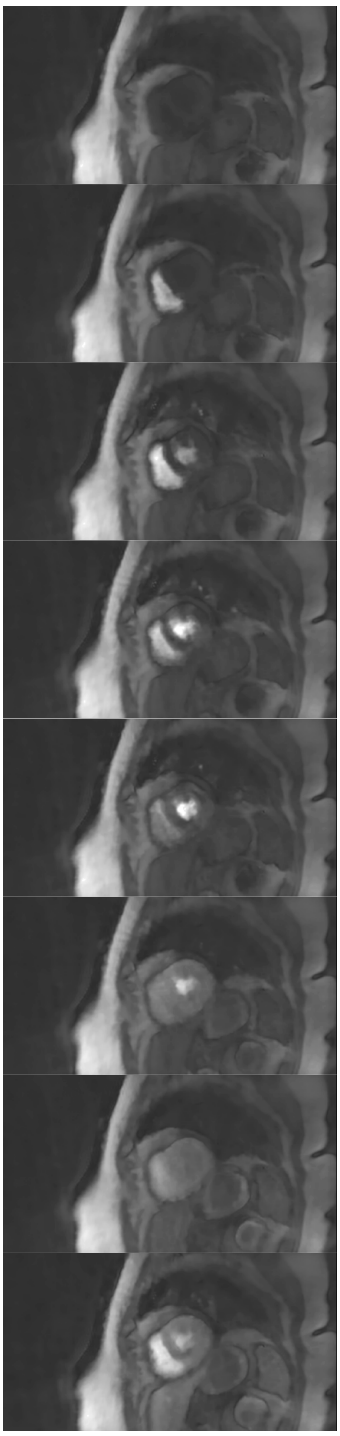

Figure 6.16.: Temporal dynamics of the FPP: Patient 4. For a single slice of the Patient 4 stress FPP, multiple frames for the first-pass of the GBCA are displayed. Transient artefacts occurred, but now persistent defects could be discerned.

The moderate to mild cases were expected to present a greater challenge to ischaemia detection and this was reflected in the lower extent to which 3D FPP displayed clear defects in agreement with the MPS. While the images of Patient 4 were degraded as explained in Results, which may have affected the ability to distinguish the small expected defect, Patient 3 showed a high apparent image quality by 3D FPP but the stress images appeared free of any hypointense regions. This raises questions over the accuracy of the technique. The basic gridded individual coil images in this dataset were examined for the presence of small hypointense regions that may have been smoothed by the STCR reconstruction algorithm. However, the myocardium appeared to have consistent intensity in these images (Figure 6.17), i.e. no mild perfusion defects were apparent underneath the gridding aliasing. It is possible or even quite likely that the degree of angular undersampling degraded the true resolution of the gridded images severely enough to conceal a small defect, which the STCR reconstruction was unable to restore on assembling the full angular resolution. Alternatively, it is conceivable that the MPS was inaccurate or overestimated the extent of a perfusion deficit. Unfortunately, CXA was not available in these patients to examine the true extent of CAD.

The healthy volunteers were clear of any persistent hypointense myocardial regions, comparative to persistent regions presenting in suspected CAD patients (Figure 6.18), but both groups contained transient myocardial artefacts.

It is clear that evaluation of 3D FPP SOS in greater numbers with known or suspected coronary artery disease is necessary.

6.4.2. Image Quality

In all previous clinical stress validations of 3D FPP techniques (Table 2.2), breath-holding was required for accurate reconstruction of the strongly reduced number of acquired k-space lines with k-t Cartesian methods. Synchronising this breath-hold request with GBCA first-pass arrival into the myocardium is a complication and the requirement for a breath-hold at stress could reduce reliability as co-operation under stress is often more difficult. The progression to free-breathing in this thesis is therefore an important one, and while SOS could be expected to perform better with undersampling than a Cartesian method, the free-breathing acquisition has nevertheless placed a greater burden on the reconstruction technique. Despite this, degradation of the image quality during the first-pass by respiratory motion was rarely

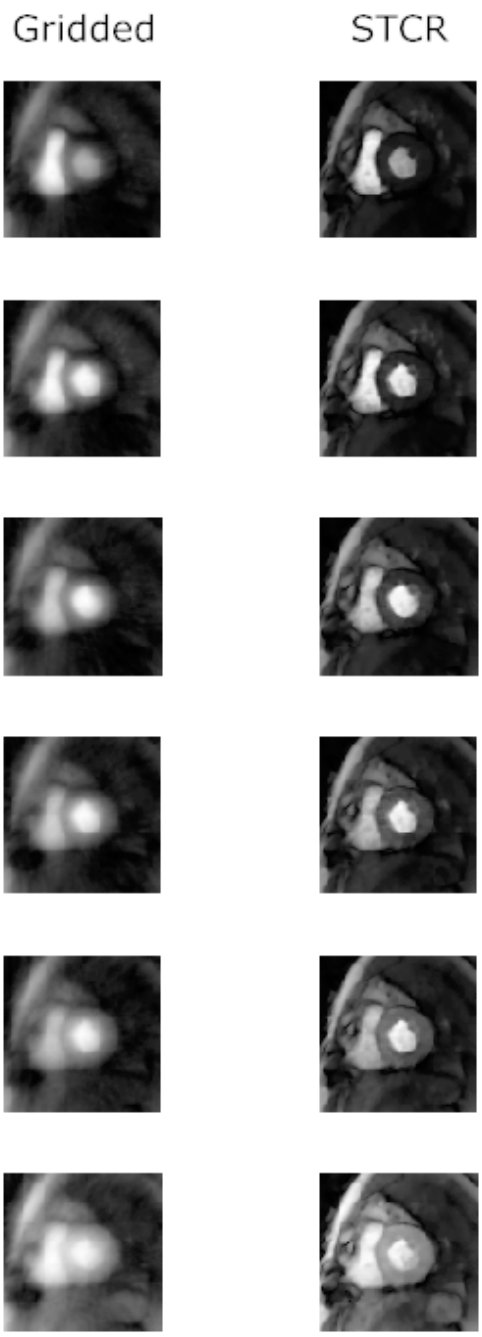

Figure 6.17.: Gridded versus STCR reconstruction comparison. For single slice of the Patient 3 stress dataset, multiple frames for the first-pass of the GBCA are displayed (top-to-bottom). On the left, pre-interpolation gridding only is used for reconstruction, while on the right the STCR reconstruction is used, as described in the methods. No obvious hypointense region, that could match the suspected perfusion defect location, could be seen in either reconstruction.

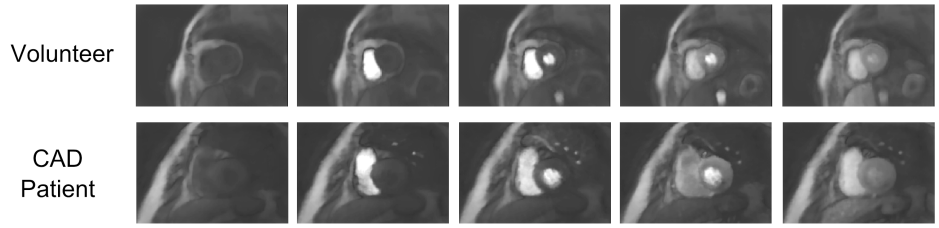

Figure 6.18.: Volunteer and CAD patient dynamics comparison. Multiple frames of a single slice taken from a stress dataset in a healthy volunteer(top) and CAD patient (bottom), showing the dynamics of the FPP and persistence of a genuine stress-induced defect in the inferior wall of the LV.

obvious.

While image quality remained high throughout the respiratory motion, the impact on the temporal fidelity of the datasets is less clear. One noticeable effect was in the major defect for the severe CAD case, where the hypointense region appeared more static across time than the rest of the myocardium. This artificial suppression of motion is similar to that seen in the earlier investigation into temporal effects (Section 4.3.5), e.g. in the chest-wall. Alongside the concern that this is affecting a true perfusion defect and what it might do to smaller hypointense regions, this also suggests that further work might be required into the reconstruction method and its temporal weighting. Whilst temporal weighting was investigated in Section 5.3.2 for a compromise between the fidelity and temporal constraint components of the reconstruction cost term, on the basis of this motion suppression it may be necessary to reduce the temporal weighting further at the expense of reintroducing some residual aliasing.

Dark transient myocardial artefacts were an issue with these images, with similar appearance to those previously described in earlier work in this project (Sections 5.1 & 5.2). The transient nature of the artefacts is a positive for their identification, but their frequent occurrence is of concern. More work is clearly needed to identify their cause, with the long term aim of reducing their presence or severity. The impact of these artefacts is discussed further in Section 6.4.4.

An increase in issues related to the ECG-triggering was seen in this work, with the higher heart-rates and free-breathing motion both potentially contributory factors. Free-breathing stress FPP protocols are run routinely with multi-slice techniques and so it should be possible to perform the 3D

SOS FPP sequence in these circumstances without significant issues, as long as great care is taken with patient setup.

6.4.3. Other Considerations

In keeping with the aim to create a simple and reliable method for the greatest chance of clinical adoption, the 3D SOS FPP sequence as used in this work required only selection of its slab position and the trigger delay for each individual patient. The only increase in complexity over a typical clinical 2D multi-slice FPP protocol was the inclusion of the additional cine acquired at stress to help optimise the cardiac end-systolic timing of the 3D acquisition.

As the additional cine was used only to look for changes in the time to end-systole, its diagnostic image quality (accurate border discrimination, etc) was not important. This allowed the sequence to be modified in such a way as to make the acquisition quick while also applicable during free-breathing. The cine was acquired only part way to the adenosine infusion time that was expected to be required to ensure causation of the full stress effect. This earlier cine acquisition timing was necessary to avoid extending the total time for which the subject had to undergo adenosine stress. The cine acquisition was only performed after at least some symptomatic response to the infusion was observed, including elevated heart-rate, and therefore was considered to provide some indication as to any changes in the end-systolic timing. Based upon this stress cine acquisition, adjustments to the FPP trigger delay were made in the majority (7/9) of patients. The changes in timing were typically small. It is impossible to know the effect this had on the 3D FPP image acquisitions, because there was no way to repeat acquisitions with different trigger delays, but this timing adjustment could potentially be important due to the short duration of the end-systolic pause in comparison with the 188ms shot duration.

There is debate over the utility of resting FPP scans, and so in general they are not always acquired [Hendel et al., 2016]. For the work in this chapter, rest FPP scans were acquired for each subject. Whilst these were not expected to (nor did) provide additional diagnostic information, it was felt their acquisitions were still useful for this project. Acquisition of the rest scans increased the total number of 3D SOS FPP scans acquired for analysis of image quality and reliability. They also allowed some comparison between the stress and rest scans for each individual patient, to look at

changes caused by heart-rate and respiratory motion increases, although the impact of residual GBCA from the stress FPP required some caution.

6.4.4. Discussion of Achieved 3D FPP Sequence Aims

The design of the 3D FPP sequence in this project had four aims, stated in Section 3.1. The extent to which each of these aims has been approached in this study is considered here.

Imaging parameters of a similar level to those currently accepted as standard in 2D multi-slice FPP. Spatial resolution has nominally been acquired at a slightly higher in-plane resolution than is typical for clinical acquisitions, although the true in-plane resolution after STCR reconstruction is harder to characterise and has not been investigated. Through-plane spatial resolution is acquired slightly coarser than the 8.0mm that is commonly used in 2D work but should in theory still be sufficient to resolve most defects. However, the apical regions do appear to undergo some through-plane partial-volume effects from the coarser partition resolution. Increased coverage of the LV myocardium was achieved comparative to typical multi-slice techniques, with the other proposed benefits of 3D FPP as previously discussed (Section 2.1.1).

Reasonable tolerance to all forms of motion including, ideally, respiratory motion. As investigated previously in this thesis (Section 4.3), the tolerance of the 3D SOS FPP method to respiratory motion is dependent on the setup of the reconstruction algorithm. In this chapter, the datasets appear to cope well with respiratory motion at stress, with no obvious additional artefacts created as a result of free-breathing. The temporal smoothing effects that had previously been occasionally identified (Section 4.3.5) were reduced with the new weighting values, although some were still discernible. Cardiac motion during the shot duration, discussed further in the next paragraph, did not appear to overly degrade the endocardial border clarity to the degree that one might expect. However, inter-frame 'motion' caused by ECG mis-triggering (i.e. shifted cardiac phase) did sometimes create issues with the STCR reconstruction. The technique appears to have acceptable tolerance to motion, but further work may still be required to determine any costs in diagnostic ability incurred.

A short enough shot duration to be feasible under stress conditions. The shot duration of 188ms is no longer than those employed in the previous clinical validations of 3D FPP sequences, that used Cartesian acquisitions (Table 2.1). It is difficult to determine if this duration is "short enough" and is almost certainly longer than ideal. Nevertheless, the fact that high diagnostic accuracy has previously been achieved with similar shot durations (Section 2.5.2), combined with no obvious cardiac blurring effects, suggests that this duration may be sufficiently short for the clinical requirement.

Reliability of application regarding artefacts, with those occurring being predictable and identifiable. While loss of image clarity due to motion and angular-undersampling effects can be expected, the most serious artefacts for clinical application were the dark transient artefacts that were first identified in Chapter 5 and again during this chapter. These impact the myocardium in a regional manner that is quite unacceptable, distinguishable from perfusion defects only by their transience and correlation with bright endocardial signal (similar as for DRAs). However, at least the nature and degree of the artefacts in 3D SOS FPP were fairly consistent, which should allow most true defects to be separately identified based on their longer persistence. However, the occurrence of these transient artefacts during the key frames of myocardial contrast enhancement could potentially mask rapidly filling genuine perfusion defects. Other types of image artefact were infrequent. The more typically sub-endocardial DRA was rarely apparent in these datasets, although as they would be expected to occur in the same frames as the more transmural artefacts discussed above, they were possibly being masked. Off-resonance artefacts were not discernible, matching with the previous phantom work (Section 3.5.2). Overall, the sequence therefore partially met this project aim, however, the described transient myocardial artefacts were more frequent and severe than likely to be acceptable for clinical application.

6.5. Conclusions

The technical reliability necessary for routine clinical use of 3D FPP at stress and rest during free-breathing has been demonstrated. This included the first known detection and confirmation of inducible perfusion defects in compressed sensing reconstructed 3D FPP and free-breathing acquired 3D

FPP. The diagnostic capability of this technique is still unknown following this first study, which had a small sample size. Within the four patients examined, some 3D FPP stress results did not match with those of MPS. Further work requires a greater number of stress CAD patient acquisitions and would ideally look at improving image quality, particularly with regards to encountered artefacts.

7. Artefacts & Simulation Work

Following on from the design and testing of various sequence and reconstruction methods, some final areas are considered to aid in the analysis and potential future work of this topic.

First, a very brief discussion is presented of some of the 3D FPP artefacts identified throughout the project work (Section 7.1). This is followed by examination of a previously undescribed artefact source in 3D FPP, that could potentially arise due to the coarse resolutions used in the secondary partition encoding direction (Section 7.2). Finally, a simulation framework is developed to replicate idealised 3D SOS FPP acquisitions and controlled factors considered likely to affect image quality (Section 7.3). This aimed to identify possible sources of some of these artefacts, as well as to examine other potential sequence parameter combinations that could improve 3D SOS FPP acquisitions in future work.

7.1. Overview of *in vivo* 3D SOS FPP Artefacts

3D SOS FPP artefacts have been detected at various stages of the *in vivo* work (Chapters 5 & 6). With the high level of undersampling required for 3D FPP, combined with the other designed sacrifices necessary to accelerate the sequence design (slab profile, spoiling effectiveness) that are well beyond what would normally be deemed acceptable for an MRI sequence, it is unavoidable that there will be loss in the image quality. This was likely to include the introduction of several, and potentially new, types of artefact. Despite this, there is a powerful clinical motivation behind the aim of 3D imaging for improved left ventricle coverage for FPP, if the artefacts can be controlled or at least understood.

Naturally the appearance of artefacts in 3D SOS FPP depended on many aspects of the sequence and reconstruction, while also varying greatly between patients. Many technical aspects of the sequence and reconstruction varied for different sections of work during the developments in this thesis.

For the radial trajectory, the selection of the reconstruction interpolation

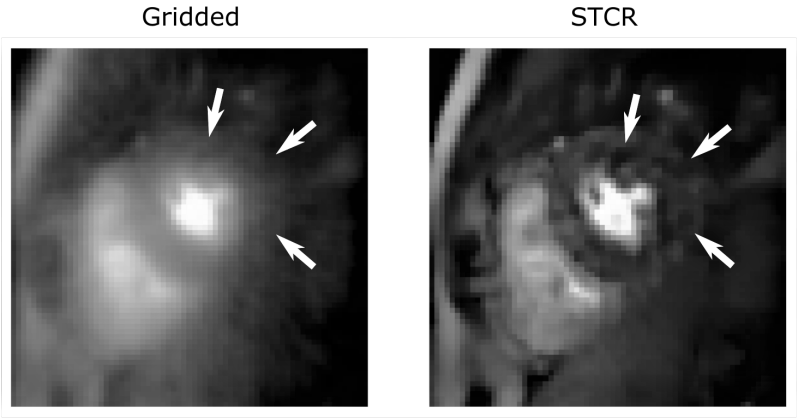

Figure 7.1.: Potential presence of artefacts in the raw data. An example comparison between gridding-only reconstruction and a STCR reconstruction, for a single slice and frame of an *in vivo* dataset. Darker regions in the LV myocardium could be distinguished in the gridded reconstruction image, matching the locations of the artefacts encountered in the STCR reconstruction.

type (NUFFT or pre-interpolation gridding, Section 4.2.2), may strongly affect the images output from the STCR compressed sensing reconstruction. This is due to the changes in the appearance of the angularly undersampled images with each type of interpolation. With a greater focus on pulse sequence design, this topic was not investigated in depth in this project, and would likely benefit from further investigation.

The main concern in this chapter is whether some of the artefacts are due to causes in the acquisition, and therefore affect the rawdata itself, rather than arising during reconstruction. An important test result that governed this decision to focus on the acquisition is shown in Figure 7.1. Artefacts that had been found in STCR reconstructed *in vivo* datasets were further examined by repeating the dataset reconstructions with pre-interpolation gridding only. In many of these cases, the hypointense myocardial region could still be discerned, albeit harder to detect. This suggests that, while the STCR reconstruction may exacerbate the appearance of these artefacts, it is unlikely to be the root cause.

The myocardial dark-rim artefact (DRA) is well known in 2D FPP and has appeared in some of the 3D SOS FPP datasets. How the DRA is affected in 3D FPP is unknown and its occurrence could potentially be due to causes that differ from those of traditional 2D FPP datasets. Likewise

many imaging conditions known to cause artefacts *in vivo* in cardiac MRI (fat, motion, etc) are potential causes of some of the artefacts seen in the 3D FPP datasets. However, again, these causes cannot be studied so easily during the GBCA arrival *in vivo*.

Therefore what follows next is an investigation of some of the potential causes of the DRA and other 3D FPP artefacts, and of other effects on the image quality in 3D SOS FPP.

7.2. "Partition" Dark-Rim Artefacts

7.2.1. Introduction

The dark-rim artefact (DRA) is well known in 2D FPP and has been discussed earlier (Section 1.5.6). While the causes and features of 2D FPP DRAs are understood, the potential for DRAs along the partition-encoding direction used for 3D FPP imaging has not previously been examined.

The contribution of Gibbs-ringing to DRAs in 2D FPP is minimised by finer resolution [Plein et al., 2007], in part because the decreased pixel size reduces the spatial extent of the ringing in the myocardium. With the much coarser through-plane resolutions currently achievable in 3D FPP, there is an implied risk of partition-axis DRAs. These new partition DRAs ("PDRAs") and partial volume effects due to coarse resolution of this direction were investigated.

7.2.2. Methods

Ideally, *in vivo* 3D FPP datasets at high in-plane and through-plane resolutions would be used to examine the existence of PDRAs. The high in-plane spatial resolution should minimise conventional in-plane DRAs (as seen in 2D FPP), which would likely have a superficially similar appearance to PDRAs. The high through-plane spatial resolution of the acquired data would generate minimal initial PDRAs, and would allow examination of how PDRAs appear by performing repeated reconstructions as the through-plane resolution is artificially reduced. However, *in vivo* 3D FPP datasets of sufficiently high spatial resolution in all directions are impossible to acquire during the first-pass, as seen in Section 5.1.

Therefore, three alternative high resolution sources were used to model a 3D FPP dataset for investigation of PDRAs in the following work, where

varying through-plane resolutions were reconstructed by truncating the sampling of the partition-direction rawdata. A similar strategy has previously been used on highly sampled 2D FPP data to evaluate in-plane Gibbs artefacts [Ferreira et al., 2009].

Simulated Model

In MATLAB, the LV blood-pool and myocardium were modelled as a cone in an array of voxels. A 5:2 intensity ratio was used between the bloodpool and myocardium, to represent the first-pass peak, with a uniform intensity of the voxels within each tissue region. The simulated object was created with a high resolution in image space, particularly in the long-axis (through-plane) direction - $256 \times 256 \times 5000$ voxels for an approximately $80 \times 80 \times 80$mm "FOV". The object was converted into k-space through a 3D FFT, where the number of partitions for reconstruction, N_p, could be truncated prior to a 3D iFFT back into image space.

From the complete simulated dataset, the truncated number of partitions, N_p, and the angle between the endocardial wall and the partition-encoding direction (Figure 7.2), θ_B, were varied over the ranges 6-40 (intervals of 2) and 9.5-27.0° (intervals of 2.5°) respectively. For each combination of N_p and θ_B the width of the created PDRAs were detected automatically by an algorithm that counted the number of consecutive pixels in the myocardium, outwards from the endocardial border, that had a negative difference from the original myocardial pixel value.

In vivo dataset

For two purposes, representative 3D *in vivo* data was collected: firstly to examine directly for PDRAs and secondly to use as a template with realistic morphology into which simulated data could be introduced, as described in the next section (*Hybrid dataset*).

A single diastolic 3D image of high-resolution data was acquired by Cartesian sampling with the aim of achieving a similar contrast and appearance to a perfusion frame at the first-pass peak GBCA LV transit. A bSSFP sequence was applied at high flip-angle ($\alpha = 65°$), using a right-diaphragm respiratory navigator[1]. The navigator echo was acquired immediately before

[1] A head-foot frequency encoded echo from a column of signal formed by the intersection of an offset sagittal slice with a sagittal-to-coronal slice, both positioned through the right diaphragm and avoiding the heart.

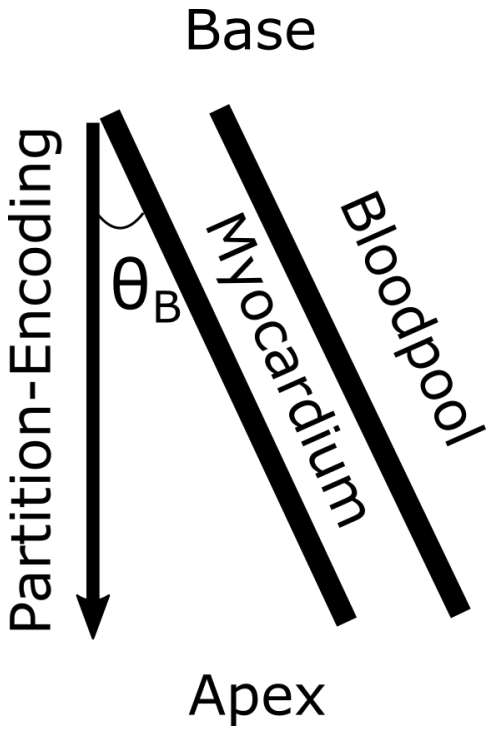

Figure 7.2.: Boundary angle θ_B definition. θ_B was defined as the angle the myocardial wall (represented here on a LAX view) makes with the partition-encoding direction. This was varied in the simulated data.

each cycle of 3D data acquisition, which occupied 269ms of the cardiac cycle timed in the diastolic pause. The acquisition lasted for 160 cardiac cycles, approximately 90 of which were accepted based on the end-expiratory position of the diaphragm.

This enabled an acquisition of the entire LV, with a similar blood to myocardium intensity ratio (approx 2:1) to the previous datasets, with a spatial resolution of 1.3x1.3x2.0mm.

Hybrid dataset

A hybrid dataset was created that combined the more realistic anatomical distribution of the second dataset with the more uniform image intensities of the simulated model.

The LV blood-pool and myocardium were manually segmented from the *in vivo* dataset and the intensity within each outlined region was uniformly set to the 5:2 blood:myocardium ratio of the simulated model. This gave a more anatomically realistic dataset than the uniform cone, but now with variations in θ_B along and around the LV, while also avoiding contaminating effects from other tissues outside the LV. This aimed to give a reliable bright-to-dark step at the endocardial boundary, which is hard to produce consistently *in vivo*.

For each of the datasets, the high in-plane resolution was maintained so that any changes seen would arise only from through-plane effects. The truncated number of partitions used (N_p) was varied for each of the reconstructions to give a 2-32mm range of through-plane resolutions.

7.2.3. Results

The series of reconstructions (Figure 7.3) showed overlapping consequences of increased PDRAs and partial volume (blurring) as the partition-encoding resolution was decreased.

For the simulated model, the arrows on Figure 7.3a show a circumferential PDRA in the short-axis image reconstructed from 8 sampled partitions. With the high in-plane resolution maintained for all reconstructions, the PDRA is formed in the through-plane direction. The corresponding line profile plots taken horizontally across each SAX image also show the PDRAs, which are similar in appearance to in-plane DRAs but here are the consequence of through-plane Gibbs ringing that arises from the partition Fourier transform.

For the lower numbers of partition-encodings (6 and 4), the myocardial border along the partition direction is instead smoothed over by the partial-volume effect between blood and myocardium within the increasingly large partition voxel size.

A similar pattern was seen in the hybrid dataset (Figure 7.3b). The hybrid dataset had the additional feature that, at the 'septal' myocardium (marked S), where the border was exactly aligned along the partition-encoding direction (at $\theta_B = 0°$), no PDRAs were created and little smoothing occurred until the partition thickness reached the 6 partition level. However, at the opposite ('lateral') myocardial border, marked L, the blood:myocardium border is at θ_B near 30° to the partition-encoding direction, and it was seen to generate PDRAs. These PDRAs were overcome by partial-volume as the partition number N_p was reduced, as in the uniform cone of the simulated model.

For the *in vivo* dataset, clear PDRA results were harder to determine (Fig 7.3c). Potential PDRAs can be seen by examination of the line profile, with a similar pattern in the lateral wall as for the previous two datasets. As for the hybrid dataset, the introduction of PDRAs was not clearly replicated in the septum.

The results obtained by the variation of θ_B along with N_p in the conical phantom significantly altered the PDRA width (Fig 7.4). The artefacts of largest width occurred at combined low partition resolution and low θ_B, where the myocardial wall approaches, but does not quite align with, the partition-encoding direction. The results at particularly low N_p values were not plotted due to the inability of the DRA detection algorithm in the situation of extreme partial-volume smoothing.

7.2.4. Discussion

The PDRA width in the simulated phantom matched the expected pattern. PDRA width increases at coarser through-plane resolution (i.e. reduced N_p), but the simultaneous impact of partial volume caused by the larger partition thickness counteracts this effect. Eventually with further reductions in N_p the blurring by partial volume dominates and destroys the endocardial border visibility as demonstrated in the images and line profiles across all three datasets. For a given N_p, variation in the border angle between partitions, θ_B, obviously affects the level of partial-volume blurring that occurs and this therefore changes the visibility of PDRAs. When the endocardial border

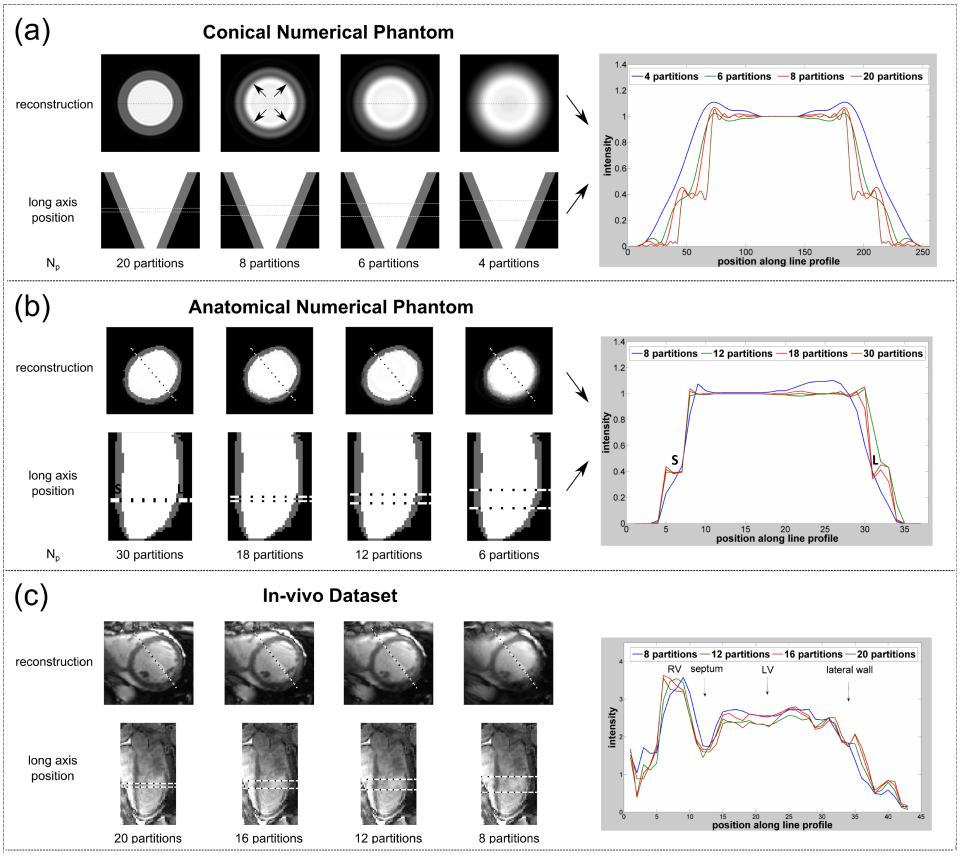

Figure 7.3.: SAX reconstructions of 'slices' at fixed high in-plane resolution, but with varying through-plane resolutions, shown with their corresponding locations along the high-resolution long-axis views. To their right are the corresponding line profiles. a) conical numerical phantom, b) anatomical numerical phantom and c) *in vivo* dataset. The N_p values were selected to demonstrate small PDRA, stronger PDRA, partial-volume/PDRA compromise and strong partial-volume effects respectively from left to right.

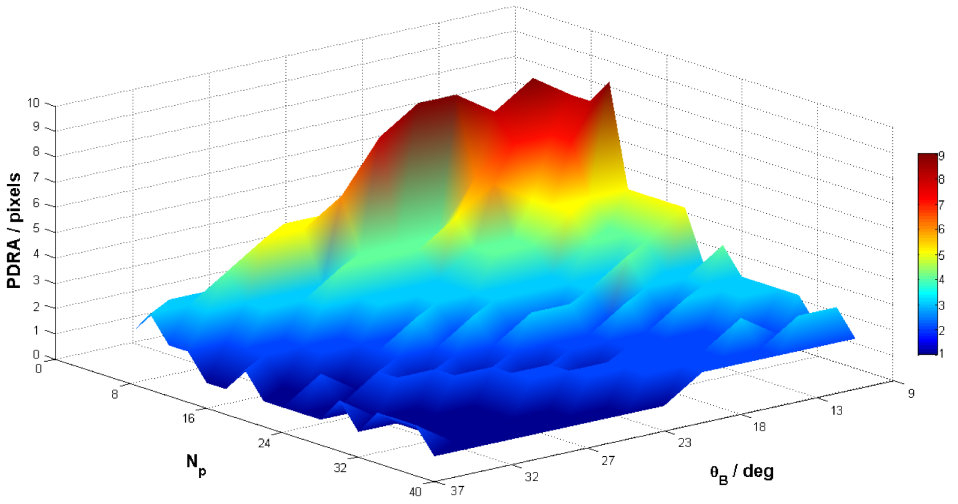

Figure 7.4.: Values of the PDRA width (in number of pixels) in the conical numerical phantom, reconstructed at varying boundary angles to the partition-axis (θ_B) and number of partitions (N_p).

is sharpest, i.e. smaller θ_B, any PDRAs caused by coarse through-plane resolution may be at their most prominent.

For some values of θ_B examined in the simulated dataset ($\sim$<25°) that are likely to occur *in vivo*, PDRAs in 3D FPP seem inevitable - obtaining sufficiently high through-plane resolution to avoid PDRAs at these angles is infeasible in the shot duration available. The best solution may be to aim for some compromise between PDRA and partial volume at the currently achievable 3D FPP parameters. The particular range of through-plane resolutions where PDRAs are at their most prominent *in vivo* was difficult to determine from this work and clearly also depends on the location along the LV long-axis (due to variations in θ_B between the SAX planes and the endocardial border).

This work has identified the potential cause for a previously undescribed artefact in 3D FPP. The identification of PDRAs *in vivo* will remain a challenge due to their similar appearance to in-plane DRAs, and the best strategy to avoid the artefact with currently achievable parameters remains uncertain.

7.2.5. Conclusions

Contrary to the initial expectation from 2D experience that increased resolution reduces DRAs, this work showed that over the range of low through-plane

resolutions available in 3D FPP, the aim for improved partition-encoding resolution may increase Gibbs-induced partition-direction DRAs. The reduction of PDRAs at low partition numbers (i.e. coarser partition resolution) is a trade-off against partition-direction partial volume effects that cause blurring of boundaries. The compromise between PDRAs and partial volume effects is also affected by the boundary angle along the through-plane partition-encode direction, which complicates the optimisation of parameters to minimise PDRAs. Further *in vivo* investigations would be required to optimise the compromise between these two effects.

7.3. Sequence Design Simulations

7.3.1. Introduction

Determining the separate causes of artefacts or other effects on image quality can be extremely difficult with *in vivo* acquisitions, as was found in the previous section (Section 7.2). This is particularly the case in 3D FPP, where multiple sequence parameters are limited simultaneously, so as to achieve the myocardial coverage, resolution and shot duration required. There are likely multiple sources of image quality degradation in each acquisition, all of differing severity. This difficulty in determining the sources of image quality reduction is compounded by the large range of potential sequence parameter combinations available with the SOS trajectory designed for this project. The initial work in Chapter 3 aimed to select suitable parameters, based upon previous literature and test acquisitions, but the large number of potential combinations combined with the difficulty in recruiting large enough volunteer sample sizes means that the selected parameters may be non-ideal. Variation between the volunteers and the inability to run repeated first-pass studies in them, were further limitations to their use.

Optimal Cartesian and spiral trajectories have been previously examined in FPP [Zhou et al., 2016] [Salerno et al., 2011], however, no such detailed investigations have previously been made for radial FPP sequence parameters.

Therefore, this work aimed to create an initial prototype simulation framework capable of replicating a FPP acquisition using variety of 2D and 3D radial sampling strategies. By including multiple "environmental" factors to model *in vivo* use of FPP in a controlled manner, the potential impact of each sequence parameter on the "real world" assessment of myocardial FPP was investigated to aid in optimisation of radial FPP.

7.3.2. Methods

Simulation Model

A simulation framework was created in MATLAB using a finely resolved 3D object representing the left ventricular myocardium and blood-pool, modelled as coaxial ellipsoids (prolate spheroids) of differing radius (Figure 7.5).

For a (1001 x 1001 x 267) matrix, values of the spheroid within the desired radius value

$$R = \sqrt{X^2 + Y^2 + (\gamma \times Z^2)} \tag{7.1}$$

were set equal to 1, and 0 everywhere else. Radius limits of $R \leq 50$ for the blood-pool object and $R \leq 100$ for the myocardium object were used. The γ value altered the elongation of the spheroid, which could be set separately for each object, and here was set as 0.04 and 0.1 for the blood-pool and myocardium objects respectively. This provided a fairly uniform myocardial wall thickness.

A segment in the mid-ventricular myocardium was zeroed to represent a local strong transmural perfusion defect. The modelled defect size was of large transmural and angular extent but of deliberately small long-axis extent, with the aim of testing 3D partition fidelity[2].

Saturation-recovery SGRE sampling of the object k-space was computed with 2D radial and 3D SOS trajectories. First-pass changes in the T_1-dependent signal evolution were modelled based on simplified Bloch equations, with partial saturation during the shot and the assumption of complete transverse magnetisation spoiling before each RF excitation pulse. The transverse magnetisation used for each ray time point, t (from 1 to the total number of rays), was given by

$$M_z(t) = M_z(t-1) \times cos(\alpha) \times e^{\frac{T_R}{T_1}} + (1 - e^{\frac{T_R}{T_1}}) \tag{7.2}$$

with

$$M_z(0) = 1 - e^{\frac{SRT}{T_1}} \tag{7.3}$$

[2]Typical CAD involving the main arteries would tend to extend into the downstream "territory" of the vessel

where α, T_R and T_1 have their typical definitions, and SRT is the saturation recovery time from the application of the saturation pulse to the beginning of the first ray acquisition[3]. As default, the T_1 was set as 50ms for the bloodpool region and 180ms for the myocardium region.

Image reconstruction was performed with a gridding algorithm, as applied previously (Section 1.5.6), with no further methods of undersampling correction used in this chapter. The aim was to investigate factors impacting the quality of the initially acquired data, rather than the outcome of different compressed sensing reconstruction methods.

Sequence Variables

The following sequence parameters[4] (Figure 7.6) were tested:

2D & 3D

- number of rays (18, 24, 36, 72, 144 ['fully-sampled'])
- in-plane ray ordering (sequential, golden angle)
- readout partial Fourier (off, 75%)

3D only

- through-plane ordering (linear, centre-out)
- slice partial Fourier (off, 75%)
- variable undersampling (VU) of the number of rays per partition (off, 100%[center k_z)-33%[outer k_z]).

Other parameters were held constant, fixed across all reconstructions: 300x300(x80)mm FOV, 2.1x2.1(x10)mm resolution, 150ms saturation recovery time, 12° flip-angle and 2ms T_R.

Sequence Environments

Different imaging "environmental" influences (Figure 7.7) were designed to expose the relative importance of the sequence parameters, under various conditions that could be expected to affect clinical application of the 3D

[3] N.b. this is different from the previous definition of saturation recovery time and therefore the SRT values actually used were modified for easier comparison.
[4] Terms defined in Section 3.2.

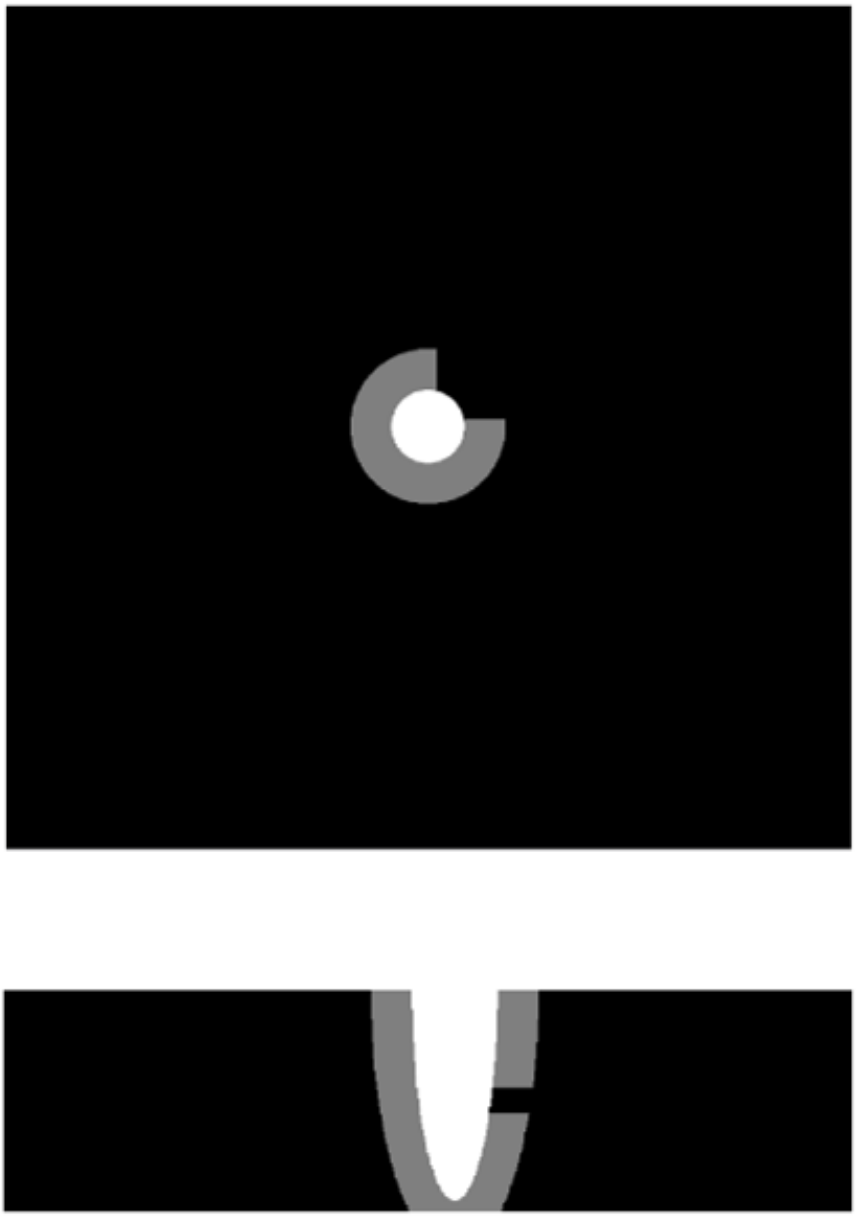

Figure 7.5.: The simulated LV model. The SAX (top) and LAX (bottom) views of the high resolution LV model, from which simulated k-space sampling could be performed. The modelled defect is of a deliberately unrealistic long-axis extent, to enable testing of through-plane fidelity of the simulated acquisitions.

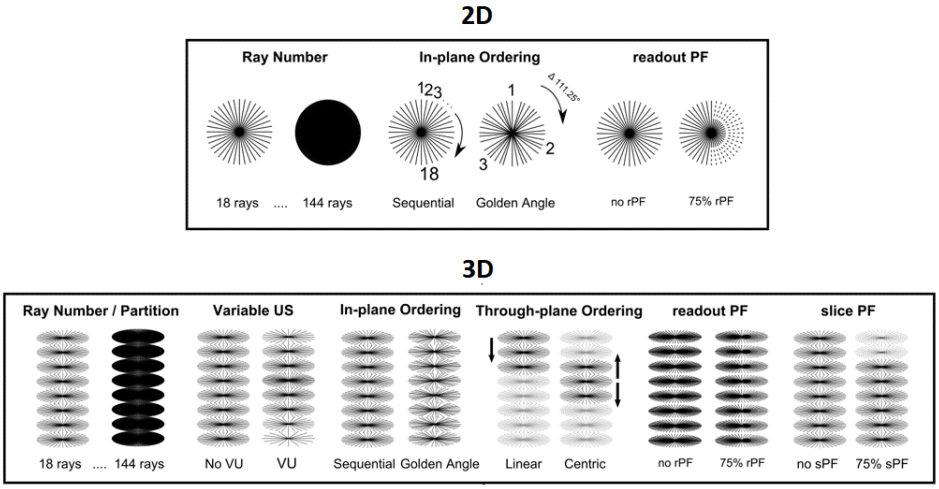

Figure 7.6.: Simulated sequence trajectory options. The full range of sequence trajectory options enabled in the simulation, with which to sample the LV object.

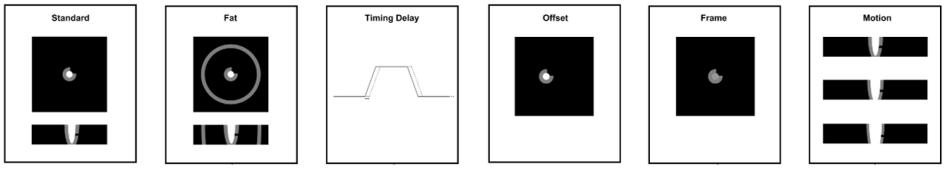

Figure 7.7.: Simulation environments. A representation of the five imaging 'environment' modifications that could be applied to the simulation, alongside the 'standard environment' which had no modifications.

SOS FPP sequence. The "Standard" environment generated a baseline set of simulations which acted as a reference standard of image quality prior to the application of the "environmental" changes. These environments were as follows:

- "Fat": An outer ellipsoidal shell (350<R<400, γ=0.1) was introduced to the simulation to represent bright subcutaneous fat. For this work the fat T_1 was set as 250ms.
- "Timing delay": a radial 'ADC-to-gridding' timing difference (Section 3.5.1) was added to each ray (1.0 ADC sample shift).
- "Offset": an offset of the simulated LV from the FOV isocenter was applied through a linear phase-slope (3cm).

- "Frame": a different blood/myocardium T_1 ratio, to represent a later stage in the first-pass with reduced intensity difference (bloodpool T_1 = 200ms, myocardium T_1 = 280ms).

- "Motion": simplified cardiac filling motion during acquisition was included in the model, i.e. moving from systole towards a diastolic state during the FPP shot (endocardial border velocity ∼4cm/s radially and ∼5cm/s longitudinally [Föll et al., 2009]). Motion changes were entirely "inter-view" with no motion modelled during each readout.

Image Measures

Six automatic measures of image quality were implemented for each simulation. The normalised signal variation (standard deviation) was calculated in the blood-pool, myocardium and background. The edge sharpness was calculated across the endo- and epi-cardial borders using a modification of the Shea Method [Shea et al., 2001]; four line profiles were obtained for each of the epi- and endo-cardial borders at 90° to each other, and the sharpness value was calculated as the inverse of the distance on the line profile between two values:

$$Upper = 0.8 \times |\overline{Region_1} - \overline{Region_2}| \tag{7.4}$$

$$Lower = 0.2 \times |\overline{Region_1} - \overline{Region_2}| \tag{7.5}$$

where $Region_1$ and $Region_2$ are the two regions either side of the border (i.e. the bloodpool and myocardium respectively for the endocardial border, and the myocardium and background for the epicardial border). For each boundary, the sharpness measures across the four line profiles were averaged.

A measure of the CNR of the simulated perfusion defect was made using the difference in brightness between the defect and myocardium, and the myocardial variation:

$$CNR_{defect} = \frac{\overline{I_{myo}} - \overline{I_{defect}}}{\sigma(I_{myo})} \tag{7.6}$$

where $\overline{I_{myo}}$ and $\overline{I_{defect}}$ are the pixel intensity values averaged over the normal myocardium and the defect regions respectively.

Model Validation

In order to verify that fundamental aspects of the simulation model were operating as expected, some initial work was performed to compare phantom acquisitions with the simulated datasets. These validations were confined to test a few simple aspects of the model that could be easily confirmed using basic phantom work.

The simulation program was modified to produce only a single cylindrical object, resembling Phantom B, imaged coaxially with the partition-encoding axis. The 3D SOS sequence, as used in the clinical validation chapter (Chapter 6), was used for the phantom acquisitions in the same orientation.

In each experiment, the sequence parameters were matched as closely as possible with the simulation inputs, and the phantom datasets were reconstructed with the same gridding algorithm[5] used for the simulated datasets.

Trajectory Combinations Simulations were performed to sample the cylinder with the standard environment, acquired with 24 rays ('undersampled') and 144 rays ('fully sampled') for both sequential and golden angle ordering of the rays. The equivalent parameters were used for the phantom acquisitions, performed on Phantom B.

ADC Delay The datasets acquired for the trajectory validation work were also used to examine a simple testable 'environment': the ADC delay. Simulations were performed both with and without the delay environment applied, with the parameters otherwise left unchanged. The phantom datasets were reconstructed with the standard delay correction applied (Section 3.5.1) as well as with a 1.0 ADC sampled shift. These were intended to match the simulations without the delay environment, and with the delay environment, respectively.

T_1 Variation Phantom B was replaced with a phantom object [Captur et al., 2016] that contained nine cylindrical tubes over a range of T_1 values. Prior to the experiment, the individual T_1 values of each tube were measured, as performed for the other phantoms in Section 3.2.7. The phantom object was imaged using the 3D SOS sequence with the 150ms saturation-recovery

[5] As previously performed for phantom acquisitions (Section 3.2.7) the in-built 'bird-cage' body coil was used for acquisition, with the two elements combined with root mean sum-of-squares.

time as listed in the methods. Corresponding simulations were performed using these same imaging and saturation parameters, and were repeated for each of the nine T_1 values measured from the phantom.

The mean pixel intensity value was plotted against T_1 for each of the nine tubes within the phantom, and was compared against the mean intensity in each of the nine corresponding T_1 simulations reconstructed.

Simulation Experiments

A total of N=1016 simulations were run for the selected combinations of sequence parameters, for 2D (N=120) and 3D (N=896), and were grouped by each of the six "environmental" conditions. The overview of the entire process is detailed in Figure 7.8.

The experiment aimed to identify which sequence variables affected different measures of image quality, and in which environments these occurred. With the relatively large number of simulations per group, the results could be examined for trends in specific parameters.

To further assist in the identification of significant sequence variables, multiple regression analysis was applied using SPSS (IBM, USA) to each separate environment group (2D: N=20/group, 3D: N=160/group[6]), with the six image quality measures as the outcomes. This helped to identify the sequence variables that were statistically significant ($p<0.05$) in impacting the quality measures, and their effect size.

7.3.3. Results

The formal separation of results and discussion was modified, to combine experiment specific discussion with the results for each of the numerous sections of the following work. The final discussion (Section 7.3.4) draws together the key findings from the many separate investigations. After the phantom validation results, the results are separated for the *2D: Standard Environment*, *2D: Modified Environments*, *3D: Standard Environment* and *3D: Modified Environments*.

Phantom Validation

For the validation work, a close agreement was seen between the phantom and simulation images in all cases (Figure 7.9). The artefacts in the background

[6]Except for the motion environment in 3D, which was limited to lower ray numbers only, with N=96.

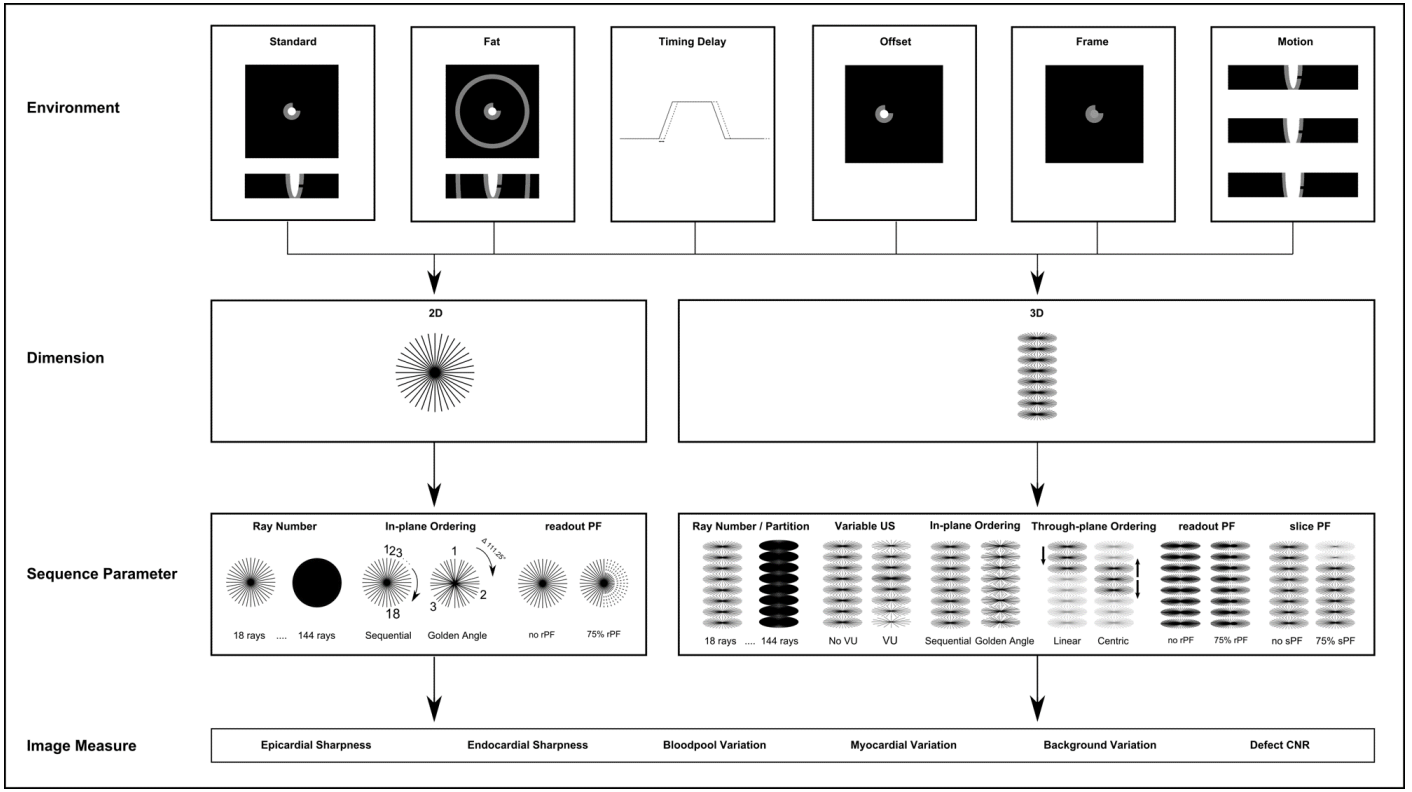

Figure 7.8.: An overview of the complete simulation framework. Six different simulation environments were used, including a "standard" baseline reference. Each environment was radially sampled in 2D or 3D, repeated with various combinations of sequence parameters. The output gridded reconstruction for each simulation then had 6 different automatic image measures calculated. Analysis was made of the relative impact of the different sequence parameters on the image measures for each of the environments.

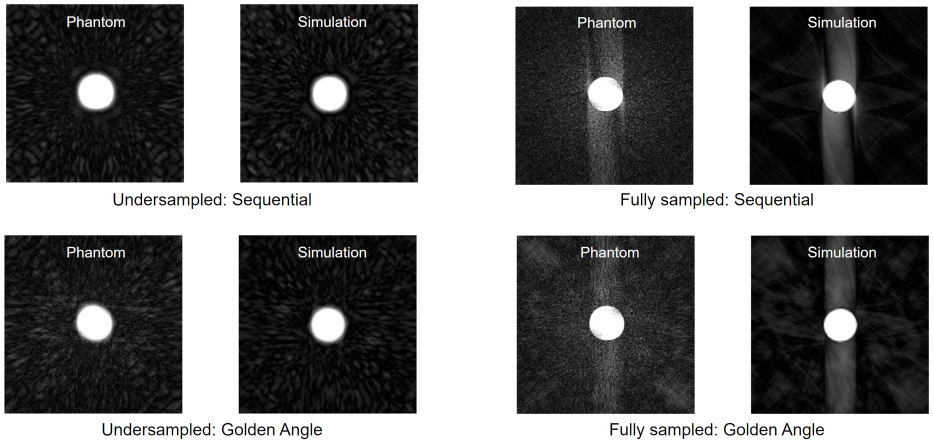

Figure 7.9.: Simulation validations - Trajectories. Comparison of phantom acquisitions and simulated datasets for different ray number (24, undersampled and 144, fully sampled) and in-plane ordering (sequential, golden angle).

outside of the object had similar appearances for the phantom and the simulation, and showed comparable changes from undersampled to fully sampled acquisitions. The vertical band of streaking in the fully-sampled imaging appeared consistently for the phantoms and simulations, and changed in appearance by the golden-angle modification similarly for phantoms and simulations.

Close agreement was also seen between the phantom and simulation images with the introduction of the delay environment (Figure 7.10).

The variation of signal intensity value with T_1 also showed agreement between the simulation and phantom measurements (Figure 7.11), with both showing similar reductions of the saturation-recovery intensities with increased T_1.

2D: Standard Environment

The acquisitions without external environmental factors ("standard simulations"), showed results largely as could be expected. The ray number predictably had a statistically significant effect on almost all of the image measures. The epicardial sharpness and defect CNR (Figure 7.12a&d) in particular showed a non-linear decreasing relationship with decreasing ray number. No similar reduction in the measurement of endocardial sharpness was found; this result was seen throughout the simulation work and is be-

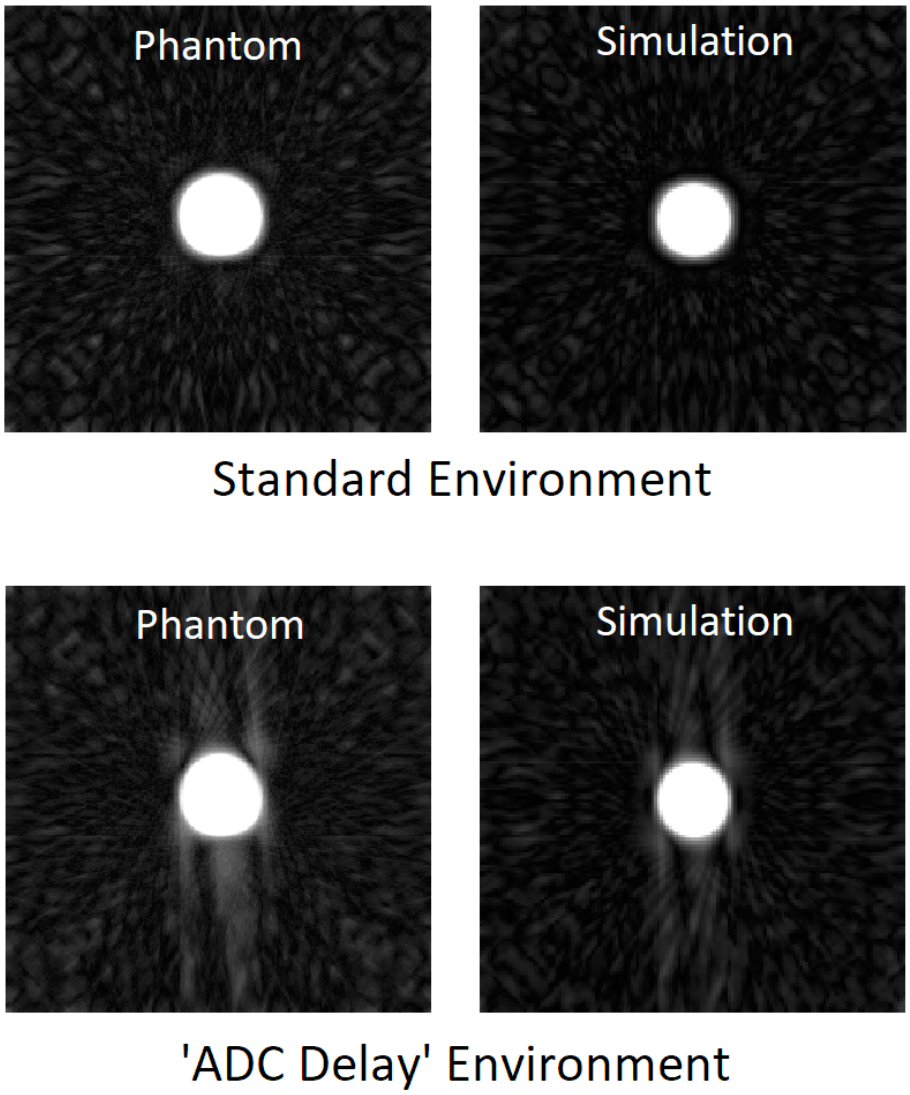

Figure 7.10.: Simulation validations - Delay environment. A phantom acquisition reconstructed with both an appropriate delay correction and with a 1.0 ADC sample shift, and the corresponding simulated datasets for the standard and ADC delay environments.

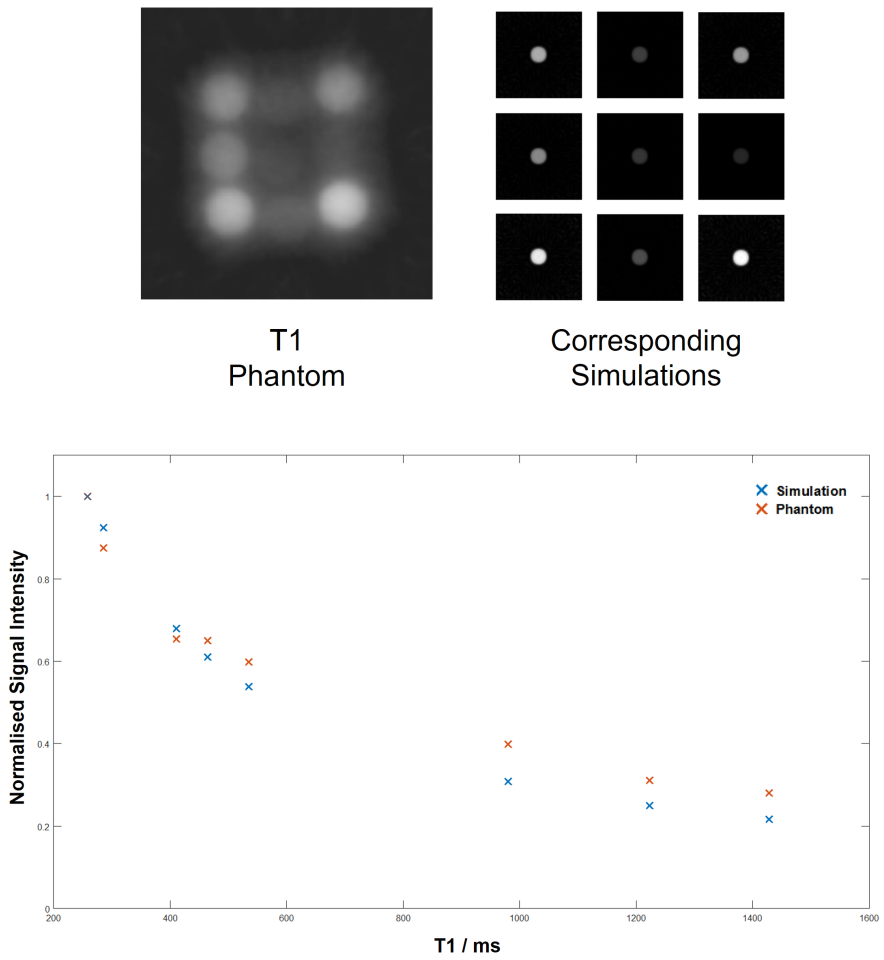

Figure 7.11.: Simulation validations - T_1 variation. The T_1 phantom image acquisition (top left) and the corresponding simulations for each of the equivalent T_1 values. The mean signal intensities for each T_1 value are plotted below. The intensity values are normalised to that of the shortest T_1 value for each dataset.

lieved to be a weakness with the automatic measure rather than a reflection of the actual image sharpness. Tissue variation (Figure 7.12b) and defect CNR (Figure 7.12c) measures in particular sharply deteriorated for the range of reduced ray numbers that would be required for short FPP shot duration. Readout partial Fourier (rPF) was significant in reducing epicardial sharpness. Golden angle ray ordering was significant in improving background variation and defect CNR compared to sequential ordering (Figure 7.13a).

2D: Modified Environments

The five environmental modifications significantly altered many of the image quality measures compared to the standard simulations (Figure 7.14). The bright superficial fat increased the intensity of undersampling aliasing across the entire image, with its impact on myocardial variation and defect CNR affected by ray ordering (Figure 7.13b). This can be explained from the ordering affect on the aliasing distribution. Likewise, due to the different overall angular ranges between sequential and golden angle methods, the ray order significantly affected the myocardial variation and defect CNR in the presence of timing delay and motion (Figure 7.13c&d). Cardiac motion had a large impact on the image measures, with the ray number unsurprisingly being by far the largest factor of contribution. The reduced bloodpool:myocardium contrast of the later perfusion frame resulted in fewer significant variables with only ray number remaining of large effect size.

3D: Standard Environment

The 3D standard environment simulations repeated with varying ray number showed similar results to 2D, with regards to border sharpness (Figure 7.15a), signal variation (Figure 7.15b), and defect CNR (Figure 7.15c).

The application of VU and sPF in 3D enabled measurements with a greater variation of total ray number, so that extra points could be plotted for a more detailed defect CNR curve. By separating the defect CNR curve in 3D (Figure 7.15)d) an apparent benefit is indicated in using fewer rays per partition without sPF, compared with acquiring the same total number of rays by combining more rays per sampled partition with sPF.

This idea is examined further separating the results by their ray reduction 'acceleration' method, as well as for their 3D trajectory combinations. Looking at these results for two of the key image measures, the acceleration does not have a clear impact on myocardial variability (Figure 7.16a), but

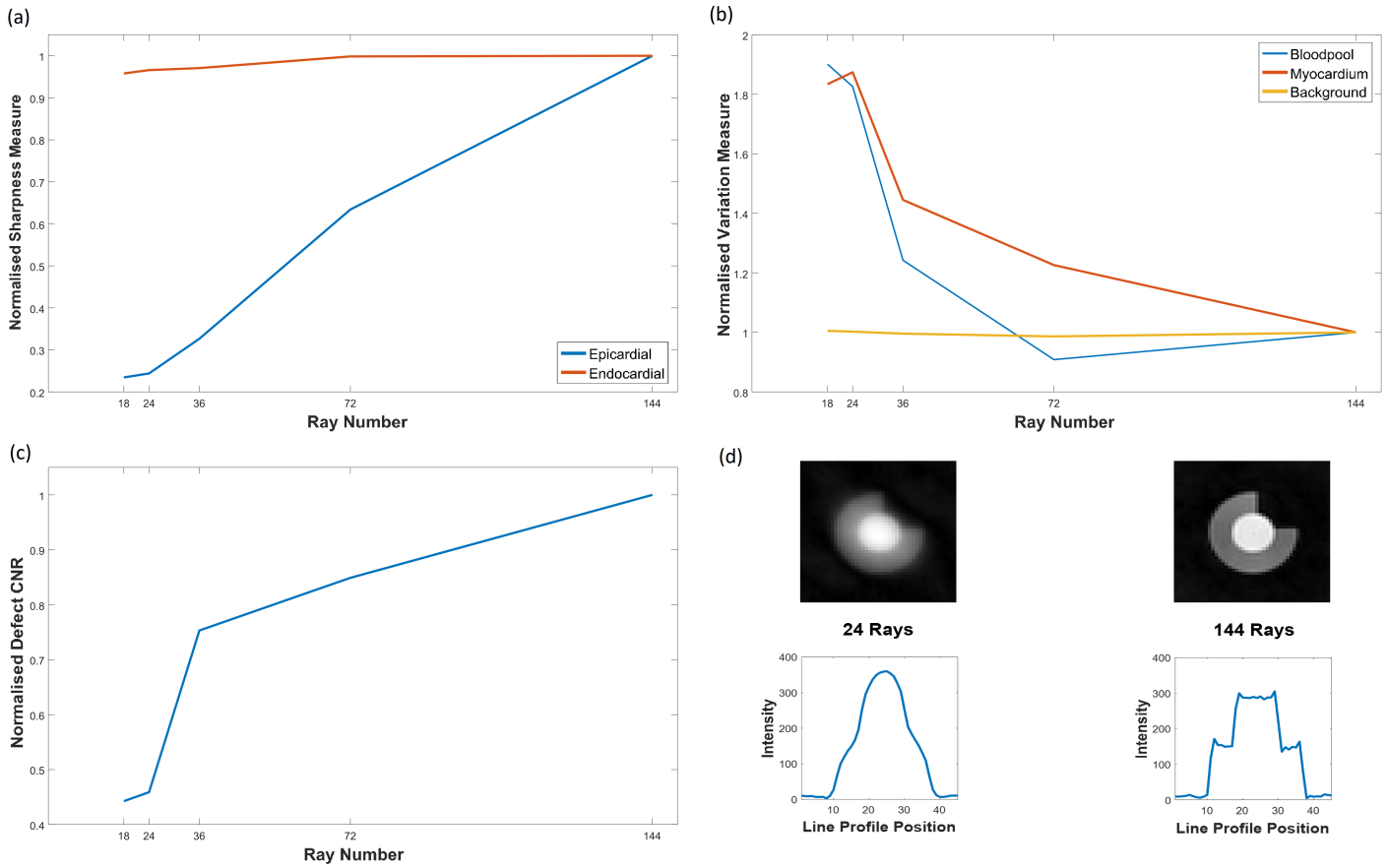

Figure 7.12.: Effect of ray number on image measures in 2D simulations. A linear relationship exists between ray number and epicardial sharpness, and slightly increased myocardial and bloodpool variations are seen for lower ray numbers. Defect CNR shows an apparent sharp drop for the lower ray numbers. Example images and corresponding line profiles are shown bottom right for simulations with low and high ray number, with otherwise identical sequence parameters. Values normalised to 144 ray number value.

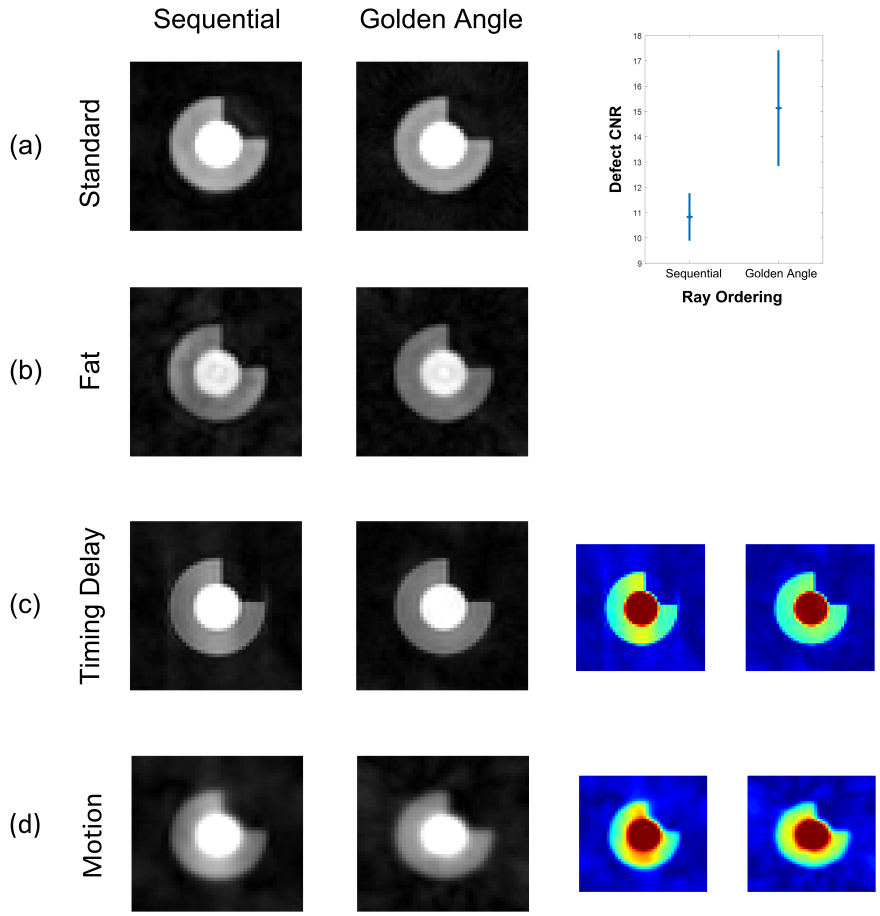

Figure 7.13.: Examples of "environmental" factors interacting with in-plane ray ordering modes on 2D simulations. The standard simulations showed a small but significant improvement in defect CNR using Golden Angle rather than sequential ordering. In the presence of fat, myocardial variation increased in all simulations, but Golden Angle simulations coped better. The different range of angles covered in the different trajectory orders led to an increased variation in the myocardium for sequential ordering, directed along one axis. In the presence of motion, the golden angle trajectory again distributed the impact more evenly. All example images were simulated with the same parameters, apart from trajectory ordering.

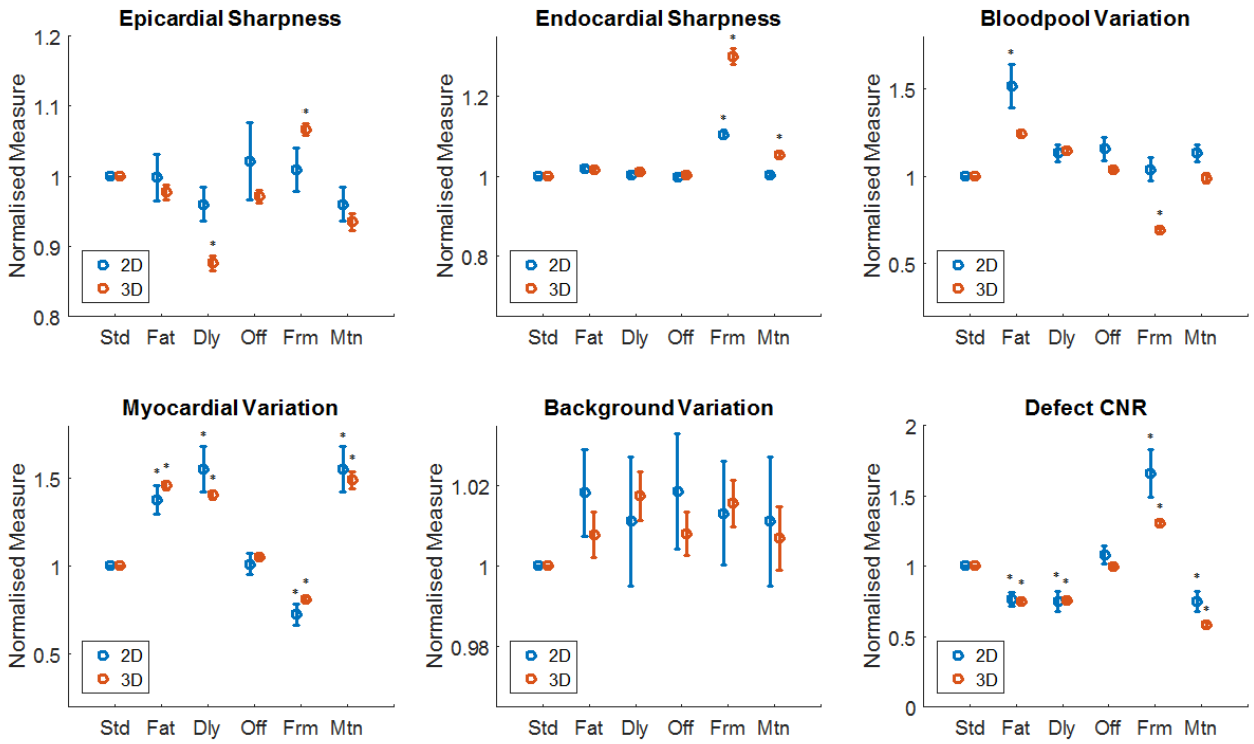

Figure 7.14.: A summary of the mean impact of the differing simulated environments on image measures for 2D and 3D imaging. Values are normalised to the image measures of the standard [Std] simulations. The Fat and Timing Delay [Dly] environments cause significant shifts in multiple measures. The in-plane offset of the radial FOV [Off] has little gross effect. For the later perfusion frame [Frm] there is greater border sharpness and defect CNR, and reduced myocardial signal variability, than when there is a higher blood:myocardium contrast. Cardiac motion [Mtn] shows multiple detrimental imaging effects. The extent to which the simulations with different sequence parameters contribute to these mean values is discussed further in the text. *denotes environment image scores significantly different than for the standard environment equivalent ($p<0.05$).

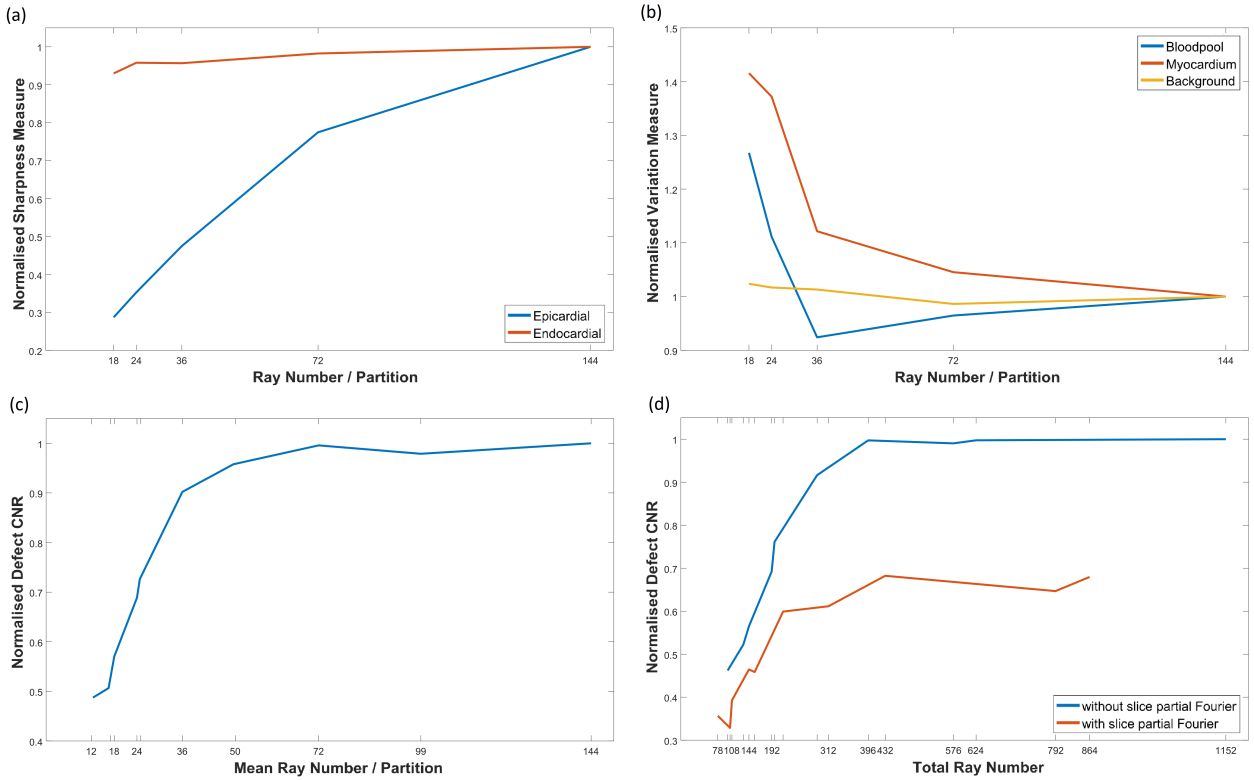

Figure 7.15.: Image quality measures plotted against varying ray number in 3D 'standard' simulations. The term "Ray Number / Partition" corresponds to the number of rays in the central k_z partition only. The term "Mean Ray Number / Partition" takes into account variable undersampling in k_z, averaging across all partitions. Unsurprisingly, all image measure scores were weakened by a reduction in the ray number.

there is a noticeable separation between the methods for the defect CNR results (Figure 7.16b). While VU reduces the defect CNR slightly for lower ray numbers, sPF consistently reduces defect CNR by a greater extent.

This negative impact on the defect CNR from the inclusion of sPF and VU in 3D FPP is likely to be due to the impact that both have on the through-plane resolution, which would increase partial volume effects. These differences in defect CNR comparative to an implementation that contained neither acceleration method are weaker for the range of total ray numbers that are most likely to be realistically useful for 3D FPP. These image quality effects may well also form a compromise against other effects that would be caused by a greater number of rays per partition, e.g. during motion (Section 7.3.3).

Trajectory order (Figure 7.16c&d) did not appear to play a significant role in the image quality measures for the standard environment.

3D: Modified Environments

The mean impact, averaged over all sequence parameter combinations, of each of the environmental factors on the image measures is shown in Figure 7.14. These results show that the presence of bright chest-wall fat or a timing delay error in 3D impacted on many of the image measures; a similar effect as noted in the 2D results (Section 7.3.3). While the "fat" environment impacted the bloodpool variation due to increased streaking and the "delay" environment affected the epicardial sharpness due to its smearing effect (Section 3.5.1), the most interesting effects could again be seen in the myocardial variation and defect CNR measures.

For the fat environment, the myocardial variation and defect CNR (Figure 7.17) showed similar patterns to the standard environment but at consistently higher values and with greater variation.

For the delay environment, while the ray reduction methods (Figure 7.18a&b) showed similar patterns to the standard environment, for the trajectory order (Figure 7.18c&d) the golden angle trajectory gave markedly improved myocardial variation and defect CNR values compared those using sequential ordering, although these affects are again reduced at lower ray numbers. This supports the 2D results while showing that other 3D imaging parameters do not appear to have as large an effect.

As for the 2D experiments, the "offset" environment produced no significant differences over the standard environment. The "frame" environment

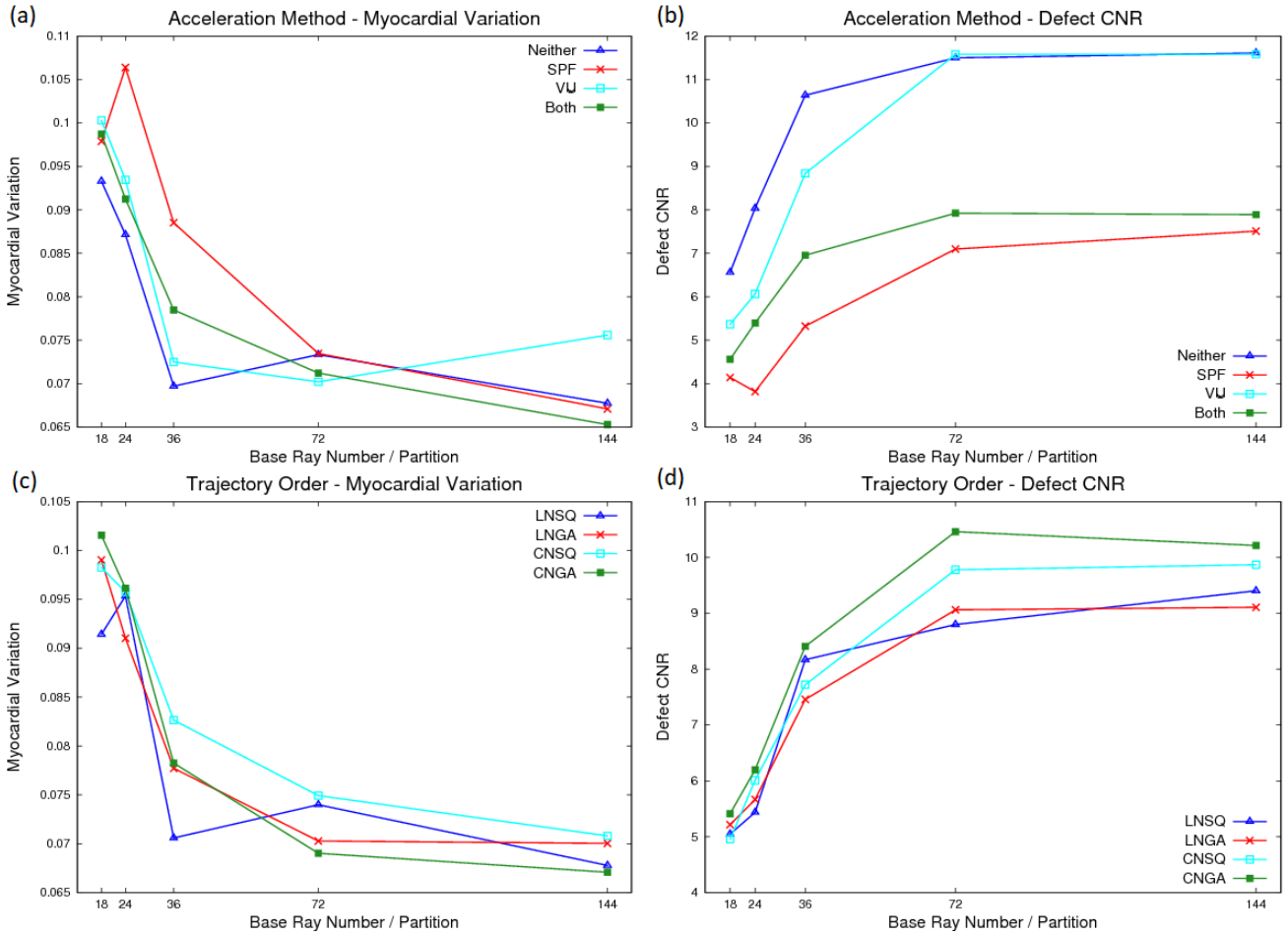

Figure 7.16.: Impact of 3D SOS trajectory parameters on image measures for the standard environment. Myocardial variation and defect CNR measure scores grouped by ray reduction 'acceleration' methods, as well as by trajectory orderings. [LNSQ] - linear through-plane, sequential in-plane. [LNGA] - Linear through-plane, golden-angle in-plane. [CNSQ] - centric through-plane, sequential in-plane. [CNGA] - centric through-plane, golden angle in-plane.

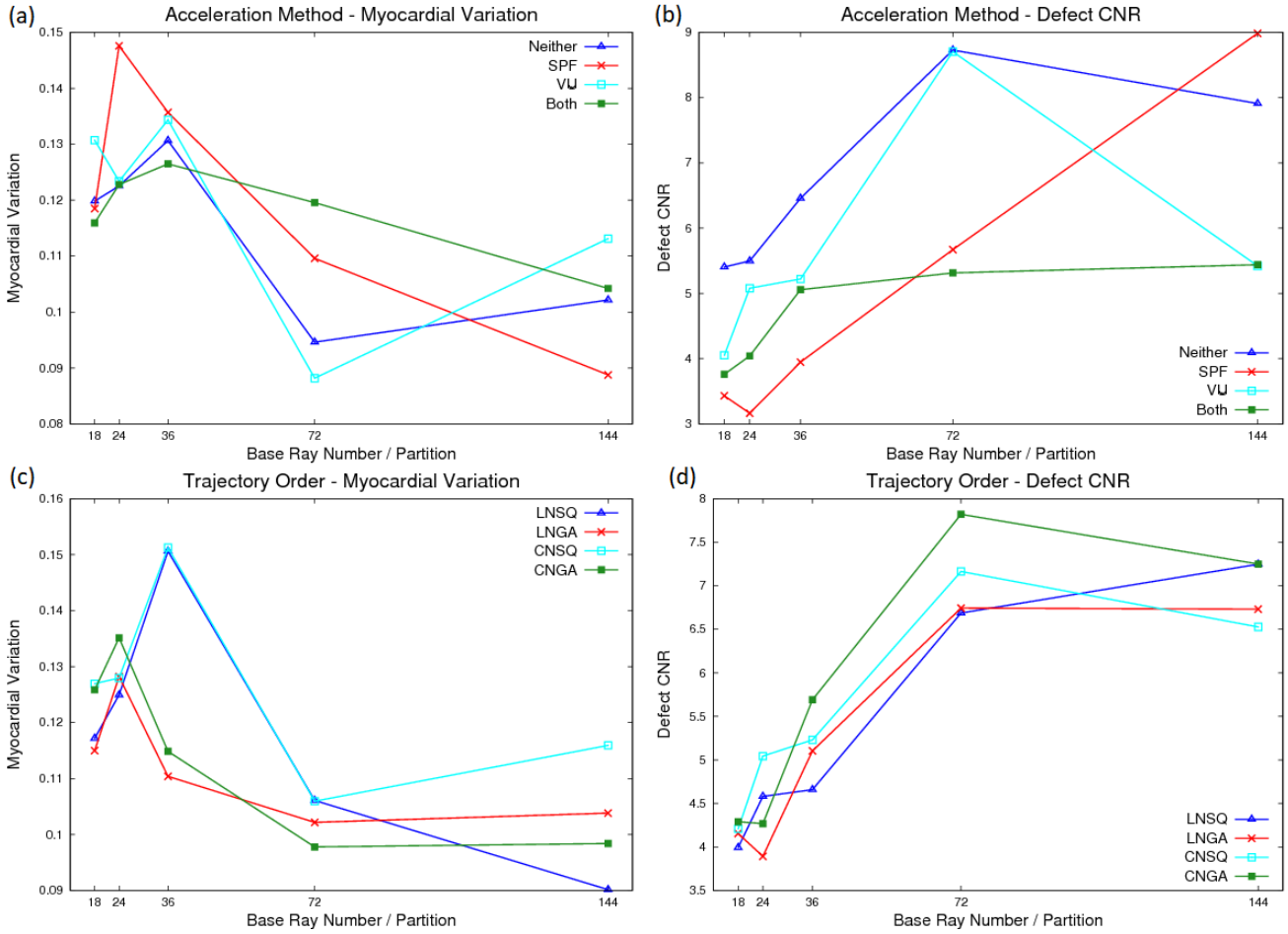

Figure 7.17.: Impact of 3D SOS trajectory parameters on image measures in the fat environment. See Figure 7.16 for the label definitions.

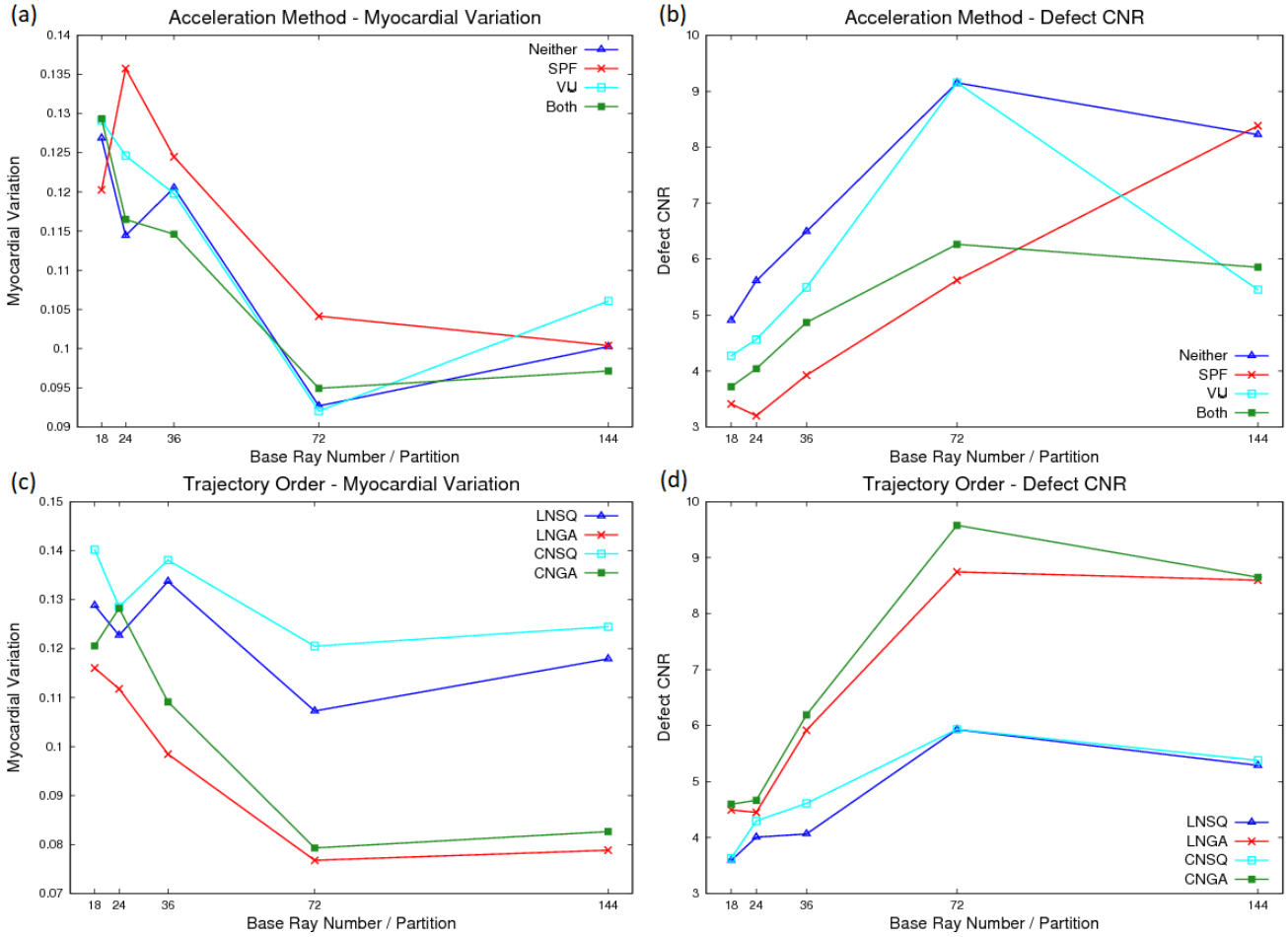

Figure 7.18.: Impact of 3D SOS trajectory parameters on image measures in the delay environment. See Figure 7.16 for the label definitions.

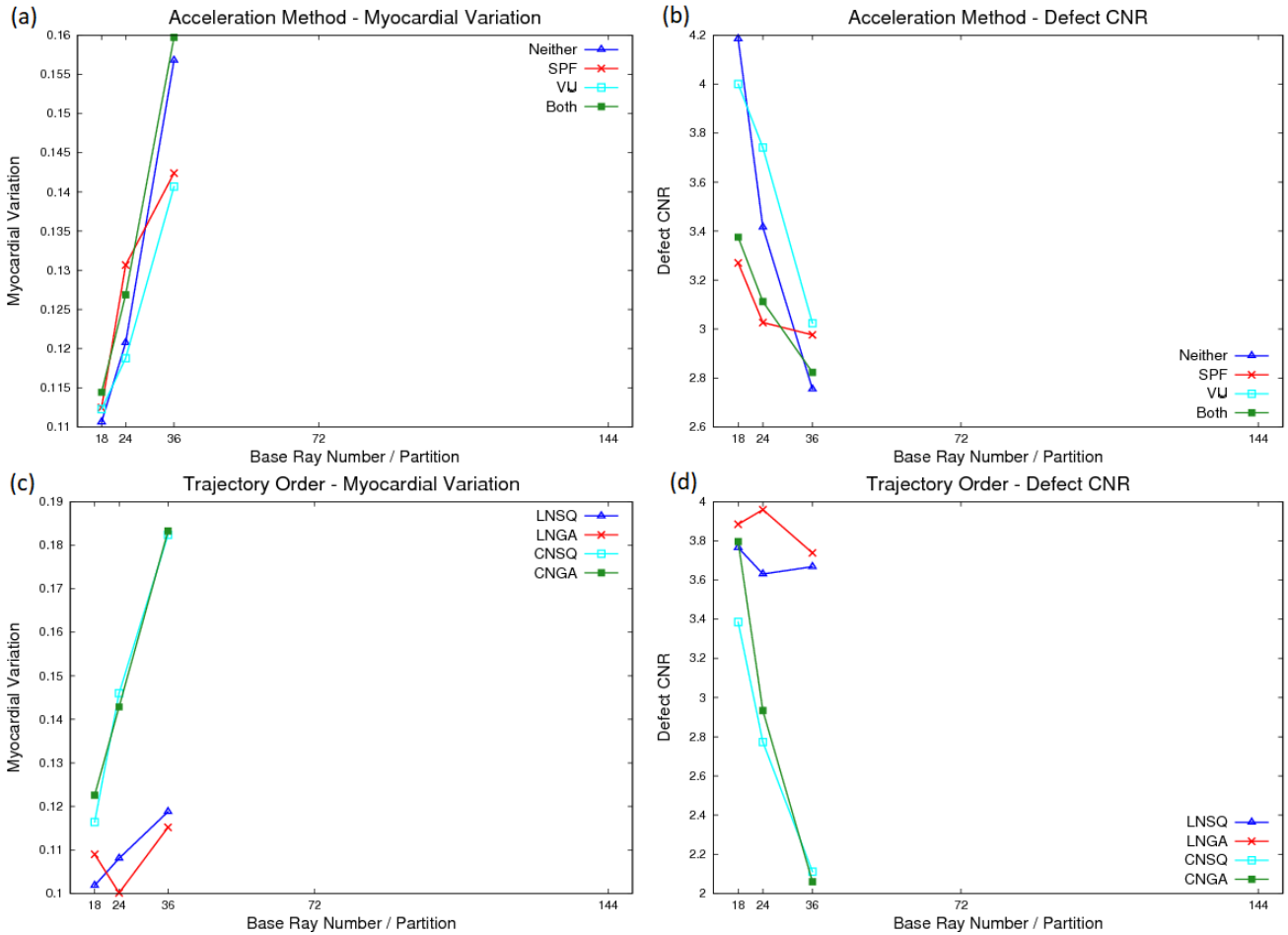

Figure 7.19.: Impact of 3D SOS trajectory parameters on image measures in the motion environment. See Figure 7.16 for the label definitions.

only affected the image measures that would be expected in relation to the altered blood:myocardium contrast, with improved edge sharpness scores and reduced myocardial and bloodpool variation.

The presence of motion quite predictably showed a strong negative impact with increasing ray number. In Figure 7.19, the benefits of not only reduced ray number, but also other ray reduction acceleration methods, are seen for the first time. Both myocardial variation and defect CNR are most strongly affected by ray number, and at the lowest ray numbers studied results showed a similar pattern to the those for the standard environment; these trends somewhat reverse with increasing ray number. Exact determination of the optimal trade-off between ray number and other acceleration methods is difficult from these simulations, particularly owing to the unrealistic motion modelled. The total ray number was restricted to keep 3D FPP shot duration semi-feasible regarding cardiac motion (<500ms), but this is still substantially longer than is realistic for cardiac filling, even at rest.

7.3.4. Discussion

Discussion of specific findings was included in the section above, with an overall discussion presented here.

Key findings were:

1. sPF and VU have a negative impact on several image features and should be considered carefully prior to use for shortening 3D shot duration. The modelled perfusion defect of unrealistic long-axis extent may have over emphasised detrimental partition-direction effects, but this model has demonstrated the existence of such worrying effects. Nevertheless, current 3D FPP methods realistically require strong reductions in shot duration, as seen in the motion simulations, and so methods such as sPF and VU are likely to continue to be applied. It is worth noting that many of the most severe effects of sPF and VU occur at a total number of rays that are far from feasible for *in vivo* 3D FPP.

2. Golden angle ordering showed apparent benefits, with greater robustness to various imaging environments comparative to sequential ordering. Many of these improved measures are hypothesised to be related to the different angular coverage ($0 \rightarrow \pi$ and $0 \rightarrow 2\pi$) between

the methods. Sequential methods could be adapted to provide similar coverage and a comparison with such an approach may be important to determine if the golden angle order inherently performs better. Golden angle ordering had not been chosen earlier, in part because of its weaker compatibility with the randomised RF spoiling method. These simulations did not model $M_{x,y}$ spoiling, which likely explains the different results seen. Investigation of spoiling in the simulation model, or of alternative spoiling methods for golden angle ordering, would be ideally be performed.

3. Simulations of the superficial bright fat signal showed a quite serious impact on image quality across the heart and this is despite not modelling the full potential effects of fat. Coil response profiles are not included in these simulations, and due to the close proximity of the receiver coils to this fat layer, the signal intensities that arise from the fat would likely often be stronger. Other sources of extra-cardiac fat (Section 1.2.1) closer to the LV myocardium were also not modelled and could be another strong source of similar artefacts.

4. The "offset" environment produced little effect, as would be expected from the spatially invariant PSF, but this also served as a validation of the simulation. Certain combinations of multiple environments, such as spatial offset and timing delay errors in particular, could be expected to have a more significant impact.

Future work should extend this simulation model. Some sequence parameters that were kept constant in this work, such as in-plane and through-plane spatial resolutions, could potentially be varied for extension to this work. However, with each new set of parameter combinations the computational time would be extended.

The motion simulation could be extended to provide more information about the end-systolic timing robustness, using a "contraction-stasis-filling" curvature of cardiac motion and "sliding" the 3D shot duration across this to illustrate its sensitivity to motion. The likely interactions of the k_z-acquisition order and angular-ray-ordering mode with this motion sensitivity should also be considered.

The altered perfusion frame environment studied here showed improved image measures, which supports the *in vivo* findings in this project that the majority of image quality issues occur in the peak LV blood-pool frames. A

wider range of perfusion first-pass changes in brightness should be simulated to explore their impact in more detail.

Finally, extension to the model could be made to produce multiple frames of the FPP for each simulation. This would allow investigation of how these investigated parameters and environments are affected by the advanced reconstruction methods, such as STCR. This could therefore also feasibly combine respiratory motion into the model for greater investigation into the role this plays for the free-breathing 3D SOS FPP acquisitions. Again, such an extension is limited by a large increase to the computational time and memory requirements that would occur with the current MATLAB implementation.

7.3.5. Conclusions

This simulation framework for 2D and 3D FPP enabled the importance of many radial imaging parameters to be tested, combined with a comprehensive range of imaging environments. However, the simulations model contained many limitations, and many of the results have generated new questions that require further investigation. The importance of particular variables has been highlighted, including a sharp drop off in image quality measures for low ray numbers and other ray reduction techniques, and how this conflicts with the demand for minimal 3D FPP shot duration. Other trajectory orders, such as golden angle and centric partition ordering, may provide greater robustness in certain environments but further *in vivo* examination of these effects is required. Extension of this model to multiple time frames would be necessary to allow examination of how these investigated image degradation effects would alter STCR reconstructed datasets.

8. Discussion

8.1. Summary of Findings

The project aimed to investigate the development of whole-heart myocardial perfusion magnetic resonance imaging, by advancing and analysing 3D first-pass perfusion (FPP) methods. A summary of the work and its findings is presented next.

The technical optimisation of the stack-of-stars (SOS) sequence design was described in Chapter 3. Detailed work there, which included implementation of a highly optimised slab-excitation RF pulse, has shown the SOS sequence to be effective for acquiring highly undersampled SGRE 3D FPP shots. A variable undersampling method of reducing the number of rays was demonstrated as a potential method of reducing the shot duration. A 'randomised' RF phase spoiling method, which avoided time-consuming additional gradients, was also tested. New insights were gained into the novel extension of this spoiling method to 3D SOS imaging, where its effectiveness was found to be weakened, particularly for the golden angle trajectories that are currently often used in radial imaging. Nevertheless, with this 'gradient-free' spoiling method applied with sequential ordering, combined with the other k-space efficiencies (defined in Chapter 2), the 3D SOS FPP sequence was reduced to a shot duration of 188ms - marginally faster than any 3D FPP sequence published to date.

In Chapter 4, a novel method for reduction of artefacts in free-breathing parallel imaging accelerated FPP reconstructions was presented. This parallel imaging calibration method, was shown to be highly effective comparative to current techniques. The method could potentially allow higher acceleration factors by parallel imaging for free-breathing FPP, however the SNR degradation that is unavoidable with parallel imaging limits its ability to support the acceleration factors required for 3D FPP. Therefore, a compressed sensing algorithm that employs spatial and temporal constraints (STCR) was next investigated for use with 3D SOS FPP. The algorithm was tested

for its response to respiratory motion and FPP changes in image contrast, and a constraint reordering method (CRM) was examined to improve the temporal fidelity of the STCR. While the CRM technique has previously been shown to perform well theoretically and in retrospectively subsampled 2D FPP datasets, here it was found to have limitations in its current form when applied to prospectively accelerated 3D SOS FPP.

The 3D SOS method was extended as part of two original 3D SOS FPP protocols in Chapter 5. An alternate cardiac cycle acquisition scheme enabled improvements to be made independently to the in-plane and through-plane resolutions of the sequence. Alongside its aim of providing some confirmation against artefacts, this alternate-cycle method also enabled good quality SAX acquisitions (which formed the basis for the finalised sequence) during the same FPP as LAX acquisitions which demonstrated the first example of more closely isotropic 3D FPP data. In the second section of Chapter 5, a bSSFP 3D SOS FPP sequence was developed, looking to gain advantages in SNR comparative to SGRE, with novel alterations of the sequence design to improve robustness to bSSFP off-resonance and stabilisation artefacts. Although these artefacts were reduced, SGRE was preferred to bSSFP with regards to artefacts and, after further modifications, a final SGRE 3D SOS FPP sequence was chosen for clinical testing.

Testing of the finalised 3D SOS FPP sequence at stress in healthy volunteers and coronary artery disease patients (Chapter 6) was important to examine the realistic application of the technique. The first detection of induced perfusion defects with a free-breathing 3D FPP sequence was demonstrated, with good agreement to SPECT MPS and confirmation by x-ray angiography. This was also the first detection of induced perfusion defects in a 3D FPP sequence that utilised a compressed sensing reconstruction. In patients with milder forms of coronary artery disease, as defined by MPS, weaker agreement was found compared with the 3D SOS FPP sequence. The sample size was below that required to draw strong conclusions, but the unclear findings in milder CAD raised some doubts over the sensitivity of this technique, particularly with the presence of localised transient dark-myocardial artefacts in the majority of the 3D FPP datasets.

Chapter 7 proposed the existence of a previously undescribed version of the troublesome dark-rim artefact (DRA), specific to the partition-direction phase-encoding used for 3D FPP, and demonstrated the creation of these partition-axis DRAs using simulated datasets. Finally, a more detailed

simulation framework was created that enabled sampling of a representative LV object with a highly flexible 3D SOS FPP sequence. This was used for some initial investigations into the impact of different 3D SOS sequence parameters, as well as different imaging conditions, on the image quality. Amongst other preliminary findings, the importance of minimised shot duration in the presence of cardiac motion was confirmed, as well as the potential benefit of golden angle ordering, if it could be implemented in combination with an improved time-efficient spoiling method.

8.2. Limitations

Specific limitations to the individual components of the project have been discussed in their respective sections. Here, a summary of some of the main overarching limitations to the project is presented.

A fundamental challenge of the project was the difficulty in achieving the required sequence acceleration, necessary to capture a 3D shot in a short enough duration within each cardiac cycle. A realistic shot duration to minimise intra-shot cardiac motion was given priority throughout the sequence development; the inevitable reduction in image quality that arises from the application of multiple extreme sequence acceleration techniques therefore became a focus of the project, the investigation of which was prioritised over other avenues of exploration.

Myocardial artefacts in the reconstructed datasets were a problem throughout the work. As is known for the DRA in multi-slice 2D FPP, artefacts are particularly troublesome for FPP as they can easily cast doubt on a diagnosis, especially in this technique for which repeated acquisitions are impractical. The artefacts encountered in this work were presented and discussed, with possible theories for their causes. It was difficult to always determine the cause of an artefact, especially as so many components to the sequence, imaging environment and reconstruction method have the potential to cause them. The simulation framework aimed to begin the separation of these factors, but further with work with this method is still required.

For a lot of the *in vivo* testing, rest imaging only was available. There are obvious limitations to rest-only tests, because heart rates and respiratory motion are reduced comparative to at stress. The tests performed were made

as realistic as possible by ensuring the minimal 3D FPP shot duration and also by requesting artificially exaggerated respiratory motion, if required. However, the free-breathing stress imaging investigation was critical to provide confidence in the 3D FPP sequence's realistic application. A greater number of patients with CAD would clearly ideally have been acquired.

A major limitation in the work was the substantial difficulty in subject recruitment, especially for stress imaging. This unfortunately leaves uncertainty in the diagnostic ability of the sequence and it restricted more realistic thorough testing of the different sequence types investigated for 3D FPP. The datasets that were acquired did allow confirmation of a detected perfusion deficit which, as previously described, was the first such demonstration for free-breathing 3D FPP with a compressed sensing reconstruction. The more mixed results in the milder coronary artery disease cases is a limitation that requires further investigation with greater patient sample sizes.

8.3. Future Work

In this section general topics for further work are suggested that could extend the development of this 3D FPP project closer to clinical application.

One of the most important areas for future work, identified through the limitations, would be with the acquisition of a greater number of *in vivo* datasets at stress. This would be critical in determining not only the diagnostic ability of the current technique, but for investigating other topics of required future work under a more accurate set of conditions.

The simulation model of Chapter 7 requires further work and additions, as discussed in the chapter itself, but some of the results drawn from the simulations would ideally be tested *in vivo*. Extension to the simulations could also be used to examine any number of possible extensions to the sequence design. Many atypical trajectories are feasibly possible in SOS, which could be tested in the current simulation model, the results of which could then be implemented and tested in the sequence itself.

More in-depth investigation of the reconstruction method is required, particularly with regard to its spatiotemporal fidelity. Free-breathing datasets were successfully acquired with the sequence and reconstruction combination, but there was still uncertainty in the accuracy of the reconstructions. An extension of the simulation work, or use of other simulated datasets

(e.g. [Wissmann et al., 2014b]), could potentially aid in the investigation of the method as well as for comparison with other feasible spatiotemporal reconstruction techniques [Pedersen et al., 2009b][Chen et al., 2014b].

Some methods to speed up the reconstruction times were implemented in Section 5.3.2, however, as is common to many advanced, iterative reconstruction methods, the time from image acquisition to the image being available to view is far beyond what would be clinically preferred. In addition, current reconstruction methods do not run fully automatically for clinical evaluation, in that they require the raw data to be exported for reconstruction in Matlab (although no "per-patient" adjustment was required). Future work could feasibly look at using reconstruction frameworks such as the Gadgetron [Hansen and Sørensen, 2013] to enable efficiently reconstructed images to be automatically returned to the scanner console for display. More realistically in the near-term future, simpler initial reconstructions could be delivered in such a way as to allow the operator to at least check for the successful arrival of the contrast agent.

The technique of principal component analysis (PCA) was applied to reduce the effective number of receiver channels 'coils' used in the reconstruction, as part of the effort to speed up the reconstruction process (Section 5.3.2). Further potential work could examine alternative methods for achieving this reduction in data input size. In some previous work, optimal image quality has been dependent on manual selection of the optimal coils to use in the reconstruction. Such a process has additional benefits of avoiding coils that are comprised mostly of noise or, for non-Cartesian datasets such as here, those which contain high levels of streaking or artefact. The downside of a coil selection process such as this is that it is manual and time-consuming, typically requiring intervention by an experienced researcher, but some automated versions of this method may be possible to explore. Machine learning is a highly active topic in the image processing community and recent work has included machine learning for automation of coil-rejection on the basis of artefacts [Cavallo et al., 2017]. The implementation of this method instead of, or as well as, PCA coil reduction, could theoretically improve the input data while reducing the reconstruction time.

8.4. Conclusions

The development of 3D first-pass myocardial perfusion magnetic resonance imaging has been approached through the use of a highly undersampled radial 'stack-of-stars' sequence and a spatiotemporally constrained compressed sensing reconstruction. Work was performed to optimise both of these areas, and different novel implementations of the sequence were tested. A final SGRE version of the 3D SOS FPP sequence and reconstruction method underwent initial testing in a clinical population at stress, which met many of the aims of the project including free-breathing acquisition. Uncertainty in the diagnostic performance of this technique remains, and dark transient artefacts in the myocardium were a consistent and serious problem in the project. Some of the potential causes of these artefacts in 3D FPP were studied and a simulation framework was designed with the aim of examining these further, as well as to optimise whole-heart perfusion to a greater extent in the future.

Bibliography

[Ablitt et al., 2004] Ablitt, N. A., Gatehouse, P. D., Firmin, D. N., and Yang, G.-Z. (2004). Respiratory reordered UNFOLD perfusion imaging. *J. Magn. Reson. Imaging*, 20(5):817–825.

[Acar and Vogel, 1994] Acar, R. and Vogel, C. R. (1994). Analysis of bounded variation penalty methods for ill-posed problems. *Inverse Problems*, 10(6):1217.

[Adluru et al., 2007] Adluru, G., Awate, S. P., Tasdizen, T., Whitaker, R. T., and DiBella, E. V. (2007). Temporally constrained reconstruction of dynamic cardiac perfusion MRI. *Magn. Reson. Med.*, 57(6):1027–1036.

[Adluru and DiBella, 2012] Adluru, G. and DiBella, E. (2012). Compression2: compressed sensing with compressed coil arrays. *J Cardiovasc Magn Reson*, 14(S1):P242.

[Adluru and DiBella, 2008] Adluru, G. and DiBella, E. V. R. (2008). Reordering for Improved Constrained Reconstruction from Undersampled k-Space Data. *Int J Biomed Imaging*, 2008.

[Adluru et al., 2015] Adluru, G., Gur, Y., Chen, L., Feinberg, D., Anderson, J., and DiBella, E. V. R. (2015). MRI reconstruction of multi-image acquisitions using a rank regularizer with data reordering. *Medical Physics*, 42(8):4734–4744.

[Adluru et al., 2009] Adluru, G., McGann, C., Speier, P., Kholmovski, E. G., Shaaban, A., and DiBella, E. V. (2009). Acquisition and reconstruction of undersampled radial data for myocardial perfusion magnetic resonance imaging. *J. Magn. Reson. Imaging*, 29(2):466–473.

[Akçakaya et al., 2014] Akçakaya, M., Basha, T. A., Pflugi, S., Foppa, M., Kissinger, K. V., Hauser, T. H., and Nezafat, R. (2014). Localized spatio-temporal constraints for accelerated CMR perfusion. *Magnetic Resonance in Medicine*, 72(3):629–639.

[Aldefeld and Börnert, 1998] Aldefeld, B. and Börnert, P. (1998). Effects of gradient anisotropy in MRI. *Magn. Reson. Med.*, 39(4):606–614.

[Armstrong, 1991] Armstrong, W. F. (1991). Stress echocardiography for detection of coronary artery disease. *Circulation*, 84(3 Suppl):I43–49.

[Armstrong et al., 1982] Armstrong, W. F., Mueller, T. M., Kinney, E. L., Tickner, E. G., Dillon, J. C., and Feigenbaum, H. (1982). Assessment of myocardial perfusion abnormalities with contrast-enhanced two-dimensional echocardiography. *Circulation*, 66(1):166–173.

[Arunachalam et al., 2007] Arunachalam, A., Samsonov, A., and Block, W. F. (2007). Self-calibrated GRAPPA method for 2d and 3d radial data. *Magn. Reson. Med.*, 57(5):931–938.

[Atkinson et al., 1990] Atkinson, D. J., Burstein, D., and Edelman, R. R. (1990). First-pass cardiac perfusion: evaluation with ultrafast MR imaging. *Radiology*, 174(3 Pt 1):757–762.

[Barger et al., 2002] Barger, A. V., Block, W. F., Toropov, Y., Grist, T. M., and Mistretta, C. A. (2002). Time-resolved contrast-enhanced imaging with isotropic resolution and broad coverage using an undersampled 3d projection trajectory. *Magn. Reson. Med.*, 48(2):297–305.

[Barkhausen et al., 2004] Barkhausen, J., Hunold, P., Jochims, M., and Debatin, J. F. (2004). Imaging of myocardial perfusion with magnetic resonance. *Journal of Magnetic Resonance Imaging*, 19(6):750–757.

[Basha et al., 2014] Basha, T. A., Roujol, S., Kissinger, K. V., Goddu, B., Berg, S., Manning, W. J., and Nezafat, R. (2014). Free-breathing cardiac MR stress perfusion with real-time slice tracking. *Magnetic Resonance in Medicine*, 72(3):689–698.

[Bateman et al., 2006] Bateman, T. M., Heller, G. V., McGhie, A. I., Friedman, J. D., Case, J. A., Bryngelson, J. R., Hertenstein, G. K., Moutray, K. L., Reid, K., and Cullom, S. J. (2006). Diagnostic accuracy of rest/stress ECG-gated Rb-82 myocardial perfusion PET: Comparison with ECG-gated Tc-99m sestamibi SPECT. *Journal of Nuclear Cardiology*, 13(1):24–33.

[Belliveau et al., 1991] Belliveau, J. W., Kennedy, D. N., McKinstry, R. C., Buchbinder, B. R., Weisskoff, R. M., Cohen, M. S., Vevea, J. M., Brady, T. J., and Rosen, B. R. (1991). Functional mapping of the human visual cortex by magnetic resonance imaging. *Science*, 254(5032):716–719.

[Bernstein et al., 2001] Bernstein, M. A., Fain, S. B., and Riederer, S. J. (2001). Effect of windowing and zero-filled reconstruction of MRI data on spatial resolution and acquisition strategy. *J. Magn. Reson. Imaging*, 14(3):270–280.

[Bernstein et al., 2006] Bernstein, M. A., Huston, J., and Ward, H. A. (2006). Imaging artifacts at 3.0t. *J. Magn. Reson. Imaging*, 24(4):735–746.

[Bernstein et al., 2004] Bernstein, M. A., King, K. F., and Zhou, X. J. (2004). *Handbook of MRI Pulse Sequences*. Elsevier Academic Press, Burlington, MA, USA.

[Bertaso et al., 2013] Bertaso, A. G., Bertol, D., Duncan, B. B., and Foppa, M. (2013). Epicardial Fat: Definition, Measurements and Systematic Review of Main Outcomes. *Arq Bras Cardiol*, 101(1):e18–e28.

[Bertschinger et al., 2001] Bertschinger, K. M., Nanz, D., Buechi, M., Luescher, T. F., Marincek, B., von Schulthess, G. K., and Schwitter, J. (2001). Magnetic resonance myocardial first-pass perfusion imaging: Parameter optimization for signal response and cardiac coverage. *J. Magn. Reson. Imaging*, 14(5):556–562.

[Betts et al., 2016] Betts, J. G., Desaix, P., Johnson, E., Johnson, J. E., Korol, O., Kruse, D., Poe, B., Wise, J., Womble, M. D., Young, K. A., OpenStax College, and Rice University (2016). *Anatomy & physiology*. OCLC: 959288423.

[Bieri et al., 2005] Bieri, O., Markl, M., and Scheffler, K. (2005). Analysis and compensation of eddy currents in balanced SSFP. *Magn. Reson. Med.*, 54(1):129–137.

[Biglands, 2012] Biglands, J. D. (2012). *Quanitifying myocardial blood flow using dynamic contrast enhanced cardiac magnetic resonance imaging*. PhD Thesis, University of Leeds.

[Biglands et al., 2012] Biglands, J. D., Radjenovic, A., and Ridgway, J. P. (2012). Cardiovascular magnetic resonance physics for clinicians: part II. *Journal of Cardiovascular Magnetic Resonance*, 14:66.

[Blaimer et al., 2011] Blaimer, M., Ponce, I. P., Breuer, F. A., Jakob, P. M., Griswold, M. A., and Kellman, P. (2011). Temporal filtering effects in dynamic parallel MRI. *Magnetic Resonance in Medicine*, 66(1):192–198.

[Block, 2005] Block, K. T. (2005). *Advanced methods for radial data sampling in magnetic resonance imaging*. PhD Thesis, University of Göttingen.

[Block et al., 2007] Block, K. T., Uecker, M., and Frahm, J. (2007). Undersampled radial MRI with multiple coils. Iterative image reconstruction using a total variation constraint. *Magnetic Resonance in Medicine*, 57(6):1086–1098.

[Brau et al., 2008] Brau, A. C., Beatty, P. J., Skare, S., and Bammer, R. (2008). Comparison of reconstruction accuracy and efficiency among autocalibrating data-driven parallel imaging methods. *Magnetic Resonance in Medicine*, 59(2):382–395.

[Breuer et al., 2005] Breuer, F. A., Kellman, P., Griswold, M. A., and Jakob, P. M. (2005). Dynamic autocalibrated parallel imaging using temporal GRAPPA (TGRAPPA). *Magnetic Resonance in Medicine*, 53(4):981–985.

[Brodsky et al., 2009] Brodsky, E. K., Samsonov, A. A., and Block, W. F. (2009). Characterizing and correcting gradient errors in non-cartesian imaging: Are gradient errors linear time-invariant (LTI)? *Magn. Reson. Med.*, 62(6):1466–1476.

[Buehrer et al., 2007] Buehrer, M., Pruessmann, K. P., Boesiger, P., and Kozerke, S. (2007). Array compression for MRI with large coil arrays. *Magn. Reson. Med.*, 57(6):1131–1139.

[Buhr et al., 2008] Buhr, C., Gössl, M., Erbel, R., and Eggebrecht, H. (2008). Regadenoson in the detection of coronary artery disease. *Vasc Health Risk Manag*, 4(2):337–340.

[Candes et al., 2006] Candes, E. J., Romberg, J., and Tao, T. (2006). Robust uncertainty principles: exact signal reconstruction from highly incomplete frequency information. *IEEE Transactions on Information Theory*, 52(2):489–509.

[Captur et al., 2016] Captur, G., Gatehouse, P., Keenan, K. E., Heslinga, F. G., Bruehl, R., Prothmann, M., Graves, M. J., Eames, R. J., Torlasco, C., Benedetti, G., Donovan, J., Ittermann, B., Boubertakh, R., Bathgate, A., Royet, C., Pang, W., Nezafat, R., Salerno, M., Kellman, P., and Moon, J. C. (2016). A medical device-grade T1 and ECV phantom for global T1 mapping quality assurancethe T1 Mapping and ECV Standardization in cardiovascular magnetic resonance (T1mes) program. *Journal of Cardiovascular Magnetic Resonance*, 18:58.

[Carlson, 1987] Carlson, J. (1987). An algorithm for NMR imaging reconstruction based on multiple RF receiver coils. *Journal of Magnetic Resonance (1969)*, 74(2):376–380.

[Caruso et al., 2016] Caruso, D., Eid, M., Schoepf, U. J., Jin, K. N., Varga-Szemes, A., Tesche, C., Mangold, S., Spandorfer, A., Laghi, A., and De Cecco, C. N. (2016). Dynamic CT myocardial perfusion imaging. *European Journal of Radiology*, 85(10):1893–1899.

[Cauley et al., 2015] Cauley, S. F., Xi, Y., Bilgic, B., Xia, J., Adalsteinsson, E., Balakrishnan, V., Wald, L. L., and Setsompop, K. (2015). Fast reconstruction for multichannel compressed sensing using a hierarchically semiseparable solver. *Magn. Reson. Med.*, 73(3):1034–1040.

[Cavallo et al., 2017] Cavallo, F., Ferreira, P. F., Khalique, Z., Scott, A. D., Nielles-Vallespin, S., and Firmin, D. N. (2017). Automatic detection of corrupted frames in

cardiac DTI with machine learning. In *25th Scientific Meeting ISMRM 2017*, Honolulu, USA.

[Cerqueira et al., 1994] Cerqueira, M. D., Verani, M. S., Schwaiger, M., Heo, J., and Iskandrian, A. S. (1994). Safety profile of adenosine stress perfusion imaging: Results from the adenoscan multicenter trial registry. *Journal of the American College of Cardiology*, 23(2):384–389.

[Cerqueira et al., 2002] Cerqueira, M. D., Weissman, N. J., Dilsizian, V., Jacobs, A. K., Kaul, S., Laskey, W. K., Pennell, D. J., Rumberger, J. A., Ryan, T., and Verani, M. S. (2002). Standardized Myocardial Segmentation and Nomenclature for Tomographic Imaging of the Heart A Statement for Healthcare Professionals From the Cardiac Imaging Committee of the Council on Clinical Cardiology of the American Heart Association. *Circulation*, 105(4):539–542.

[Chang et al., 2012] Chang, Y., Liang, D., and Ying, L. (2012). Nonlinear GRAPPA: A kernel approach to parallel MRI reconstruction. *Magnetic Resonance in Medicine*, 68(3):730–740.

[Chao et al., 2010] Chao, T.-C., Chung, H.-W., Hoge, W. S., and Madore, B. (2010). A 2d MTF approach to evaluate and guide dynamic imaging developments. *Magn. Reson. Med.*, 63(2):407–418.

[Chen et al., 2013] Chen, C., Li, Y., and Huang, J. (2013). Calibrationless parallel MRI with joint total variation regularization. *Med Image Comput Comput Assist Interv*, 16(Pt 3):106–114.

[Chen et al., 1997] Chen, E. Q., MacIntyre, W. J., Go, R. T., Brunken, R. C., Saha, G. B., Wong, C. Y., Neumann, D. R., Cook, S. A., and Khandekar, S. P. (1997). Myocardial viability studies using fluorine-18-FDG SPECT: a comparison with fluorine-18-FDG PET. *J. Nucl. Med.*, 38(4):582–586.

[Chen et al., 2012] Chen, L., Adluru, G., Schabel, M. C., McGann, C. J., and DiBella, E. V. R. (2012). Myocardial perfusion MRI with an undersampled 3d stack-of-stars sequence. *Medical Physics*, 39(8):5204–5211.

[Chen et al., 2014a] Chen, L., Wang, X., Bao, J., Geng, C., Xia, Y., and Wang, J. (2014a). Direct Comparison of Cardiovascular Magnetic Resonance and Single-Photon Emission Computed Tomography for Detection of Coronary Artery Disease: A Meta-Analysis. *PLoS ONE*, 9(2):e88402.

[Chen et al., 2014b] Chen, X., Salerno, M., Yang, Y., and Epstein, F. H. (2014b). Motion-compensated compressed sensing for dynamic contrast-enhanced MRI using regional spatiotemporal sparsity and region tracking: Block low-rank sparsity with motion-guidance (BLOSM). *Magn. Reson. Med.*, 72(4):1028–1038.

[Chow et al., 2015] Chow, K., Kellman, P., Spottiswoode, B. S., Nielles-Vallespin, S., Arai, A. E., Salerno, M., and Thompson, R. B. (2015). Saturation pulse design for quantitative myocardial T1 mapping. *Journal of Cardiovascular Magnetic Resonance*, 17(1).

[Christian et al., 2004] Christian, T. F., Rettmann, D. W., Aletras, A. H., Liao, S. L., Taylor, J. L., Balaban, R. S., and Arai, A. E. (2004). Absolute Myocardial Perfusion in Canines Measured by Using Dual-Bolus First-Pass MR Imaging. *Radiology*, 232(3):677–684.

[Chung et al., 2004] Chung, C. S., Karamanoglu, M., and Kovcs, S. J. (2004). Duration of diastole and its phases as a function of heart rate during supine bicycle exercise. *American Journal of Physiology - Heart and Circulatory Physiology*, 287(5):H2003–H2008.

[Codella et al., 2011] Codella, N. C. F., Spincemaille, P., Prince, M., and Wang, Y. (2011). A Radial Self-Calibrated (RASCAL) GRAPPA method using Weight Interpolation. *NMR Biomed*, 24(7):844–854.

[Cohen, 1960] Cohen, J. (1960). A Coefficient of Agreement for Nominal Scales. *Educational and Psychological Measurement*, 20(1):37–46.

[Crawley et al., 1988] Crawley, A. P., Wood, M. L., and Henkelman, R. M. (1988). Elimination of transverse coherences in FLASH MRI. *Magn. Reson. Med.*, 8(3):248–260.

[Cui et al., 2012] Cui, X., Gore, J. C., and Welch, E. B. (2012). Static Magnetic Field Inhomogeneity Correction of Radial MRI Using an Alternating Gradient Readout Acquisition. In *20th Scientific Meeting ISMRM 2012*, Melbourne, Australia.

[Cuppen and van Est, 1987] Cuppen, J. and van Est, A. (1987). Reducing MR imaging time by one-sided reconstruction. *Magnetic Resonance Imaging*, 5(6):526–527.

[De Cecco et al., 2015] De Cecco, C. N., Varga-Szemes, A., Meinel, F. G., Renker, M., and Schoepf, U. J. (2015). Beyond stenosis detection: computed tomography approaches for determining the functional relevance of coronary artery disease. *Radiol. Clin. North Am.*, 53(2):317–334.

[Deshmane et al., 2012] Deshmane, A., Gulani, V., Griswold, M. A., and Seiberlich, N. (2012). Parallel MR imaging. *Journal of Magnetic Resonance Imaging*, 36(1):55–72.

[Detre et al., 1994] Detre, J. A., Zhang, W., Roberts, D. A., Silva, A. C., Williams, D. S., Grandis, D. J., Koretsky, A. P., and Leigh, J. S. (1994). Tissue specific perfusion imaging using arterial spin labeling. *NMR Biomed*, 7(1-2):75–82.

[Di Bella et al., 2005] Di Bella, E., Parker, D., and Sinusas, A. (2005). On the dark rim artifact in dynamic contrast-enhanced MRI myocardial perfusion studies. *Magnetic Resonance in Medicine*, 54(5):1295–1299.

[Di Carli and Hachamovitch, 2006] Di Carli, M. F. and Hachamovitch, R. (2006). Should PET replace SPECT for evaluating CAD? The end of the beginning. *Journal of Nuclear Cardiology*, 13(1):2–7.

[DiBella et al., 2012] DiBella, E. V. R., Chen, L., Schabel, M. C., Adluru, G., and McGann, C. J. (2012). Myocardial perfusion acquisition without magnetization preparation or gating. *Magn. Reson. Med.*, 67(3):609–613.

[Ding et al., 1998] Ding, S., Wolff, S. D., and Epstein, F. H. (1998). Improved coverage in dynamic contrast-enhanced cardiac MRI using interleaved gradient-echo EPI. *Magnetic Resonance in Medicine*, 39(4):514–519.

[Ding et al., 2011] Ding, Y., Chung, Y.-C., Jekic, M., and Simonetti, O. P. (2011). A new approach to autocalibrated dynamic parallel imaging based on the Karhunen-Loeve transform: KL-TSENSE and KL-TGRAPPA. *Magnetic Resonance in Medicine*, 65(6):1786–1792.

[Ding et al., 2015] Ding, Y., Xue, H., Ahmad, R., Chang, T.-c., Ting, S. T., and Simonetti, O. P. (2015). Paradoxical effect of the signal-to-noise ratio of GRAPPA calibration lines: A quantitative study. *Magn. Reson. Med.*, 74:231–239.

[Donoho, 2006] Donoho, D. (2006). Compressed sensing. *IEEE Transactions on Information Theory*, 52(4):1289 –1306.

[Edelman and Li, 1994] Edelman, R. R. and Li, W. (1994). Contrast-enhanced echo-planar MR imaging of myocardial perfusion: preliminary study in humans. *Radiology*, 190(3):771–777.

[Edelstein et al., 1986] Edelstein, W. A., Glover, G. H., Hardy, C. J., and Redington, R. W. (1986). The intrinsic signal-to-noise ratio in NMR imaging. *Magn. Reson. Med.*, 3(4):604–618.

[Ehman and Felmlee, 1989] Ehman, R. L. and Felmlee, J. P. (1989). Adaptive technique for high-definition MR imaging of moving structures. *Radiology*, 173(1):255–263.

[Einstein et al., 2007] Einstein, A. J., Moser, K. W., Thompson, R. C., Cerqueira, M. D., and Henzlova, M. J. (2007). Radiation Dose to Patients From Cardiac Diagnostic Imaging. *Circulation*, 116(11):1290–1305.

[Elkington et al., 2005] Elkington, A. G., He, T., Gatehouse, P. D., Prasad, S. K., Firmin, D. N., and Pennell, D. J. (2005). Optimization of the arterial input function for myocardial perfusion cardiovascular magnetic resonance. *J. Magn. Reson. Imaging*, 21(4):354–359.

[Epstein and Meyer, 2011] Epstein, F. H. and Meyer, C. H. (2011). Measuring Myocardial Perfusion Using Arterial Spin Labeled MRI: Promise and Challenges. *JACC Cardiovasc Imaging*, 4(12):1262–1264.

[Ernst and Anderson, 1966] Ernst, R. R. and Anderson, W. A. (1966). Application of Fourier Transform Spectroscopy to Magnetic Resonance. *Review of Scientific Instruments*, 37(1):93–102.

[Fathala, 2011] Fathala, A. (2011). Myocardial Perfusion Scintigraphy: Techniques, Interpretation, Indications and Reporting. *Ann Saudi Med*, 31(6):625–634.

[Feinberg et al., 1986] Feinberg, D. A., Hale, J. D., Watts, J. C., Kaufman, L., and Mark, A. (1986). Halving MR imaging time by conjugation: demonstration at 3.5 kG. *Radiology*, 161(2):527–531.

[Feinberg et al., 1985] Feinberg, D. A., Hoenninger, J. C., Crooks, L. E., Kaufman, L., Watts, J. C., and Arakawa, M. (1985). Inner volume MR imaging: technical concepts and their application. *Radiology*, 156(3):743–747.

[Ferreira et al., 2008] Ferreira, P., Gatehouse, P., Bucciarelli-Ducci, C., Wage, R., and Firmin, D. (2008). Measurement of myocardial frequency offsets during first pass of a gadolinium-based contrast agent in perfusion studies. *Magn. Reson. Med.*, 60(4):860–870.

[Ferreira et al., 2012] Ferreira, P., Gatehouse, P., and Firmin, D. (2012). Myocardial first-pass perfusion imaging with hybrid-EPI: frequency-offsets and potential artefacts. *Journal of Cardiovascular Magnetic Resonance*, 14(1):44.

[Ferreira et al., 2009] Ferreira, P., Gatehouse, P., Kellman, P., Bucciarelli-Ducci, C., and Firmin, D. (2009). Variability of myocardial perfusion dark rim Gibbs artifacts due to sub-pixel shifts. *Journal of Cardiovascular Magnetic Resonance*, 11(1):17.

[Ferreira et al., 2013] Ferreira, P. F., Gatehouse, P. D., Mohiaddin, R. H., and Firmin, D. N. (2013). Cardiovascular magnetic resonance artefacts. *Journal of Cardiovascular Magnetic Resonance*, 15(1):41.

[Fessler and Sutton, 2003] Fessler, J. and Sutton, B. (2003). Nonuniform fast Fourier transforms using min-max interpolation. *IEEE Transactions on Signal Processing*, 51(2):560–574.

[Fleiss, 1981] Fleiss, J. L. (1981). *Statistical methods for rates and proportions*. Wiley series in probability and mathematical statistics. New York; Chichester : Wiley, 2nd edition.

[Flotats et al., 2012] Flotats, A., Bravo, P. E., Fukushima, K., Chaudhry, M. A., Merrill, J., and Bengel, F. M. (2012). 82rb PET myocardial perfusion imaging is superior to 99mtc-labelled agent SPECT in patients with known or suspected coronary artery disease. *Eur J Nucl Med Mol Imaging*, 39(8):1233–1239.

[Föll et al., 2009] Föll, D., Jung, B., Staehle, F., Schilli, E., Bode, C., Hennig, J., and Markl, M. (2009). Visualization of multidirectional regional left ventricular dynamics by high-temporal-resolution tissue phase mapping. *J. Magn. Reson. Imaging*, 29(5):1043–1052.

[Friedrich and Karamitsos, 2013] Friedrich, M. G. and Karamitsos, T. D. (2013). Oxygenation-sensitive cardiovascular magnetic resonance. *J Cardiovasc Magn Reson*, 15(1):43.

[Friedrich et al., 2003] Friedrich, M. G., Niendorf, T., Schulz-Menger, J., Gross, C. M., and Dietz, R. (2003). Blood oxygen level-dependent magnetic resonance imaging in patients with stress-induced angina. *Circulation*, 108(18):2219–2223.

[Fritz-Hansen et al., 2008] Fritz-Hansen, T., Hove, J. D., Kofoed, K. F., Kelbaek, H., and Larsson, H. B. (2008). Quantification of MRI measured myocardial perfusion reserve in healthy humans: A comparison with positron emission tomography. *J. Magn. Reson. Imaging*, 27(4):818–824.

[Fuster et al., 2011] Fuster, V., Hunt, S., and Hurst, J. W., editors (2011). *Hurst's the heart*. McGraw-Hill Medical, New York, 13. ed edition.

[Gatehouse et al., 2000] Gatehouse, P., Panting, J., Grothues, F., and Firmin, D. (2000). Multislice Zonal EPI Myocardial Perfusion Imaging. In *8th Scientific Meeting ISMRM 2000*, Colorado, USA.

[Gatehouse, 1999] Gatehouse, P. D. (1999). *Rapid magnetic resonance imaging of flow*. PhD Thesis, University of London.

[Gatehouse et al., 2004] Gatehouse, P. D., Elkington, A. G., Ablitt, N. A., Yang, G.-Z., Pennell, D. J., and Firmin, D. N. (2004). Accurate assessment of the arterial input function during high-dose myocardial perfusion cardiovascular magnetic resonance. *J. Magn. Reson. Imaging*, 20(1):39–45.

[Ge et al., 2010] Ge, L., Kino, A., Griswold, M., Carr, J. C., and Li, D. (2010). Free-breathing myocardial perfusion MRI using SW-CG-HYPR and motion correction. *Magnetic Resonance in Medicine*, 64(4):1148–1154.

[Gerber et al., 2008] Gerber, B., Raman, S., Nayak, K., Epstein, F., Ferreira, P., Axel, L., and Kraitchman, D. (2008). Myocardial first-pass perfusion cardiovascular magnetic resonance: history, theory, and current state of the art. *Journal of Cardiovascular Magnetic Resonance*, 10(1):18.

[Giang et al., 2004] Giang, T. H., Nanz, D., Coulden, R., Friedrich, M., Graves, M., Al-Saadi, N., Lüscher, T. F., Schulthess, G. K. v., and Schwitter, J. (2004). Detection of coronary artery disease by magnetic resonance myocardial perfusion imaging with various contrast medium doses: first european multi-centre experience. *Eur Heart J*, 25(18):1657–1665.

[Giri et al., 2014] Giri, S., Xue, H., Maiseyeu, A., Kroeker, R., Rajagopalan, S., White, R. D., Zuehlsdorff, S., Raman, S. V., and Simonetti, O. P. (2014). Steady-state first-pass perfusion (SSFPP): A new approach to 3d first-pass myocardial perfusion imaging. *Magnetic Resonance in Medicine*, 71(1):133–144.

[Glagov et al., 1987] Glagov, S., Weisenberg, E., Zarins, C. K., Stankunavicius, R., and Kolettis, G. J. (1987). Compensatory enlargement of human atherosclerotic coronary arteries. *N. Engl. J. Med.*, 316(22):1371–1375.

[Glover et al., 1992] Glover, G. H., Pauly, J. M., and Bradshaw, K. M. (1992). Boron-11 imaging with a three-dimensional reconstruction method. *J. Magn. Reson. Imaging*, 2(1):47–52.

[Go et al., 1990] Go, R. T., Marwick, T. H., MacIntyre, W. J., Saha, G. B., Neumann, D. R., Underwood, D. A., and Simpfendorfer, C. C. (1990). A prospective comparison of rubidium-82 PET and thallium-201 SPECT myocardial perfusion imaging utilizing a single dipyridamole stress in the diagnosis of coronary artery disease. *J. Nucl. Med.*, 31(12):1899–1905.

[Gould et al., 1986] Gould, K. L., Goldstein, R. A., Mullani, N. A., Kirkeeide, R. L., Wong, W.-H., Tewson, T. J., Berridge, M. S., Bolomey, L. A., Hartz, R. K., Smalling, R. W., Fuentes, F., and Nishikawa, A. (1986). Noninvasive assessment of coronary stenoses by myocardial perfusion imaging during pharmacologic coronary vasodilation. VIII. Clinical feasibility of positron cardiac imaging without a cyclotron using generator-produced Rubidium-82. *J Am Coll Cardiol*, 7(4):775–789.

[Greenwood et al., 2012] Greenwood, J. P., Maredia, N., Younger, J. F., Brown, J. M., Nixon, J., Everett, C. C., Bijsterveld, P., Ridgway, J. P., Radjenovic, A., Dickinson, C. J., Ball, S. G., and Plein, S. (2012). Cardiovascular magnetic resonance and single-photon emission computed tomography for diagnosis of coronary heart disease (CE-MARC): a prospective trial. *The Lancet*, 379(9814):453–460.

[Griswold et al., 2002] Griswold, M. A., Jakob, P. M., Heidemann, R. M., Nittka, M., Jellus, V., Wang, J., Kiefer, B., and Haase, A. (2002). Generalized autocalibrating partially parallel acquisitions (GRAPPA). *Magnetic Resonance in Medicine*, 47(6):1202–1210.

[Haacke et al., 1999] Haacke, E., Brown, R., Thompson, M., and Venkatesan, R. (1999). *Magnetic Resonance Imaging: Physical Principles and Dequence Design*. Wiley-Liss.

[Haacke et al., 1991] Haacke, E. M., Lindskogj, E. D., and Lin, W. (1991). A fast, iterative, partial-fourier technique capable of local phase recovery. *Journal of Magnetic Resonance (1969)*, 92(1):126–145.

[Hamilton et al., 2014] Hamilton, J. I., Barkauskas, K., and Seiberlich, N. (2014). Accelerated 2d multi-slice first-pass contrast-enhanced myocardial perfusion using through-time radial GRAPPA. *Journal of Cardiovascular Magnetic Resonance*, 16(Suppl 1):P378.

[Hansen et al., 2008] Hansen, M. S., Atkinson, D., and Sørensen, T. S. (2008). Cartesian SENSE and k-t SENSE reconstruction using commodity graphics hardware. *Magn. Reson. Med.*, 59(3):463–468.

[Hansen and Sørensen, 2013] Hansen, M. S. and Sørensen, T. S. (2013). Gadgetron: An open source framework for medical image reconstruction. *Magnetic Resonance in Medicine*, 69(6):1768–1776.

[Hansen, 2000] Hansen, P. C. (2000). The L-Curve and its Use in the Numerical Treatment of Inverse Problems. In *in Computational Inverse Problems in Electrocardiology, ed. P. Johnston, Advances in Computational Bioengineering*, pages 119–142. WIT Press.

[Harrison et al., 2013] Harrison, A., Adluru, G., Damal, K., Shaaban, A. M., Wilson, B., Kim, D., McGann, C., Marrouche, N. F., and DiBella, E. V. R. (2013). Rapid ungated myocardial perfusion cardiovascular magnetic resonance: preliminary diagnostic accuracy. *Journal of Cardiovascular Magnetic Resonance*, 15(1):26.

[Hendel et al., 2016] Hendel, R. C., Friedrich, M. G., Schulz-Menger, J., Zemmrich, C., Bengel, F., Berman, D. S., Camici, P. G., Flamm, S. D., Le Guludec, D., Kim, R., Lombardi, M., Mahmarian, J., Sechtem, U., and Nagel, E. (2016). CMR First-Pass Perfusion for Suspected Inducible Myocardial Ischemia. *JACC: Cardiovascular Imaging*, 9(11):1338–1348.

[Hinton et al., 2003] Hinton, D. P., Wald, L. L., Pitts, J., and Schmitt, F. (2003). Comparison of cardiac MRI on 1.5 and 3.0 Tesla clinical whole body systems. *Invest Radiol*, 38(7):436–442.

[Huang et al., 2005] Huang, F., Akao, J., Vijayakumar, S., Duensing, G. R., and Limkeman, M. (2005). k-t GRAPPA: A k-space implementation for dynamic MRI with high reduction factor. *Magnetic Resonance in Medicine*, 54(5):1172–1184.

[Huang et al., 2008] Huang, F., Vijayakumar, S., Li, Y., Hertel, S., and Duensing, G. R. (2008). A software channel compression technique for faster reconstruction with many channels. *Magnetic Resonance Imaging*, 26(1):133–141.

[Huang et al., 2014] Huang, T.-Y., Tseng, Y.-S., and Chuang, T.-C. (2014). Automatic calibration of trigger delay time for cardiac MRI. *NMR Biomed.*, 27(4):417–424.

[Hutchinson and Raff, 1988] Hutchinson, M. and Raff, U. (1988). Fast MRI data acquisition using multiple detectors. *Magnetic Resonance in Medicine*, 6(1):87–91.

[Ishida et al., 2003] Ishida, N., Sakuma, H., Motoyasu, M., Okinaka, T., Isaka, N., Nakano, T., and Takeda, K. (2003). Noninfarcted Myocardium: Correlation between Dynamic First-Pass Contrast-enhanced Myocardial MR Imaging and Quantitative Coronary Angiography1. *Radiology*, 229(1):209–216.

[Jackson et al., 1992] Jackson, J. I., Nishimura, D. G., and Macovski, A. (1992). Twisting radial lines with application to robust magnetic resonance imaging of irregular flow. *Magnetic Resonance in Medicine*, 25(1):128–139.

[Jakob et al., 1998] Jakob, P. M., Griswold, M. A., Edelman, R. R., and Sodickson, D. K. (1998). AUTO-SMASH: A self-calibrating technique for SMASH imaging. *MAGMA*, 7(1):42–54.

[Jerosch-Herold et al., 1999] Jerosch-Herold, M., Wilke, N., Wang, Y., Gong, G.-R., Mansoor, A. M., Huang, H., Gurchumelidze, S., and Stillman, A. E. (1999). Direct comparison

of an intravascular and an extracellular contrast agent for quantification of myocardial perfusion. *Int J Cardiovasc Imaging*, 15(6):453–464.

[Jogiya et al., 2012] Jogiya, R., Kozerke, S., Morton, G., De Silva, K., Redwood, S., Perera, D., Nagel, E., and Plein, S. (2012). Validation of Dynamic 3-Dimensional Whole Heart Magnetic Resonance Myocardial Perfusion Imaging Against Fractional Flow Reserve for the Detection of Significant Coronary Artery Disease. *Journal of the American College of Cardiology*, 60(8):756–765.

[Jogiya et al., 2014a] Jogiya, R., Morton, G., Silva, K. D., Reyes, E., Hachamovitch, R., Kozerke, S., Nagel, E., Underwood, R., and Plein, S. (2014a). Ischemic Burden by Three-dimensional Myocardial Perfusion Cardiovascular Magnetic Resonance: Comparison with Myocardial Perfusion Scintigraphy. *Circ Cardiovasc Imaging*, page DOI:10.1161/CIRCIMAGING.113.001620.

[Jogiya et al., 2014b] Jogiya, R., Schuster, A., Zaman, A., Motwani, M., Kouwenhoven, M., Nagel, E., Kozerke, S., and Plein, S. (2014b). Three-dimensional balanced steady state free precession myocardial perfusion cardiovascular magnetic resonance at 3t using dual-source parallel RF transmission: initial experience. *Journal of Cardiovascular Magnetic Resonance*, 16(1):90.

[Jung et al., 2009] Jung, H., Sung, K., Nayak, K. S., Kim, E. Y., and Ye, J. C. (2009). k-t FOCUSS: A general compressed sensing framework for high resolution dynamic MRI. *Magn. Reson. Med.*, 61(1):103–116.

[Kellman and Arai, 2007] Kellman, P. and Arai, A. E. (2007). Imaging sequences for first pass perfusion –a review. *J Cardiovasc Magn Reson*, 9(3):525–537.

[Kellman et al., 2004a] Kellman, P., Derbyshire, J., Agyeman, K., McVeigh, E., and Arai, A. (2004a). Extended coverage first-pass perfusion imaging using slice-interleaved TSENSE. *Magnetic Resonance in Medicine*, 51(1):200–204.

[Kellman et al., 2001] Kellman, P., Epstein, F. H., and McVeigh, E. R. (2001). Adaptive sensitivity encoding incorporating temporal filtering (TSENSE). *Magnetic Resonance in Medicine*, 45(5):846–852.

[Kellman et al., 2017] Kellman, P., Hansen, M. S., Nielles-Vallespin, S., Nickander, J., Themudo, R., Ugander, M., and Xue, H. (2017). Myocardial perfusion cardiovascular magnetic resonance: optimized dual sequence and reconstruction for quantification. *Journal of Cardiovascular Magnetic Resonance*, 19:43.

[Kellman et al., 2004b] Kellman, P., Zhang, Q., Larson, A. C., Simonetti, O. P., Mcveigh, E. R., and Arai, A. E. (2004b). Cardiac First-pass Perfusion MRI using 3d trueFISP Parallel Imaging using TSENSE. In *Proceedings of the 12th Annual Meeting of ISMRM*, Kyoto, Japan.

[Kholmovski and DiBella, 2007] Kholmovski, E. G. and DiBella, E. V. (2007). Perfusion MRI with radial acquisition for arterial input function assessment. *Magn. Reson. Med.*, 57(5):821–827.

[Kim et al., 2005] Kim, D., Cernicanu, A., and Axel, L. (2005). B0 and B1-insensitive uniform T1-weighting for quantitative, first-pass myocardial perfusion magnetic resonance imaging. *Magn. Reson. Med.*, 54(6):1423–1429.

[Kim et al., 2008] Kim, D., Gonen, O., Oesingmann, N., and Axel, L. (2008). Comparison of the effectiveness of saturation pulses in the heart at 3t. *Magn. Reson. Med.*, 59(1):209–215.

[Klocke et al., 2003] Klocke, F. J., Baird, M. G., Lorell, B. H., Bateman, T. M., Messer, J. V., Berman, D. S., OGara, P. T., Carabello, B. A., Russell, R. O., Cerqueira, M. D., Sutton, M. G. S. J., DeMaria, A. N., Udelson, J. E., Kennedy, J. W., Verani, M. S., Williams, K. A., Antman, E. M., Smith, S. C., Alpert, J. S., Gregoratos, G., Anderson, J. L., Hiratzka, L. F., Faxon, D. P., Hunt, S. A., Fuster, V., Jacobs, A. K., Gibbons, R. J., and Russell, R. O. (2003). ACC/AHA/ASNC Guidelines for the Clinical Use of Cardiac Radionuclide ImagingExecutive Summary A Report of the American College of Cardiology/American Heart Association Task Force on Practice Guidelines (ACC/AHA/ASNC Committee to Revise the 1995 Guidelines for the Clinical Use of Cardiac Radionuclide Imaging). *Circulation*, 108(11):1404–1418.

[Knoll et al., 2012] Knoll, F., Clason, C., Bredies, K., Uecker, M., and Stollberger, R. (2012). Parallel imaging with nonlinear reconstruction using variational penalties. *Magn. Reson. Med.*, 67(1):34–41.

[Kober et al., 2016] Kober, F., Jao, T., Troalen, T., and Nayak, K. S. (2016). Myocardial arterial spin labeling. *Journal of Cardiovascular Magnetic Resonance*, 18(1):1.

[Köstler et al., 2003] Köstler, H., Sandstede, J. J., Lipke, C., Landschütz, W., Beer, M., and Hahn, D. (2003). Auto-SENSE perfusion imaging of the whole human heart. *Journal of Magnetic Resonance Imaging*, 18(6):702–708.

[Kramer et al., 2013] Kramer, C. M., Barkhausen, J., Flamm, S. D., Kim, R. J., Nagel, E., $author.lastName, a. f., and $author.lastName, a. f. (2013). Standardized cardiovascular magnetic resonance (CMR) protocols 2013 update. *Journal of Cardiovascular Magnetic Resonance*, 15(1):91.

[Larkman and Nunes, 2007] Larkman, D. J. and Nunes, R. G. (2007). Parallel magnetic resonance imaging. *Physics in Medicine and Biology*, 52(7):R15–R55.

[Laurent et al., 2006] Laurent, S., Elst, L. V., and Muller, R. N. (2006). Comparative study of the physicochemical properties of six clinical low molecular weight gadolinium contrast agents. *Contrast Media Mol Imaging*, 1(3):128–137.

[Leong-Poi et al., 2002] Leong-Poi, H., Rim, S.-J., Le, D. E., Fisher, N. G., Wei, K., and Kaul, S. (2002). Perfusion versus function: the ischemic cascade in demand ischemia: implications of single-vessel versus multivessel stenosis. *Circulation*, 105(8):987–992.

[Li and Sun, 2009] Li, C. and Sun, Y. (2009). Nonrigid registration of myocardial perfusion MRI using pseudo ground truth. *Med Image Comput Comput Assist Interv*, 12(Pt 1):165–172.

[Liang et al., 2009] Liang, D., Liu, B., Wang, J., and Ying, L. (2009). Accelerating SENSE using compressed sensing. *Magn. Reson. Med.*, 62(6):1574–1584.

[Likes, 1981] Likes, R. S. (1981). Moving gradient zeugmatography. U.S. Classification: 324/307 International Classification: :G01N 2700.

[Likhite et al., 2016] Likhite, D., Suksaranjit, P., Adluru, G., Hu, N., Weng, C., Kholmovski, E., McGann, C., Wilson, B., and DiBella, E. (2016). Interstudy repeatability of self-gated quantitative myocardial perfusion MRI. *J. Magn. Reson. Imaging*, 43(6):1369–1378.

[Lin and Song, 2009] Lin, W. and Song, H. K. (2009). Improved signal spoiling in fast radial gradientecho imaging: Applied to accurate T1 mapping and flip angle correction. *Magnetic Resonance in Medicine*, 62(5):1185–1194.

[Lingala et al., 2011] Lingala, S., Hu, Y., DiBella, E., and Jacob, M. (2011). Accelerated Dynamic MRI Exploiting Sparsity and Low-Rank Structure: k-t SLR. *IEEE Transactions on Medical Imaging*, 30(5):1042–1054.

[Lingala et al., 2013] Lingala, S. G., DiBella, E., Adluru, G., McGann, C., and Jacob, M. (2013). Accelerating free breathing myocardial perfusion MRI using multi coil radial k-t SLR. *Phys Med Biol*, 58(20):7309–7327.

[Ljunggren, 1983] Ljunggren, S. (1983). A simple graphical representation of fourier-based imaging methods. *Journal of Magnetic Resonance (1969)*, 54(2):338–343.

[Lusis, 2012] Lusis, A. J. (2012). Genetics of atherosclerosis. *Trends in Genetics*, 28(6):267–275.

[Lustig et al., 2007] Lustig, M., Donoho, D., and Pauly, J. M. (2007). Sparse MRI: The application of compressed sensing for rapid MR imaging. *Magnetic Resonance in Medicine*, 58(6):1182–1195.

[Lustig et al., 2008] Lustig, M., Donoho, D., Santos, J., and Pauly, J. (2008). Compressed Sensing MRI. *IEEE Signal Processing Magazine*, 25(2):72–82.

[Lustig and Pauly, 2010] Lustig, M. and Pauly, J. M. (2010). SPIRiT: Iterative self-consistent parallel imaging reconstruction from arbitrary k-space. *Magnetic Resonance in Medicine*, 64(2):457–471.

[Lustig et al., 2006] Lustig, M., Santas, J. M., Donoho, D. L., and Pauly, J. M. (2006). k-t SPARSE: High frame rate dynamic MRI exploiting spatio-temporal sparsity. In *Proceedings of the 14th Annual Meeting of ISMRM*, Seattle, Washington, USA.

[Lyne et al., 2007] Lyne, J. C., Gatehouse, P. D., Assomull, R. G., Smith, G. C., Kellman, P., Firmin, D. N., and Pennell, D. J. (2007). Direct comparison of myocardial perfusion cardiovascular magnetic resonance sequences with parallel acquisition. *Journal of Magnetic Resonance Imaging*, 26(6):1444–1451.

[Madore, 2004] Madore, B. (2004). UNFOLD-SENSE: A parallel MRI method with self-calibration and artifact suppression. *Magn. Reson. Med.*, 52(2):310–320.

[Madore et al., 1999] Madore, B., Glover, G. H., and Pelc, N. J. (1999). Unaliasing by Fourier-encoding the overlaps using the temporal dimension (UNFOLD), applied to cardiac imaging and fMRI. *Magnetic Resonance in Medicine*, 42(5):813–828.

[Manka et al., 2011] Manka, R., Jahnke, C., Kozerke, S., Vitanis, V., Crelier, G., Gebker, R., Schnackenburg, B., Boesiger, P., Fleck, E., and Paetsch, I. (2011). Dynamic 3-Dimensional Stress Cardiac Magnetic Resonance Perfusion ImagingDetection of Coronary Artery Disease and Volumetry of Myocardial Hypoenhancement Before and After Coronary Stenting. *J Am Coll Cardiol*, 57(4):437–444.

[Manka et al., 2012] Manka, R., Paetsch, I., Kozerke, S., Moccetti, M., Hoffmann, R., Schroeder, J., Reith, S., Schnackenburg, B., Gaemperli, O., Wissmann, L., Wyss, C. A., Kaufmann, P. A., Corti, R., Boesiger, P., Marx, N., Lüscher, T. F., and Jahnke, C. (2012). Whole-heart dynamic three-dimensional magnetic resonance perfusion imaging for the detection of coronary artery disease defined by fractional flow reserve: determination

of volumetric myocardial ischaemic burden and coronary lesion location. *Eur Heart J*, 33(16):2016–2024.

[Manka et al., 2015] Manka, R., Wissmann, L., Gebker, R., Jogiya, R., Motwani, M., Frick, M., Reinartz, S., Schnackenburg, B., Niemann, M., Gotschy, A., Kuhl, C., Nagel, E., Fleck, E., Marx, N., Luescher, T. F., Plein, S., and Kozerke, S. (2015). Multicenter evaluation of dynamic three-dimensional magnetic resonance myocardial perfusion imaging for the detection of coronary artery disease defined by fractional flow reserve. *Circ Cardiovasc Imaging*, 8(5):10.1161/CIRCIMAGING.114.003061.

[Manning et al., 1991] Manning, W. J., Atkinson, D. J., Grossman, W., Paulin, S., and Edelman, R. R. (1991). First-pass nuclear magnetic resonance imaging studies using gadolinium-DTPA in patients with coronary artery disease. *Journal of the American College of Cardiology*, 18(4):959–965.

[Mansfield, 1977] Mansfield, P. (1977). Multi-planar image formation using NMR spin echoes. *Journal of Physics C: Solid State Physics*, 10(3):L55–L58.

[Maredia et al., 2010] Maredia, N., Radjenovic, A., Kozerke, S., Larghat, A., Greenwood, J. P., and Plein, S. (2010). Effect of improving spatial or temporal resolution on image quality and quantitative perfusion assessment with k-t SENSE acceleration in first-pass CMR myocardial perfusion imaging. *Magnetic Resonance in Medicine*, 64(6):1616–1624.

[McGibney et al., 1993] McGibney, G., Smith, M. R., Nichols, S. T., and Crawley, A. (1993). Quantitative evaluation of several partial fourier reconstruction algorithms used in mri. *Magn. Reson. Med.*, 30(1):51–59.

[Meyer et al., 2008] Meyer, C., Strach, K., Thomas, D., Naehle, C. P., Schwenger, U., Schild, H. H., Sommer, T., Litt, H., and Tiemann, K. (2008). High-resolution myocardial stress perfusion at 3 T in patients with suspected coronary artery disease. *European Radiology*, 18(2):226–233.

[Mistretta, 2009] Mistretta, C. A. (2009). Undersampled radial MR acquisition and highly constrained back projection (HYPR) reconstruction: Potential medical imaging applications in the post-Nyquist era. *J. Magn. Reson. Imaging*, 29(3):501–516.

[Mitchell and Wang, 2014] Mitchell, J. R. and Wang, J.-J. (2014). Expanding application of the Wiggers diagram to teach cardiovascular physiology. *Adv Physiol Educ*, 38(2):170–175.

[Motwani et al., 2012] Motwani, M., Fairbairn, T. A., Larghat, A., Mather, A. N., Biglands, J. D., Radjenovic, A., Greenwood, J. P., and Plein, S. (2012). Systolic versus Diastolic Acquisition in Myocardial Perfusion MR Imaging. *Radiology*, 262(3):816–823.

[Motwani et al., 2013] Motwani, M., Jogiya, R., Kozerke, S., Greenwood, J. P., and Plein, S. (2013). Advanced Cardiovascular Magnetic Resonance Myocardial Perfusion Imaging High-Spatial Resolution Versus 3-Dimensional Whole-Heart Coverage. *Circ Cardiovasc Imaging*, 6(2):339–348.

[Motwani et al., 2014] Motwani, M., Kidambi, A., Sourbron, S., Fairbairn, T. A., Uddin, A., Kozerke, S., Greenwood, J. P., and Plein, S. (2014). Quantitative three-dimensional cardiovascular magnetic resonance myocardial perfusion imaging in systole and diastole. *Journal of Cardiovascular Magnetic Resonance*, 16(1):19.

[Murphy et al., 2012] Murphy, M., Alley, M., Demmel, J., Keutzer, K., Vasanawala, S., and Lustig, M. (2012). Fast -SPIRiT Compressed Sensing Parallel Imaging MRI: Scalable Parallel Implementation and Clinically Feasible Runtime. *IEEE Transactions on Medical Imaging*, 31(6):1250–1262.

[Nagel et al., 2003] Nagel, E., Klein, C., Paetsch, I., Hettwer, S., Schnackenburg, B., Wegscheider, K., and Fleck, E. (2003). Magnetic Resonance Perfusion Measurements for the Noninvasive Detection of Coronary Artery Disease. *Circulation*, 108(4):432–437.

[Nehrke and Börnert, 2005] Nehrke, K. and Börnert, P. (2005). Prospective correction of affine motion for arbitrary MR sequences on a clinical scanner. *Magn. Reson. Med.*, 54(5):1130–1138.

[Nesto and Kowalchuk, 1987] Nesto, R. W. and Kowalchuk, G. J. (1987). The ischemic cascade: Temporal sequence of hemodynamic, electrocardiographic and symptomatic expressions of ischemia. *The American Journal of Cardiology*, 59(7):C23–C30.

[NICE, 2010] NICE (2010). Chest pain of recent onset (CG 95). Guidance/Clinical Guidelines. The summary of the published clinical guideline on Chest pain of recent onset. It links to the published guidance and key documents.

[Niendorf et al., 2013] Niendorf, T., Graessl, A., Thalhammer, C., Dieringer, M. A., Kraus, O., Santoro, D., Fuchs, K., Hezel, F., Waiczies, S., Ittermann, B., and Winter, L. (2013). Progress and promises of human cardiac magnetic resonance at ultrahigh fields: A physics perspective. *Journal of Magnetic Resonance*, 229:208–222.

[Niendorf et al., 2010] Niendorf, T., Sodickson, D. K., Krombach, G. A., and Schulz-Menger, J. (2010). Toward cardiovascular MRI at 7 T: clinical needs, technical solutions and research promises. *Eur Radiol*, 20(12):2806–2816.

[Nishimura and Vasanawala, 2000] Nishimura, D. and Vasanawala, S. S. (2000). Analysis and reduction of the transient response in SSFP imaging. page 301, Denver, USA.

[Ogawa et al., 1990] Ogawa, S., Lee, T.-M., Nayak, A. S., and Glynn, P. (1990). Oxygenation-sensitive contrast in magnetic resonance image of rodent brain at high magnetic fields. *Magn. Reson. Med.*, 14(1):68–78.

[Ogilby et al., 1992] Ogilby, J. D., Iskandrian, A. S., Untereker, W. J., Heo, J., Nguyen, T. N., and Mercuro, J. (1992). Effect of intravenous adenosine infusion on myocardial perfusion and function. Hemodynamic/angiographic and scintigraphic study. *Circulation*, 86(3):887–895.

[Ohliger and Sodickson, 2006] Ohliger, M. A. and Sodickson, D. K. (2006). An introduction to coil array design for parallel MRI. *NMR Biomed.*, 19(3):300–315.

[Opie, 2004] Opie, L. (2004). *Heart Physiology: From Cell to Circulation*. Lippincott Williams & Wilkins, Philadelphia, PA, USA, 4th edition.

[Otazo et al., 2010] Otazo, R., Kim, D., Axel, L., and Sodickson, D. K. (2010). Combination of compressed sensing and parallel imaging for highly accelerated first-pass cardiac perfusion MRI. *Magn. Reson. Med.*, 64(3):767–776.

[Otazo et al., 2011] Otazo, R., Kim, D., Axel, L., and Sodickson, D. K. (2011). Combination of compressed sensing and parallel imaging with respiratory motion correction for highly-accelerated cardiac perfusion MRI. *Journal of Cardiovascular Magnetic Resonance*, 13(Suppl 1):O98.

[Panting et al., 2001] Panting, J. R., Gatehouse, P. D., Yang, G. Z., Jerosch-Herold, M., Wilke, N., Firmin, D. N., and Pennell, D. J. (2001). Echo-planar magnetic resonance myocardial perfusion imaging: Parametric map analysis and comparison with thallium SPECT. *J. Magn. Reson. Imaging*, 13(2):192–200.

[Pauly et al., 1989] Pauly, J., Nishimura, D., and Macovski, A. (1989). A k-space analysis of small-tip-angle excitation. *Journal of Magnetic Resonance (1969)*, 81(1):43–56.

[Pedersen et al., 2009a] Pedersen, H., Kelle, S., Ringgaard, S., Schnackenburg, B., Nagel, E., Nehrke, K., and Kim, W. Y. (2009a). Quantification of myocardial perfusion using free-breathing MRI and prospective slice tracking. *Magn Reson Med*, 61(3):734–738.

[Pedersen et al., 2009b] Pedersen, H., Kozerke, S., Ringgaard, S., Nehrke, K., and Kim, W. Y. (2009b). k-t PCA: Temporally constrained k-t BLAST reconstruction using principal component analysis. *Magnetic Resonance in Medicine*, 62(3):706–716.

[Peterson and Furenlid, 2011] Peterson, T. E. and Furenlid, L. R. (2011). SPECT detectors: the Anger Camera and beyond. *Phys. Med. Biol.*, 56(17):R145.

[Pflugi et al., 2015] Pflugi, S., Roujol, S., Akçakaya, M., Kawaji, K., Foppa, M., Heydari, B., Goddu, B., Kissinger, K., Berg, S., Manning, W. J., Kozerke, S., and Nezafat, R. (2015). Accelerated cardiac MR stress perfusion with radial sampling after physical exercise with an MR-compatible supine bicycle ergometer. *Magn. Reson. Med.*, 74(2):384–395.

[Picano et al., 1991] Picano, E., Lattanzi, F., Orlandini, A., Marini, C., and L'Abbate, A. (1991). Stress echocardiography and the human factor: The importance of being expert. *Journal of the American College of Cardiology*, 17(3):666–669.

[Pipe, 1999] Pipe, J. G. (1999). Motion correction with PROPELLER MRI: Application to head motion and free-breathing cardiac imaging. *Magn. Reson. Med.*, 42(5):963–969.

[Plein et al., 2008a] Plein, S., Kozerke, S., Suerder, D., Luescher, T. F., Greenwood, J. P., Boesiger, P., and Schwitter, J. (2008a). High spatial resolution myocardial perfusion cardiac magnetic resonance for the detection of coronary artery disease. *Eur Heart J*, 29(17):2148–2155.

[Plein et al., 2007] Plein, S., Ryf, S., Schwitter, J., Radjenovic, A., Boesiger, P., and Kozerke, S. (2007). Dynamic contrast-enhanced myocardial perfusion MRI accelerated with k-t sense. *Magnetic Resonance in Medicine*, 58(4):777–785.

[Plein et al., 2008b] Plein, S., Schwitter, J., Suerder, D., Greenwood, J. P., Boesiger, P., and Kozerke, S. (2008b). k-Space and Time Sensitivity Encodingaccelerated Myocardial Perfusion MR Imaging at 3.0 T: Comparison with 1.5 T1. *Radiology*, 249(2):493–500.

[Ponce et al., 2014] Ponce, I. P., Blaimer, M., Breuer, F. A., Griswold, M. A., Jakob, P. M., and Kellman, P. (2014). Auto-calibration approach for kt SENSE. *Magn. Reson. Med.*, 71(3):1123–1129.

[Pople et al., 1959] Pople, J., Schneider, W., and Bernstein, H. (1959). *High-resolution Nuclear Magnetic Resonance*. McGraw-Hill Series in Advanced Chemistry. McGraw-Hill Book Company, Inc, New York, USA.

[Porter and Xie, 2010] Porter, T. R. and Xie, F. (2010). Myocardial Perfusion Imaging With Contrast Ultrasound. *J Am Coll Cardiol Img*, 3(2):176–187.

[Pruessmann, 2006] Pruessmann, K. P. (2006). Encoding and reconstruction in parallel MRI. *NMR Biomed.*, 19(3):288–299.

[Pruessmann et al., 2001] Pruessmann, K. P., Weiger, M., Börnert, P., and Boesiger, P. (2001). Advances in sensitivity encoding with arbitrary k-space trajectories. *Magnetic Resonance in Medicine*, 46(4):638–651.

[Pruessmann et al., 1999] Pruessmann, K. P., Weiger, M., Scheidegger, M. B., and Boesiger, P. (1999). SENSE: Sensitivity encoding for fast MRI. *Magnetic Resonance in Medicine*, 42(5):952–962.

[Pullan et al., 2010] Pullan, A. J., Cheng, L. K., Nash, M. P., Ghodrati, A., MacLeod, R., and Brooks, D. H. (2010). The Inverse Problem of Electrocardiography. In Macfarlane, P. W., Oosterom, A. v., Pahlm, O., Kligfield, P., Janse, M., and Camm, J., editors, *Comprehensive Electrocardiology*, pages 299–344. Springer London. DOI: 10.1007/978-1-84882-046-3_9.

[Rasche et al., 1997] Rasche, V., Holz, D., Köhler, J., Proksa, R., and Röschmann, P. (1997). Catheter tracking using continuous radial MRI. *Magn. Reson. Med.*, 37(6):963–968.

[Ravichandran et al., 2012] Ravichandran, L., Wick, C. A., and Tridandapani, S. (2012). Detection of Quiescent Phases in Echocardiography Data using Non-Linear Filtering and Boundary Detection. *Conf Proc IEEE Eng Med Biol Soc*, 2012:1562–1565.

[Reeder et al., 2005] Reeder, S. B., Wintersperger, B. J., Dietrich, O., Lanz, T., Greiser, A., Reiser, M. F., Glazer, G. M., and Schoenberg, S. O. (2005). Practical approaches to the evaluation of signal-to-noise ratio performance with parallel imaging: Application with cardiac imaging and a 32-channel cardiac coil. *Magn. Reson. Med.*, 54(3):748–754.

[Reyes et al., 2008] Reyes, E., Loong, C. Y., Harbinson, M., Donovan, J., Anagnostopoulos, C., and Underwood, S. R. (2008). High-Dose Adenosine Overcomes the Attenuation of Myocardial Perfusion Reserve Caused by Caffeine. *Journal of the American College of Cardiology*, 52(24):2008–2016.

[Robinson et al., 1986] Robinson, T. F., Factor, S. M., and Sonnenblick, E. H. (1986). The heart as a suction pump. *Sci. Am.*, 254(6):84–91.

[Robson et al., 2008] Robson, P. M., Grant, A. K., Madhuranthakam, A. J., Lattanzi, R., Sodickson, D. K., and McKenzie, C. A. (2008). Comprehensive quantification of signal-to-noise ratio and g-factor for image-based and k-space-based parallel imaging reconstructions. *Magn. Reson. Med.*, 60(4):895–907.

[Roeloffs et al., 2016] Roeloffs, V., Voit, D., and Frahm, J. (2016). Spoiling without additional gradients: Radial FLASH MRI with randomized radiofrequency phases. *Magn. Reson. Med.*, 75(5):2094–2099.

[Salerno and Beller, 2009] Salerno, M. and Beller, G. A. (2009). Noninvasive Assessment of Myocardial Perfusion. *Circ Cardiovasc Imaging*, 2(5):412–424.

[Salerno et al., 2013] Salerno, M., Sica, C., Kramer, C. M., and Meyer, C. H. (2013). Improved first-pass spiral myocardial perfusion imaging with variable density trajectories. *Magnetic Resonance in Medicine*, 70(5):1369–1379.

[Salerno et al., 2011] Salerno, M., Sica, C. T., Kramer, C. M., and Meyer, C. H. (2011). Optimization of spiral-based pulse sequences for first-pass myocardial perfusion imaging. *Magnetic Resonance in Medicine*, 65(6):1602–1610.

[Samsonov et al., 2004] Samsonov, A. A., Kholmovski, E. G., Parker, D. L., and Johnson, C. R. (2004). POCSENSE: POCS-based reconstruction for sensitivity encoded magnetic resonance imaging. *Magn. Reson. Med.*, 52(6):1397–1406.

[Schang and Pepine, 1977] Schang, S. J. and Pepine, C. J. (1977). Transient asymptomatic S-T segment depression during daily activity. *The American Journal of Cardiology*, 39(3):396–402.

[Scheffler and Lehnhardt, 2003] Scheffler, K. and Lehnhardt, S. (2003). Principles and applications of balanced SSFP techniques. *Eur Radiol*, 13(11):2409–2418.

[Schinkel et al., 2003] Schinkel, A. F. L., Bax, J. J., Geleijnse, M. L., Boersma, E., Elhendy, A., Roelandt, J. R. T. C., and Poldermans, D. (2003). Noninvasive evaluation of ischaemic heart disease: myocardial perfusion imaging or stress echocardiography? *Eur Heart J*, 24(9):789–800.

[Schmidt et al., 2014] Schmidt, J. F. M., Wissmann, L., Manka, R., and Kozerke, S. (2014). Iterative k-t principal component analysis with nonrigid motion correction for dynamic three-dimensional cardiac perfusion imaging. *Magnetic Resonance in Medicine*, 72(1):68–79.

[Schmitt et al., 2008] Schmitt, M., Potthast, A., Sosnovik, D. E., Polimeni, J. R., Wiggins, G. C., Triantafyllou, C., and Wald, L. L. (2008). A 128-channel receive-only cardiac coil for highly accelerated cardiac MRI at 3 Tesla. *Magn. Reson. Med.*, 59(6):1431–1439.

[Schuppert et al., 2014] Schuppert, M., Keil, B., Guerin, B., Fischer, S., Rehner, R., Wald, L. L., and Schreiber, L. M. (2014). A 64-channel cardiac receive-only phased array coil for cardiac imaging at 3t. In *Joint Annual Meeting ISMRM-ESMRMB 2014*, Milan, Italy.

[Schwitter, 2006] Schwitter, J. (2006). Myocardial perfusion. *Journal of Magnetic Resonance Imaging*, 24(5):953–963.

[Schwitter et al., 2001] Schwitter, J., Nanz, D., Kneifel, S., Bertschinger, K., Büchi, M., Knüsel, P. R., Marincek, B., Lüscher, T. F., and Schulthess, G. K. v. (2001). Assessment of Myocardial Perfusion in Coronary Artery Disease by Magnetic Resonance A Comparison With Positron Emission Tomography and Coronary Angiography. *Circulation*, 103(18):2230–2235.

[Schwitter et al., 2012] Schwitter, J., Wacker, C., Wilke, N., Al-Saadi, N., Sauer, E., Huettle, K., Schönberg, S., Debl, K., Strohm, O., Ahlstrom, H., Dill, T., Hoebel, N., Simor, T., and $author.lastName, a. f. (2012). Superior diagnostic performance of perfusion-cardiovascular magnetic resonance versus SPECT to detect coronary artery disease: The secondary endpoints of the multicenter multivendor MR-IMPACT II (Magnetic Resonance Imaging for Myocardial Perfusion Assessment in Coronary Artery Disease Trial). *Journal of Cardiovascular Magnetic Resonance*, 14(1):61.

[Schwitter et al., 2008] Schwitter, J., Wacker, C. M., Rossum, A. C. v., Lombardi, M., Al-Saadi, N., Ahlstrom, H., Dill, T., Larsson, H. B. W., Flamm, S. D., Marquardt, M., and Johansson, L. (2008). MR-IMPACT: comparison of perfusion-cardiac magnetic resonance with single-photon emission computed tomography for the detection of coronary artery disease in a multicentre, multivendor, randomized trial. *Eur Heart J*, 29(4):480–489.

[Scott et al., 2009] Scott, A. D., Keegan, J., and Firmin, D. N. (2009). Motion in Cardiovascular MR Imaging. *Radiology*, 250(2):331–351.

[Scott, 1986] Scott, E. (1986). *Cardiovascular Physiology: An Integrative Approach*. Studies in Integrative Physiology. Manchester University Press, Manchester, UK, 1st edition.

[Seiberlich et al., 2008] Seiberlich, N., Breuer, F., Heidemann, R., Blaimer, M., Griswold, M., and Jakob, P. (2008). Reconstruction of undersampled non-Cartesian data sets using pseudo-Cartesian GRAPPA in conjunction with GROG. *Magn. Reson. Med.*, 59(5):1127–1137.

[Seiberlich et al., 2011a] Seiberlich, N., Ehses, P., Duerk, J., Gilkeson, R., and Griswold, M. (2011a). Improved radial GRAPPA calibration for real-time free-breathing cardiac imaging. *Magn. Reson. Med.*, 65(2):492–505.

[Seiberlich et al., 2011b] Seiberlich, N., Lee, G., Ehses, P., Duerk, J. L., Gilkeson, R., and Griswold, M. (2011b). Improved temporal resolution in cardiac imaging using through-time spiral GRAPPA. *Magn. Reson. Med.*, 66(6):1682–1688.

[Sharif et al., 2014] Sharif, B., Dharmakumar, R., LaBounty, T., Arsanjani, R., Shufelt, C., Thomson, L., Bairey Merz, C. N., Berman, D. S., and Li, D. (2014). Towards elimination of the dark-rim artifact in first-pass myocardial perfusion MRI: Removing Gibbs ringing effects using optimized radial imaging. *Magn. Reson. Med.*, 72(1):124–136.

[Sharma et al., 2006] Sharma, P., Socolow, J., Patel, S., Pettigrew, R. I., and Oshinski, J. N. (2006). Effect of Gd-DTPA-BMA on blood and myocardial T1 at 1.5t and 3t in humans. *J. Magn. Reson. Imaging*, 23(3):323–330.

[Shaw et al., 2008] Shaw, L. J., Berman, D. S., Maron, D. J., Mancini, G. B. J., Hayes, S. W., Hartigan, P. M., Weintraub, W. S., ORourke, R. A., Dada, M., Spertus, J. A., Chaitman, B. R., Friedman, J., Slomka, P., Heller, G. V., Germano, G., Gosselin, G., Berger, P., Kostuk, W. J., Schwartz, R. G., Knudtson, M., Veledar, E., Bates, E. R., McCallister, B., Teo, K. K., and Boden, W. E. (2008). Optimal Medical Therapy With or Without Percutaneous Coronary Intervention to Reduce Ischemic Burden Results From the Clinical Outcomes Utilizing Revascularization and Aggressive Drug Evaluation (COURAGE) Trial Nuclear Substudy. *Circulation*, 117(10):1283–1291.

[Shaw et al., 1999] Shaw, L. J., Hachamovitch, R., Berman, D. S., Marwick, T. H., Lauer, M. S., Heller, G. V., Iskandrian, A. E., Kesler, K. L., Travin, M. I., Lewin, H. C., Hendel, R. C., Borges-Neto, S., and Miller, D. (1999). The economic consequences of available diagnostic and prognostic strategies for the evaluation of stable angina patients: an observational assessment of the value of precatheterization ischemia. *Journal of the American College of Cardiology*, 33(3):661–669.

[Shea et al., 2001] Shea, S. M., Kroeker, R. M., Deshpande, V., Laub, G., Zheng, J., Finn, J. P., and Li, D. (2001). Coronary artery imaging: 3d segmented kspace data acquisition with multiple breathholds and realtime slab following. *Journal of Magnetic Resonance Imaging*, 13(2):301–307.

[Sherry et al., 2009] Sherry, A. D., Caravan, P., and Lenkinski, R. E. (2009). A primer on gadolinium chemistry. *J Magn Reson Imaging*, 30(6):1240–1248.

[Shin et al., 2014] Shin, P. J., Larson, P. E. Z., Ohliger, M. A., Elad, M., Pauly, J. M., Vigneron, D. B., and Lustig, M. (2014). Calibrationless parallel imaging reconstruction based on structured low-rank matrix completion. *Magn. Reson. Med.*, 72(4):959–970.

[Shin et al., 2008] Shin, T., Hu, H. H., Pohost, G. M., and Nayak, K. S. (2008). Three dimensional first-pass myocardial perfusion imaging at 3t: feasibility study. *Journal of Cardiovascular Magnetic Resonance*, 10(1):57.

[Shin et al., 2013] Shin, T., Nayak, K. S., Santos, J. M., Nishimura, D. G., Hu, B. S., and McConnell, M. V. (2013). Three-dimensional first-pass myocardial perfusion MRI using a stack-of-spirals acquisition. *Magnetic Resonance in Medicine*, 69(3):839–844.

[Shin et al., 2010] Shin, T., Pohost, G. M., and Nayak, K. S. (2010). Systolic 3d first-pass myocardial perfusion MRI: Comparison with diastolic imaging in healthy subjects. *Magnetic Resonance in Medicine*, 63(4):858–864.

[Sidebotham, 2007] Sidebotham, D., editor (2007). *Cardiothoracic critical care*. Butterworth-Heinemann, Philadelphia.

[Sieber et al., 2008] Sieber, M. A., Lengsfeld, P., Frenzel, T., Golfier, S., Schmitt-Willich, H., Siegmund, F., Walter, J., Weinmann, H.-J., and Pietsch, H. (2008). Preclinical investigation to compare different gadolinium-based contrast agents regarding their propensity to release gadolinium in vivo and to trigger nephrogenic systemic fibrosis-like lesions. *Eur Radiol*, 18(10):2164–2173.

[Skinner et al., 2010] Skinner, J. S., Smeeth, L., Kendall, J. M., Adams, P. C., and Timmis, A. (2010). NICE guidance. Chest pain of recent onset: assessment and diagnosis of recent onset chest pain or discomfort of suspected cardiac origin. *Heart*, 96(12):974–978.

[Slavin et al., 2001] Slavin, G. S., Wolff, S. D., Gupta, S. N., and Foo, T. K. F. (2001). First-Pass Myocardial Perfusion MR Imaging with Interleaved Notched Saturation: Feasibility Study. *Radiology*, 219(1):258–263.

[Slomka et al., 2005] Slomka, P. J., Nishina, H., Berman, D. S., Akincioglu, C., Abidov, A., Friedman, J. D., Hayes, S. W., and Germano, G. (2005). Automated quantification of myocardial perfusion SPECT using simplified normal limits. *J Nucl Cardiol*, 12(1):66–77.

[Smith et al., 2012] Smith, D. S., Gore, J. C., Yankeelov, T. E., and Welch, E. B. (2012). Real-Time Compressive Sensing MRI Reconstruction Using GPU Computing and Split Bregman Methods. *International Journal of Biomedical Imaging*, 2012:e864827.

[Sodickson and Manning, 1997] Sodickson, D. K. and Manning, W. J. (1997). Simultaneous acquisition of spatial harmonics (SMASH): Fast imaging with radiofrequency coil arrays. *Magnetic Resonance in Medicine*, 38(4):591–603.

[Sørensen et al., 2008] Sørensen, T., Schaeffter, T., Noe, K., and Hansen, M. (2008). Accelerating the Nonequispaced Fast Fourier Transform on Commodity Graphics Hardware. *IEEE Transactions on Medical Imaging*, 27(4):538–547.

[Stäb et al., 2014] Stäb, D., Wech, T., Breuer, F. A., Weng, A. M., Ritter, C. O., Hahn, D., and Köstler, H. (2014). High resolution myocardial first-pass perfusion imaging with extended anatomic coverage. *J. Magn. Reson. Imaging*, 39(6):1575–1587.

[Stone et al., 2008] Stone, S. S., Haldar, J. P., Tsao, S. C., Hwu, W. m. W., Sutton, B. P., and Liang, Z. P. (2008). Accelerating advanced MRI reconstructions on GPUs. *Journal of Parallel and Distributed Computing*, 68(10):1307–1318.

[Storey et al., 2002] Storey, P., Chen, Q., Li, W., Edelman, R. R., and Prasad, P. V. (2002). Band artifacts due to bulk motion. *Magnetic Resonance in Medicine*, 48(6):1028–1036.

[Storm and Slump, 2010] Storm, C. and Slump, C. (2010). Automated myocardial perfusion from coronary x-ray angiography. In Karssemeijer, N. and Summers, R., editors, *Medical Imaging 2010*, Proceedings of SPIE, page 76242S, United States. SPIE. 10.1117/12.840018.

[Taillefer et al., 1997] Taillefer, M., DePuey, M., Udelson, M., Beller, M., Latour, M., and Reeves, M. (1997). Comparative Diagnostic Accuracy of Tl-201 and Tc-99m Sestamibi SPECT Imaging (Perfusion and ECG-Gated SPECT) in Detecting Coronary Artery Disease in Women. *J Am Coll Cardiol*, 29(1):69–77.

[Takase et al., 2004] Takase, B., Nagata, M., Kihara, T., Kameyawa, A., Noya, K., Matsui, T., Ohsuzu, F., Ishihara, M., and Kurita, A. (2004). Whole-Heart Dipyridamole Stress First-Pass Myocardial Perfusion MRI for the Detection of Coronary Artery Disease. *Japanese Heart Journal*, 45(3):475–486.

[Task Force Members et al., 2013] Task Force Members, Montalescot, G., Sechtem, U., Achenbach, S., Andreotti, F., Arden, C., Budaj, A., Bugiardini, R., Crea, F., Cuisset, T., Di Mario, C., Ferreira, J. R., Gersh, B. J., Gitt, A. K., Hulot, J.-S., Marx, N., Opie, L. H., Pfisterer, M., Prescott, E., Ruschitzka, F., Sabaté, M., Senior, R., Taggart, D. P., van der Wall, E. E., Vrints, C. J. M., ESC Committee for Practice Guidelines, Zamorano, J. L., Achenbach, S., Baumgartner, H., Bax, J. J., Bueno, H., Dean, V., Deaton, C., Erol, C., Fagard, R., Ferrari, R., Hasdai, D., Hoes, A. W., Kirchhof, P., Knuuti, J., Kolh, P., Lancellotti, P., Linhart, A., Nihoyannopoulos, P., Piepoli, M. F., Ponikowski, P., Sirnes, P. A., Tamargo, J. L., Tendera, M., Torbicki, A., Wijns, W., Windecker, S., Document Reviewers, Knuuti, J., Valgimigli, M., Bueno, H., Claeys, M. J., Donner-Banzhoff, N., Erol, C., Frank, H., Funck-Brentano, C., Gaemperli, O., Gonzalez-Juanatey, J. R., Hamilos, M., Hasdai, D., Husted, S., James, S. K., Kervinen, K., Kolh, P., Kristensen, S. D., Lancellotti, P., Maggioni, A. P., Piepoli, M. F., Pries, A. R., Romeo, F., Rydén, L., Simoons, M. L., Sirnes, P. A., Steg, P. G., Timmis, A., Wijns, W., Windecker, S., Yildirir, A., and Zamorano, J. L. (2013). 2013 ESC guidelines on the management of stable coronary artery disease: the Task Force on the management of stable coronary artery disease of the European Society of Cardiology. *Eur. Heart J.*, 34(38):2949–3003.

[Taubman and Marcellin, 2002] Taubman, D. and Marcellin, M. (2002). *JPEG2000 Image Compression Fundamentals, Standards and Practice - Image Compression Fundamentals,*. Kluwer International Series in Engineering and Computer Science.

[Thulborn et al., 1982] Thulborn, K. R., Waterton, J. C., Matthews, P. M., and Radda, G. K. (1982). Oxygenation dependence of the transverse relaxation time of water protons in whole blood at high field. *Biochim. Biophys. Acta*, 714(2):265–270.

[Thygesen et al., 2007] Thygesen, K., Alpert, J. S., and White, H. D. (2007). Universal Definition of Myocardial Infarction. *Journal of the American College of Cardiology*, 50(22):2173–2195.

[Tian et al., 2017] Tian, Y., Erb, K. C., Adluru, G., Likhite, D., Pedgaonkar, A., Blatt, M., Kamesh Iyer, S., Roberts, J., and DiBella, E. (2017). Technical Note: Evaluation of prereconstruction interpolation methods for iterative reconstruction of radial kspace data. *Medical Physics*.

[Timmis et al., 1997] Timmis, A., Nathan, A., and Sullivan, I. (1997). *Essential Cardiology*. Blackwell Science Ltd, Cornwall, UK, 3rd edition.

[Townsend et al., 2015] Townsend, N., Bhatnagar, P., Wilkins, E., Wickramasinghe, K., and Rayner, M. (2015). Cardiovascular disease statistics 2015. Technical report, British Heart Foundation, London.

[Tsai and Nishimura, 2000] Tsai, C.-M. and Nishimura, D. G. (2000). Reduced aliasing artifacts using variable-density k-space sampling trajectories. *Magn. Reson. Med.*, 43(3):452–458.

[Tsao, 2002] Tsao, J. (2002). On the UNFOLD method. *Magn. Reson. Med.*, 47(1):202–207.

[Tsao et al., 2003] Tsao, J., Boesiger, P., and Pruessmann, K. P. (2003). k-t BLAST and k-t SENSE: Dynamic MRI with high frame rate exploiting spatiotemporal correlations. *Magnetic Resonance in Medicine*, 50(5):1031–1042.

[Tsao and Kozerke, 2012] Tsao, J. and Kozerke, S. (2012). MRI temporal acceleration techniques. *Journal of Magnetic Resonance Imaging*, 36(3):543–560.

[Tsekos et al., 1995] Tsekos, N. V., Zhang, Y., Merkle, H., Wilke, N., Jerosch-Herold, M., Stillman, A., and Uurbil, K. (1995). Fast anatomical imaging of the heart and assessment of myocardial perfusion with arrhythmia insensitive magnetization preparation. *Magnetic Resonance in Medicine*, 34(4):530–536.

[Tune et al., 2004] Tune, J. D., Gorman, M. W., and Feigl, E. O. (2004). Matching coronary blood flow to myocardial oxygen consumption. *Journal of Applied Physiology*, 97(1):404–415.

[Uecker et al., 2008] Uecker, M., Hohage, T., Block, K. T., and Frahm, J. (2008). Image reconstruction by regularized nonlinear inversionJoint estimation of coil sensitivities and image content. *Magnetic Resonance in Medicine*, 60(3):674–682.

[Uecker et al., 2014] Uecker, M., Lai, P., Murphy, M. J., Virtue, P., Elad, M., Pauly, J. M., Vasanawala, S. S., and Lustig, M. (2014). ESPIRiTan eigenvalue approach to autocalibrating parallel MRI: Where SENSE meets GRAPPA. *Magnetic Resonance in Medicine*, 71(3):990–1001.

[Uecker et al., 2012] Uecker, M., Zhang, S., Voit, D., Merboldt, K.-d., and Frahm, J. (2012). Real-time mri: recent advances using radial Flash. *Imaging in Medicine*, 4(4):461–476.

[Usman et al., 2013] Usman, M., Atkinson, D., Odille, F., Kolbitsch, C., Vaillant, G., Schaeffter, T., Batchelor, P. G., and Prieto, C. (2013). Motion corrected compressed sensing for free-breathing dynamic cardiac MRI. *Magn. Reson. Med.*, 70(2):504–516.

[Vallée et al., 1999] Vallée, J.-P., Lazeyras, F., Kasuboski, L., Chatelain, P., Howarth, N., Righetti, A., and Didier, D. (1999). Quantification of myocardial perfusion with FAST sequence and Gd bolus in patients with normal cardiac function. *Journal of Magnetic Resonance Imaging*, 9(2):197–203.

[van Heeswijk et al., 2012] van Heeswijk, R. B., Bonanno, G., Coppo, S., Coristine, A., Kober, T., and Stuber, M. (2012). Motion Compensation Strategies in Magnetic Resonance Imaging. *Critical Reviews in Biomedical Engineering*, 40(2):99–119.

[Varga-Szemes et al., 2015] Varga-Szemes, A., Meinel, F. G., De Cecco, C. N., Fuller, S. R., Bayer, R. R., and Schoepf, U. J. (2015). CT myocardial perfusion imaging. *AJR Am J Roentgenol*, 204(3):487–497.

[Vitanis et al., 2008] Vitanis, V., Gamper, U., Boesiger, P., and Kozerke, S. (2008). Compressed sensing cardiac perfusion imaging: feasibility and comparison to k-t BLAST. *Journal of Cardiovascular Magnetic Resonance*, 10(Suppl 1).

[Vitanis et al., 2009] Vitanis, V., Manka, R., Boesiger, P., and Kozerke, S. (2009). Accelerated cardiac perfusion imaging using k-t SENSE with SENSE training. *Magnetic Resonance in Medicine*, 62(4):955–965.

[Vitanis et al., 2011] Vitanis, V., Manka, R., Giese, D., Pedersen, H., Plein, S., Boesiger, P., and Kozerke, S. (2011). High resolution three-dimensional cardiac perfusion imaging using compartment-based k-t principal component analysis. *Magnetic Resonance in Medicine*, 65(2):575–587.

[Vogel-Claussen, 2012] Vogel-Claussen, J. (2012). Will 3d at 3-T Make Myocardial Stress Perfusion Magnetic Resonance Imaging Even More Competitive? *J Am Coll Cardiol*, 60(8):766–767.

[Walsh et al., 2000] Walsh, D. O., Gmitro, A. F., and Marcellin, M. W. (2000). Adaptive reconstruction of phased array MR imagery. *Magn. Reson. Med.*, 43(5):682–690.

[Wang et al., 2014a] Wang, H., Bangerter, N. K., Kholmovski, E., Taylor, M. I., and DiBella, E. V. (2014a). Dark rim artifacts from motion in highly accelerated 3d cardiac perfusion imaging. In *Joint Annual Meeting ISMRM-ESMRMB 2014*, Milan, Italy.

[Wang et al., 2014b] Wang, H., Bangerter, N. K., Park, D. J., Adluru, G., Kholmovski, E. G., Xu, J., and DiBella, E. (2014b). Comparison of centric and reverse-centric trajectories for highly accelerated three-dimensional saturation recovery cardiac perfusion imaging. *Magn. Reson. Med.*, page DOI: 10.1002/mrm.25478.

[Wang and Fernndez-Seara, 2006] Wang, Z. and Fernndez-Seara, M. A. (2006). 2d partially parallel imaging with k-space surrounding neighbors-based data reconstruction. *Magn. Reson. Med.*, 56(6):1389–1396.

[Watt and Routledge, 1985] Watt, A. and Routledge, P. (1985). Adenosine stimulates respiration in man. *British Journal of Clinical Pharmacology*, 20(5):503–506.

[Weiger et al., 2002] Weiger, M., Pruessmann, K. P., and Boesiger, P. (2002). 2d sense for faster 3d MRI. *MAGMA*, 14(1):10–19.

[Weiger et al., 2001] Weiger, M., Pruessmann, K. P., Leussler, C., Röschmann, P., and Boesiger, P. (2001). Specific coil design for SENSE: A six-element cardiac array. *Magnetic Resonance in Medicine*, 45(3):495–504.

[Weinmann et al., 1984] Weinmann, H. J., Brasch, R. C., Press, W. R., and Wesbey, G. E. (1984). Characteristics of gadolinium-DTPA complex: a potential NMR contrast agent. *AJR*, 142(3):619–624.

[White et al., 1984] White, C. W., Wright, C. B., Doty, D. B., Hiratza, L. F., Eastham, C. L., Harrison, D. G., and Marcus, M. L. (1984). Does Visual Interpretation of the Coronary Arteriogram Predict the Physiologic Importance of a Coronary Stenosis? *New England Journal of Medicine*, 310(13):819–824.

[Wiesinger et al., 2006] Wiesinger, F., Van de Moortele, P.-F., Adriany, G., De Zanche, N., Ugurbil, K., and Pruessmann, K. P. (2006). Potential and feasibility of parallel MRI at high field. *NMR in Biomedicine*, 19(3):368–378.

[Williams et al., 1992] Williams, D. S., Detre, J. A., Leigh, J. S., and Koretsky, A. P. (1992). Magnetic resonance imaging of perfusion using spin inversion of arterial water. *PNAS*, 89(1):212–216.

[Winkelmann et al., 2007] Winkelmann, S., Schaeffter, T., Koehler, T., Eggers, H., and Doessel, O. (2007). An Optimal Radial Profile Order Based on the Golden Ratio for Time-Resolved MRI. *IEEE Transactions on Medical Imaging*, 26(1):68–76.

[Wissmann et al., 2014a] Wissmann, L., Niemann, M., Manka, R., and Kozerke, S. (2014a). Quantitative 3d myocardial perfusion imaging at high does with accurate arterial input function assessment. In *Joint Annual Meeting ISMRM-ESMRMB 2014*, Milan, Italy.

[Wissmann et al., 2014b] Wissmann, L., Santelli, C., Segars, W. P., and Kozerke, S. (2014b). MRXCAT: Realistic numerical phantoms for cardiovascular magnetic resonance. *J Cardiovasc Magn Reson*, 16(1):63.

[Wolff et al., 2004] Wolff, S. D., Schwitter, J., Coulden, R., Friedrich, M. G., Bluemke, D. A., Biederman, R. W., Martin, E. T., Lansky, A. J., Kashanian, F., Foo, T. K. F., Licato, P. E., and Comeau, C. R. (2004). Myocardial First-Pass Perfusion Magnetic Resonance Imaging A Multicenter Dose-Ranging Study. *Circulation*, 110(6):732–737.

[Wong and Roos, 1994] Wong, S. T. S. and Roos, M. S. (1994). A strategy for sampling on a sphere applied to 3d selective RF pulse design. *Magn. Reson. Med.*, 32(6):778–784.

[Wright et al., 2014] Wright, K. L., Lee, G. R., Ehses, P., Griswold, M. A., Gulani, V., and Seiberlich, N. (2014). Three-dimensional through-time radial GRAPPA for renal MR angiography. *Journal of Magnetic Resonance Imaging*, 40(4):864–874.

[Xue et al., 2012] Xue, H., Shah, S., Greiser, A., Guetter, C., Littmann, A., Jolly, M.-P., Arai, A. E., Zuehlsdorff, S., Guehring, J., and Kellman, P. (2012). Motion correction for myocardial T1 mapping using image registration with synthetic image estimation. *Magnetic Resonance Medicine*, 67(6):1644–1655.

[Xue et al., 2009] Xue, H., Zuehlsdorff, S., Kellman, P., Arai, A., Nielles-Vallespin, S., Chefdhotel, C., Lorenz, C. H., and Guehring, J. (2009). Unsupervised inline analysis of cardiac perfusion MRI. *Med Image Comput Comput Assist Interv*, 12(Pt 2):741–749.

[Yang and Kim, 2017] Yang, D. H. and Kim, Y.-H. (2017). CT myocardial perfusion imaging: current status and future perspectives. *Int J Cardiovasc Imaging*, pages 1–12.

[Yang et al., 2014] Yang, Y., Chen, X., Epstein, F. H., Meyer, C. H., Kramer, C. M., and Salerno, M. (2014). 3d whole-heart quantitative first-pass perfusion imaging with a stack-of-spirals trajectory. In *Joint Annual Meeting ISMRM-ESMRMB 2014*, Milan, Italy.

[Yang et al., 2017] Yang, Y., Zhao, L., Chen, X., Shaw, P. W., Gonzalez, J. A., Epstein, F. H., Meyer, C. H., Kramer, C. M., and Salerno, M. (2017). Reduced field of view single-shot spiral perfusion imaging. *Magn. Reson. Med.*, page In press.

[Ying et al., 2004] Ying, L., Xu, D., and Liang, Z.-P. (2004). On Tikhonov regularization for image reconstruction in parallel MRI. In *26th Annual International Conference of the IEEE Engineering in Medicine and Biology Society, 2004. IEMBS '04*, volume 1, pages 1056–1059.

[Yudilevich and Stark, 1987] Yudilevich, E. and Stark, H. (1987). Spiral Sampling in Magnetic Resonance Imaging-The Effect of Inhomogeneities. *IEEE Transactions on Medical Imaging*, 6(4):337–345.

[Zheng, 2013] Zheng, J. (2013). Assessment of myocardial oxygenation with MRI. *Quant Imaging Med Surg*, 3(2):67–72.

[Zhou and Pu, 2016] Zhou, P. and Pu, W. T. (2016). Recounting cardiac cellular composition. *Circ Res*, 118(3):368–370.

[Zhou et al., 2016] Zhou, Z., Bi, X., Wei, J., Yang, H.-J., Dharmakumar, R., Arsanjani, R., Merz, B., Noel, C., Li, D., and Sharif, B. (2016). Firstpass myocardial perfusion MRI with reduced subendocardial darkrim artifact using optimized Cartesian sampling. *Journal of Magnetic Resonance Imaging*.

[Zun et al., 2011] Zun, Z., Varadarajan, P., Pai, R. G., Wong, E. C., and Nayak, K. S. (2011). Arterial Spin Labeled CMR Detects Clinically Relevant Increase in Myocardial Blood Flow With Vasodilation. *JACC: Cardiovascular Imaging*, 4(12):1253–1261.

A. 3D FPP Trajectory Shot Duration Comparisons

Timings of potential 3D FPP sequences are estimated here for typical FLASH, h-EPI and spiral sequences. With no other acceleration techniques applied to reduce these timings, and given the proposed allowed acquisition time, these should allow the reader an idea of the approximate relative acceleration achievable through these sequence types and the level of acceleration still required through other methods. Care has been taken to choose values appropriate to the application, but with adjustment of these parameters a topic by itself the examples provided are clearly only for illustrative purposes.

T_{RF} duration of single RF excitation pulse.
T_{RO} duration of single ADC readout.
T_{DEAD} other time per TR, not due to T_{RF} or T_{RO}

Desired Parameters	
FOV / mm	(300 × 225)
Acquired in-plane resolution / mm	(2.3 × 2.3)
Acquired phase-encodes, N_Y	98
Acquired partition-encodes, N_Z	12*
Allowed acquisition window, T_A / ms	150

*to give 100mm coverage at 10mm resolution + 2 partitions oversampling

Calculations			
	FLASH	**h-EPI**	**Spiral**
TR / ms	$T_{RF} + T_{DEAD} + T_{RO}$	$T_{RF} + T_{DEAD} + T_{RO}$	$T_{RF} + T_{DEAD} + T_{RO}$
Total Acquisition Time / ms	$TR \times N_Y \times N_Z$	$TR \times N_Y \times N_Z$ / N_E	$TR \times N_Z \times N_{INT}$
Examples			
T_{RF} / ms	0.6	0.6	0.6
T_{RO} / ms	0.6	Echo train length, N_E, dependent. E.g $N_E = 4$ giving 2.4	Number of interleaves, N_{INT}, dependent. E.g. $N_{INT} = 16$ giving 4.4
T_{DEAD} / ms	1.2	1.2	1.2
Total Acquisition Time / ms	2820	1230	1190
Required Acceleration (Total Acquisition Time / T_A)	$\sim$19	$\sim$9	$\sim$8

B. Ethics Forms

The following information sheets and consent forms were used during the testing of the sequence at stress.

PATIENT INFORMATION SHEET

Development of Cardiovascular Magnetic Resonance Sequences for Future Clinical Use

(For patients having a CMR stress test)

We would like to invite you to take part in this research study to help develop Cardiovascular Magnetic Resonance (CMR) sequences for future use in patients. Your participation is entirely voluntary and the following information may help you decide if you wish to take part. Before you decide it is important for you to understand why the research is being done and what it will involve. Please take time to read the following information carefully.

- Part one tells you the purpose of this study and what will happen to you if you take part.
- Part two gives you more detailed information about the conduct of the study.

Please ask us if there anything that is not clear or if you would like more information. Take time to decide whether or not you wish to take part.

PART ONE

What is the purpose of the study?

The techniques that we use to take images are known as CMR sequences and these can be modified to obtain different information from the inside of your body. The purpose of this study is to develop new CMR sequences for clinical use in Cardiovascular Magnetic Resonance. In the future these sequences may improve the quality of information that we obtain, and may reduce the time needed to scan a patient. MR scanning is very safe and does not use X-rays.

Why have I been chosen?

The research team of the CMR Unit are continuously updating, modifying and developing new sequences. You are well suited to help test our sequence and technique developments.

What would the study involve?

The CMR scan will involve lying in the scanner and you may be asked to follow breath-hold instructions. As in a regular stress test, ECG electrodes will be attached to your chest which will allow us to monitor your heart rate. A blood pressure cuff will be placed around your arm to monitor your blood pressure. We will monitor closely your heart rate, blood pressure, and ECG during the study. If we are worried about any of these, the test will be stopped. Close observations are also made before, during, or after either exercise stress or adenosine infusion. The complete scan will last approximately one hour.

As part of our study, you may be having an injection of dye that would show up on the images. This dye would normally be injected by hand using a syringe and line into a vein in your forearm. For this project we would like to inject the dye in a more controlled way by using an injector that is used routinely for patients having MR scans to look at the blood vessels. By using this injector, there is a very slight risk of damaging the vein, but in more than ten years of regularly using an injector we have no record of this happening. Additional scans will be acquired during the injection of the dye which will add approximately 2 minutes to the scan. If you are above the age of 60 or have had kidney problems, it may be necessary to have blood drawn in the lab prior to the MRI to check your kidney function. A previous history of kidney failure, dialysis, or liver transplant will prohibit you from receiving the contrast injection. Please inform your physician and technologist of this prior to the exam.

You will be asked either to undertake exercise stress or adenosine infusion. Physical exercise would be done either inside or outside the scanner in a variety of ways including running on a treadmill, cycling a stationary bicycle, turning a crank, or leg raising. During the test, the exercise would generally start slowly and get harder, but would accommodate and be regulated by your ability and feedback. Pharmacological stress would be generated by adenosine infusion usually through a separate drip. This will increase the flow of blood through the coronary arteries and/or make your heart beat faster and work harder to simulate exercise. The medicine may make you flushed and/or anxious, but the effects will disappear as soon as the infusion is over. You will be asked to abstain from tea, coffee, chocolate and other caffeine containing drinks, for example cola, for 24 hours before the scan because these counteract the effects of adenosine.

We may invite you to undergo a repeat scan after a short period (1 to 4 weeks) to test the reproducibility of the developed technique, or a relatively long period (6 to 60 months) to test the method's ability to measure small changes in the structure or function of the heart or vessels. Should this happen, we will ask for your permission again before these scans are arranged.

Do I have to take part?

No. Your participation in this study is entirely voluntary and it is up to you to decide whether or not you want to take part. We will describe the study and go through this information sheet which we will then give to you. If you choose to participate, you will be asked to sign a consent form. You are free to withdraw your consent at any time or choose not to participate. This will not affect your future normal care or treatment in any way and you do not have to give any reasons if you wish to withdraw.

What will happen to me if I take part?

If you agree to take part, we will ask you for some information about your health and medical condition. We will record details of your heart scan, information from previous heart scans you have had and information from your hospital notes on a confidential computer database. This will be done at the time of your scan.

You will not be charged for any of the scans and if you agree to have this research scan, you will be reimbursed for your reasonable travel expenses.

What are the risks involved when taking part?

Personal information held on a database

The information will be kept on a database on NHS computers. This is kept strictly confidential and we will take great care of the personal data you give us. Data protection procedures are explained in Part Two of this information sheet.

Contrast Agent

The contrast agent is usually well tolerated; on rare occasions it can cause a sensation of warmth or pressure in the area where the injection is given and occasionally patients describe a slight metallic taste in the mouth. The injection has no known long-term side effects. In subjects with impaired kidney function there are reports of the occurrence of a disease called Nephrogenic Systemic Fibrosis for which the symptoms are: swelling and tightening of the skin, usually limited to the extremities. If not tested in the last three months a small blood sample will be used to test kidney function before administering the contrast agent. No cases of Nephrogenic Systemic Fibrosis have been reported in people with normal kidney function. There have been documented allergic reactions to the contrast agent, but that has been an extremely rare occurrence.

Potential complications of Adenosine

The risks of the test are very small and are associated with the medication that is used. Adenosine is commonly used in routine CMR scans but may occasionally cause some minor side effects, such as facial flushing, mild headache, mild shortness of breath, arm or jaw discomfort, changes in heart rate and blood pressure, dizziness and lightheadedness. In most cases, these effects subside within a few seconds of stopping the adenosine infusion or can be easily reversed. Severe complications such as the possibility of heart attack and/or death are extremely rare. The careful monitoring of your blood pressure and continuous heart monitoring serve to minimise the small risks of the test. However, if you suffer with asthma or other forms of breathing complaints such as chronic obstructive airways disease you may not be suitable for this particular part of the study.

People with a history of allergy are more likely to suffer a more severe reaction, but this is rare (less than 1 in 3000). The department is equipped to cope with allergic reactions if they happen. If you have any queries regarding your suitability, we would be happy to discuss this further.

What are the possible benefits of taking part?

There's no obvious benefit to you at this time but we expect the developments will improve the ability of CMR to assess patients with a relevant cardiovascular disease in the future.

These scans are for sequence development only and are not intended to screen for any pathology. However, if any further pathology were detected, you would be informed and the details would be passed on to the CMR consultant who dealt with your clinical scan.

What if there is a problem?

Any complaint about the way you have been dealt with during the study or any possible harm you might suffer will be addressed.

If you have a concern about any aspect of this study, you should ask to speak with the researchers (Professor Firmin or one of his team) who will do their best to answer your question. They can be contacted between 9am and 5pm on:

Professor David Firmin – 020 7351 8800

Will my taking part in the study be kept confidential?
Yes. All the information about your participation in this study will be kept confidential. The details are included in Part 2.

This completes part one of the information sheet.
If the information in Part one has interested you and you are considering participation, please continue to read the additional information in Part two before making any decision.

PART TWO

What will happen if I don't want to carry on with the study?

If you choose not to participate or withdraw your consent at anytime, this will not affect your future medical care and you will not lose any benefits that you would ordinarily receive. If you decide to withdraw from the study, you should inform **Professor Firmin or one of his team**. You do not have to give any reasons why you have decided to withdraw.

If you withdraw from the study, your data will not be used and will be deleted.

What if there is a problem?

Complaints:

If you have a concern about any aspect of this study, you should ask to speak with the researchers who will do their best to answer your question. They can be contacted between 9am and 5pm on:

Professor David N Firmin	**Professor Dudley J Pennell**
020 7351 8800	**020 7351 8800**

If you remain unhappy and wish to complain formally, you can do this through the NHS Complaints Procedure/Patient Advice and Liaison Service on 020 7352 8121.

Harm:

If you are harmed as a direct result of taking part in this study, there are no special compensation arrangements. If you are harmed due to someone's negligence, then you may have grounds for legal action. Regardless of this, if you have any cause to complain about any aspects of the way you have been approached or treated during the course of this study, the normal National Health Service complaints mechanisms are available to you.

Will my taking part in this study be kept confidential?

By signing this consent form you will be giving permission for the research staff involved in this study to review your medical records at the Royal Brompton and your local hospital. All data we collect will be kept strictly confidential. Confidential information will not be released for any reason unless disclosure is required by law. The doctors at the Royal Brompton Hospital will keep your name and address in case they need to contact you about the study.

Data protection

The data will be stored on NHS computers at the Royal Brompton Hospital. Our procedures for handling, processing, storage and destruction of your data are compliant with the Data Protection Act 1998.

What will happen to the results of the research study?

After the study has been completed, we may wish to publish the results of the study in a medical journal and present the results at local and international medical meetings. You will not be identifiable in the publication. We would be happy to provide you with a copy of the results if requested.

What happens to my data and images?

Your images and data will be labelled so that they are anonymous to anyone outside of the Royal Brompton and Harefield NHS Foundation Trust Project team. As part of developing new techniques and products to enhance or optimise the use of clinical imaging techniques or products, we often work with academic and commercial collaborators and may need to send them some of your images and data. Any use of the images or data by these academic and commercial partners is for research and development purposes only and has been approved by an independent research ethics committee.

Who is organising and funding the research?

The study is organised by Imperial College and the Cardiovascular Magnetic Resonance (CMR) Unit at the Royal Brompton & Harefield NHS Trust Hospital in London. The study will be funded by one of a variety of sources including charitable and health service grants.

Who has reviewed the study?

This study has been given a favourable opinion by East London REC 3. This is an independent group of people whose responsibility it is to protect your safety, rights, wellbeing and dignity.

QUESTIONS:

You will be given a copy of this patient information sheet and a copy of a signed consent form to keep. If you have any questions, please do not hesitate to contact us on 020 7351 8800 from 9 am until 5 pm.

Professor David Firmin
020 7351 8800

Professor Dudley Pennell
020 7351 8800

For objective information on taking part in research, you can talk to the Patient Advice and Liaison Service (PALS) at the Royal Brompton Hospital. They can be contacted on: 020 7352 8121.

Thank you for considering taking part in this study and taking time to read this patient information sheet.

Royal Brompton & Harefield NHS
NHS Foundation Trust

Cardiovascular Magnetic Resonance Unit

Sydney Street
London
SW3 6NP
Enquiries: 020 7351 8800
020 7351 8805
Fax: 020 7351 8816

NOTES FOR PARTICIPANTS

1. Please do not hesitate to ask the Doctor any questions you may have about this project before you decide whether you wish to participate.
2. If you decide, now or at any other stage, that you no longer wish to participate in the project, this will not in any way prejudice your future treatment.
3. If you decide to take part in this project, you will be given a copy of this form for your information.

CONSENT FORM

Title of Project: **Development of Cardiovascular Magnetic Resonance Sequences for Future Clinical Use (For patients having a CMR stress test)**

Name of Researchers: Professor David N Firmin & Professor Dudley J Pennell **Please initial box**

1. I confirm that I have read and understand the information sheet dated 25/04/2012 (Version 2) for the above study. I have had the opportunity to consider the information, ask questions and have had these answered satisfactorily. ☐
2. I understand that my participation is voluntary and that I am free to withdraw at any time, without giving any reason, without my medical care or legal rights being affected. ☐
3. I understand that relevant sections of any of my medical notes and data collected during the study may be looked at by responsible individuals from the Trust, regulatory authorities or from Imperial College, where it is relevant to my taking part in this research. I give my permission for these individuals to have direct access to the records. ☐
4. I am happy for the research team to contact me by telephone. ☐
5. I agree to take part in the above study. ☐

_____	_____	_____
Name of Patient	Date	Signature
_____	_____	_____
Name of Person taking consent	Date	Signature
_____	_____	_____
Researcher	Date	Signature

SUBJECT INFORMATION SHEET

Development of Cardiovascular Magnetic Resonance Sequences for Future Clinical Use

(For subjects having a CMR stress test)

We would like to invite you to take part in this research study to help develop Cardiovascular Magnetic Resonance (CMR) sequences for future use in patients. Your participation is entirely voluntary and the following information may help you decide if you wish to take part. Before you decide it is important for you to understand why the research is being done and what it will involve. Please take time to read the following information carefully.

- Part one tells you the purpose of this study and what will happen to you if you take part.
- Part two gives you more detailed information about the conduct of the study.

Please ask us if there anything that is not clear or if you would like more information. Take time to decide whether or not you wish to take part.

PART ONE

What is the purpose of the study?

The techniques that we use to take images are known as CMR sequences and these can be modified to obtain different information from the inside of your body. The purpose of this study is to develop new CMR sequences for clinical use in Cardiovascular Magnetic Resonance. In the future these sequences may improve the quality of information that we obtain, and may reduce the time needed to scan a patient. MR scanning is very safe and does not use X-rays.

Why have I been chosen?

The research team of the CMR Unit are continuously updating, modifying and developing new sequences. You are well suited to help test our sequence and technique developments.

What would the study involve?

The CMR scan will involve lying in the scanner and you may be asked to follow breath-hold instructions. As in a regular stress test, ECG electrodes will be attached to your chest which will allow us to monitor your heart rate. A blood pressure cuff will be placed around your arm to monitor your blood pressure. We will monitor closely your heart rate, blood pressure, and ECG during the study. If we are worried about any of these, the test will be stopped. Close observations are also made before, during, or after either exercise stress or adenosine infusion. The complete scan will last approximately one hour.

As part of our study, you may be having an injection of dye that would show up on the images. This dye would normally be injected by hand using a syringe and line into a vein in your forearm. For this project we would like to inject the dye in a more controlled way by using an injector that is used routinely for patients having MR scans to look at the blood vessels. By using this injector, there is a very slight risk of damaging the vein, but in more than ten years of regularly using an injector we have no record of this happening. Additional scans will be acquired during the injection of the dye which will add approximately 2 minutes to the scan. If you are above the age of 60 or have had kidney problems, it may be necessary to have blood drawn in the lab prior to the MRI to check your kidney function. A previous history of kidney failure, dialysis, or liver transplant will prohibit you from receiving the contrast injection. Please inform your physician and technologist of this prior to the exam.

You will be asked either to undertake exercise stress or adenosine infusion. Physical exercise would be done either inside or outside the scanner in a variety of ways including running on a treadmill, cycling a stationary bicycle, turning a crank, or leg raising. During the test, the exercise would generally start slowly and get harder, but would accommodate and be regulated by your ability and feedback. Pharmacological stress would be generated by adenosine infusion usually through a separate drip. This will increase the flow of blood through the coronary arteries and/or make your heart beat faster and work harder to simulate exercise. The medicine may make you flushed and/or anxious, but the effects will disappear as soon as the infusion is over. You will be asked to abstain from tea, coffee, chocolate and other caffeine containing drinks, for example cola, for 24 hours before the scan because these counteract the effects of adenosine.

We may invite you to undergo a repeat scan after a short period (1 to 4 weeks) to test the reproducibility of the developed technique, or a relatively long period (6 to 60 months) to test the methods ability to measure small changes in the structure or function of the heart or vessels. Should this happen, we will ask for your permission again before these scans are arranged.

Do I have to take part?

No. Your participation in this study is entirely voluntary and it is up to you to decide whether or not you want to take part. We will describe the study and go through this information sheet which we will then give to you. If you choose to participate, you will be asked to sign a consent form. You are free to withdraw your consent at any time or choose not to participate. This will not affect your future normal care or treatment in any way and you do not have to give any reasons if you wish to withdraw.

What will happen to me if I take part?

If you agree to take part, we will ask you for some information about your health and medical condition. You will not be charged for any of the scans and if you agree to have this research scan, you will be reimbursed for your reasonable travel expenses.

What are the risks involved when taking part?

Personal information held on a database

The information will be kept on a database on NHS computers. This is kept strictly confidential and we will take great care of the personal data you give us. Data protection procedures are explained in Part Two of this information sheet.

Contrast Agent

The contrast agent is usually well tolerated; on rare occasions it can cause a sensation of warmth or pressure in the area where the injection is given and occasionally patients describe a slight

metallic taste in the mouth. The injection has no known long-term side effects. In subjects with impaired kidney function there are reports of the occurrence of a disease called Nephrogenic Systemic Fibrosis for which the symptoms are: swelling and tightening of the skin, usually limited to the extremities. If not tested in the last three months a small blood sample will be used to test kidney function before administering the contrast agent. No cases of Nephrogenic Systemic Fibrosis have been reported in people with normal kidney function. There have been documented allergic reactions to the contrast agent, but that has been an extremely rare occurrence.

Potential complications of Adenosine

The risks of the test are very small and are associated with the medication that is used. Adenosine is commonly used in routine CMR scans but may occasionally cause some minor side effects, such as facial flushing, mild headache, mild shortness of breath, arm or jaw discomfort, changes in heart rate and blood pressure, dizziness and lightheadedness. In most cases, these effects subside within a few seconds of stopping the adenosine infusion or can be easily reversed. Severe complications such as the possibility of heart attack and/or death are extremely rare. The careful monitoring of your blood pressure and continuous heart monitoring serve to minimise the small risks of the test. However, if you suffer with asthma or other forms of breathing complaints such as chronic obstructive airways disease you may not be suitable for this particular part of the study.

People with a history of allergy are more likely to suffer a more severe reaction, but this is rare (less than 1 in 3000). The department is equipped to cope with allergic reactions if they happen. If you have any queries regarding your suitability, we would be happy to discuss this further.

What are the possible benefits of taking part?

There's no obvious benefit to you at this time but we expect the developments will improve the ability of CMR to assess patients with a relevant cardiovascular disease in the future.

These scans are for sequence development only and are not intended to screen for any pathology. However, if any further pathology were detected, you would be informed and the details would be passed on to the CMR consultant who dealt with your clinical scan.

What if there is a problem?

Any complaint about the way you have been dealt with during the study or any possible harm you might suffer will be addressed.

If you have a concern about any aspect of this study, you should ask to speak with the researchers (Professor Firmin or one of his team) who will do their best to answer your question. They can be

contacted between 9am and 5pm on:

Professor David Firmin – 020 7351 8800

Will my taking part in the study be kept confidential?
Yes. All the information about your participation in this study will be kept confidential. The details are included in Part 2.

This completes part one of the information sheet.
If the information in Part one has interested you and you are considering participation, please continue to read the additional information in Part two before making any decision.

PART TWO

What will happen if I don't want to carry on with the study?

If you choose not to participate or withdraw your consent at anytime, this will not affect your future medical care and you will not lose any benefits that you would ordinarily receive. If you decide to withdraw from the study, you should inform **Professor Firmin or one of his team**. You do not have to give any reasons why you have decided to withdraw.

If you withdraw from the study, your data will not be used and will be deleted.

What if there is a problem?

Complaints:

If you have a concern about any aspect of this study, you should ask to speak with the researchers who will do their best to answer your question. They can be contacted between 9am and 5pm on:

Professor David N Firmin	**Professor Dudley J Pennell**
020 7351 8800	**020 7351 8800**

If you remain unhappy and wish to complain formally, you can do this through the NHS Complaints Procedure/Patient Advice and Liaison Service on 020 7352 8121.

Harm:

If you are harmed as a direct result of taking part in this study, there are no special compensation arrangements. If you are harmed due to someone's negligence, then you may have grounds for legal action. Regardless of this, if you have any cause to complain about any aspects of the way you have been approached or treated during the course of this study, the normal National Health Service complaints mechanisms are available to you.

Will my taking part in this study be kept confidential?

By signing this consent form you will be giving permission for the research staff involved in this study to review your medical records at the Royal Brompton and your local hospital. All data we collect will be kept strictly confidential. Confidential information will not be released for any reason unless disclosure is required by law. The doctors at the Royal Brompton Hospital will keep your name and address in case they need to contact you about the study.

Data protection

The data will be stored on NHS computers at the Royal Brompton Hospital. Our procedures for handling, processing, storage and destruction of your data are compliant with the Data Protection Act 1998.

What will happen to the results of the research study?

After the study has been completed, we may wish to publish the results of the study in a medical journal and present the results at local and international medical meetings. You will not be identifiable in the publication. We would be happy to provide you with a copy of the results if requested.

What happens to my data and images?

Your images and data will be labelled so that they are anonymous to anyone outside of the Royal Brompton and Harefield NHS Foundation Trust Project team. As part of developing new techniques and products to enhance or optimise the use of clinical imaging techniques or products, we often work with academic and commercial collaborators and may need to send them some of your images and data. Any use of the images or data by these academic and commercial partners is for research and development purposes only and has been approved by an independent research ethics committee.

Who is organising and funding the research?

The study is organised by Imperial College and the Cardiovascular Magnetic Resonance (CMR) Unit at the Royal Brompton & Harefield NHS Trust Hospital in London. The study will be funded by one of a variety of sources including charitable and health service grants.

Who has reviewed the study?

This study has been given a favourable opinion by East London REC 3. This is an independent group of people whose responsibility it is to protect your safety, rights, wellbeing and dignity.

QUESTIONS:

You will be given a copy of this patient information sheet and a copy of a signed consent form to keep. If you have any questions, please do not hesitate to contact us on 020 7351 8800 from 9 am until 5 pm.

Professor David Firmin
020 7351 8800

Professor Dudley Pennell
020 7351 8800

For objective information on taking part in research, you can talk to the Patient Advice and Liaison Service (PALS) at the Royal Brompton Hospital. They can be contacted on: 020 7352 8121.

Thank you for considering taking part in this study and taking time to read this patient information sheet.

Royal Brompton & Harefield NHS
NHS Foundation Trust

Cardiovascular Magnetic Resonance Unit

Sydney Street
London
SW3 6NP
Enquiries: 020 7351 8800
020 7351 8805
Fax: 020 7351 8816

NOTES FOR PARTICIPANTS

1. Please do not hesitate to ask the Doctor any questions you may have about this project before you decide whether you wish to participate.
2. If you decide, now or at any other stage, that you no longer wish to participate in the project, this will not in any way prejudice your future treatment.
3. If you decide to take part in this project, you will be given a copy of this form for your information.

CONSENT FORM

Title of Project: **Development of Cardiovascular Magnetic Resonance Sequences for Future Clinical Use (For subjects having a CMR stress test)**

Name of Researchers: Professor David N Firmin & Professor Dudley J Pennell **Please initial box**

1. I confirm that I have read and understand the information sheet dated 25/04/2012 (Version 2) for the above study. I have had the opportunity to consider the information, ask questions and have had these answered satisfactorily. ☐
2. I understand that my participation is voluntary and that I am free to withdraw at any time, without giving any reason, without my medical care or legal rights being affected. ☐
3. I understand that relevant sections of any of my medical notes and data collected during the study may be looked at by responsible individuals from the Trust, regulatory authorities or from Imperial College, where it is relevant to my taking part in this research. I give my permission for these individuals to have direct access to the records. ☐
4. I am happy for the research team to contact me by telephone. ☐
5. I agree to take part in the above study. ☐

_____	_____	_____
Name of Patient	Date	Signature
_____	_____	_____
Name of Person taking consent	Date	Signature
_____	_____	_____
Researcher	Date	Signature

C. Supplementary Files

Access to video files of 3D FPP datasets is made available at:

`https://tinyurl.com/ydbuatzw`

This contains the files:

Patient1_stress.avi
Patient1_rest.avi
Patient2_stress.avi
Patient2_rest.avi
Patient3_stress.avi
Patient3_rest.avi
Patient4_stress.avi
Patient4_rest.avi

which are the corresponding stress and rest FPP datasets for the four CAD patients imaged in Chapter 6.

D. Figure Reuse Permissions

Figure	Reference	Original ID	Publisher	License #
Figure 1.3	[Cerqueira et al., 2002]	Figure 1	Wolters Kluwer Health, Inc.	4230311315705
Figure 1.5	[Sidebotham, 2007]	Figure 1.3	Elsevier	4210840622268
Figure 1.8	[Lusis, 2012]	Figure 1	Elsevier	4210840762519
Figure 1.9	[Schinkel et al., 2003]	Figure 1	Oxford University Press	4210841012081
Figure 1.10	[Gerber et al., 2008]	Figure 2	BioMed Central	*
Figure 1.11	[Lyne et al., 2007]	Figure 4	John Wiley and Sons	4210850093435
Figure 2.4	[Pedersen et al., 2009b]	Figure 3	John Wiley and Sons	4210851181948
Figure 2.5	[Madore et al., 1999]	Figure 9	John Wiley and Sons	4210851278524
Figure 2.6	[Tsao et al., 2003]	Figure 1	John Wiley and Sons	4210851416125
Figure 2.7	[Vitanis et al., 2011]	Figure 10	John Wiley and Sons	4211831436426
Figure 2.8	[Lingala et al., 2011]	Figure 1	IEEE	†
Figure 2.9	[Chen et al., 2012]	Figure 6	John Wiley and Sons	4211941273699
Figure 2.10	[Shin et al., 2013]	Figure 4	John Wiley and Sons	4211860865717
Figure 3.7	[Chow et al., 2015]	Figure 7	BioMed Central	*
Figure 4.13	[Adluru and DiBella, 2008]	Figure 5	Hindawi	*
Figure 5.16	[Pullan et al., 2010]	Figure 7	Springer	4211861179179
Table 1.1	[Salerno and Beller, 2009]	Table 1	Wolters Kluwer Health, Inc.	4210841239783
Table 1.2	[Yang and Kim, 2017]	Table 4	Springer	4210850238096

*This is an open access article distributed under the Creative Commons Attribution License, which permits unrestricted use, distribution, and reproduction in any medium, provided the original work is properly cited.
†The IEEE does not require individuals working on a thesis to obtain a formal reuse license.

E. List of Publications

Full Papers

Fair MJ, Gatehouse PD, Drivas P, Firmin DN. (2016), Improved dynamic parallel imaging coil calibration method robust to respiratory motion with application to first-pass contrast-enhanced myocardial perfusion imaging. *Magn Reson Med*, 75(6):23152323. doi:10.1002/mrm.25819

Fair MJ, Gatehouse PD, DiBella EVR, Firmin DN. (2015), A review of 3D first-pass, whole-heart, myocardial perfusion cardiovascular magnetic resonance. *J Cardiovasc Magn Reson*, 17:68. doi:10.1186/s12968-015-0162-9

International Conference Abstracts

Fair MJ, Reyes E, Gatehouse PD, Adluru G, Mendes J, Wage R, DiBella EVR, Firmin DN., Free breathing 3D whole-heart stress myocardial perfusion using compressed sensing. *ISMRM*, 2017. Abstract #0527 [**Summa Cum Laude**]

Fair MJ, Gatehouse PD, DiBella EVR, Firmin DN., An analysis of radial sequence parameters in myocardial first-pass perfusion for optimised imaging. *ISMRM*, 2017. Abstract #3248

Fair MJ, Gatehouse PD, Chen L, Wage R, DiBella EVR, Firmin DN., 3D first-pass myocardial perfusion stack-of-stars imaging using balanced steady-state free precession. *ISMRM*, 2016. Abstract #3144

Fair MJ, Gatehouse PD, Chen L, Wage R, DiBella EVR, Firmin DN., An extended 3D whole-heart myocardial first-pass perfusion sequence: alternate-cycle views with isotropic and high-resolution imaging. *ISMRM*, 2016.

Abstract #0993

Fair MJ, Gatehouse PD, Drivas P, Firmin DN., Comparison of a multiple free-breathing prescans (MFP) method of coil sensitivity calibration against TGRAPPA during free-breathing myocardial first-pass perfusion. *ISMRM*, 2015. Abstract #3798 [**Magna Cum Laude**]

Fair MJ, Gatehouse PD, Firmin DN., Through-plane dark-rim artefacts in 3D first-pass myocardial perfusion imaging. *ISMRM*, 2015. Abstract #4494

Fair MJ, Gatehouse PD, Drivas P, Firmin DN., Method for correcting respiratory artefacts in parallel-accelerated first-pass myocardial perfusion imaging. *ISMRM*, 2014. Abstract #3935

+5 *SCMR* abstracts